DISS. ETH NO. 25594

DEVELOPMENT OF SELF-CENTERING SYSTEMS WITH GEOMETRY-CONTROLLED STIFFNESS FOR EARTHQUAKE HAZARD MITIGATION

A thesis submitted to attain the degree of

DOCTOR OF SCIENCES of ETH ZURICH

(Dr. sc. ETH Zurich)

presented by

JONAS ANDRIN BACHMANN

MSc ETH in Civil Engineering

born on 04.06.1987
citizen of
Strengelbach AG and Chêne-Bougeries GE

accepted on the recommendation of

Prof. Dr. Božidar Stojadinović
Prof. Dr. Ioannis N. Psycharis
Prof. Dr. Ioannis Anastasopoulos

2018

ACKNOWLEDGEMENTS

The present doctoral thesis concludes my activity as a research assistant at the Chair of Structural Dynamics and Earthquake Engineering of the Institute of Structural Engineering (IBK) at the Swiss Federal Institute of Technology in Zurich (ETHZ). I had the privilege of working in this inventive environment and being part of an excellent team.

To Prof. Božidar Stojadinović I express my sincere gratitude for this opportunity and for the belief, trust, and support I received during these years. I would like to thank my co-examiners Prof. Ioannis Psycharis and Prof. Ioannis Anastasopoulos for carefully reviewing this thesis. Special thanks go to Michalis Vassiliou for accompanying me throughout the entire thesis and being always open for discussions that led to a committed and constructive cooperation.

I gratefully acknowledge the financial support by ETHZ and the Swiss National Science Foundation (SNSF) under Grant 20021_153240. The methods, results, opinions, findings, and conclusions presented in this thesis are those of me and involved co-authors, and do not necessarily reflect the views of the funding agencies.

Furthermore, I thank the team of the IBK laboratory, in particular, Dominik Werne and Christoph Gisler, for the excellent cooperation, their enthusiasm about the research project, and for fabricating all the specimen parts of the experimental campaign.

My sincere thanks go to all my friends and colleagues from the groups of Prof. Stojadinović, Prof. Fontana, Prof. Puzrin, Prof. Chatzi, and Prof. Sudret, as well as M. Neuhaus, for the countless support, the valuable discussions, and their friendship, which made me enjoy the time that I spent at ETH Zurich. I would also like to thank all the students who spent time with me in the laboratory.

Lastly, I would like to express my deep gratitude to my family and, in particular, to my wife Sofia for encouraging and supporting me during my PhD.

Zurich, November 2018 Jonas Bachmann

ABSTRACT

In this thesis the dynamic response of structures that are allowed to uplift, roll, and rock when subjected to ground excitation is investigated. High potential for successful mitigation of the harmful effects of earthquake ground excitation is associated with rocking structures and has been an important topic of researcher for decades. However, the lack of relatively simple rocking structure design models, as opposed to complex response simulation models, deters from widespread use of rocking structures in earthquake engineering practice. The aim of this thesis is to try to close the gap between practicing engineers and researchers and to contribute to the understanding of the fundamental dynamics of rocking systems. A new rolling-and-rocking solution for a rocking oscillator is developed, achieved by extending its base.

In the present study analytical response models are developed for various kinds of solitary oscillators, planar podium structures, and three-dimensional rocking cylinders. For each system that is investigated, equations of motion and characterizing rocking parameters are derived and verified. Subsequently, a selected number of the developed models are experimentally validated. Numerical and experimental analyses showed that the rocking response of the above mentioned systems is sensitive to initial conditions as well as characteristic response parameters such as the coefficient of restitution. However, the conducted studies also revealed that, despite this sensitivity in the response, the simple model of a rigid rocking oscillator can be predicted probabilistically. It is further shown that the planar responses of different types of rocking systems are similar, within a dimensional analysis context, to the response of Housner's simple rocking model. Additionally, it could be shown that, given certain preconditions, the responses of these models are similar, *e.g.*, the rocking response of an oscillator with a curved base can be reproduced with the simple rocking model of a solitary rigid block. Design recommendations for such curved bases are proposed with respect to key parameters.

The development of extended planar SDOF oscillators allows the investigation of so called podium structures; a superstructure possibly isolated on a rocking ground floor (*i.e.*, kinematic bearings). The developed dynamic model is verified and validated experimentally, and further employed to analyze the seismic response of a wide range of rocking podium structures to analytical pulse and recorded ground motion excitations. The computed responses indicate that rocking podium structures remain stable under ground motion excitation and that the rule-of-thumb guidelines of Polyakov are conservative in most of the examined cases. However, assuming the superstructure to be rigid is shown to be a justifiable assumption that reduces the dynamic system to a SDOF problem.

The data collected when performing numerous shaking table tests are used in a probabilistic study investigating the statistical predictability of the response of a rigid rocking oscillator subject to a given stochastic ground motion model. Results show that Housner's model of the rigid block can be used to predict the statistics of the response of a rocking oscillator subject to a given stochastic ground motion model when the modeled structure is stiff enough to be assumed rigid. Thereby, cornerstones for design guidelines implementation, in which the statistical nature of different systems can be included, are laid.

A step towards closing the gap between the numerous possibilities that the rocking design methodology offers and the lacking acceptance in the engineering community was taken. A model, simple enough to be understood by an educated engineer while still being able to accurately represent the dynamic behavior of a variety of rocking structures, was developed, verified, and validated within this thesis.

KURZFASSUNG

In der vorliegenden Doktorarbeit wird die dynamische Antwort von Tragwerken untersucht, die unter Einwirkung von Bodenverschiebungen abheben, rollen und schaukeln können (von den englischen Ausdrücken «uplift», «roll», und «rock»). Ein hohes Potential für eine erfolgreiche Abschwächung der Schäden infolge Erdbebeneinwirkung wird mit solch schaukelnden Tragwerken verbunden, weshalb sie seit Jahrzehnten von Forschern untersucht werden. Das Fehlen einfacher Entwurfsmodelle, im Gegensatz zu komplexen Antwortsimulationsmodellen, hält Erdbebeningenieure jedoch davon ab, schaukelnde Tragwerke in der Praxis einzusetzen. Ziel dieser Doktorarbeit ist es, die Lücke zwischen praktizierenden Ingenieuren und Forschern zu schliessen und zum Verständnis der grundlegenden Dynamik von schaukelnden Tragwerken beizutragen. Ein neues Modell, das zuerst rollt und erst danach schaukelt, wird entwickelt, indem dessen Basis erweitert wird.

In der vorliegenden Studie werden analytische Antwortmodelle für verschiedene Arten von alleinstehenden Oszillatoren («solitary oscillators»), ebenen Podeststrukturen («planar podium structures») und schaukelnden Zylindern im dreidimensionalen Raum («3D rocking cylinders») entwickelt. Für jedes untersuchte System werden Bewegungsgleichungen und charakteristische, auf die Schaukelbewegung bezogene Parameter hergeleitet und verifiziert. Einige der entwickelten Modelle werden zudem auch experimentell validiert. Numerische und experimentelle Analysen zeigten, dass die Schaukelbewegung der oben genannten Systeme sowohl auf Anfangsbedingungen als auch auf charakteristische Antwortparameter, wie den Energiedissipationskoeffizienten, empfindlich sind. Die durchgeführten Studien offenbarten jedoch auch, dass trotz dieser Empfindlichkeit der Antwort das einfache Modell eines starren, schaukelnden Oszillators statistisch vorhergesagt werden kann. Es wird weiter gezeigt, dass die ebene Antwort verschiedener Arten von schaukelnden Systemen im Kontext der Dimensionsanalyse jener des einfachen Modells von Housner ähnlich ist. Darüber hinaus konnte gezeigt werden, dass die Reaktionen dieser Modelle unter bestimmten Voraussetzungen ähnlich sind. Die Antwort eines alleinstehenden Oszillators mit einer gekrümmt erweiterten Basis kann beispielsweise mit dem einfachen Modell eines massiven, rechteckigen Blocks reproduziert werden. Entwurfsempfehlungen für Oszillatoren mit einer gekrümmt erweiterten Basis werden in Bezug auf definierte Schlüsselparameter vorgeschlagen.

Die Weiterentwicklung ebener Oszillatoren mit nur einem Freiheitsgrad («SDOF oscillators») ermöglicht die Untersuchung von sogenannten Podeststrukturen, die ein Gebäude, isoliert auf einem mit schaukelnden Stützen versehenen Erdgeschoss (d.h. kinematische Lager), darstellen. Das entwickelte dynamische Modell wird experimentell verifiziert und validiert, und anschliessend verwendet, um die dynamische Reaktion eines breiten Spektrums von Podeststrukturen zu untersuchen, die von analytischen Impulsen sowie von aufgezeichneten Bodenbewegungen während Erdbeben angeregt werden. Die Berechnungen deuten darauf hin, dass die Podeststrukturen unter Anregung im Erdbebenfall stabil bleiben und dass Polyakovs Faustregeln in den meisten untersuchten Fällen konservativ sind. Es wird jedoch gezeigt, dass die Annahme einer starren Überstruktur (isoliertes Gebäude oberhalb) berechtigt ist und sich das dynamische System damit auf ein SDOF-Problem reduziert.

Die Daten, die bei der Durchführung zahlreicher Tests auf dem Rütteltisch gesammelt wurden, werden im Rahmen einer probabilistischen Studie verwendet. Deren Ergebnisse zeigen, dass das von Housner entwickelte Modell des starren Blocks verwendet werden kann, um die Statistik der Antwort eines alleinstehenden starren Oszillators vorherzusagen, der einem bestimmten stochastischen Anregungsmodell unterworfen wird, wenn die modellierte Struktur steif genug ist, um als starr angenommen werden zu können. Dabei werden Grundsteine für die Umsetzung von Entwurfsrichtlinien gelegt, in denen der statistische Charakter verschiedener Systeme enthalten sein kann.

Ein Schritt, der die Lücke zwischen den zahlreichen Möglichkeiten der vorgestellten Methodik der Schaukelbewegung und der mangelnden Akzeptanz der praktizierenden Ingenieure zu schliessen versucht, wurde unternommen. Ein Modell, das einfach genug ist, um von einem ausgebildeten Ingenieur verstanden zu werden, und fähig ist, das dynamische Verhalten einer Vielzahl von schaukelnden Strukturen genau darstellen zu können, wurde in dieser Doktorarbeit entwickelt, verifiziert und validiert.

TABLE OF CONTENTS

LIST OF SYMBOLS

Acronyms

2D	two-dimensional
2DOF	two degree-of-freedom
3D	three-dimensional
ASCE	American society of civil engineers
CAV	cumulative absolute velocity
CDF	cumulative distribution function
CI	confidence interval
CoAM	conservation of angular momentum
DAD	damage avoidance design
DEM	discrete element method
DOF	degree of freedom
EOM	equation of motion
ETHZ	Swiss Federal Institute of Technology in Zurich
FE	finite element
FEMA	federal emergency management agency
FPB	friction pendulum bearing
FVA	free vibration analysis
IBK	German abbreviation for institute of structural engineering
LRB	lead rubber bearing
MDOF	multiple degree-of-freedom
NGA	Next Generation Attenuation
NLTHA	nonlinear time history analysis
PGA	peak ground acceleration
RHA	response history analysis
SDOF	single degree-of-freedom
SNSF	Swiss National Science Foundation

Greek Symbols

α	slenderness angle
α'	slenderness angle of a block with respect to its extended base
β	angle defining the geometry of the wedge that extends the base of an oscillator
η	superstructure mass ratio (can be interpreted as the number of stories above the rocking podium frame)
φ	rolling angle
$\dot{\varphi}$	angular spin velocity
γ	mass ratio of cap-beam and columns
λ	mass eccentricity factor
μ_s	static friction coefficient
ω_p	frequency of an analytical pulse ground motion
ω_s	fixed-base natural frequency of the elastic oscillator atop the cap-beam
$\omega_{s,u}$	natural frequency of the elastic oscillator atop the cap-beam when uplifted
ρ	dimensionless parameter of the curvature of the wedge that extends the base of an oscillator

ρ_{c}	critical curvature for an oscillator with an extended curved base
θ	tilt angle (rotation)
θ_0	initial tilt angle
θ_{c}	rotation capacity of the respective oscillator
$\dot{\theta}$	tilt angle velocity
$\dot{\theta}_0$	initial tilt angle velocity
$\theta_{\max}$	maximum tilt angle
ζ_s	viscous damping ratio of the elastic oscillator atop the cap-beam

Roman Symbols

$\boldsymbol{A}_1$, $\boldsymbol{A}_2$, $\boldsymbol{A}_3$	rotation matrices that correspond to the Euler angles
B	semi-width of a rocking oscillator
B'	semi-width of an oscillator with an extended base
C	geometric center of oscillator
D	dissipated energy
E_{tot}	total energy
F	force
F_R	restoring force
H	semi-height of a rocking oscillator
$\mathbf{I}$	moment of inertia tensor of the cylinder about its principle axes
$\mathbf{I}$	unit matrix
I_0	moment of inertia around pivot point O
I_{C}	rotational inertia of the oscillator around the center C
N	number of oscillators that are capped with a rigid beam
R	semi-diagonal of a rocking oscillator; also referred to as ‘size’
R'	semi-diagonal of a block with an extended base
$\hat{R}$	equivalent size of a solitary free-standing rigid oscillator
$\mathrm{SD}_{\max}$	maximum of ground motion elastic displacement spectrum
S_r	amplification factor for the uplifted state
T	kinetic energy
T_p	period of analytical pulse ground motions
T_R	rocking period
T_s	fixed-base natural period of the elastic oscillator atop the cap-beam
T_{w}	wobbling period
V	potential energy
V_s	resulting shear force acting at the base of the SDOF oscillator
W	weight of the oscillator
a_p	amplitude of an analytical pulse ground motion
b	width of the wedge that extends the base of an oscillator
c_r	coefficient of restitution
$c_{r\mathrm{emp}}$	empirical coefficient of restitution
$c_{r\mathrm{th}}$	theoretical coefficient of restitution
d_s	thickness of the steel plates that protect the ends of the column
g	earth’s gravitational acceleration
$\mathbf{i}$	unit vectors of each coordinate system
${}^{\mathrm{I}}k$	post-uplift stiffness for phase I (rolling)

${}^{\mathrm{II}}k$	post-uplift stiffness for phase II (rocking)
k_{rock}	post-uplift stiffness during rocking
k^{*}_{rock}	non-dimensional form of k_{rock}
k_s	stiffness of the elastic oscillator atop the cap-beam
m	mass
m_{B}	mass of cap-beam
m_b	mass of base
m_{C}	mass of an oscillator
m_{T}	mass of the elastic oscillator atop the cap-beam
n_s	number of stories above the cap-beam
p	frequency parameter
p_{o}	probability of overturning
r	radius of curvature of the wedge that extends the base of an oscillator
t	time
t_{up}	time of uplift
u	horizontal displacement
u_{B}	horizontal displacement of the cap-beam
${}^{\mathrm{I}}u_{\mathrm{B}}$	horizontal displacement of the cap-beam for phase I (rolling)
${}^{\mathrm{II}}u_{\mathrm{B}}$	horizontal displacement of the cap-beam for phase II (rolling)
$u_{\mathrm{B,max}}$	maximum displacement at the top of the rocking podium columns
u_{C}	horizontal displacement of the center C
${}^{\mathrm{I}}u_{\mathrm{C}}$	horizontal displacement of the center C for phase I (rolling)
${}^{\mathrm{II}}u_{\mathrm{C}}$	horizontal displacement of the center C for phase II (rocking)
$\ddot{u}_g$	ground acceleration
$\ddot{u}_{g,up}$	ground acceleration leading to uplift
u_{gx}, u_{gy}	horizontal displacement components of the bidirectional earthquake ground motion excitation
u_{T}	horizontal displacement (total) of the elastic oscillator atop the cap-beam
u, v, w	coordinates for displacement
u_y	yield displacement of base isolated system
u_{B}	vertical displacement of the cap-beam
${}^{\mathrm{I}}w_{\mathrm{B}}$	vertical displacement of the cap-beam for phase I (rocking)
${}^{\mathrm{II}}w_{\mathrm{B}}$	vertical displacement of the cap-beam for phase II (rocking)
w_{C}	vertical displacement of the center C
${}^{\mathrm{I}}w_{\mathrm{C}}$	vertical displacement of the center C for phase I (rolling)
${}^{\mathrm{II}}w_{\mathrm{C}}$	vertical displacement of the center C for phase II (rocking)
x, y, z	coordinates

Chapter 1

Introduction

1.1 Concept of Rocking

The fascinating motion called *rocking* is the tilting motion of an unrestrained object displaced from its equilibrium position due to gravity.

An initially tilted object unrestrained at its base will rotate about the edge of its base in contact with the support, assuming that it does not overturn and no external forces are acting on it, until it attains a stable equilibrium (at-rest position). At a certain point in time impact occurs and the base of the object is again in full contact with the support. However, the object may not rest: if sufficient angular velocity remains, the object will uplift and continue tilting towards the other side. Energy is dissipated when the object impacts such that the motion will slowly decay and, ultimately — when enough of the potential energy introduced by the initial tilt angle has worn off — the object will come to a full stop. This planar cyclic motion, illustrated in Figure 1.1 for a free-standing rigid block, will be referred to hereafter as *planar rocking motion*. Its equation of motion was derived by Housner [16] in 1963 and can be described with a single degree of freedom (DOF): the *tilt angle*, denoted with the parameter θ. At '1' the block is released from a tilt angle $\theta_1 > 0$ ($\dot{\theta}_1 = 0$). Impact occurs at '2' and the block starts to tilt towards the other side, until $\theta_3 < 0$ is reached ($\dot{\theta}_3 = 0$). $|\theta_3| < |\theta_1|$ follows due to energy dissipation at impact.

Apart from imposing an initial tilt angle on the object and then releasing it, rocking motion can be caused by the inertia forces induced by horizontal displacement of the support, *e.g.*, during a seismic event, or by strong wind loads. A prerequisite for rocking is that the block does not slide on the support surface. This is either achieved by ensuring a large enough static friction coefficient μ_s between the contact surfaces or edges, or by shear locking the object at its base, forcing it to tilt.

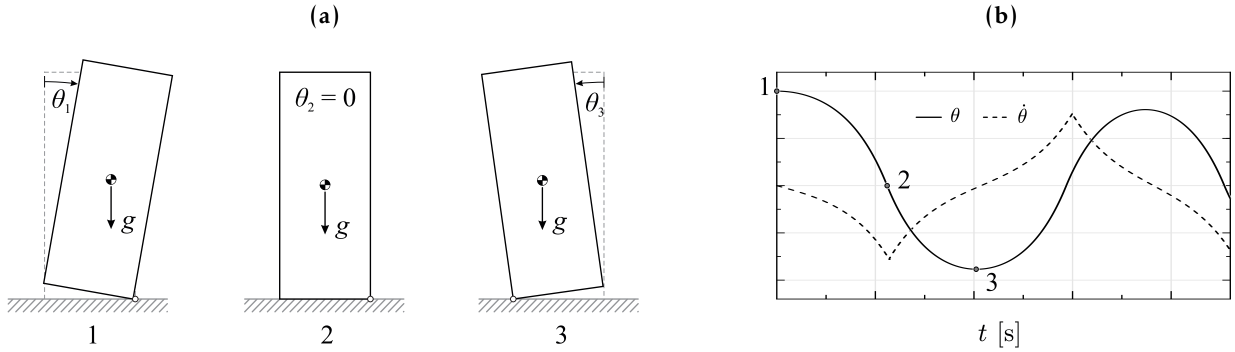

Figure 1.1: Planar rocking motion: (a) Different stages of a rocking half-cycle; (b) Time history responses of the tilt angle θ and the tilt angle velocity $\dot{\theta}$.

1.1.1 Isolation Effect

Modern seismic design is dominated by structures fixed to the ground, using foundation systems that prevent uplift and sliding. However, two distinctly different seismic design concepts, centered on the idea of seismic response modification rather than resistance, have emerged over the last half century. One is the concept of seismic base isolation, where an additional soft layer is inserted between the foundation and the superstructure (Figure 1.2a) and is specially designed such that it can take most of the seismic displacement demand in a sliding-like motion. Consequently, the seismic demand in the isolated superstructure is decreased, allowing for better-performing and safer structures.

The other concept centers on allowing the structure to uplift from its foundation and rock in response to ground motion excitation (Figure 1.2b). Uplift serves as a mechanical fuse, limiting the forces transmitted to the structure and the foundation, while the energy of the input ground motion is dissipated through impacts at the rocking interfaces. In Figure 1.2c the pushover curves (force F applied vs. displacement u measured at the isolation layer) of both concepts are drawn schematically.

Initially the rocking system resists much more than the base isolated system, but its resistance decreases once uplift has happened (negative stiffness). When the rocking system that does not overturn (*i.e.*, does not collapse) is unloaded ($F = 0$) it returns to its original position, without any residual displacement like it inevitably occurs in a yielding fixed-base structure. This property of rocking structures contributes very significantly to improving their seismic performance for downtime and repair cost performance objectives.

In contrast, the resisting force F of the base isolated system increases monotonically (albeit with different, but still positive rates) with increasing displacement. Note that at displacement u_y the base isolation system reaches the yield displacement, after which inelastic displacement occur that might result in *residual displacements* after unloading.

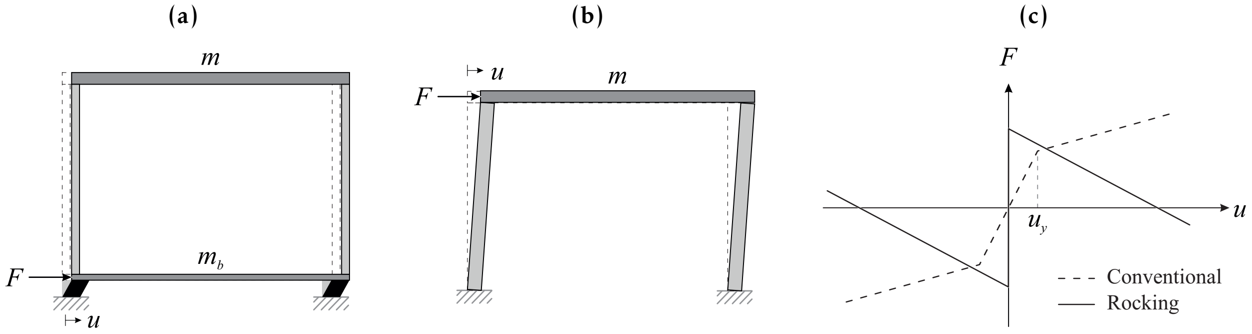

Figure 1.2: Seismic isolation design concepts: (a) Conventional base isolation; (b) Rocking base isolation; (c) Idealized pushover curves.

1.1.2 Rocking Objects

Non-Structural Rocking Objects

Non-structural rocking objects are present in our daily life: some might intentionally be allowed to rock while others, in principal, should not rock. Figure 1.3 shows three such items that are able to rock — unless any horizontal movement is restricted (*e.g.*, by bolting them to the ground).

1) The purpose of the chair in Figure 1.3a is to allow movement and, in that sense, rocking. Due to its shape the resistance against rotational movement is low and a person sitting on the chair can move the chair back and forth with little effort: the required horizontal force applied at the center of mass of the entire system (chair plus the person sitting on it) initially is low and grows with increasing tilt angle. To avoid that someone might fall over the chair has an extended base at the back giving it more stability. If the chair had a flat instead of a curved base, its initial resistance against movement would be larger, but would decrease with increasing tilt angle.

2) The shelf in Figure 1.3b is an example of an object that can but should not rock. Storage shelves are usually tall and narrow which means they are slender. Therefore, the slenderness value given by the ratio width-to-height is small. As a result, they are prone to falling over (*e.g.*, when someone is pushing them). This poses a threat which is why shelves (or wardrobes) should be protected against excessive horizontal movement.

3) The can in Figure 1.3c is axially symmetrical and represents the most basic three-dimensional (3D) rocking object: a cylinder. With respect to horizontal movement of the ground, the dynamic response of the can does not depend on its orientation.

Unlike the can, both the chair and the shelf exhibit different rotational resistances and inertiae around their principle axes. Naturally, movement would be concentrated around the axis with the lowest resistance: the storage shelf would rather rock around the long edge than the short one. Similarly, the chair will rather move forth and back than sideways.

Figure 1.3: Non-structural rocking objects: (a) Chair ; (b) Shelf; (c) Can.

Structural Rocking Objects

Structural objects are important for the integrity of the entire structure and fulfill a role in the force path that was assigned to them, be it a concrete slab in a building that needs to distribute the vertical loads acting on it to the vertical load carrying elements, or a retaining wall alongside a road that needs to act against the earth pressure. Similarly, structural objects with the ability to rock exist, as exemplary shown in Figure 1.4:

1) Radioactive waste is often disposed of in cylindrical containers as shown in Figure 1.4a and stored in a temporary storage facility. If the containers are not connected to the ground their seismic response will be similar to the one of a can shown in Figure 1.3c. The distance between the containers required to prevent them from bumping into each other is an important constraint for radioactive waste storage facilities.
2) Various structures made of stone (or other stiff materials) that were built many centuries ago are still standing today, like the famous pyramids in Egypt. Another example is the ancient temple shown in Figure 1.4b whose load carrying columns are not connected to the ground nor to the superstructure. The fact that they survived many centuries indicates that their seismic performance must be exceptional.
3) The first bridge that deliberately used rocking elements at the bottom of the piers is the South Rangitikei Viaduct in New Zealand (Figure 1.4c-d), opened in 1981. The piers can uplift to either side and, thus, temporarily separate from the support. Due to the shape of the interface, the piers will always re-center when the connection closes. The bridge has survived numerous earthquakes without major damage.

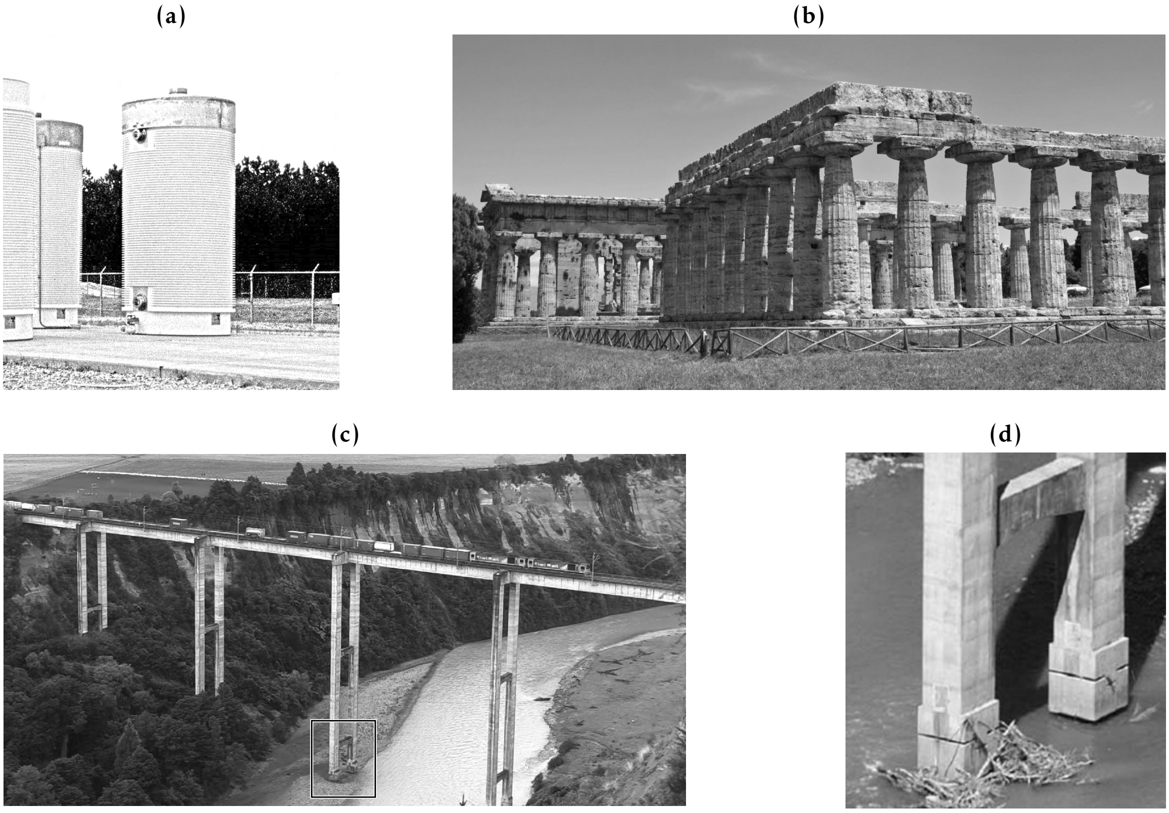

Figure 1.4: Structural rocking objects: (a) Container for radioactive waste; (b) Ancient temple; (c) South Rangitikei Viaduct in New Zealand [17]; (d) Pier detail [18].

1.2 Literature Review

This literature review is intended to give a rough and broad perspective on the state of the scientific knowledge preceding the dissertation. However, for a more detailed view on rocking, especially on what has been done in the last 50–60 years, I refer to the publication «A half-century of rocking isolation» by Makris [19] published in 2014.

1.2.1 Early Studies

To my knowledge, the first modern interest in rocking structures originated from the need to estimate the peak acceleration of ground motions by studying overturned blocks. In 1885, Milne [20] published a study that assumes that the uplifting acceleration of a rigid block is enough to overturn it. In an effort to construct an acceleration measuring device in 1927, Kirkpatrick [21] uncovered that the overturning of a block does not only depend on the ground motion peak ground acceleration (PGA) and on the block slenderness but also on the ground motion duration and the block size.

1.2.2 Studies since 1963

In 1963, Housner [16] published his seminal paper in which he explained the remarkable properties of rocking structures: i) the larger of two geometrically similar blocks can survive the excitation that will topple the smaller block (in displacement-based design terminology, larger blocks have a larger *displacement capacity*); ii) out of two acceleration pulses with the same acceleration amplitude, the one with longer duration is more capable of inducing overturning. After Housner's publication the interest in rocking increased and was investigated more and more.

In 1980, Yim, Chopra, & Penzien [22] investigated the rocking response of rigid blocks subjected to earthquake ground motion. They numerically solved the nonlinear equation of motion and identified the sensitiveness of the system's parameters, *i.e.*, the size and the slenderness of the block. But, they also found out that there is a correlation between the ground motion intensity and the probability of a certain level of rotation, *e.g.*, overturning. Three years later, Psycharis & Jennings [23] extended the previous assumption of a rigid foundation to foundations that are able to capture different compression states of the support and damping (horizontal displacement was restricted).

In 1984, Spanos & Koh [24] investigated the harmonic response of rigid blocks. After that, the free-standing rigid block was revisited many times and has been systematically studied [25–32].

1.2.3 Modern Rocking Structures

The dynamic properties explained by Housner, as well as the observation that modern and ancient structures, that were unintentionally designed to rock, behaved well during earthquakes, have motivated researchers to study rocking structures and engineers to try to use uplifting of structures as a seismic response modification strategy. In doing so, different types of rocking structures were addressed, which I gathered into five classes.

Class I

In the first class are large structures that use uplift and rocking as a seismic response modification technique. In these structures, uplifting at the interface between rocking structural elements works as a mechanical fuse and limits the forces transmitted to the structure.

In 1997, Mander & Cheng [33] published a technical report on the seismic resistance of bridge piers that are designed to rock. The motivation for this research originated from the high level of destruction leading to limited serviceability of bridges after strong earthquakes such as Loma Prieta (1989), Northridge (1994), and Kobe (1995). Their goal was to develop a new design philosophy called *Damage Avoidance Design (DAD)* that combined the state-of-the-art ductile and isolation design.

In 2008, Cheng [34] continued the research on such precast bridge piers connected to the concrete deck and to the foundations with high strength post-tensioning rods with a series of shake table test. The results were quite impressive: up to at least 5 % of the column rotation the bridge model rocked without damage or residual deformation.

A parametric study of Deng, Kutter, & Kunnath [35] in 2012 compared the conventional fixed-base bridges with bridges that used rocking foundations from a statistical standpoint. The results presented indicate that bridges with rocking foundations are more stable than bridges with fixed connections, given that their fundamental vibration periods are identical and that the base shear force coefficients for rocking initiation and forming of a plastic hinge are the same.

Further publications followed on the planar response of rocking frames (which can be compared to the longitudinal response of rocking bridge piers) when they were freely rocking [36–42] or when the rocking motion was restrained [43, 44] or additionally damped [45, 46].

Class II

In class two are precious museum artifacts and unanchored equipment whose seismic overturning stability is important.

In 2009, Contento & Di Egidio [47] analyzed the different response behaviors of base isolated pieces of art with a passive control system. The artifacts were assumed to be rigid but with non-symmetrical mass distribution with a focus on the eccentricity. The study involved the dynamic response comparison of the isolated and the non-isolated system when subjected to analytical and seismic excitations. It was shown that base isolation normally improves the response behavior while excessive eccentricity within the system negatively influences the outcome.

Other free-standing block-like structures are unanchored equipment, as the one that is illustrated in Figure 1.4a. Dar, Konstantinidis, & El-Dakhakhni [48] investigated the seismic performance of nuclear power plant components (spent-fuel dry storage casks, portable standby generators, electrical transformers, unreinforced masonry radiation shielding walls, *etc.*) whose post-earthquake condition might be of utmost importance for the serviceability of the power plant as experience from the 2011 Tōhoku earthquake in Japan has shown: a series of unfortunate events resulted in a major nuclear catastrophe and evacuation of 170’000 people [49] — all due to systematic failure of various components that impaired the cooling circuit of the power plant.

In 2005, the American Society of Civil Engineers (ASCE) published a book on the seismic design criteria for nuclear facilities in which they presented an approximate method for the computation of the maximum tilt angle of free-standing power plant components.

In their study, Dar *et al.* [48] evaluated this method by comparing it to the nonlinear time history analysis (NLTHA), giving the exact solution for the expected tilt angle. They concluded:

> “[. . .] the ASCE/SEI 43-05 method (which has also been adopted in FEMA P-58-1 and is expected to be adopted in the new revision of ASCE 4) provides highly unreliable, and in many cases unconservative, estimates of peak rocking rotation for a wide range of block geometries, under various levels of excitation.” [48]

This is not the first study to show the difficulty in estimating the maximum tilt angle response with simplified methods. In 2001, Makris & Konstantinidis [50] discussed the shortcomings of the FEMA 356 [51] report and concluded that “the approximate method (to estimate the maximum tilt angle of a rocking body) is fundamentally flawed and should be abandoned.”

Class III
The third class comprises ancient structures (*e.g.*, temples, columns, monuments, *etc.*) whose seismic performance must be surprisingly good: otherwise none of them would still be standing today, especially in the seismically active region of Greece. This must be why numerous researchers investigated such structures [52–56].

In 2003, Psycharis, Lemos, Papastamatiou, Zambas, & Papantonopoulos [57] took a closer look at a proposed restoration of the Parthenon Pronaos and studied it numerically. The multi-element structure (multidrum columns, epistyle, *etc.*) was represented using the discrete element method (DEM) with frictional joints. The analysis focused on the deformations and the failure modes of the multidrum columns when the system is subjected to seismic excitation. It was found that for moderate earthquake motions it is generally beneficial (there are few cases where it is not the case) if additional shear resistance (*e.g.*, provided using center-line plugs) is added between the epistyles and the supporting columns to avoid excessive slippage at the interface. However, stronger ground motions could impair this positive effect due to the occurrence of uplifting epistyles. More studies followed focusing on ancient columns or monuments [58–65].

Class IV
In the forth class are deformable solitary rocking oscillators which have been studied in [66–74], to conclude that deformable rocking structures are also remarkably stable when excited by earthquakes. If the ends of the columns are protected, energy dissipation during rocking motion happens instantaneously when the body impacts the ground. Several different modeling approaches have been proposed to describe this phenomenon [75–77]. The probabilistic treatment of the rocking problem [78–80] further confirms the remarkable stability of deformable rocking structures.

Class V

Most of the aforementioned studies treat rocking as a planar (2D) problem. The published research on the dynamic response of 3D rocking of rigid bodies is much more limited, and is gathered in class five.

In the early 1990s, Koh & Mustafa [81] and Koh & Hsiung [82, 83] studied the motion of a rigid cylinder under seismic excitation. Further research of 3D rocking followed in publications on ancient conical or cylindrical columns [56, 61, 62, 65]. All the studies conclude that 3D motion (so-called *wobbling*) is present even under in-plane initial conditions and/or under uniaxial horizontal component ground excitation.

Stefanou, Vardoulakis, & Mavraganis [84] proved the aforementioned observation theoretically. In fact, when the initial spin tends to zero, the motion of a rigid cylinder involves a sudden and rapid motion of the contact point around the circular base (wobbling) instead of an impact (rocking). Srinivasian & Ruina [85] proved that the net angle of turn of the contact point is nearly independent of initial conditions. Instead, this angle of turn depends simply on the geometry and the mass distribution of the body.

Pappas, Sextos, da Porto, & Modena [86] numerically explored the behavior of an ancient cylindrical column with a height of 6 m and a diameter of 0.66 m with the intention of defining proper ground motion intensity measures to characterize the rocking response of such structures. Studies on the 3D behavior of non-cylindrical bodies are discussed in [87–92].

1.2.4 Structures Constructed Using the Rocking Concept

Pioneering rocking structures have been investigated, designed, and built in New Zealand [93,94], Russia and the USSR [95], and the USA [96] in the 1970s. Modern rocking buildings evolved in two directions.

One direction, developed mainly by North American and New Zealand engineers, focuses on controlling the displacements of rocking buildings using a variety of mechanical restrainers (*e.g.*, post-tensioning cables and yielding bolts) and/or hysteretic or viscous dampers [43,44,46,97–99].

Another direction, developed mainly in Russia and the USSR, is based on the concept of *kinematic bearings*, where the columns of the entire bottom story of the structures are allowed to rock freely in response to earthquake ground motion excitation, effectively forming a *flexible story* with the ability to return to its pre-excitation configuration [95, 100]. More than 400 buildings with such flexible stories were built in Russia over the past four decades [101]. The buildings performed well in earthquakes they were exposed to, and the ability of the columns to rock did not deteriorate over the years [101,102]. Notably, full-scale dynamic tests have been performed on real structures [103, 104].

Design guidelines for such rocking structures were presented in the early 1970s in Polyakov's well-known textbook [95]. He suggested that i) the superstructure on top of the flexible story behave as a rigid body, and that ii) the dynamics of the flexible first story (the kinematic bearing ground floor) be described using an elastic fixed-base cantilever single degree-of-freedom (SDOF) model. A similar modeling approach for rocking structures was later suggested by Priestley, Evison, & Carr [105].

1.2.5 Experimental Studies and Probabilistic Rocking Response Models

As the response of the rocking oscillator is highly nonlinear because of its negative stiffness [106] many have suggested treating the rocking oscillator as a *chaotic system*, in the sense that small perturbations of its governing parameters (be it the oscillator properties or the excitation) result in widely diverging outcomes. Researchers who tried to experimentally validate Housner's model have shown that, given the modeling uncertainty, especially of the one related to impact, it is difficult to confidently predict the time history response of a rocking oscillator to a specific ground motion [67,75,76,105,107–109].

However, an accurate model prediction of the dynamic response of a rocking oscillator prototype to a single ground motion is a sufficient, but not a necessary condition to validate, and ultimately trust, the model. Validation is a process of determining if a verified model accurately represents the experimental results. In the presence of uncertainties (in the ground motion excitation, in the coefficient of restitution, and in the model), an objective approach to model validation necessarily involves a statistical comparison of probability distributions of response quantities that characterize the seismic response of the rocking oscillator prototype and its models [110].

It is notable that Yim *et al.* [22] pioneered the probabilistic approach to modeling the response of a rocking oscillator. Using Jennings' model for synthetic ground motion excitation [111] and Housner's rigid block [16], they observed order in the response of the rocking oscillator and indicated that it could be predicted in a statistical sense.

1.3 Motivation

Although rocking has been a subject of research for more than a century and it is present in our daily life, it is still a form of motion that — compared to other types of motions — has not been studied as extensively. I think this is mostly due to its relatively low scientific importance which is highly correlated to the reluctance of engineers to apply the rocking concept when designing structures for lateral loads. Furthermore, guidelines and codes are either missing or not sophisticated enough.

In relation to conventional design, very few structures exist where rocking is used to reduce the seismic demand: the idea of not fixing a structure to the ground leaves engineers that are unaware of the system's capabilities anxious because it is unusual and it contradicts the conventional design. There, the response is separated into its uncoupled modal responses. Each modal response is represented by an SDOF elastic oscillator whose response can be computed analytically. For nonlinear systems, *i.e.*, when yielding occurs, simplified but not always reliable methods are available. Thus, sophisticated finite-element (FE) software come into play and the nonlinear response can be computed in a relatively timely manner. This is possible because, even for nonlinear behavior, the stiffness remains positive (monotonic relation between force and displacement).

The response of rocking objects, however, is highly nonlinear (negative post-uplift stiffness) and can be solved analytically or with the use of modern finite-element software only with significant effort: the software struggles with systems that exhibit negative stiffness because common solution methods will not converge or simply will not work (due to occurring singularities). As Dar *et al.* [48] and Makris & Konstantinidis [50] have pointed out, there is no reliable simplified method available that is capable of estimating the maximum tilt angle response, and one should stick to the nonlinear dynamic analysis. Therefore, in order to compute the dynamic response of rocking structures exceeding the classical rocking rigid block only special purpose (often self-coded) software solutions have been used to date, a time-consuming practice that does not scale well at all.

The lack of relatively simple rocking structure design models, as opposed to complex response simulation models, deters from widespread use of rocking structures in earthquake engineering practice. In today's society the value of time increases, and engineers and design offices have to compete in the market and cannot afford or simply do not have the knowledge to use such time consuming computations on rather simple structures, *e.g.*, a low-rise apartment building.

It is this gap between the huge possibilities that the rocking design methodology offers and the lacking acceptance in the engineering community as well as the missing design solutions that primarily motivated the work presented in this thesis. The intention is to contribute to the understanding and development of design methodologies, possibly simple enough to be understood by an educated engineer and applicable to a variety of structures.

1.4 Research Objectives

This doctoral dissertation research aims to investigate the dynamic response of rolling-and-rocking structural systems. These systems work as mechanical fuses to limit the seismic forces transmitted to the structure. Moreover, structures employing such systems are resilient: after an earthquake they re-center to their original position without damage to the load carrying structure.

The dynamic response of the rolling-and-rocking systems is controlled by the geometric characteristics of the contact surface with the foundation. The principal idea is to engineer the post-uplift stiffness of such rocking systems by extending their flat base using concave surfaces, thus, introducing a rolling phase in between the at-rest state and the rocking motion phase.

The analytical, numerical, and experimental studies on the dynamic response of 2D rolling-and-rocking and 3D rocking systems planned for this doctoral dissertation research will contribute to providing a basis for engineering such systems to fulfill the desired seismic performance objectives.

1.5 Relevance to Science and Economy

1.5.1 Scientific Significance

The thesis aims to develop and test a design concept that is applicable to buildings, bridges, and tall slender structures such as wind turbines and chimneys. The main characteristic of this design concept is to let such structures uplift and engineer the post-uplift stiffness of the system, ranging from positive to negative, by making the structures roll before they start to rock. Hence, this thesis challenges the usual practice of anchoring the structures to the foundation to fully transmit the internal forces induced by earthquakes and other loads to the underlying soil, and the widely established belief that structures should have a positive post-yield stiffness to remain stable.

Even though rocking has been proposed as an earthquake hazard mitigation strategy, its effectiveness has only been shown theoretically for the planar motion, thus, leaving numerous theoretical and practical questions for the 3D motion unanswered. This thesis aims to contribute to the study of the 3D motion. It will be a step towards practical application of the method to buildings and prefabricated bridge structures.

While rocking and rolling structures have been implemented in practice, the development of analytical and computer methods to describe this behavior is a new contribution to the state-of-the-art. If successful, the proposed models will serve as the basis for development of sound design provisions for structures with engineered post-uplift stiffness, as well as for further investigations in using stable and stabilized mechanisms to modify and control the seismic response of structures.

1.5.2 Economic Significance

Letting a structure yield and taking advantage of its plastic strength was the method proposed by the engineering community and adopted by the society to mitigate the risk of rare hazardous events, such as strong earthquakes, almost a half century ago. This strategy is adequate for saving human lives. However, it does not guarantee that structures will not have to be demolished after an earthquake due to large residual displacement and low residual strength. This is why financially developed societies demand new methods of design that not only protect human lives but to also protect property and preserve the operativeness of critical facilities.

The proposed rolling-and-rocking seismic response modification method does not rely on the plastic deformation of structures to achieve its objectives. Should the design earthquake happen, it is expected that the structure designed following the proposed method would absorb the shock by rolling and rocking, but return to their pre-event state and remain undamaged. Such behavior is very desirable for facilities that should be fully functional right after an earthquake (*e.g.*, hospitals, fire stations, *etc.*). Building structures with a rolling-and-rocking seismic protection mechanism should translate into significant economic benefits through shortening the post-earthquake recovery period of the impacted communities. From the standpoint of construction costs, the proposed system is quite simple and should be more affordable than the conventional monolithic columns and foundations, or the established seismic base isolation systems with lead rubber (LRB) or friction pendulum (FPS) seismic isolation bearings.

Rolling-and-rocking systems, based on rocking column solutions proposed in this dissertation, could be used to seismically upgrade existing structures. This is particularly important for Switzerland where the design earthquake forces used in the past are smaller than modern hazard estimates suggest.

1.6 Outline and Methodological Approach

This thesis is structured in chapters as follows:

Chapter 2 provides background knowledge from selected publications that lay the foundation to better understand the work presented in this thesis.

Chapter 3 investigates the dynamic response of planar SDOF systems:

Rolling-and-Rocking Oscillator
In the first part SDOF models of rolling-and-rocking rigid bodies are studied. First, the equation of motion of rolling-and-rocking rigid oscillators under a ground excitation is derived. Then, it is solved numerically for analytical pulse excitations. The results are presented in an overturning spectrum format for different characteristics of the concave base. As part of the experimental campaign, the rocking oscillator is also subjected to real and synthetic ground motions. The results obtained in this phase provide the basis for the application of the rolling-and-rocking systems where the oscillator can be assumed rigid.

Rolling-and-Rocking Frame
In the second part SDOF models of rolling-and-rocking frame structures are investigated. The analytical approach developed in the first part of this chapter is extended. Numerical modeling tasks aimed at developing the overturning spectra for such frame structures are repeated. The emphasis in the modeling effort invested in this task is on the development of a numerical (finite element) procedure for treating combined rolling and rocking, and for accounting for the energy dissipated during impact in the rocking phases of the response. The prototype structure inspiring the work in this part is a single- or multispan bridge.

Chapter 4 explores the dynamic response of planar two degree-of-freedom (2DOF) systems by extending selected models discussed in Chapter 3:

Rolling-and-Rocking Podium with an Elastic Oscillator
The system to be investigated is a rolling-and-rocking frame system with a SDOF elastic oscillator attached on the top of the cap-beam. This model is intended to describe the response of a building structure placed on top of the rolling-and-rocking first story (similar buildings have been built in Russia). The analytical and numerical models developed in this part are used to examine the dynamics of this 2DOF system and to investigate the interaction between the superstructure and the rolling-and-rocking frame.

Chapter 5 extends the planar dynamics of a rocking body presented in Chapter 3 to the 3D space:

Undamped Free-Standing Rigid Cylinder
In the first part the 3D response of a cylindrical rigid body with a flat base constrained to rock on its circumference without sliding is studied. The ground excitation is assumed bidirectional (2D). This problem is significantly more complicated than the planar rocking problem because describing it (for a rigid body) requires two DOFs (one for the position of the pivot point on the circumference and one for the tilt angle). However, it is much simpler (but more useful in the case of rocking columns) than the problem of an unconstrained rolling of a cylinder on a plane [81, 85], which is a 5DOF problem.

Damped Free-Standing Rigid Cylinder
In order to account for energy dissipation, in the second part a damping mechanism is added to the free-standing rigid cylinder model by implementing a spring and dashpot system, resulting in a 3DOF system.

Parametric and spectral studies are performed, using dimensional analysis whenever possible, to extract patterns and qualitative results that could be used in design. Since combining two analytical pulses that have the same phase does not create an excitation that has two independent components in the horizontal plane, but just a unidirectional pulse, real bidirectional ground motions are used.

Chapter 6 explains the experimental campaign that was conducted in the progress of this thesis. Due to practical limitations of the IBK structural testing laboratory uniaxial shaking table at ETH, only planar experiments were planned and executed, focusing on the following systems:

Podium with an Elastic Oscillator
In the first part of the experimental campaign the numerical model of the 2DOF rocking podium structure, developed in Chapter 4, is experimentally investigated. In a series of 2×12 shaking table tests (excited by analytical pulse ground motions) it is verified and validated.

Rolling-and-Rocking Oscillator
In the second part free vibration analyses (FVA) and response history analyses (RHA) are performed for the SDOF rolling-and-rocking oscillator developed in the framework of Chapter 3. The height of the oscillators made of aluminum is constant with 0.50 m. To validate the numerically computed system's parameters (*i.e.*, rotational inertia, coefficient of restitution) first only free vibration tests are conducted. Once the model parameters are verified and the numerical model is validated for free vibration response, ground excitation is considered. Accelerations are measured on the specimen and on the shaking table and serve as input for the numerical model. In a series of 6×100 executed experiments the statistical nature of the classical rocking block (Housner's model) is examined.

Chapter 7 provides an excursion into the probabilistic examination of rocking. A statistical approach is employed to validate Housner's numerical model [16] of a rocking oscillator against experimental data obtained during the experimental campaign. Namely, statistical test methods are used to adopt or reject a hypothesis that a response probability distribution obtained using a numerical model represents the one realized by the prototype. To constrain the uncertainty in the excitation, synthetic record ensembles are generated from a stochastic ground motion model matching the statistics of two target records and used in the analyses and tests.

Chapter 8 draws conclusions and summarizes the thesis contribution.

CHAPTER 2

BACKGROUND

This chapter aims at introducing specific topics in more depth. The here presented and summarized material is revisited, modified, and/or extended at various points in the thesis. It is, therefore, regarded as fundamental knowledge, and it serves as an introduction into the topics relevant for this thesis.

2.1 Housner's Rocking Block

The most basic rocking system is a free-standing rectangular rigid block on a rigid surface, as shown in Figure 2.1a. It was first thoroughly investigated in 1963 by G. W. Housner who himself called it an «inverted pendulum structure» [16].

The considered block has a total mass m that is evenly distributed, a total height of $2H$, and a total width of $2B$. The the slenderness angle α and the length of the semi-diagonal R, also referred to as the *size*, are equivalent parameters, and can be computed from these dimensions, and *vice versa*:

$$\alpha = \operatorname{atan}(B/H), \tag{2.1}$$

$$R = \sqrt{B^2 + H^2}. \tag{2.2}$$

Notably, the slenderness angle designates the static stability limit of the block: if the block is tilted beyond this angle, it will overturn. The slenderness of the block is often quantified as $\tan\alpha = B/H$.

In this thesis other rocking systems are developed based on Housner's simple free-standing rigid block model. Hence, Housner's theory on the rocking block will discussed subsequently.

Inspired by the fact that several tall and slender structures like elevated water tanks or stone pillars in graveyards survived strong earthquakes like the 1960 Chilean earthquake or the 1952

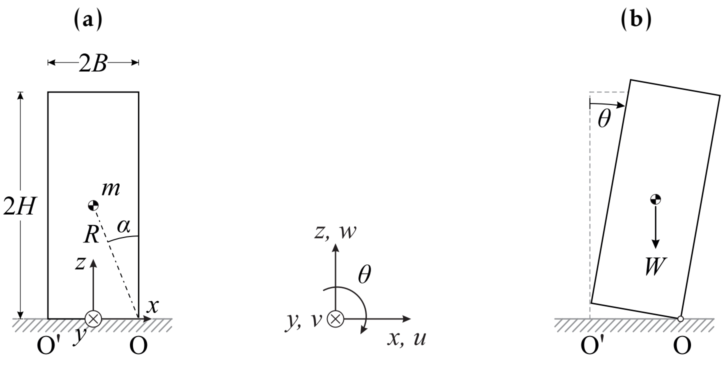

Figure 2.1: Rigid block rocking on a rigid surface: (a) Geometry; (b) Rocking motion.

Arvin-Tehachapi earthquake in the United States (California) while other smaller structures (*e.g.*, box-like power transformers) rocked and overturned, Housner investigated the dynamic response of this kind of structure. He derived equations of motion (EOM) and solutions for the linearized systems (where the sine of the slenderness angle α is approximated by α for $\alpha < 20°$) for four different cases:

1) Free vibration
2) Constant acceleration
3) Sinusoidal acceleration
4) Earthquake ground motion acceleration

Further, Housner derived expressions for the minimum ground motion pulse acceleration amplitude required to overturn the block, given a certain duration of this acceleration pulse (rectangular or sinusoidal). Although Housner's pulses are not physically realizable, his pioneering work uncovered a size effect that explained why the larger of two geometrically similar blocks can survive the excitation that will topple the smaller block.

Free Vibration

Important block parameters are its weight $W = g\,m$, the moment of inertia[1] I_0 around the point O, and the fact that its center of mass coincides with the geometrical center of the block (mass evenly distributed, no eccentricity). In this thesis I introduce a mass distribution factor, denoted as λ, which is able to take into account vertical asymmetry. Eccentric rocking blocks have also been investigated by Di Egidio & Conento [112].

When one assumes that the coefficient of friction is large enough to prevent sliding between the block and the support surface and that no external forces are acting on the block, the equation of motion for the tilt angle, θ, becomes

$$I_0\,\ddot{\theta} = -W\,R\,\sin\left(\mathrm{sgn}\left(\theta\right)\cdot\alpha - \theta\right), \tag{2.3}$$

where $W\,R\,\sin\left(\mathrm{sgn}\left(\theta\right)\cdot\alpha - \theta\right)$ represents the restoring moment. Linearization with respect to θ and α allows for rewriting Equation (2.3) to

$$I_0\,\ddot{\theta} - W\,R\,\theta = -\,\mathrm{sgn}\left(\theta\right)\cdot W\,R\,\alpha\,. \tag{2.4}$$

With the definition of the frequency parameter of a rigid rocking block defined as

$$p^2 = \frac{W\,R}{I_0} = \frac{3\,g}{4\,R}, \tag{2.5}$$

Equation (2.4) becomes

$$\ddot{\theta} - p^2\,\theta = -\,\mathrm{sgn}\left(\theta\right)\cdot p^2\,\alpha\,, \tag{2.6}$$

for which an exact solution exists. Given $\theta_0 > 0$ and $\dot{\theta}_0 = 0$ at $t = 0$, the solution is

$$\theta = \alpha - \left(\alpha - \theta_0\right)\cosh\left(p\,t\right). \tag{2.7}$$

---

[1] For a rectangular block of size R with evenly distributed mass the moment of inertia is $I_0 = 4/3\cdot m\,R^2$.

The time that elapses between the block being released from θ_0 and the block impacting ($\theta = 0$) corresponds to a quarter of the rocking period T_R: the time needed to complete a full rocking cycle and arrive at the same position. Solving Equation (2.7) for $\theta = 0$ yields the following correlation between initial tilt angle $\theta_0 > 0$ and the rocking period T_R:

$$T_R = \frac{4}{p}\cosh^{-1}\left(\frac{1}{1-\frac{\theta_0}{\alpha}}\right). \tag{2.8}$$

The non-dimensional value $T_R{\cdot}p$ is plotted against θ_0/α in Figure 2.2. It can be seen that there is a strong dependence of T_R on the initial tilt angle θ_0: when θ_0/α is close to zero the rocking period is short; for $\theta_0/\alpha = 0$ the rocking period becomes ∞ because the block is at equilibrium. This interaction between tilt angle θ and rocking period T_R illustrates the highly nonlinear behavior of a rocking block.

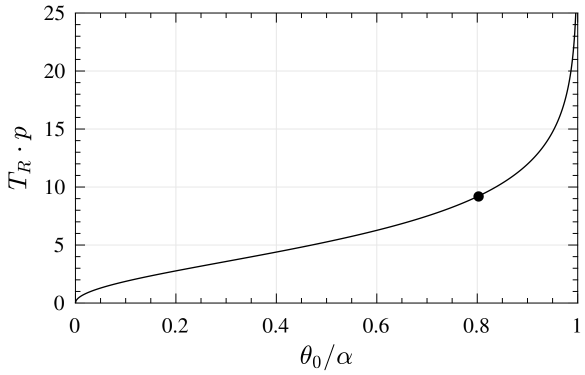

Figure 2.2: Dependence of the rocking period T_R of a rigid block on the initial tilt angle θ_0.

Energy Dissipation at Impact

When a rigid block performs rocking motion and air friction is neglected, energy is only dissipated during impacts. This means that energy dissipation happens step-wise after every half-cycle (*i.e.*, when $T_R/2$, according to Eq. 2.8, has passed). At impact the tilt angle velocity $\dot{\theta}$ is maximal while $\theta = 0$; all of the energy is stored as kinetic energy, given by

$$T = \frac{1}{2} I_0 \dot{\theta}^2. \tag{2.9}$$

When the tilt angle is maximal (during a half-cycle) the tilt angle velocity is zero. Thus, all of the energy is stored as potential energy, given by

$$V = W R \cdot \Big(\cos(\operatorname{sgn}(\theta)\cdot\alpha - \theta) - \cos\alpha\Big). \tag{2.10}$$

Assuming that no bouncing occurs during impact (no *inelastic* impacts), the pivot point quickly moves from O to O' (when the block is rocking from right to left), and *vice versa*. Housner assumed that the angular momentum around the new pivot point O' is conserved, and computed the ratio of the remaining kinetic energy after impact to be

$$\frac{\frac{1}{2} I_0 \dot{\theta}_2^2}{\frac{1}{2} I_0 \dot{\theta}_1^2} = \frac{\dot{\theta}_2^2}{\dot{\theta}_1^2}. \tag{2.11}$$

Therefore, a the block with a pre-impact tilt angle velocity of $\dot{\theta}_1$ exhibits a post-impact tilt angle velocity equal to $\dot{\theta}_2 = \sqrt{c_r} \cdot \dot{\theta}_1$. At every impact ΔE is dissipated:

$$\Delta E = (1 - \sqrt{c_r}) \cdot T\,. \tag{2.12}$$

This implies that every half-cycle that follows after an impact has a slightly lower period than the one preceding it, which correlates with Figure 2.2. The angular momentum around O' with respect to the y-axis before impact is $\mathbf{L}_1$ and after impact is $\mathbf{L}_2$. They yield:

$$\mathbf{L}_1 = \dot{\theta}_1 \cdot \left(I_0 - 2\,m R^2 \sin^2\alpha\right), \tag{2.13}$$

$$\mathbf{L}_2 = \dot{\theta}_2\, I_0\,. \tag{2.14}$$

Conservation of angular momentum (CoAM) presumes $\mathbf{L}_1 = \mathbf{L}_2$, which leads to the following expression for the so called *coefficient of restitution*:

$$c_r = \left(\frac{I_0 - 2\,m R^2 \sin^2\alpha}{I_0}\right)^2 = \left(1 - \frac{2\,m R^2}{I_0}\sin^2\alpha\right)^2 = \left(1 - \frac{3}{2}\sin^2\alpha\right)^2. \tag{2.15}$$

Induced Rocking by Constant Acceleration

When a block is subjected to ground acceleration, its inertia force $W\,\ddot{u}_g$ acting horizontally at the center of gravity, can initiate rocking motion. Then, the equation of motion in its linearized form becomes

$$\ddot{\theta} - p^2\,\theta = p^2\,\frac{\ddot{u}_g}{g} - \mathrm{sgn}(\theta)\cdot p^2\,\alpha\,. \tag{2.16}$$

Example 2.1: Free vibration response of a rigid block

Figure 2.3 plots a free vibration response for a rigid block ($\tan\alpha = 0.1$, $p = 2.2\,\mathrm{s}^{-1}$) when released from an initial tilt angle of $\theta_0 = 0.08$ rad. At first ($t = 0$ s), the kinetic energy is zero as $\dot{\theta} = 0$. Equation (2.10) yields $V/(m_C R^2) = g/R \cdot (\cos(\alpha - 0.08) - \cos\alpha) = 0.031\,\mathrm{s}^{-2}$. The first impact occurs at $t_1 = 1.044$ s which corresponds to $T_R/4$ of the current rocking cycle. Using Figure 2.2 or Equation (2.8) one would get $T_R/4 = 1.048$ s (the difference is due to the linearization incorporated in Eq. 2.8). The difference in potential energy $\Delta V = V_0 - V_1$ between t_0 and t_1 is fully transformed into kinetic energy imminent to impact. The pre-impact tilt angle velocity is $\dot{\theta}_1 = 0.2156$ rad/s. The post-impact velocity follows as $\dot{\theta}_2 = \sqrt{0.9705} \cdot \dot{\theta}_1 = 0.2124$ rad/s.

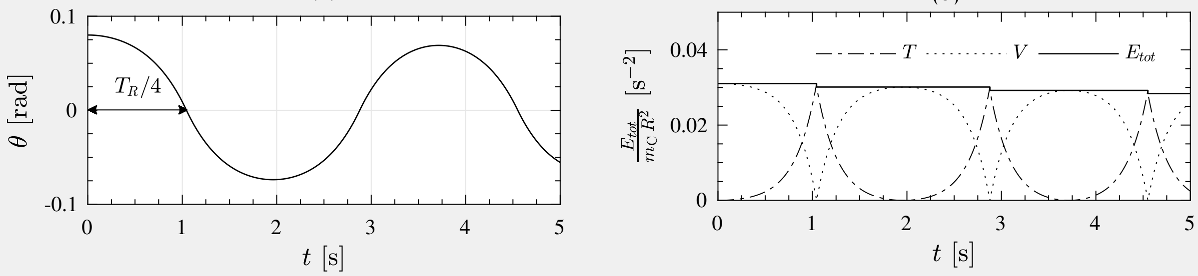

Figure 2.3: Free vibration response of a rigid block ($\tan\alpha = 0.1$, $p = 2.2\ \mathrm{s}^{-1}$) on a rigid surface when released from an initial tilt angle of $\theta_0 = 0.08$ rad: (a) Tilt angle response history; (b) Energy distribution over time.

From Equation (2.16) if follows that a necessary condition for uplift is

$$\frac{\left|\ddot{u}_g\right|}{g} > \alpha \,. \tag{2.17}$$

Given that $\ddot{u}_g = a_g$ is constant, and acting over a duration of t_1, the solution of Equation (2.16), considering the initial conditions $\dot{\theta}_0 = \theta_0 = 0$, is given by

$$\frac{\theta}{\alpha} = \left(\frac{a_g\,\alpha}{g} - 1\right)\cosh\left(p\,t - 1\right) . \tag{2.18}$$

The minimum duration $t_{1,\min}$ during which a constant acceleration of amplitude a_g needs to act to overturn a rigid block can be computed by comparing the energy needed the lift the block to $\theta = \alpha$ and the work done by the inertial force $W\,\ddot{u}_g$, and it follows:

$$\cosh\left(p\ t_1\right) = 1 + \frac{1}{2\,\frac{a_g}{g\,\alpha}\left(\frac{a_g}{g\,\alpha} - 1\right)} . \tag{2.19}$$

Similarly can the minimum acceleration $a_{g,\min}$ acting over a duration t_1 be computed that is needed to overturn a rigid block.

2.2 Rocking Response of Free-Standing Rigid Blocks

In their publication «Rocking Response of Free-Standing Blocks under Cycloidal Pulses» from 2001, Zhang & Makris [25] picked up the approach of Housner to compute the minimum acceleration needed to overturn a rigid block, applied it to cycloidal pulse ground motions, and plotted the result in an overturning acceleration spectrum. This spectrum allows for reading either the amplitude a_p or the pulse frequency ω_p needed to overturn a block of size R and evenly distributed mass.

They revealed that free-standing rigid blocks subjected to cycloidal pulse excitations can overturn with two distinct modes:

1) they overturn with impact,
2) they overturn without impacting (to the side toward which uplift occurred).

$$\ddot{u}_g = \begin{cases} -a_p\ \sin\left(\omega_p\ t\right), & \text{if} \quad 0 \le t \le \frac{2\pi}{\omega_p} , \\ 0 , & \text{otherwise} . \end{cases} \tag{2.20}$$

Figure 2.4a plots an overturning acceleration spectrum for sinusoidal pulses, as defined by Equation (2.20), and a coefficient of restitution c_r equal to 0.81. The pulse frequency ω_p is normalized with the frequency parameter p (Eq. 2.5) and the pulse amplitude is normalized with the uplifting acceleration $\alpha\,g$ according to Equation (2.17). The two overturning modes are captured in two overturning areas: the overturning area at the top (shaded clockwise) depicts the area where overturning without impact occurs; the bottom overturning area (shaded counterclockwise) encloses all the cases where the block would overturn with impact.

(a) **(b)** Case ‘a’

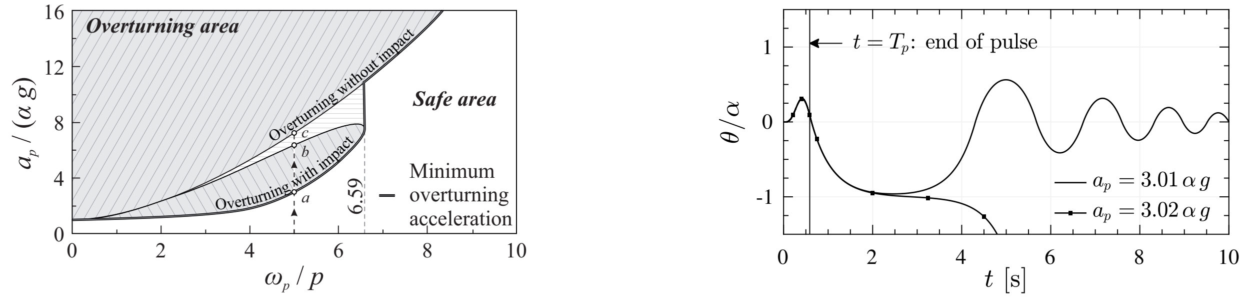

(c) Case ‘b’ **(d)** Case ‘c’

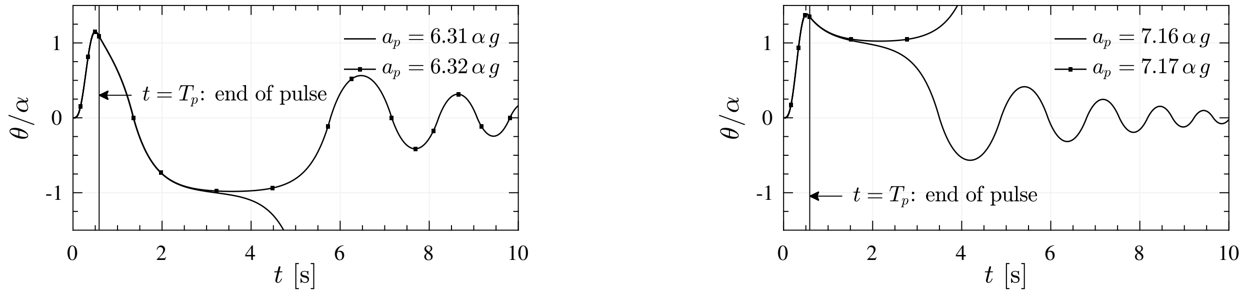

Figure 2.4: Free-standing rigid block (p = 2.14 s^{-1}, α = 0.25, and c_r = 0.81) subjected to a sinusoidal pulse acceleration (Eq. 2.20): (a) overturning acceleration spectrum; (b) – (d) Response time histories for amplitude levels ‘a’–‘c’.

The black double line indicates the minimum acceleration needed to overturn a free-standing rigid block with frequency parameter p, given a pulse frequency ω_p. The larger the block is, the larger is the value ω_p/p, and the larger is the needed overturning acceleration amplitude a_p. When $\omega_p/p > 8.5$, the block will practically no longer overturn unless a unrealistically large value for the amplitude a_p is applied ($a_p > 16\,\alpha g$).

Zhang & Makris [25] showed that the existence of the second mode results in a safe region that is located over the minimum overturning acceleration line, corresponding to the white area with horizontal light gray lines enclosed by the borders of the overturning areas and the minimum overturning acceleration line in Figure 2.4a. This means that the same block may either overturn with either of the two overturning modes, or survive a sine-pulse acceleration with identical ω_p but different amplitude levels a_p.

To illustrate this behavior, the response of a free-standing rigid block (EOM defined by Eq. 2.16) with $p = 2.14\,\mathrm{s}^{-1}$, $\alpha = 0.25$, and $c_r = 0.81$ is investigated for three different amplitudes levels (‘a’, ‘b’, and ‘c’) and for a fixed spectral value of $\omega_p/p = 5$, resulting in a sine-pulse frequency of $\omega_p = 10.7\ \mathrm{s}^{-1}$ (equivalent to a pulse period of $T_p = 0.59$ s).

For $a_p = 3.01\,\alpha\,g$ (case ‘a’) the block does not overturn, whereas for $a_p = 3.02\,\alpha\,g$ it does, after experiencing one impact (mode 1). Figure 2.4b compares the two response time histories. One can see that the impact occurs after the pulse has passed ($t_{\text{impact}} > T_p$). When the amplitude a_p is further increased an analog response behavior applies until the acceleration amplitude reaches $a_p = 6.31\,\alpha\,g$ at point ‘b’. Interestingly, the pulse now induces tilt angles beyond α, but is able to bring it back below α before the pulse expires. For $a_p = 6.32\,\alpha\,g$, the block will no longer overturn. This is due to the fact that the initially induced tilt angle towards one side is so large that it allows the block to recover when tilting to the other side after impacting, as indicated in Figure 2.4c. This effect prevails until the amplitude reaches $a_p = 7.17\,\alpha\,g$ at point 'c'. Then, the amplitude of the pulse becomes too large for the block to even recover on the uplifting side. Figure 2.4d shows that after the pulse has ended the tilt angle is not able to reach a stable condition anymore ($\theta \leq \alpha$) and, therefore, overturns without impact.

Consequently, the response of a free-standing rigid block with the aforementioned parameters subjected to a sinusoidal pulse with $\omega_p/p = 5$ can be divided into four different types ($a_p \leq 0$):

1) $\frac{a_p}{\alpha\,g} \in [0, 3.01]$: Safe response with $|\theta_{\max}| \leq 1.0\,\alpha$.
2) $\frac{a_p}{\alpha\,g} \in [3.02, 6.31]$: Unsafe response: overturning with impact (mode 1).
3) $\frac{a_p}{\alpha\,g} \in [6.32, 7.16]$: Safe response with $|\theta_{\max}| > 1.0\,\alpha$.
4) $\frac{a_p}{\alpha\,g} \in [7.17, \infty)$: Unsafe response: overturning without impact (mode 2).

However, these four response types only appear if $\omega_p/p \leq 6.59$ (Fig. 2.4a). In this part of the spectrum mode 1 comes before mode 2 when the amplitude is gradually increased from zero. For $\omega_p/p > 6.59$, only two response types remain: 1) and 4). Then, mode 1 is inexistent and blocks only overturn with mode 2, independent of the amplitude of the pulse.

Note that the response behavior of the rigid block (*i.e.*, number of overturning modes, number of response types) depends on the shape of the excitation pulse. For other than the discussed cycloidal pulses, there might be more than two overturning modes, and/or more than four response types.

2.3 Planar Response of a Rocking Frame

In the framework of attaining his Doctor of Philosophy, M. Vassiliou investigated the dynamic response of multiple columns capped with a rigid beam, and published his work in 2010 [38] (written in Greek). In 2013, Makris & Vassiliou [39] republished the work under the name «Planar rocking response and stability analysis of an array of free-standing columns capped with a freely supported rigid beam».

The intention of Makris & Vassiliou was to explain the appreciable seismic stability of ancient free-standing columns that support heavy epistyles together with the even heavier frieze atop. Their model, which they called «rocking frame», comprises N free-standing rigid blocks with evenly distributed mass capped by a single rigid beam as shown in Figure 2.5 such that a planar rocking SDOF response results. Uplift of the oscillators is not restrained, but their sliding on the rocking surface is precluded at the base and at the cap-beam.

The corresponding equation of motion becomes

$$\ddot{\theta} = -\hat{p}^2 \cdot \Big(\sin(\operatorname{sgn}(\theta) \cdot \alpha - \theta) + \frac{\ddot{u}_g}{g} \cos(\operatorname{sgn}(\theta) \cdot \alpha - \theta) \Big), \tag{2.21}$$

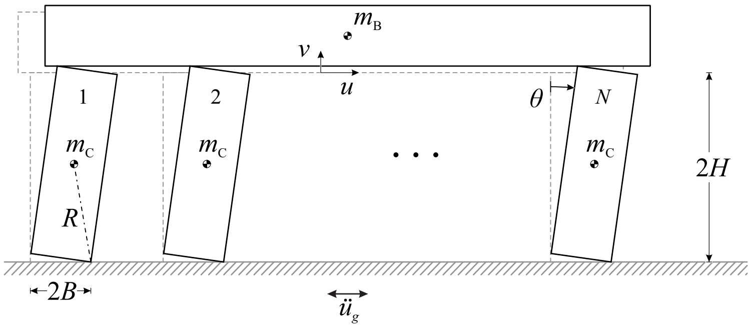

Figure 2.5: Rocking of an array of N free-standing columns capped with a freely supported rigid beam.

where the frequency parameter of the rocking frame, $\hat{p}$, is

$$\hat{p} = \sqrt{\frac{1+2\gamma}{1+3\gamma}} \cdot p, \quad \text{with} \quad p = \sqrt{\frac{3g}{4R}}, \tag{2.22}$$

and γ is the ratio of the mass of the cap-beam, m_B, divided by the mass of all N columns:

$$\gamma = \frac{m_\mathrm{B}}{N\, m_\mathrm{C}}. \tag{2.23}$$

Equation (2.21), describing the planar rocking motion of the rocking frame, is identical to the equation of motion that describes the planar rocking motion of a single free-standing rigid block with the same slenderness, except that the term $\hat{p}^2$ instead of p^2 is used which differs only by the factor $(1+2\gamma)/(1+3\gamma)$.

Makris & Vassiliou showed that the dynamic behavior of a rocking frame with a heavy cap-beam supported on columns with slenderness α and frequency parameter, $p = (3g)/(4R)$, is identical to the dynamic rocking response of a single rigid column with slenderness α and frequency parameter $p = \sqrt{2/3}p$. The value for p is smaller for the rocking frame and, thus, equal to a larger (and more stable) column. Using Equation (2.22) the size $\hat{R}$ of a solitary free-standing rigid block that responds in the same way can be determined:

$$\hat{R} = \left(1 + \frac{\gamma}{1+2\gamma}\right) \cdot R. \tag{2.24}$$

The only difference in the dynamic response occurs during impacts due to a different coefficient of restitution of the rocking frame:

$$c_r = \left(\frac{1 - \frac{3}{2}\sin^2\alpha + 3\gamma\cos(2\alpha)}{1+3\gamma}\right)^2. \tag{2.25}$$

It can be concluded that the rocking frame dissipates more energy than the solitary block of size $\hat{R}$.

2.4 Dimensional Analysis and Similitude Theory

This section will briefly introduce the basics of dimensional analysis and similitude theory [113–116]. Most of the material presented is selective content of the mentioned sources (quoted or paraphrased).

2.4.1 Dimensional Analysis

In engineering and science, dimensional analysis is the analysis of the relationships between different physical quantities by identifying their base quantities (such as length, mass, time) and units of measure (such as miles vs. kilometers, or pounds vs. kilograms) and tracking these dimensions as calculations or comparisons are performed. The conversion of units from one dimensional unit to another is often somewhat complex. Dimensional analysis, or more specifically the factor-label method, also known as the unit-factor method, is a widely used technique for such conversions using the rules of algebra.

Any physically meaningful equation (and any inequality) will have the same dimensions on its left and right sides, a property known as *dimensional homogeneity*. Checking for dimensional homogeneity is a common application of dimensional analysis, serving as a plausibility check on derived equations and computations. It also serves as a guide and constraint in deriving equations that may describe a physical system in the absence of a more rigorous derivation.

Dimensional Homogeneity

The most basic rule of dimensional analysis is that of dimensional homogeneity. The rule implies that in a physically meaningful expression only quantities of the same dimension (= commensurable quantities) can be compared, equated, added, or subtracted. Even when two physical quantities have identical dimensions, it may still be meaningless to compare or add them. For example, although torque and energy share the dimension $[L]^2[M][T]^{-2}$, they are fundamentally different physical quantities.

A related principle is that any physical law that accurately describes the real world must be independent of the units used to measure the physical variables. For example, Newton's laws of motion must hold true whether distance is measured in miles or kilometers.

Mathematical Properties

The dimensions that can be formed from a given collection of basic physical dimensions, such as $[M]$, $[L]$, and $[T]$, form an abelian group[1]. This group can be described as a vector space over the rational numbers, with for example dimensional symbol $[M]^i[L]^j[T]^k$ corresponding to the vector (i, j, k). The group identity 1, the dimension of dimensionless quantities, corresponds to the origin in this vector space.

The set of units of the physical quantities involved in a problem correspond to a set of vectors (or a matrix). The nullity describes some number (*e.g.*, n) of ways in which these vectors can be

---

[1] An abelian group is a group in which the result of applying the group operation to two group elements does not depend on the order in which they are written.

combined to produce a zero vector. These correspond to producing (from the measurements) a number of dimensionless quantities, $\{\Pi_1 \dots \Pi_n\}$ [117].

Dynamic Behavior

The dimension of physical quantities of interest in mechanics can be expressed in terms of three base dimensions $[M]$, $[L]$, and $[T]$, forming a 3-dimensional vector space. This is not the only valid choice of base dimensions, but it is the one most commonly used. For example, one might choose force, length and mass as the base dimensions (as some have done), with associated dimensions $[F]$, $[L]$, $[M]$; this corresponds to a different basis, and one may convert between these representations by a change of basis. The choice of the base set of dimensions is thus a convention, with the benefit of increased utility and familiarity. The choice of base dimensions is not arbitrary, because the dimensions must form a basis: they must span the space, and be linearly independent.

2.4.2 Similitude Theory

Similitude is a concept that is used in the testing of engineering models. A model is said to have similitude with the real application if the two share geometric similitude, kinematic similitude and dynamic similitude. The term *dynamic similitude* is often used as a catch-all because it implies that geometric and kinematic similitude has already been met. Similitude's main application is in hydraulic and aerospace engineering to test fluid flow conditions with scaled models. It is also the primary theory behind many textbook formulas in fluid mechanics. The concept of similitude is strongly tied to dimensional analysis.

Engineering models are used to study complex problems where calculations and computer simulations might not be reliable. Usually, these models are smaller than the final design, but not always. The use of scaled models allows testing of a design prior to building, and in many cases such tests are a critical step in the development process. The condition that a model reproduces all aspects of behavior of the prototype represented by it is know as *condition of similitude*. The primary goal of any experiment is to provide a result as part of a prototype and final build. To achieve that end, the concept of similitude is often used such that measurements made on a system in the laboratory environment can be used to describe the behavior of other similar system either in another laboratory environment or in real world.

Model and Prototype The laboratory built systems are often thought as *model*(m) while the first build beyond laboratory frame is called *prototype*(p).

Criteria for Similitude

The construction of a scaled model, however, must be accompanied by an analysis to determine what conditions it is tested under. While the geometry may be simply scaled, other parameters, such as inertia, temperature, or velocity may need to be altered. Similitude is achieved when testing conditions are created such that the test results are applicable to the real design.

Two systems, described by the same physics, operating under different sets of conditions, are said to be physically similar in respect of certain specified physical quantities when the ratio of corresponding magnitudes of these quantities between the two systems is the same everywhere.

In the field of dynamic testing, there is the concept of three types of similarities, which together constitute the complete similitude. They are recognized as *geometric similitude*, *kinematic similitude*, and *dynamic similitude*. Note that there might also be other types of similarities which must be satisfied in order to have a complete similitude. However, for purpose of arguments these three seem to be sufficient.

Table 2.1: Criteria required to achieve similitude and represent types of physical similitude.

Criterion	Description
Geometric similitude	Geometric similitude will exist between the model and the prototype if the ratios (r), usually known as scale factor, of all corresponding dimensions in both, model and prototype, are equal and can be presented mathematically as follows: $\frac{L_{(m)}}{L_{(p)}} = L_{(r)}. \qquad (2.26)$ Note, however, that the model does not necessarily need to be smaller than the prototype. In fact, the model and the prototype might be of identical size but differ concerning other factors such as inertia (mass distribution).
Kinematic similitude	Since motions are described by distance and time, it implies similitude of lengths and similitude of time intervals. If the corresponding lengths in the two systems are in a fixed ratio, the velocities of corresponding parts must be in a fixed ratio of magnitude of corresponding time intervals. If the ratio of corresponding lengths, known as the scale factor, is $l_{(r)}$ and the ratio of corresponding time intervals is $t_{(r)}$, then the magnitudes of corresponding velocities are in the ratio $l_{(r)}/t_{(r)}$ and the magnitudes of corresponding accelerations are in the ratio $l_{(r)}/t^2_{(r)}$. Note that it is impossible to maintain kinematic similitude in a distorted model.
Dynamic similitude	The ratios of all forces acting on corresponding part and boundary surfaces in the two systems are constant. The term ‘forces’ contains properties like gravity, friction, density, viscosity, elasticity, *etc.* As an example, expressing the force due to inertia by $F_i = \rho\, V\, a$ and that due to friction $F_f = \rho\, V\, g\, \mu$, and requiring that their ratio remains constant at all homologous points of model and the prototype, leads to $\frac{F_{i(m)}}{F_{f(m)}} = \frac{F_{i(p)}}{F_{f(p)}}. \qquad (2.27)$

Procedure for Achieving Similitude

To satisfy all three above conditions the application of each case is analyzed;

- All parameters required to describe the system are identified using principles from continuum mechanics.
- Dimensional analysis is used to express the system with as few independent variables and as many dimensionless parameters as possible.
- The values of the dimensionless parameters are held to be the same for both the scale model and application. This can be done because they are dimensionless and will ensure dynamic similitude between the model and the application. The resulting equations are used to derive scaling laws, which dictate model-testing conditions.

Problems

A perfect geometric similitude is not always easy to attain. Problems in achieving perfect geometric similitude are:

- For a small model, the surface roughness might not be reduced according to the scale factor (unless the model surfaces can be made very much smoother than those of the prototype). If for any reason, the scale factor is not the same throughout, a distorted model results.
- Sometimes it may so happen that to have a perfect geometric similitude within the available laboratory space, physics of the problem changes. For example, in case of large prototypes the size of the model is limited by the available floor space of the laboratory. The extent to which perfect geometric similitude should be sought therefore depends on the problem being investigated, and the accuracy required from the solution.
- It is often impossible to achieve strict similitude during a model test. The greater the departure from the application's operating conditions, the more difficult achieving similitude is. In these cases, some aspects of similitude may be neglected, focusing on only the most important parameters.

Chapter 3

Planar SDOF Rocking

In this chapter planar rocking systems that can be described with one degree of freedom are presented and discussed. The main parts of this chapter have been published or presented. At the EMI Conference at Stanford University, CA, the numerical model of the rolling-and-rocking oscillator, covered in Section 3.2.4, was presented orally [1]. At the 2016 ECCOMAS Congress an experimental study of the same model was presented [2].

3.1 Introduction

The first part of this chapter covers solitary rigid oscillators, *e.g.*, the free-standing rigid block first investigated by Housner. Based on this simple model, more complex solitary rigid oscillators are introduced in Sections 3.2.3 (extended flat base) and 3.2.4 (extended curved base), and compared against each other in Section 3.3. The systems being investigated are displayed in Figure 3.1.

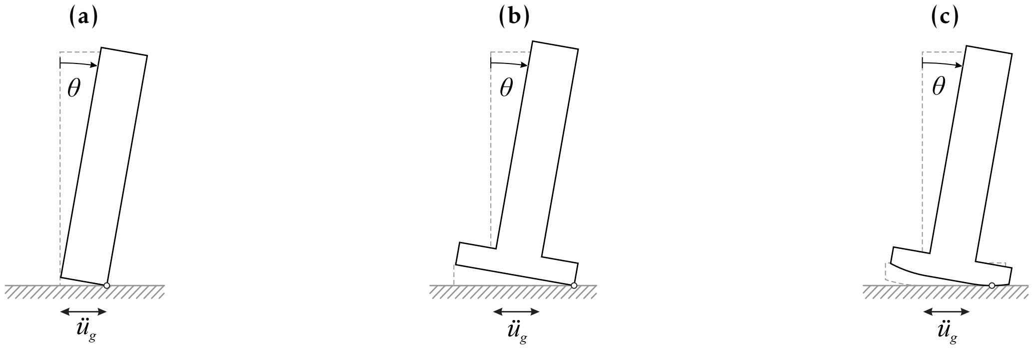

Figure 3.1: Different investigated solitary rigid oscillators: (a) Housner's block; (b) Extended flat block; (c) Rolling-and-rocking oscillator.

The second part of this chapter addresses rocking systems that comprise more than one oscillator ($N > 1$) but still can be described with just one degree of freedom. The model of the rocking frame, investigated by Vassiliou [38] and Makris & Vassiliou [39], serves as the base model for my extended model discussed in Section 3.4.2. The systems being investigated are displayed in Figure 3.2.

The impressive remains of the temple of Poseidon in Greece (Fig. 3.3), supposedly built around 700 BC [118], illustrate where the investigated models could be applied. The columns on the right are linked through their common cap-beam. Their identical in-plane response can be represented by a frame structure similar to the one in Figure 3.2. In contrast, the response of the free-standing solitary column on the far left is represented by an oscillator similar to the ones in Figure 3.1.

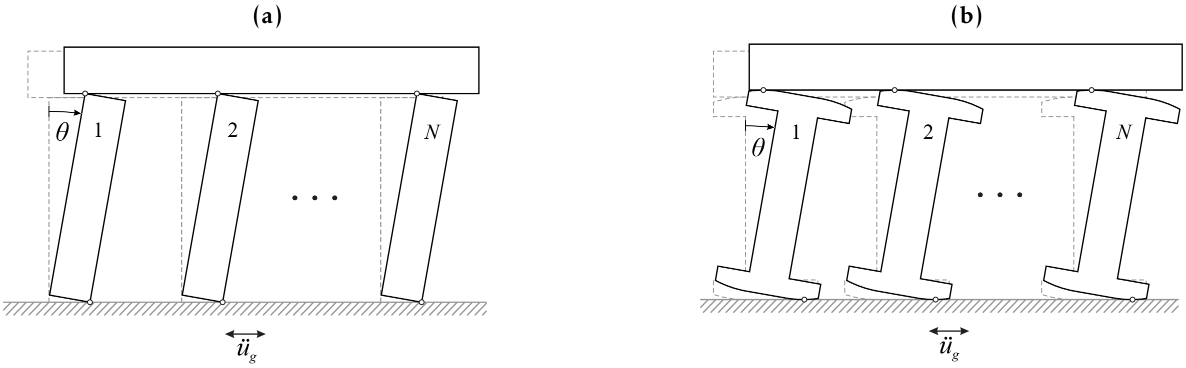

Figure 3.2: Different investigated frame structures: (a) Classical rocking frame; (b) Rolling-and-rocking frame.

Figure 3.3: Cape Sunion, Greece: Temple of Poseidon.

3.2 Rolling-and-Rocking Oscillators

3.2.1 Rectangular Free-Standing Rigid Oscillator

In this section, I revisit the free-standing rigid oscillator discussed by Housner in his seminal paper [16] and introduced in Chapter 2, and present it using the nomenclature chosen for this thesis, including additionally covered topics, *e.g.*, pushover analyses or varying rotational inertia. Due to its simple shape it is often referred to as the 'rigid rocking block' which is why I will use the abbreviation «B» for referencing to free-standing rigid oscillators.

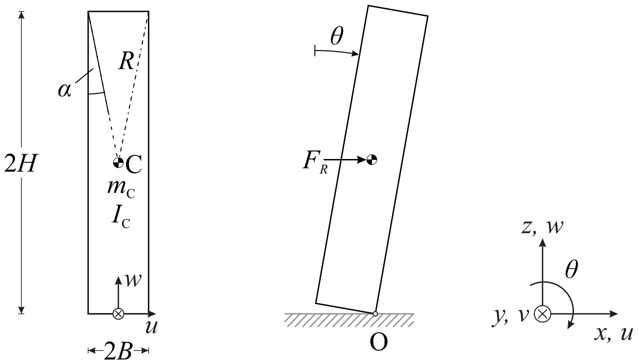

Figure 3.4: Model of a rectangular free-standing rigid oscillator.

Geometry

The horizontal and vertical displacement of the center C, both functions of the rotational degree of freedom θ, is given by

$$u_C = R\sin(\pm\alpha) - R\sin(\pm\alpha - \theta), \tag{3.1}$$

$$w_C = R\cos(\pm\alpha - \theta). \tag{3.2}$$

The upper sign '+' corresponds to the case of a positive tilt angle ($\theta > 0$) and the lower sign '−' to the case of a negative tilt angle ($\theta < 0$) with respect to the defined coordinate system (Fig. 3.4). In the literature, the to '±' equivalent expression '$\operatorname{sgn}(\theta)$' is also commonly used.

Mass and Rotational Inertia

The rocking oscillator has a total mass m_C and a rotational inertia I_C around the center of mass C. For the case presented by Housner, which assumed an evenly distributed mass, the application of the general definition for the rotational inertia,

$$I = \int_M r^2 dm, \tag{3.3}$$

where $M = V \cdot \rho$ is the total mass and r the distance from the center of mass to the infinitesimally small mass dm, yields

$$I_C = \frac{m_C}{2B \cdot 2H} \iint_V x^2 + z^2 \, dx\, dz = \frac{m_C}{3} \cdot \left(B^2 + H^2\right) = \frac{1}{3} m_C R^2. \tag{3.4}$$

The rotational inertia around the pivot point O follows with the *parallel axis theorem*:

$$I_0 = I_C + m_C R^2 = \frac{4}{3} m_C R^2. \tag{3.5}$$

By introducing a mass eccentricity factor, λ, defined as

$$\lambda = \frac{I_C}{m_C R^2}, \tag{3.6}$$

the rotational inertia around the pivot point O reads

$$I_0 = (1 + \lambda) \cdot m_C R^2. \tag{3.7}$$

The introduction of the value λ lets us consider different mass distributions within the oscillator, *e.g.*, when heavy steel plates are used for protection at the base and the top. Table 3.1 lists the values of λ for the different oscillators illustrated in Figure 3.5. From Equation (3.4) it follows that $\lambda = 1/3$ for a solid solitary oscillator with evenly distributed mass and with a rectangular shape.

Theoretically, λ can take values between 0 (mass concentrated in the center of mass C) and 1 (mass distributed at the outside edges of the oscillator). Realistic values for λ, however, range from 0.33 to 0.50, depending on the slenderness $\tan\alpha$ and the thickness d_s of the steel plates that protect the ends. The value of λ is only marginally affected by the slenderness $\tan\alpha$. Much more is it affected by the thickness d_s of the steel plates. Figure 3.6 plots λ vs. $d_s/2H$. For both rectangular blocks and cylinders, $\lambda_{\max} \approx 0.49$ occurs when $d_s = 0.30H$. Note that the value λ is independent of the size R.

Table 3.1: Free-standing rigid oscillators: moment of inertia for oscillators of different shapes and materials (assuming $\rho_{steel} = 3.25\,\rho_{concrete}$).

Oscillator	Shape	Body	Description	$d_s/2H$	λ^1	λ^2
(a)	rectangular	solid	uniformly distributed		0.333	0.333
(b)	rectangular	solid	reinforced concrete column with steel end plates at the bottom and top	0.02	0.385	0.383
				0.04	0.422	0.420
(c)	rectangular	hollow	uniformly distributed, thin walled^3		0.337	0.346
(d)	cylindrical	solid	uniformly distributed		0.333	0.330
(e)	cylindrical	solid	reinforced concrete column with steel end plates at the bottom and top	0.02	0.391	0.409
				0.04	0.429	0.445
(f)	cylindrical	hollow	uniformly distributed, thin walled^3		0.333	0.330

^{1}: $\tan\alpha = 0.10$, ^{2}: $\tan\alpha = 0.20$, ^{3}: $t \ll 2H$.

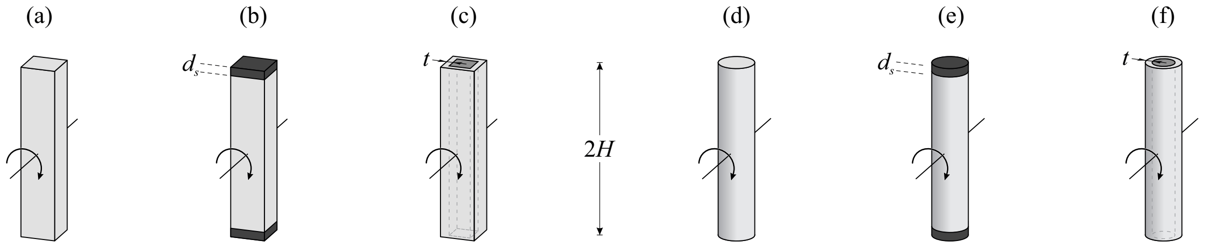

Figure 3.5: Differently shaped free-standing rigid oscillators (Tab. 3.1).

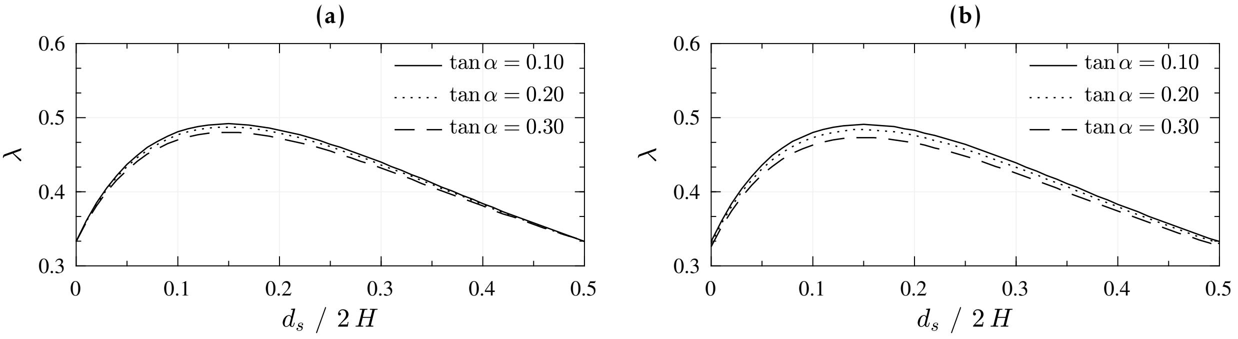

Figure 3.6: Free-standing rigid oscillators: moment of inertia for reinforced concrete columns with steel end protection (assuming $\rho_{steel} = 3.25\,\rho_{concrete}$): (a) Rectangular blocks; (b) Cylinders.

Equation of Motion

The equation of motion is computed using the *Lagrangian Equation* $L = T - V$ described in Section A.2. To do so, the kinetic and the potential energy of the oscillator have to determined: the kinetic energy is given by

$$T = \frac{1}{2} I_C\,\dot{\theta}^2 + \frac{1}{2} m_C \cdot \left(\dot{u}_C^2 + \dot{w}_C^2\right) = \frac{1}{2}\dot{\theta}^2\, m_C\, R^2 \cdot (1 + \lambda), \tag{3.8}$$

and the potential energy is given by

$$V = g\, m_C\, R \cdot \Big(\cos\alpha\,\cos\theta + \sin(\pm\alpha)\,\sin\theta\Big). \tag{3.9}$$

The equation of motion for θ can now be derived by applying

$$\frac{\mathrm{d}}{\mathrm{d}t}\left(\frac{\partial L}{\partial \dot{\theta}}\right) - \frac{\partial L}{\partial \theta} = 0. \tag{3.10}$$

It follows:

$$\ddot{\theta} \cdot \left(m_{\mathrm{C}} R^2 + I_{\mathrm{C}}\right) = m_{\mathrm{C}} R \cdot \Big(-g \sin(\pm\alpha - \theta) - \ddot{u}_g \cos(\pm\alpha - \theta) \Big), \tag{3.11}$$

or:

$$\ddot{\theta} = -p^2 \cdot \left(\sin(\pm\alpha - \theta) + \frac{\ddot{u}_g}{g} \cos(\pm\alpha - \theta) \right), \tag{3.12}$$

where p is the frequency parameter which, using Equation (3.7), can be expressed as

$$p = \sqrt{\frac{g\, m_{\mathrm{C}} R}{I_0}} = \sqrt{\frac{g}{R}\, \frac{1}{1+\lambda}}. \tag{3.13}$$

Assuming CoAM [16], the coefficient of restitution c_r is

$$c_r = \left(1 - \frac{2}{1+\lambda} \sin^2\alpha\right)^2. \tag{3.14}$$

Equation (3.12) can be linearized with respect to α and θ to yield

$$\ddot{\theta} = -p^2 \cdot \left(\pm\alpha - \theta + \frac{\ddot{u}_g}{g} \right). \tag{3.15}$$

Size Effect

The size parameter R only appears in the denominator of Equation (3.13); its influence is reciprocal on the tilt angle acceleration $\ddot{\theta}$. To illustrate this fact, free vibration responses of two solid rigid oscillators with the identical slenderness $\tan\alpha_1 = \tan\alpha_2 = 0.20$ but different sizes (B1: $R_1 = 2$ m, B2: $R_2 = 3$ m) are computed for an initial tilt angle $\theta_0 = 0.75 \cdot \alpha = 0.148$ rad.

Applying Equation (3.13) yields $p_1 = 1.918\ \mathrm{s}^{-1}$ and $p_2 = 1.566\ \mathrm{s}^{-1}$. The resulting response time histories, using the linearized equation of motion (Eq. 3.15), are plotted in Figure 3.7. Oscillator 1 first impacts at $t_1 = 1.076$ s while the larger oscillator 2 impacts for the first time, a little bit later, at $t_2 = 1.318$ s.

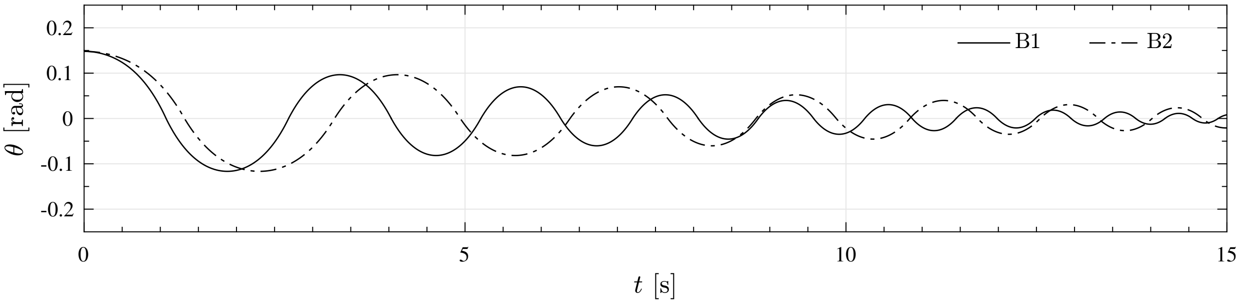

Figure 3.7: Free vibration response comparison for two solid rigid oscillators with identical slenderness ($\tan\alpha_1 = \tan\alpha_2 = 0.20$) but with different sizes ($R_1 = 2$ m, $R_2 = 3$ m) released from $\theta_0 = 0.75 \cdot \alpha = 0.148$ rad.

Computation of the tilt angle acceleration $\ddot{\theta}$ at t_0 yields

$$\ddot{\theta}_1(t = t_0) = -p_1^2 \cdot (\alpha - \theta_0) = -0.182\ \mathrm{s}^{-2}, \quad \text{and} \tag{3.16}$$

$$\ddot{\theta}_2(t = t_0) = -p_2^2 \cdot (\alpha - \theta_0) = -0.121\ \mathrm{s}^{-2}\,. \tag{3.17}$$

Hence, oscillator 1 experiences a rotational acceleration that is 50 % larger than the one of oscillator 2 due to its smaller size ($p_1 > p_2$).

Uplift and Post-Uplift Behavior

Rocking motion is initiated when the uplifting force exceeds the restoring force, that is when when $\ddot{u}_g = \ddot{u}_{g,up} = g \tan\alpha$. Figure 3.8 plots the restoring force F_R against the tilt angle θ in a pushover curve in the normalized space $\frac{F_R}{m_C g}$ vs θ.

$$F_R = g\, m_C \tan(\alpha - \theta)\,. \tag{3.18}$$

At rest ($\theta = 0$) the restoring force F_R is maximal and equal to the static uplifting force $F_{up} = g\, m_C \tan\alpha$. When the tilt angle reaches $\theta = \alpha$ the restoring force is zero ($F_R = 0$) and the oscillator is at the verge of tipping over.

The post-uplift stiffness k_{rock} can be computed via the derivative $\frac{\partial}{\partial\theta} F_R$ of Equation (3.18):

$$k_{rock} = -g\, m_C \cdot \Big(1 + \tan^2(\alpha - \theta)\Big). \tag{3.19}$$

When k_{rock} is linearized for α and θ one gets:

$$k_{rock} = -g\, m_C\,, \tag{3.20}$$

which results in $k^*_{rock} = k_{rock}/(g\, m_c) = -1$ in the non-dimensional form — implied with *. The tilt angle for which the restoring force is zero will be referred to as the rotation capacity θ_c of the respective oscillator; for the rigid rocking block it is $\theta_c = \alpha$. The corresponding horizontal displacement capacity, measured at the C, is $u_{C,c}$. By plugging in $\theta = \alpha$ into Equation (3.1) the displacement capacity for the rigid rocking block reads: $u_{C,c} = R \sin\alpha = B$.

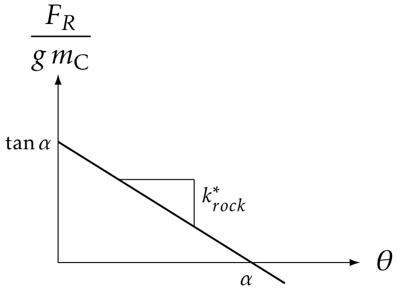

Figure 3.8: Static nonlinear pushover response curve of a rectangular free-standing rigid oscillator.

3.2.2 Similitude

As briefly introduced in Section 2.4.2, similitude is similarity of behavior for different systems with equal similarity parameters. Hence, in this section the similarity parameters for free-standing rigid oscillators are analytically derived, and then validated by performing numerical experiments.

Analytical Ground Motion Signals

Strong ground motions often contain a distinguishable acceleration pulse, which is responsible for most of the inelastic deformation of fixed-base structures [119–121]. Physically realizable analytical ground motion pulses can qualitatively describe the impulsive character of near-fault ground motions. For a particular pulse shape, two parameters are needed to describe it:

1) the acceleration amplitude, a_p, and
2) the dominant cyclic frequency, ω_p [122].

$$\ddot{u}_g = \mathcal{F}\left(a_p, \omega_p\right). \tag{3.21}$$

Another pair of parameters is the velocity amplitude, v_p, and dominant cyclic frequency, ω_p [120]. Now, let us substitute the acceleration amplitude a_p with $\hat{a}_p \cdot \ddot{u}_{g,up}$ where $\hat{a}_p$ is a scaling factor of the ground acceleration $\ddot{u}_{g,up}$ that leads to uplift. Then, $\ddot{u}_g$ is a function of three variables:

$$\ddot{u}_g = \mathcal{F}\left(\hat{a}_p, \ddot{u}_{g,up}, \omega_p\right). \tag{3.22}$$

When excited by an analytical pulse ground motion of a specific shape, acceleration amplitude a_p, and dominant frequency ω_p [122], the linearized equation describing the response θ of a free-standing rocking oscillator (Eq. 3.15) is a function of eight variables:

$$\mathcal{F}\left(\theta, t, \alpha, p, g, \hat{a}_p, \ddot{u}_{g,up}, \omega_p\right) = 0. \tag{3.23}$$

Dimensional Analysis

In 1914, Buckingham published a study on physically similar systems and the use of dimensional equations [117]. According to Vashy-Buckingham's Π-theorem [113, 117, 123], the number of dimensionless products with which the problem can be completely described is equal to number of variables minus the number of reference dimensions:

$$i = n - k. \tag{3.24}$$

For the eight variables in Equation (3.23), there are two reference dimensions: length $[L]$ and time $[T]$. In Table 3.2 the dimensions of every variable are listed. Applying Equation (3.24) yields that the rocking response of a free-standing rigid oscillator can be described with $i = 8 - 2 = 6$ dimensionless products, Π_i, defined by

$$\Pi_i = Q_1^{a_i} \cdots Q_k^{\kappa_i} P_i = 1, \qquad i = 1 \ldots 6,\ k = 1 \ldots 2, \tag{3.25}$$

where P_i represent the quantities that are regarded as derived. To find a specific form of Equation (3.23), we select $k = 2$ of the variables as fundamental and proceed to use Equation (3.25).

Table 3.2: Reference dimensions for the eight variables of Equation 3.23.

Name	Symbol	Dimensions	Name	Symbol	Dimensions
Tilt angle	θ	$[\cdot]$	Gravitation	g	$[L][T]^{-2}$
Time	t	$[T]$	Scaling factor of $\ddot{u}_{g,up}$	$\hat{a}_p$	$[\cdot]$
Slenderness	α	$[\cdot]$	Uplifting acceleration	$\ddot{u}_{g,up}$	$[L][T]^{-2}$
Frequency parameter	p	$[T]^{-1}$	Acceleration frequency	ω_p	$[T]^{-1}$

Let us set $Q_1 = p$ and $Q_2 = g$ as the fundamental variables. Then, applying Equation (3.25) yields the following set of equations:

$$\begin{aligned} &p^{a_1}\, g^{b_1}\ \theta = 1\,, && p^{a_2}\, g^{b_2}\ t = 1\,, && p^{a_3}\, g^{b_3}\ \alpha = 1\,,\\ &p^{a_4}\, g^{b_4}\ \hat{a}_p = 1\,, && p^{a_5}\, g^{b_5}\ \ddot{u}_{g,up} = 1\,, && p^{a_6}\, g^{b_6}\ \omega_p = 1\,. \end{aligned} \tag{3.26}$$

If we take the first equation and insert the dimensions of Q_1 and Q_2 we get

$$[T]^{-a_1}\quad [L]^{b_1}\,[T]^{-2\,b_1} = 1\,. \tag{3.27}$$

The above equation is satisfied when $b_1 = 0$ and $a_1 = 0$. Therefore, it follows that

$$\Pi_1 = \theta\,. \tag{3.28}$$

Similarly, the remaining dimensionless products are found:

$$\begin{aligned} &[T]^{-a_2}\quad [L]^{b_2}\,[T]^{-2\,b_2}\quad [T]^{1} &&= 1 \longrightarrow b_2 = 0\,, a_2 = 1 &&\longrightarrow \Pi_2 = p\,t\,,\\ &[T]^{-a_3}\quad [L]^{b_3}\,[T]^{-2\,b_3} &&= 1 \longrightarrow b_3 = 0\,, a_3 = 0 &&\longrightarrow \Pi_3 = \alpha\,,\\ &[T]^{-a_4}\quad [L]^{b_4}\,[T]^{-2\,b_4} &&= 1 \longrightarrow b_4 = 0\,, a_4 = 0 &&\longrightarrow \Pi_4 = \hat{a}_p\,,\\ &[T]^{-a_5}\quad [L]^{b_5}\,[T]^{-2\,b_5}\quad [L]\,[T]^{-2} &&= 1 \longrightarrow b_5 = -1\,, a_5 = 0 &&\longrightarrow \Pi_5 = \frac{\ddot{u}_{g,up}}{g}\,,\\ &[T]^{-a_6}\quad [L]^{b_6}\,[T]^{-2\,b_6}\quad [T]^{-1} &&= 1 \longrightarrow b_6 = 0\,, a_6 = -1 &&\longrightarrow \Pi_6 = \frac{\omega_p}{p}\,. \end{aligned} \tag{3.29}$$

Finally, Equation (3.23) becomes a function of six dimensionless products:

$$\mathcal{F}\left(\theta, p\,t, \alpha, \hat{a}_p, \frac{\ddot{u}_{g,up}}{g}, \frac{\omega_p}{p}\right) = 0\,. \tag{3.30}$$

In the literature $\ddot{u}_g$ is usually represented by only by the two parameters a_p and ω_p. Then, Equation (3.30) is a function of only five dimensionless products. But the dimensional analyses that follow in the next sections and chapters will show the reasoning behind representing $\ddot{u}_g$ with three parameters instead of two (Eq. 3.22).

Orientational Analysis

The two products θ and α from Equation (3.30) are dimensionless, but they can be assigned to an orientation. Hence, they are not orientationless. Siano supplemented the orientational analysis to the dimensional analysis in 1985 [124]. The procedure is similar to the one used for dimensional analysis, however, I will refrain from going into this here, and refer to the available literature [26,79,124].

Eventually, also counting the coefficient of restitution (c_r is assumed dimensionless and orientationless [26]), the linearized rocking response of a rigid oscillator is a function of five dimension- and orientationless products:

$$\mathcal{F}\left(\frac{\theta}{\alpha}, p\,t, \frac{\omega_p}{p}, \hat{a}_p, c_r\right) = 0\,. \tag{3.31}$$

When $\ddot{u}_g$ is defined according to Equation (3.21) the linearized rocking response of a rigid oscillator is a function of following five dimension- and orientationless products [26, 28, 32, 43]:

$$\mathcal{F}\left(\frac{\theta}{\alpha}, p\,t, \frac{\omega_p}{p}, \frac{a_p}{g\,\alpha}, c_r\right) = 0\,. \tag{3.32}$$

Note that '$g\,\alpha$' represents the linearized uplifting acceleration. The dimensionless term '$\frac{a_p}{g\,\alpha}$' is, therefore, the acceleration amplitude $a_p = \hat{a}_p \cdot \ddot{u}_{g,up}$ divided by the linearized uplifting acceleration $g\,\alpha$. Often, the exact value $\ddot{u}_{g,up} = g\tan\alpha$ is used instead ([28, 32, 43] among others) such that

$$\mathcal{F}\left(\frac{\theta}{\alpha}, p\,t, \frac{\omega_p}{p}, \frac{a_p}{g\tan\alpha}, c_r\right) = 0\,. \tag{3.33}$$

Note that by introducing $\hat{a}_p$ from the beginning (Eq. 3.31) both solutions are possible, and depend solely on the definition of the uplifting acceleration:

$$\ddot{u}_{g,up} = \begin{cases} g\,\alpha\,, & \text{linearized}\,, \\ g\tan\alpha\,, & \text{exact}\,. \end{cases} \tag{3.34}$$

Example 3.1: FVA of free-standing rigid oscillators

Let us revisit the free vibration response in Figure 3.7 where the tilt angle response θ is plotted vs. the time t for two rigid oscillators B1 (R_1 = 2 m, $\tan\alpha_1$ = 0.20) and B2 (R_2 = 3 m, $\tan\alpha_2$ = 0.20). Since it is a FVA the governing equation of motion is, according to Equation (3.31), a function of only three dimension- and orientationless products: $\mathcal{F}(\theta/\alpha, p\,t, c_r) = 0$ ($\hat{a}_p$ and ω_p are related to a pulse acceleration).

Using the linearized equation of motion (Eq. 3.15), the time histories are computed and plotted in the dimensionless space θ/α vs. $p\,t$, as shown in Figure 3.9a. Quite clearly, the responses overlap flawlessly. If we compute the dimensionless times of impact τ_i, we get: $\tau_1 = p_1 \cdot t_1 = 1.918\ \mathrm{s}^{-1} \cdot 1.076\ \mathrm{s} = 2.064$, and $\tau_2 = p_2 \cdot t_2 = 1.566\ \mathrm{s}^{-1} \cdot 1.318\ \mathrm{s} = 2.064$. Adding a third oscillator B3 with a different slenderness (R_3 = 3 m, $\tan\alpha$ = 0.30) leads to diverging time histories after the first impact occurs (Fig. 3.9b). This indicates the dependency of the response on c_r: for B3a the coefficient of restitution is computed with Equation (3.14) while the one of B3b is set equal to c_r of B2.

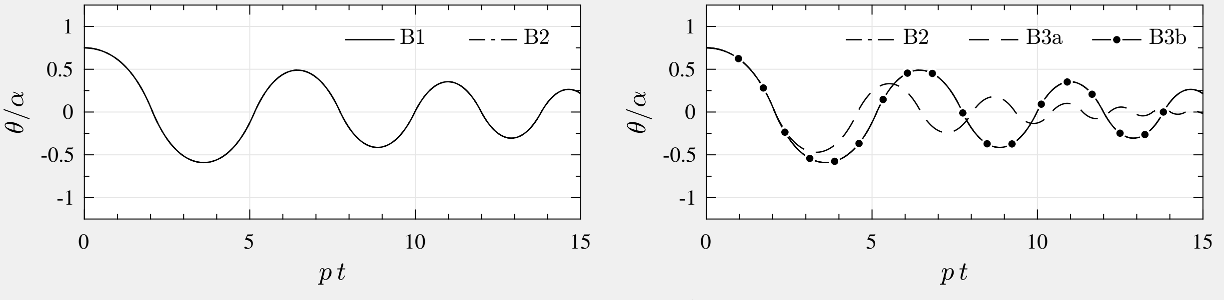

Figure 3.9: FVA of three solid rigid oscillators B1, B2, and B3 (R_1 = 2 m, $\tan\alpha_1$ = 0.20; R_2 = 3 m, $\tan\alpha_2$ = 0.20; R_3 = 3 m, $\tan\alpha_3$ = 0.30) when released from θ_0/α = 0.75.

Example 3.2: RHA of free-standing rigid oscillators

In this example the similitude law will be illustrated when two solid rigid oscillators B4 ($R_4 = 2$ m, $\tan\alpha_4 = 0.20$) and B5 ($R_5 = 3$ m, $\tan\alpha_5 = 0.30$) are subjected to a sine-pulse ground motion. Then, the response is a function of five dimensionless products, according to Equation (3.31). The coefficient of restitution is fixed to $c_r = 0.9$ for both oscillators. The sine-pulse is defined by Equation (2.20), and is characterized by the chosen dimensionless parameters $\omega_p/p = 5$ and $\hat{a}_p = 2$. For the latter it is important whether the exact or the linearized value is used for $\ddot{u}_{g,up}$. To show the difference, the responses of two different cases are computed: (a) $\ddot{u}_{g,up}$ linearized; (b) $\ddot{u}_{g,up}$ exact.

Using the linearized equation of motion, Equation (3.15), the time histories are computed and plotted in the dimensionless space θ/α vs. $p\,t$, as shown in Figure 3.10. As one notices, the responses for case (a) are identical while for case (b) a difference can be identified. However, the magnitude of the error (*i.e.*, the difference in response) depends on the values of $\hat{a}_p$ and ω_p/p.

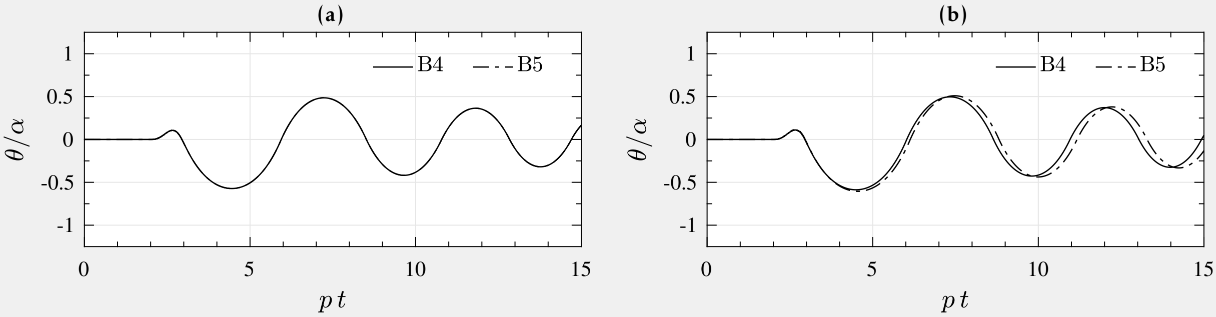

Figure 3.10: RHA of two solid rigid oscillators B4 and B5 ($R_4 = 2$ m, $\tan\alpha_4 = 0.20$; $R_5 = 3$ m, $\tan\alpha_5 = 0.30$; c_r fixed at 0.9 for both) when subjected to a sine-pulse ($\hat{a}_p = 2$, $\omega_p/p = 5$): (a) $\ddot{u}_{g,up}$ linearized; (b) $\ddot{u}_{g,up}$ exact.

3.2.3 Free-Standing Rigid Oscillator with Flat Extensions

In this section, I extend the base of the free-standing rigid rocking block with flat wedges, derive the equation of motion, and compute the force–rotation behavior. I use the abbreviation «B^{ef}» (**b**lock with an **e**xtended **f**lat base) for referencing to free-standing rigid oscillators with flat extensions.

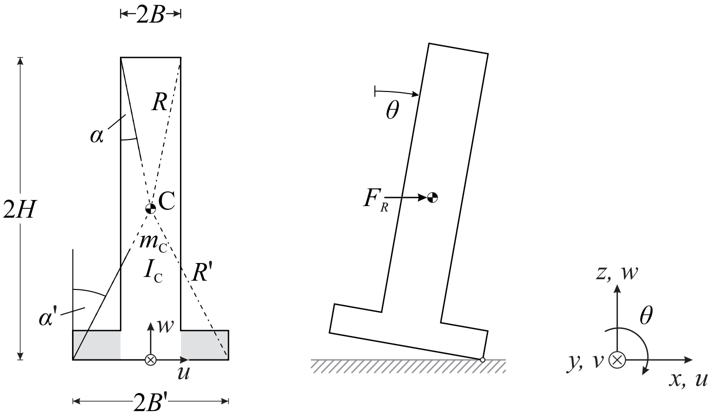

Figure 3.11: Model of a free-standing rigid oscillator with flat extensions.

Geometry

The flat extensions indicated with light gray color in Figure 3.11 increase the total width of the oscillator. They are assumed to be rigid and massless, keeping both the total mass m_C and the rotational inertia I_C identical to Housner's block. The horizontal and vertical displacement of the center C of the extended base system is given by

$$u_\mathrm{C} = R' \sin(\pm\alpha') - R' \sin(\pm\alpha' - \theta), \tag{3.35}$$

$$w_\mathrm{C} = R' \cos(\pm\alpha' - \theta), \tag{3.36}$$

where $R' = R\,\frac{\cos\alpha}{\cos\alpha'}$. The width of the extensions controls the new total base width $2B'$, increasing the slenderness from $B:H$ to $B':H$ (Fig. 3.11).

Updated Equations

Consequently, the equation of motion, the frequency parameter, and the coefficient of restitution change as follows:

$$\ddot{\theta} = -\hat{p}^2 \cdot \left(\sin(\pm\alpha' - \theta) + \frac{\ddot{u}_g}{g} \cos(\pm\alpha' - \theta) \right) \tag{3.37}$$

$$\hat{p} = \sqrt{\frac{4\cos\alpha'\cos\alpha}{\cos^2\alpha' + 3\cos^2\alpha}} \cdot p \tag{3.38}$$

$$c_r = \left(1 - \frac{2}{1 + \lambda\,\frac{\cos^2\alpha'}{\cos^2\alpha}} \sin^2\alpha \right)^2 \tag{3.39}$$

Equation (3.37) can be linearized with respect to α' and θ to yield

$$\ddot{\theta} = -\hat{p}^2 \cdot \left(\pm\,\alpha' - \theta + \frac{\ddot{u}_g}{g} \right), \tag{3.40}$$

where $\hat{p} = p$ (Eq. 3.13) follows from linearization. The coefficient of restitution c_r analogously collapses to the value afore derived (Eq. 3.14).

Uplift and Post-Uplift Behavior

The linearized post-uplift stiffness remains $k^*_{rock} = k_{rock}/(g\, m_c) = -1$. Although the rotation capacity of the extended block increases to $\theta_c = \alpha'$ (Fig. 3.12), there is a drawback: the force needed to induce uplift also increases due to the increased slenderness, to $F_R = g\, m_C \tan\alpha'$. This means that uplift will be accompanied by a higher force demand on the oscillator and its potential superstructure. A way to partly avoid this force increase without losing the beneficiary increased capacity ($\theta_c = \alpha'$) is presented in Section 3.2.4.

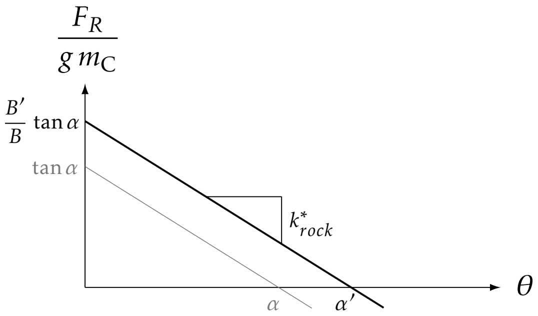

Figure 3.12: Static nonlinear pushover response curve of a free-standing rigid oscillator with flat extensions.

Similarity Parameters

For the linearized equations, dimensional and orientational analysis yields

$$\mathcal{F}\left(\frac{\theta}{\alpha'}, \hat{p}\, t, \frac{\omega_p}{\hat{p}}, \hat{a}_p, c_r\right) = 0, \tag{3.41}$$

where $\hat{a}_p = \frac{a_p}{\ddot{u}_{g,up}}$ as defined by Equation (3.34). Note that $\hat{p} = p$ follows when Equation (3.38) is linearized ($\cos\alpha \approx \cos\alpha' \approx 1$).

Example 3.3: RHA of free-standing rigid oscillators with flat extensions «B$^{\text{ef}}$»

Let us apply the dimensional and orientational analysis to two free-standing solid rigid oscillators B1$^{\text{ef}}$ ($R_1 = 2$ m, $\tan\alpha_1 = 0.10$, $\tan\alpha'_1 = 0.20$, $c_r = 0.9$) and B2$^{\text{ef}}$ ($R_2 = 3$ m, $\tan\alpha_2 = 0.10$, $\tan\alpha'_2 = 0.30$, $c_r = 0.9$) where the bases are extended with flat rigid and massless wedges. Both oscillators are subjected to a sine-pulse with $\hat{a}_p = 2$ and $\omega_p/p = 5$. Using the linearized equation of motion (Eq. 3.40) the time histories are computed and plotted in Figure 3.13.

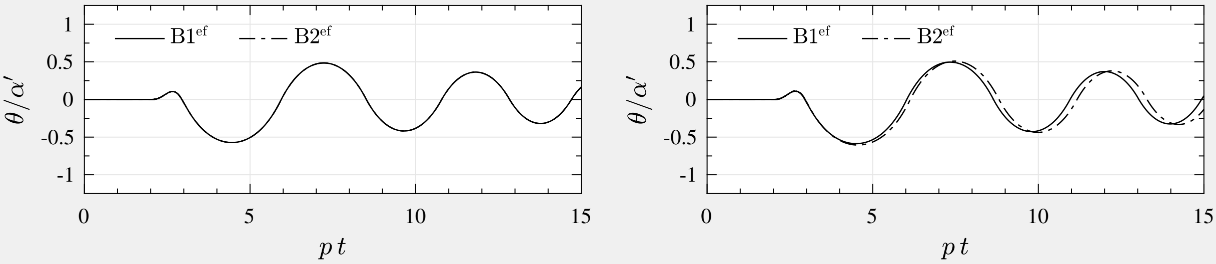

Figure 3.13: RHA of two free-standing rigid oscillators with flat extensions ($R_1 = 2$ m, $\tan\alpha_1 = 0.10$, $\tan\alpha'_1 = 0.20$; $R_2 = 3$ m, $\tan\alpha_2 = 0.20$, $\tan\alpha'_2 = 0.30$; $c_r = 0.9$ for both): (a) $\ddot{u}_{g,up}$ linearized; (b) $\ddot{u}_{g,up}$ exact.

3.2.4 Free-Standing Rigid Oscillator with Curved Extensions

In this section, I extend the base of the free-standing rigid rocking block with curved wedges, derive the equations of motion, and compute the force–rotation behavior. I use the abbreviation «B^{ec}» (**b**lock with an **e**xtended **c**urved base) for referencing to free-standing rigid oscillators with curved extensions.

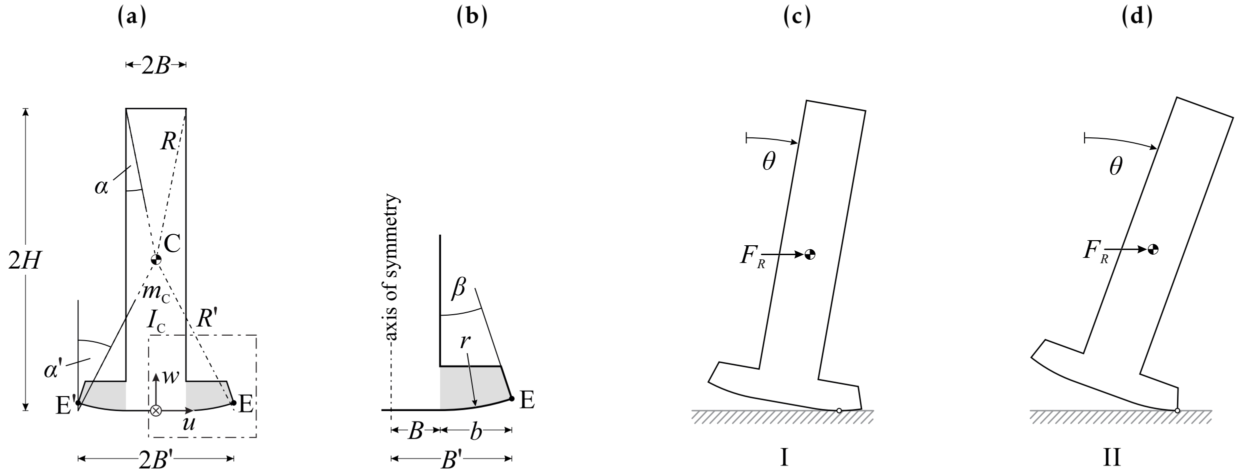

Figure 3.14: Model of a free-standing rigid oscillator with curved extensions: (a) Model; (b) Wedge detail; (c) Phase I: Rolling; (d) Phase II: Rocking.

Geometry

Extending the base with curved wedges as shown in Figure 3.14 introduces an additional form of motion that I call *rolling*. The entire motion of the oscillator, therefore, has to be separated into two phases:

I: *Rolling*

After uplift occurs the oscillator will *roll* on the curved part of the wedge until either the contact point reaches the edge at E or E', respectively, and phase II begins ($|\theta| = \beta$), or until the oscillator impacts ($\theta = 0$).

II: *Rocking*

If the oscillator tilts beyond $|\theta| = \beta$ it experiences *rocking* motion around the pivot points E or E', respectively, until either the oscillator returns to phase I ($|\theta| = \beta$), or until it overturns (numerically defined as $|\theta| = \pi/2$).

The geometry of the wedge can be described by the following parameters: the width b, the radius of curvature r, and the angle β that separates the two phases *rolling* and *rocking*. The parameters are coupled through the geometrical equation

$$b = r\sin\beta = B' - B, \tag{3.42}$$

where $B = H\tan\alpha$ and $B' = H\tan\alpha'$. Dividing r by the total oscillator height $2H$ yields the dimensionless parameter ρ for the radius of curvature:

$$\rho = \frac{r}{2H} = \frac{r}{2R\cos\alpha}. \tag{3.43}$$

Assuming the extended width b and the radius ρ are given, the wedge angle β can be computed by combining Equations (3.42) and (3.43):

$$\beta = \operatorname{asin}\left(\frac{\tan\alpha' - \tan\alpha}{2\rho}\right). \tag{3.44}$$

Equation (3.44) only holds if $\rho \leq \frac{1}{2}(\tan\alpha' - \tan\alpha)$. Otherwise, the curvature ρ is too small to geometrically enable an extended total base width of $2B' = 2H\tan\alpha'$.

Linearization of Equation (3.44) gives

$$\beta = \frac{\alpha' - \alpha}{2\rho}. \tag{3.45}$$

Uplift and Post-Uplift Behavior

The horizontal and vertical displacement of the center C during phase I is given by

$$^{\mathrm{I}}u_{\mathrm{C}} = R\sin(\pm\alpha) - R\sin(\pm\alpha - \theta) + r\cdot\Big(\theta - \sin\theta\Big), \tag{3.46}$$

$$^{\mathrm{I}}w_{\mathrm{C}} = R\cos(\pm\alpha - \theta) + r\cdot\Big(1 - \cos\theta\Big). \tag{3.47}$$

The restoring force $^{\mathrm{I}}F_R$ and the stiffness $k_{roll} = {}^{\mathrm{I}}k = \frac{\partial}{\partial\theta}{}^{\mathrm{I}}F_R$ of phase I yield:

$$^{\mathrm{I}}F_R = g\,m_{\mathrm{C}}\,\frac{R\sin(\alpha - \theta) + r\sin\theta}{R\cos(\alpha - \theta) + r\cdot\Big(1 - \cos\theta\Big)}, \tag{3.48}$$

$$^{\mathrm{I}}k = g\,m_{\mathrm{C}}\cdot\left(\frac{R\cos(\alpha - \theta) - r\cos\theta}{R\cos(\alpha - \theta) + r\cdot\Big(1 - \cos\theta\Big)} - \left(\frac{R\sin(\alpha - \theta) + R\sin\theta}{R\cos(\alpha - \theta) + r\cdot\Big(1 - \cos\theta\Big)}\right)^2\right). \tag{3.49}$$

Linearization with respect to α and θ simplifies Equation (3.49) to

$$^{\mathrm{I}}k^* = \frac{^{\mathrm{I}}k}{g\,m_{\mathrm{c}}} = 2\rho - 1. \tag{3.50}$$

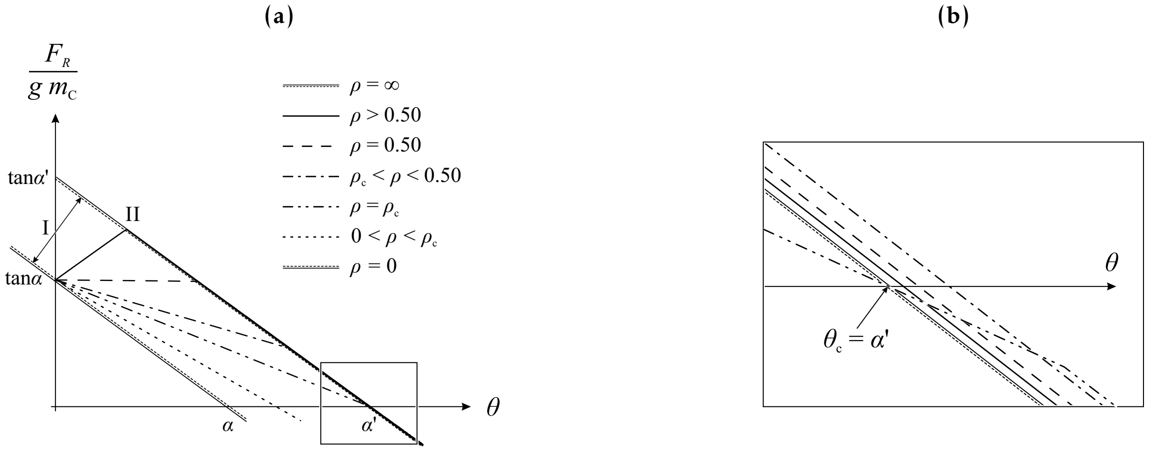

Figure 3.15: Static nonlinear pushover response curves of free-standing rigid oscillators with curved extensions: (a) Pushover curves for different radii of curvature ρ; (b) Close-up at $\theta = \alpha'$.

Similarly, with the horizontal and vertical displacement of the center C,

$$^{\mathrm{II}}u_{\mathrm{C}} = R\sin(\pm\alpha) - R\sin(\pm\alpha-\theta) + r\cdot\Big(\pm\beta - \sin(\pm\beta-\theta) - \sin\theta\Big), \tag{3.51}$$

$$^{\mathrm{II}}w_{\mathrm{C}} = R\cos(\pm\alpha-\theta) + r\cdot\Big(\cos(\pm\beta-\theta) - \cos\theta\Big), \tag{3.52}$$

the restoring force $^{\mathrm{II}}F_R$ and the stiffness $k_{rock} = {}^{\mathrm{II}}k$ can be determined for phase II. In the end, one gets $^{\mathrm{II}}k^* = -1$. The comparison of the two linearized post-uplift stiffness reveals that

$$^{\mathrm{I}}k^* = {}^{\mathrm{II}}k^* + 2\rho. \tag{3.53}$$

Capacity and Critical Curvature

Let the capacity of an oscillator, denoted as θ_{c}, be the tilt angle at which the restoring force F_R is zero. Then, θ_{c} is equal to α for the oscillators without, and equal to α' for the oscillators with flat extensions. If the extensions, however, are curved, θ_{c} cannot be determined that easily.

Figure 3.15a plots various pushover curves for different radii of curvature ρ, given α and α'. Note that for oscillators with curvatures $\rho \geq \rho_{\mathrm{c}}$ the pushover curves go through the point (α', 0); therefore, all these oscillators exhibit the identical capacity $\theta_{\mathrm{c}} = \alpha'$ that an oscillator with flat extensions has. If $\rho < \rho_{\mathrm{c}}$, the pushover curve will not go through this point and, thus: $\theta_{\mathrm{c}} < \alpha'$.

Depending on the values of α and α', the critical curvature that still yields $\theta_{\mathrm{c}} = \alpha'$ during phase I (rolling) can be computed by setting Equation (3.48) to zero for $\theta = \alpha'$:

$$\sin(\alpha-\alpha') + r\sin\alpha' = 0 \quad\longrightarrow\quad \frac{r}{R} = -\frac{\sin\alpha\cos\alpha' - \cos\alpha\sin\alpha'}{\sin\alpha'}. \tag{3.54}$$

Using Equation (3.43) that links r with ρ_{c} yields:

$$\rho_{\mathrm{c}} = \frac{1}{2}\left(1 - \frac{\tan\alpha}{\tan\alpha'}\right). \tag{3.55}$$

The lower the value of ρ is, the higher is the tilt angle at which phase II is initiated (β increases when ρ decreases for constant values of b). When $\rho > \rho_{\mathrm{c}}$ the oscillator will exhibit both *rolling* and *rocking* before the capacity θ_{c} is reached. This means that overturning (= instability) will occur in phase II. However, when $\rho \leq \rho_{\mathrm{c}}$, the oscillator will become unstable ($F_R < 0$) during phase I.

Hence, the capacity of a curved oscillator can be determined with Equation (3.56).

$$\theta_{\mathrm{c}} = \begin{cases} \operatorname{atan}\dfrac{\tan\alpha}{1-2\rho}, & \text{if } \rho \leq \rho_{\mathrm{c}} \quad \text{(instability in phase I)} \\ \operatorname{atan}\dfrac{\tan\alpha'}{1-2\rho\cdot(1-\cos\beta)}, & \text{if } \rho > \rho_{\mathrm{c}} \quad \text{(instability in phase II)} \end{cases} \tag{3.56}$$

Linearizing Equation (3.56) with respect to β shows that all the pushover curves have roughly the same capacity: $\theta_{\mathrm{c}} = \alpha'$.

Table 3.3 describes the different post-uplift behaviors that result due to different possible values for the curvature ρ.

Table 3.3: Post-uplift rolling stiffness of oscillators with a curved base: distinction of cases for different curvature ratios ρ.

Curvature ρ	Stiffness ${}^{\mathrm{I}}k^{*}$	Post-uplift behavior
$\rho = 0$	-	Phase I is inexistent: the behavior of the oscillator corresponds to a block without an extended base as discussed in Section 3.2.1.
$0 < \rho < \rho_{\mathrm{c}}$	negative	Phase II will be initiated when $F_R < 0$.
$\rho = \rho_{\mathrm{c}}$	negative	The value ρ_{c} is selected such that $\theta_{\mathrm{c}} = \alpha'$. Phase II will be initiated when $F_R \simeq 0$. The value of ρ_{c} can be determined with Equation (3.55).
$\rho_{\mathrm{c}} < \rho < 0.50$	negative	Phase II will be initiated when $F_R > 0$.
$\rho = 0.50$	zero	${}^{\mathrm{I}}k^{*} = 0$ leads to a constant restoring force until the start of phase II.
$\rho > 0.50$	positive	For tilt angles $\theta < \beta$ the oscillator will exhibit an *effective* period and respond like an elastic oscillator. Once the tilt angle reaches β, the oscillator starts rocking.
$\rho = \infty$	-	Phase I is inexistent: the behavior of the oscillator corresponds to a block with an extended flat base as discussed in Section 3.2.3.

Equations of Motion

The equations of motion are derived using the *Lagrangian Equation* $L = T - V$ described in Section A.2. For phase I one gets:

$$\begin{aligned}
&\ddot{\theta}\cdot\Big(\lambda + 1 + 4\rho\cos\alpha\cdot\big(\cos(\pm\alpha-\theta)-\cos\alpha\big) + 8\rho^2\cos^2\alpha\cdot\big(1-\cos\theta\big)\Big)\\
&= -\dot{\theta}^2\cdot\Big(2\rho\cos\alpha\sin(\pm\alpha-\theta) + 4\rho^2\cos^2\alpha\sin\theta\Big)\\
&\quad -\frac{g}{R}\cdot\Big(\sin(\pm\alpha-\theta)+2\rho\cos\alpha\sin\theta\Big) - \frac{\ddot{u}_g}{R}\cdot\Big(\cos(\pm\alpha-\theta)+2\rho\cos\alpha\cdot\big(1-\cos\theta\big)\Big),
\end{aligned} \tag{3.57}$$

and for phase II:

$$\begin{aligned}
&\ddot{\theta}\cdot\Big(\lambda + 1 + 4\rho\cos\alpha\cdot\big(\cos(\alpha-\beta)-\cos\alpha\big) + 8\rho^2\cos^2\alpha\cdot\big(1-\cos\beta\big)\Big)\\
&= -\frac{g}{R}\cdot\Big(\sin(\pm\alpha-\theta)+2\rho\cos\alpha\cdot\big(\sin(\pm\beta-\theta)+\sin\theta\big)\Big)\\
&\quad -\frac{\ddot{u}_g}{R}\cdot\Big(\cos(\pm\alpha-\theta)+2\rho\cos\alpha\cdot\big(\cos(\pm\beta-\theta)-\cos\theta\big)\Big).
\end{aligned} \tag{3.58}$$

Similarities between Equations (3.57), (3.58), and Equation (3.11) can be found. Three identical terms appear in both equations: one for the rotational acceleration $\ddot{\theta}$, one for the gravitational acceleration g, and one for the ground acceleration $\ddot{u}_g$. However, in Equation (3.57) an additional term for $\dot{\theta}^2$ appears. Note that the instant center of rotation during phase I lies below the rigid supporting surface and is constantly moving.

Linearization of Equations (3.57) and (3.58) with respect to α and θ yields

$$\ddot{\theta} = -p^2\cdot\Big(\pm\alpha - \theta\cdot\big(1-2\rho\big) + \frac{\ddot{u}_g}{g}\Big), \qquad \text{for phase I, and} \tag{3.59}$$

$$\ddot{\theta} = -p^2\cdot\Big(\pm\alpha - \theta \pm 2\beta\rho + \frac{\ddot{u}_g}{g}\Big), \qquad \text{for phase II.} \tag{3.60}$$

When $\rho = 0$, Equation (3.59) collapses to Equation (3.15), the linearized equation of motion of Housner's block. Using Equation (3.45) allows for rewriting Equation (3.60) to

$$\ddot{\theta} = -p^2 \cdot \left(\pm \alpha' - \theta + \frac{\ddot{u}_g}{g} \right), \qquad \text{for phase II.} \tag{3.61}$$

Comparing Equations (3.59), (3.61) and Equation (3.15) shows that up to a linear approximation the addition of the curved parts only adds an extra stiffness term for $\theta < \beta$ (the term '$2\theta\rho$'), while for $\theta > \beta$ the block behaves like a block with an extended flat base with a width equal to the total width of the curved based system.

Interestingly, the curved based system presents remarkable similarity with a rocking body restrained with a prestressed elastic tendon [43, 44]. The effect of the flat part of the base is equivalent to the prestressing force of the tendon, while the curvature of the curved part correlates to the axial stiffness of the tendon.

Similarity Parameters

Let a rocking oscillator with a curved base like illustrated in Figure 3.14 with frequency parameter p, slenderness parameters α and α', and curvature parameter ρ, be excited by a pulse with acceleration amplitude $a_p = \hat{a}_p \cdot \ddot{u}_{g,up}$ and cyclic frequency ω_p.

Example 3.4: RHA of free-standing rigid oscillators with curved extensions «B^{ec}»

Using Equation (3.59) the responses of two solid rigid oscillators B1^{ec} and B2^{ec} with curved extensions are computed when subjected to a sine-pulse with $\hat{a}_p = 2$. The details of the oscillators are listed in the following table:

Oscillator	R [m]	$\tan\alpha$	$\tan\alpha'$	λ	ρ	β	c_r	p [s^{-1}]	a_p [g]	ω_p [s^{-1}]	T_p [s]
B1^{ec}	2.0	0.11	0.16	0.33	0.25	0.10	0.90	1.920	0.219	9.60	0.655
B2^{ec}	3.0	0.12	0.15	0.40	0.25	0.06	0.90	1.528	0.239	7.64	0.822

In case (a) the frequency of the pulse is defined by $\omega_p/p = 5$, and for (b) it is $\omega_p/p = 4$. Due to the geometry parameters, B2^{ec} will make the transition from phase I to phase II at $\theta = \beta_2 = 0.50\,\alpha_2$. For B1^{ec} this happens at $\theta = \beta_1 = 0.91\,\alpha_1$. In the first case both blocks experience pure rolling, and similitude is achieved throughout the entire response history (Fig. 3.16a). In the second case the sine-pulse has a longer period and, as a result, block B2^{ec} will experience rocking at $\tau = 4.27$ (Fig. 3.16b). At this point, the post-uplift stiffness has a significant decrease (${}^{\mathrm{I}}k \rightarrow {}^{\mathrm{II}}k$) which reduces the restoring force and elongates the rocking period of B2^{ec}, resulting in diverging response time histories.

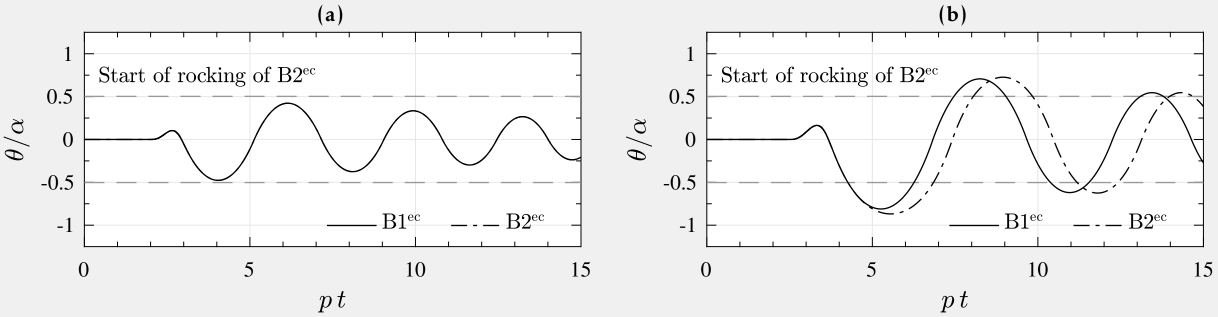

Figure 3.16: RHA of two solid rigid oscillators B1^{ec} and B2^{ec} with curved extensions: (a) Pure rolling ($\omega_p/p = 5$); (b) Mixed response ($\omega_p/p = 4$).

Then, dimensional analysis (see page 33) of the linearized equations (Eqs. 3.59 and 3.61) yields:

$$\mathcal{F}\left(\frac{\theta}{\alpha}, p\,t, \frac{\omega_p}{p}, \hat{a}_p, c_r, \rho\right) = 0, \qquad \text{for phase I, and,} \tag{3.62}$$

$$\mathcal{F}\left(\frac{\theta}{\alpha'}, p\,t, \frac{\omega_p}{p}, \hat{a}_p, c_r\right) = 0, \qquad \text{for phase II.} \tag{3.63}$$

For the rolling phase I, there is one additional dimensionless product: $\Pi_6 = \rho$ (the curvature parameter ρ is already dimensionless due to the way it is defined, see Eq. 3.43).

By comparing Equations (3.62) and (3.63) one observes that the dimensionless and orientationless products are similar for phase I and II, with the exception of the missing product $\Pi = \rho$ in phase II. This means that between two solid rigid blocks similitude law can never be achieved if one is rolling (phase I) while the other is rocking (phase II). Similitude in both phases is only possible, if the transition from one to the other phase happens at the same time ($\tau = p\,t$); which is the case if the following parameters of both blocks are identical: α, α', c_r, and ρ. This means that only the size R can be changed when one wants to retain similitude.

3.3 Response Comparison of Free-Standing Oscillators

In the previous sections various parameters that define the rolling-and-rocking oscillator as shown in Figure 3.14 have been introduced and studied in the dimensionless space. So far no judgment was made or could be made about what a good choice for each of the parameters would be. This section aims to investigate the behavior of the oscillators for a set of given boundary conditions.

In the first part the rolling-and-rocking responses of five oscillators with equal heights and total base widths (Fig. 3.17) to idealized acceleration pulses (antisymmetric Ricker [125, 126], see Section A.1), characterized by their amplitude, a_p, and dominant cyclic period, $T_p = 2\pi/\omega_p$, are investigated.

In the second part, the response behavior of rolling-and-rocking oscillators is studied with the help of response spectra.

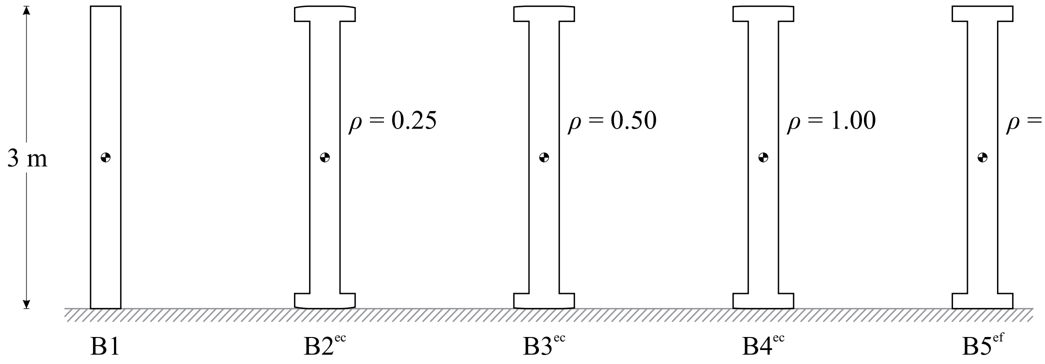

Figure 3.17: Solitary rigid oscillators: B1 – B5^{ef}. $2H = 3.0$ m, $\tan\alpha = 0.1$.

3.3.1 Time History Response Comparison

The tilt angle time history responses of the five solid rigid oscillators illustrated in Figure 3.17 to an idealized antisymmetric Ricker acceleration pulse ($a_p = 0.38\,g$, $T_p = 0.95$ s) are computed using the exact equations of motion (Eqs. 3.57 and 3.58) and plotted in Figure 3.18. All the oscillators exhibit the same height $2H = 3$ m. The rest of the characterizing parameters, however, are different, as listed in Table 3.4. Oscillator B1 does not have an extended base and represents Housner's block ($\rho = 0$), and B5$^{\mathrm{ef}}$ has flat extensions ($\rho = \infty$). The three oscillators B2$^{\mathrm{ec}}$–B4$^{\mathrm{ec}}$ exhibit three different radii of curvature which results in different post-uplift stiffness: ${}^{\mathrm{I}}k$ is either negative, zero, or positive. Their pushover curves of the oscillators are drawn in Figure 3.18b.

To goal is to compare the curved base oscillators against their flat counterparts: 1) against the block with no base extensions (B1); and 2) against the block with flat base extensions (B5$^{\mathrm{ef}}$). Figure 3.18a illustrates the highly nonlinear nature of the rocking problem.

A larger value for the uplift acceleration (B5$^{\mathrm{ef}}$) or a larger post-uplift stiffness (B3$^{\mathrm{ec}}$, B4$^{\mathrm{ec}}$) do not necessarily decrease the amplitude $\theta_{\max}$ of the response. The right part of Table 3.4 lists the individual maximum responses $\theta_{\max}$ of the oscillators: the response with the lowest value, $\theta_{\max} = 1.13\,\alpha$, is achieved by oscillator B2$^{\mathrm{ec}}$. On the opposite, the flat extended oscillator overturns for the given acceleration pulse. Therefore, single time history comparisons do not suffice, and wide parametric studies are needed in order to identify trends in the response.

Table 3.4: Details of solitary rigid oscillators (B1–B5$^{\mathrm{ef}}$).

Oscillator details								Response time history details		
Oscillator	$2H$	$\tan\alpha'$	$2B'$	ρ	${}^{\mathrm{I}}k^{*}$	$\ddot{u}_{g,up}$	c_r	t_{up}	$\theta_{\max}$	$\Delta\theta_{\max}$
B1	3 m	-	0.3 m	-	-	$0.1\,g$	0.971	0.78 s	$1.19\,\alpha$	0
B2$^{\mathrm{ec}}$	3 m	0.2	0.6 m	0.25	< 0	$0.1\,g$	0.971	0.78 s	$1.06\,\alpha$	$-0.13\,\alpha$
B3$^{\mathrm{ec}}$	3 m	0.2	0.6 m	0.50	0	$0.1\,g$	0.971	0.78 s	$1.13\,\alpha$	$-0.06\,\alpha$
B4$^{\mathrm{ec}}$	3 m	0.2	0.6 m	1.00	> 0	$0.1\,g$	0.971	0.78 s	$1.54\,\alpha$	$+0.35\,\alpha$
B5$^{\mathrm{ef}}$	3 m	0.2	0.6 m	∞	-	$0.2\,g$	0.970	1.08 s	*overturn*	$\geq 1.00\,\alpha$

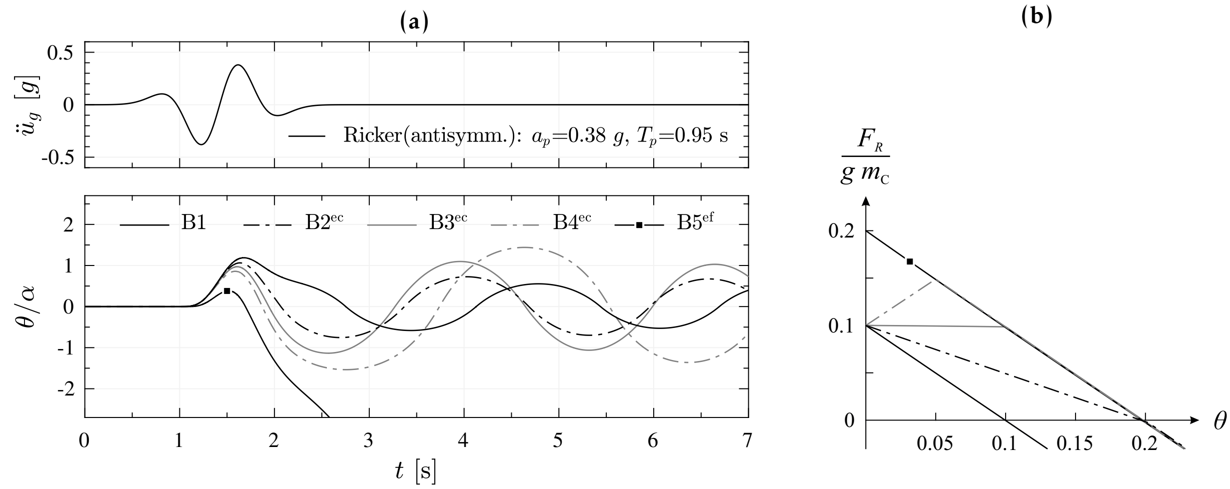

Figure 3.18: Solitary rigid oscillators: (a) Tilt angle time history responses; (b) Static nonlinear pushover response curves.

3.3.2 Spectral Response Comparison

Orientational analysis shows that the tilt angle θ can be normalized with slenderness parameters α or α'. Therefore, contour plots of the maxima of the normalized tilt angle $\theta_{\max}/\alpha$ can be plot in the $\frac{a_p}{g\tan\alpha}$, $\frac{\omega_p}{p}$ plane, for constant slenderness (α or α') and varying curvature parameters (ρ). These contour plots are commonly referred to as *rocking spectra*.

Maximum Tilt Angle Response Spectra

The rocking spectra for oscillators of type equal B1 (*i.e.*, oscillators without base extensions) to antisymmetric and symmetric Ricker wavelet excitations are shown in Figures 3.19a and 3.20a. They plot the tilt angle $\theta_{\max}/\alpha = \max(|\theta|)/\alpha$ for a total of 321 201 nonlinear response time history analyses (801×401). The axes of the spectra are dimensionless according to similitude theory: on the x-axis the pulse frequency ω_p is normalized with the frequency parameter p, and on the y-axis the pulse amplitude a_p is normalized with the uplifting acceleration $\ddot{u}_{g,up}$ (= $\hat{a}_p$).

The spectra shown in Figures 3.19b and 3.20b represent a simpler way of interpreting the results by answering the question: "Will the block overturn or not?". The black area indicates overturning (= unsafe), which corresponds to $\theta_{\max}/\alpha \geq 1.5$, while the white area indicates a non-overturning (= safe) response ($\theta_{\max}/\alpha < 1.5$). The unsafe (black) areas can further be divided into subareas:

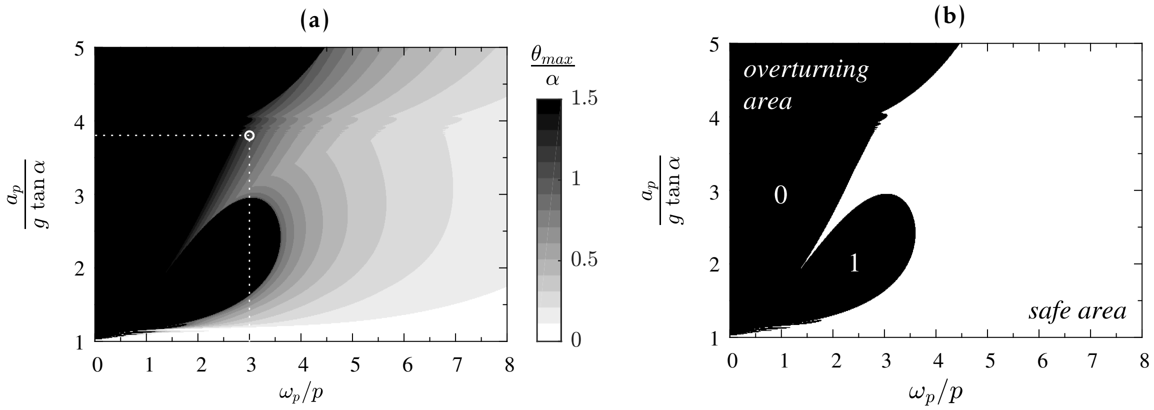

Figure 3.19: Maximum tilt angle response spectra of B1 subjected to antisymmetric Ricker wavelets: (a) Unfiltered; (b) Filtered (safe/unsafe).

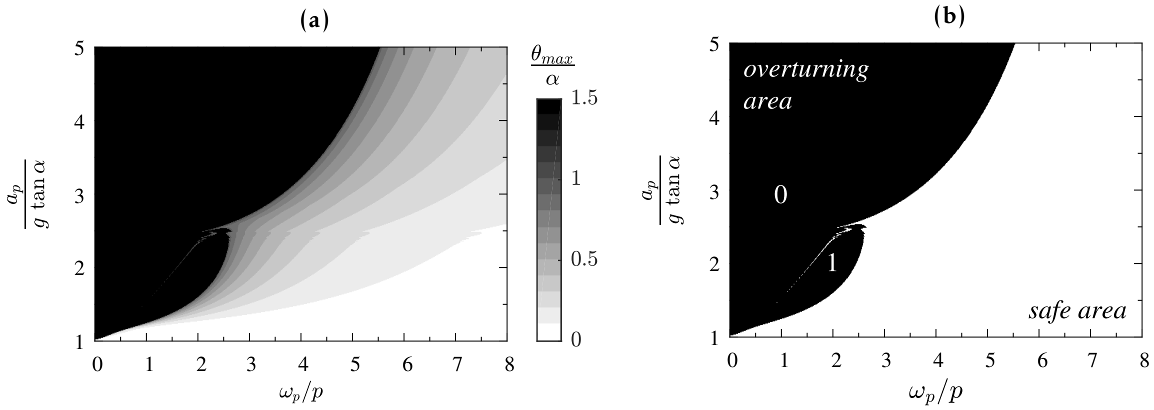

Figure 3.20: Maximum tilt angle response spectra of B1 subjected to symmetric Ricker wavelets: (a) Unfiltered; (b) Filtered (safe/unsafe).

Example 3.5: Reading a maximum tilt angle response value from the spectrum (Fig. 3.19a)

The time history response comparison presented in Section 3.3.1 yields $\theta_{\max} = 1.19\,\alpha$ for oscillator B1. We can confirm this using the spectrum in Figure 3.19a. The p-value of oscillator B1 is $\sqrt{(3g)/(4R)}$ where $R = H/\cos\alpha$. Hence, $p_1 = 2.2\,\mathrm{s}^{-1}$, and $\omega_p/p = 3.0$. The amplitude $a_p = 0.38\,g$ yields $\hat{a}_p = 3.8$ for the y-axis. The intersecting point, marked with a white circle, indicates that $1.10\,\alpha \le \theta_{\max} \le 1.20\,\alpha$.

depending on the shape of the acceleration pulse there could be overturning with 0, 1, 2, …, impacts. In the presented cases of Ricker wavelets, there are two subareas: *overturning without impact* (labeled '0'); and *overturning with 1 impact* (labeled '1').

Taking into account both display formats of maximum tilt angle response spectra allows for stating the following observations:

- For long pulses, *i.e.*, when $\omega_p/p \le 1$, an oscillator will almost always overturn if uplift occurs. This is because the acceleration increases over such a long period of time that its resulting force applied to the oscillator resembles a static force and, hence, once the resisting force is overcome, overturning is practically inevitable.
- When the response is getting close to overturning ($0.5 \le \theta_{\max} \le 1.5$) there is an drastic increase in the spectrum.
- For values of $\omega_p/p \ge 5.5$ a solid rigid oscillator of type B1 will respond in a safe manner (*i.e.*, no overturning will occur) for as long as the acceleration amplitude is lower than $5g\tan\alpha$, which is 5 times the uplifting acceleration.

Limit State Line Spectra

The contour plots in Figures 3.19–3.20 visualize the lines of equal response (along these lines the maximum tilt angle response is equal). If certain limit states (*i.e.*, maximum response tilt angles) are defined the corresponding lines can be extracted from the contour plots (as minimum overturning lines) and be plotted on their own. Additionally, multiple limit state lines of different oscillators can be compared in this way.

Limit state lines according to their definition in Table 3.5 are plotted in Figure 3.21 for the five afore presented oscillators (B1–B5$^{\mathrm{ef}}$). The limit state I stands for a relatively small maximum tilt angle of 0.25 α and could represent the rotation demand of less rare seismic events. Limit state II represents already significantly higher demands with $\theta_{\max} = 0.50\,\alpha$, *e.g.*, of a rare seismic event. Although numerically very far, 0.50 α is actually close to overturning in the sense that only a slight increase in acceleration amplitude or elongation of pulse period will result in a significant increase in demand. The limit states III and IV are investigated for comparative reasons only.

Table 3.5: Defined limit states to extract the limit state lines from the contour plots in Figures 3.19–3.20.

Limit state	I	II	III	IV
$\theta_{\max}$	$0.25\,\alpha$	$0.50\,\alpha$	$1.00\,\alpha$	*overturn*

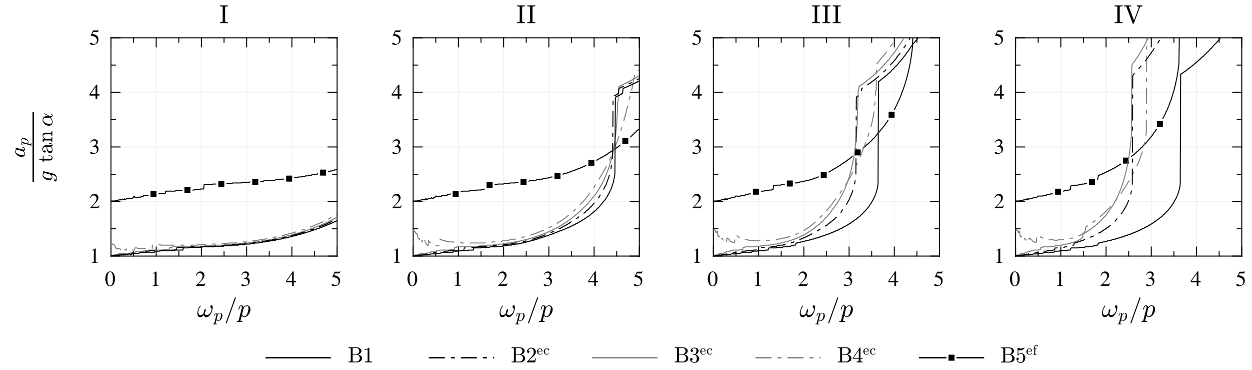

Figure 3.21: Comparison of limit state lines of oscillators B1–B5$^{\text{ef}}$ for the defined limit states in Table 3.5 to antisymmetric Ricker wavelets.

For the oscillator B1 a value of $\theta_{\text{max}} = 1.00\,\alpha$ signifies overturning (the capacity of B1 is $\theta_{\text{c}} = \alpha$). Hence, no difference can be determined between limit state III and IV for B1. However, the limit state III does not automatically imply overturning: depending on the shape of the excitation oscillators might recover and actually survive (= not overturn). For limit states that are further away from overturning, *i.e.*, when $\theta_{\text{max}} \leq 0.50\,\alpha$, the limit state lines of oscillators B1–B4$^{\text{ec}}$ fall close to each other. Only for larger tilt angles do the oscillators show significantly different response behavior, mainly due to their different post-uplift behavior (Fig. 3.18b).

Interestingly, all the limit state lines (I–IV) of B2$^{\text{ec}}$ and B3$^{\text{ec}}$ are close to each other seeming there is no eminent behavioral difference between them. This confirms the observation first made in [38] that negative stiffness systems of the same strength present roughly the same displacement demand, no matter what the exact value of stiffness is. In contrast, the lines representing the behavior of B5$^{\text{ef}}$ are constantly further aside, because the uplift acceleration is significantly different.

Relative Maximum Tilt Angle Response Spectra

In an effort to further investigate the response behaviors of the oscillators a new form of spectrum is introduced that allows a more detailed comparison of just two oscillators; I call it the *relative spectrum* for the maximum tilt angle θ_{max}.

$$\Delta\theta_{\text{max},i} = \theta_{\text{max},i} - \theta_{\text{max},1}\,. \tag{3.64}$$

The corresponding spectra are denoted Bi_Δ, as shown in Fig. 3.22. Brighter areas indicate a better ($\Delta\theta_{\text{max}} < 0$), darker areas a worse ($\Delta\theta_{\text{max}} > 0$), and gray areas an indifferent outcome for Bi when

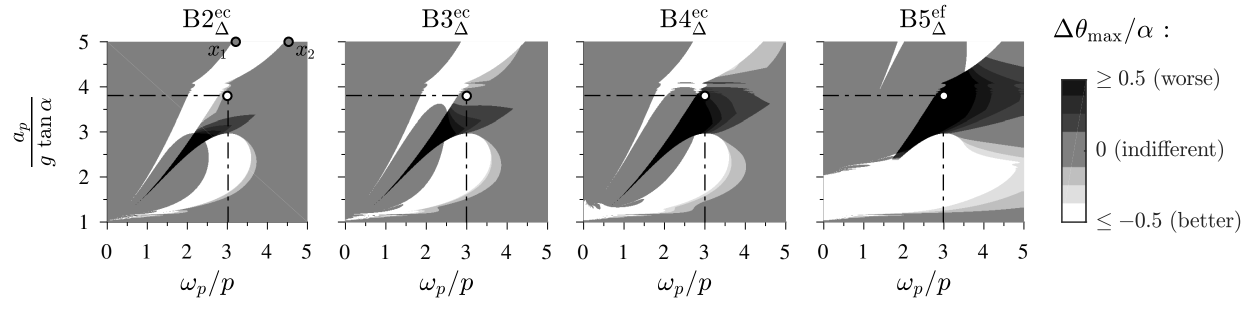

Figure 3.22: Relative maximum tilt angle response spectra: antisymmetric Ricker.

Example 3.6: Interpreting the relative maximum tilt angle response spectra (Fig. 3.22)

Table 3.4 lists the difference $\Delta\theta_{\max}$ for the individual response comparison; when compared to oscillator B1, B2$^{\text{ec}}$ and B3$^{\text{ec}}$ with negative and respectively zero post-uplift stiffness have a slightly lower value for $\theta_{\max}$ while B4$^{\text{ec}}$ and B5$^{\text{ef}}$ have significantly higher response values. The same observation can be made by examining the relative maximum tilt angle response spectra (Fig. 3.22): the circles (∘) indicate the responses of oscillators B2$^{\text{ec}}$–B5$^{\text{ef}}$ in comparison to B1 for the given acceleration pulse (Fig. 3.18). B5$^{\text{ef}}$ overturns while B1 does not, hence, the black color in the spectrum B5$^{\text{ef}}_{\Delta}$.

compared with B1. Note that *indifferent* means that no significant difference can be noticed between the two outcomes, or that both oscillators overturn. When $\Delta\theta_{\max}/\alpha \leq -0.5$ oscillator Bi survives while B1 overturns, and *vice versa* when $\Delta\theta_{\max}/\alpha \geq 0.5$.

In comparison to the limit state spectra the relative spectra do not focus on one single line and allow for a better comparison within the whole spectral region.

The following observations can be made:

- All the extended oscillator are more stable than B1: the safe (non-overturning) area enlarges. This is most obvious when comparing the lines for the limit state IV (*overturn*) in Figure 3.21.
- The response spectrum of oscillator B2$^{\text{ec}}$ appears to be a scaled (on the x-axis) version of the spectra of B1 (for the limit state IV). This indicates that there is a size $\hat{R} \neq R$ for the oscillator of type B1 (no curved extensions) such that the overturning behavior of B2$^{\text{ec}}$ is equivalent to the behavior of an oscillator B1 of larger size. By comparing the limit state lines for overturning for B1 and B2$^{\text{ec}}$ the spectral scaling factor can be quantified via the two abscissae given the same ordinate. The gray circles (⊙) in Figure 3.22 indicate the selected points: for $y = \frac{a_p}{g\tan\alpha} = 5$, x_1 and x_2 read: $x_1 = \omega_p/p = 4.53$, $x_2 = \omega_p/p = 3.21$:

$$\hat{R} = \left(\frac{x_1}{x_2}\right)^2 R = \left(\frac{4.53}{3.21}\right)^2 = 1.99R \simeq 2R. \tag{3.65}$$

  Similar behavior can be observed when comparing different classes or rocking structures like frames [127], arches, conical shells, and masonry wall mechanisms [29].

3.3.3 Size Equivalency

Due to the fact that oscillators B2$^{\text{ec}}$ and B1 appear to behave similarly, a more detailed study comparing these two oscillators is initiated. A new time history response comparison is performed between two oscillators: B2a$^{\text{ec}}$ has the same properties as before (B2a$^{\text{ec}}$ = B2) and B1a is now double its previous size — based on the indication of Equation (3.65). The two oscillators being compared are shown in Figure 3.23b and their detailed information is listed in Table 3.6.

Figure 3.23a plots the response time histories for the tilt angle (normalized with α and θ_c, respectively) and the horizontal displacement of C for an antisymmetric Ricker pulse ($a_p = 0.28\,g$, $T_p = 1.02\,\text{s}$) against the time t. Note that the time axis, therefore, is not dimensionless. The responses match well, even though system B1a rocks and system B2a$^{\text{ec}}$ purely rolls. The pushover

Table 3.6: Oscillator details.

Oscillator	$2H$	$\tan\alpha$	$\tan\alpha'$	λ	$\rho=\rho_\mathrm{c}$	$\frac{\tan\alpha'}{\tan\alpha}$	α'	θ_c	$u_{\mathrm{C,c}}$
B1a	6.0 m	0.1	-	0.333	-	-	-	$1.000\,\alpha$	0.300 m
B2a$^{\mathrm{ec}}$	3.0 m	0.1	0.2	0.333	0.25	2.0	$1.981\,\alpha$	$1.981\,\alpha$	0.298 m

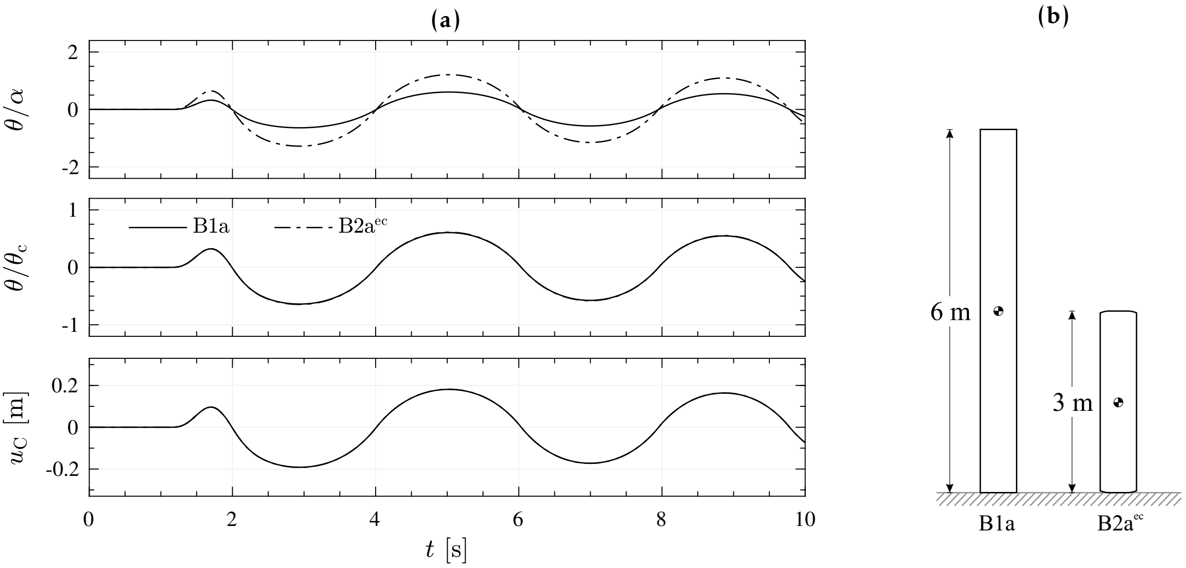

Figure 3.23: Oscillator comparison: B1a vs. B2a$^{\mathrm{ec}}$: (a) Response time histories when subjected to an antisymmetric Ricker wavelet ($a_p = 0.28\,g$, $T_p = 1.02$ s); (b) Drawing.

curves of the two oscillators reveal that they coincide in the plane $\frac{F_R}{g\,m_\mathrm{C}}$ vs. $\frac{\theta}{\theta_\mathrm{c}}$ for $\theta \le \theta_\mathrm{c}$ (Fig. 3.24b): both oscillators share the same displacement capacity, even though B2a$^{\mathrm{ec}}$ needs to rotate twice as much to reach it.

This observation emerges naturally from the linearized equations of motion of the oscillators with flat (Eq. 3.15) and curved bases (Eq. 3.59) when ρ is equal to ρ_c, and when they are solved for θ/θ_c.

Case of Critical Curvature

Let the size and the tilt angle of a block with a flat base be denoted with $\hat{R}$ and $\hat{\theta}$, respectively. Then, the linearized equations of motion, Eq. (3.15) and Eq. (3.59), of the respective oscillators yield:

$$\text{flat}: \quad \frac{\ddot{\hat{\theta}}}{\alpha} = -\frac{g}{\hat{R}}\,\frac{1}{1+\hat{\lambda}}\cdot\left(\pm 1 - \frac{\hat{\theta}}{\alpha} + \frac{\ddot{u}_g}{g\,\alpha}\right), \qquad \theta_\mathrm{c} = \alpha, \tag{3.66}$$

$$\text{curved}: \quad \frac{\ddot{\theta}}{\alpha'} = -\frac{g}{R}\,\frac{1}{1+\lambda}\cdot\left(\pm\frac{\alpha}{\alpha'} - \frac{\theta}{\alpha'}\cdot\left(1-2\rho\right) + \frac{\ddot{u}_g}{g\,\alpha'}\right), \quad \theta_\mathrm{c} = \alpha'. \tag{3.67}$$

Using the linearization of Equation (3.55),

$$\rho_\mathrm{c} = \frac{1}{2}\left(1 - \frac{\alpha}{\alpha'}\right) \quad \longleftrightarrow \quad 1 - 2\rho_\mathrm{c} = \frac{\alpha}{\alpha'}, \tag{3.68}$$

for the curved base oscillator B2a$^{\mathrm{ec}}$ ($\rho = \rho_\mathrm{c}$) enables reformulation of Equation (3.67) to

$$\frac{\ddot{\theta}}{\alpha'} = -\frac{g}{R}\,\frac{1}{1+\lambda}\,\frac{\alpha}{\alpha'}\cdot\left(\pm 1 - \frac{\theta}{\alpha'} + \frac{\ddot{u}_g}{g\,\alpha}\right). \tag{3.69}$$

A comparison of Equations (3.66) and (3.69) uncovers that if

$$\hat{R} = \frac{\alpha'}{\alpha} \cdot \frac{1+\lambda}{1+\hat{\lambda}} \cdot R \quad \text{given} \quad \rho = \rho_\mathrm{c}, \tag{3.70}$$

or further simplified,

$$\hat{R} = \frac{\alpha'}{\alpha} \cdot R \quad \text{given} \quad \rho = \rho_\mathrm{c} \text{ and } \hat{\lambda} = \lambda, \tag{3.71}$$

the time histories of θ/α and $\hat{\theta}/\alpha'$ (both equivalent to θ/θ_c) will coincide at the accuracy of the linear approximation, as seen in the θ/θ_c plot in Figure 3.23a, upto a maximum normalized tilt angle of $\theta/\theta_\mathrm{c} = 1$. The design implication of this is that increasing the size of the block n times has the same effect as increasing the base n times by using a curved part with curvature ρ_c.

For the present case with oscillators B1a and B2a$^\mathrm{ec}$ the above stated equivalency is achieved because the condition in Equation (3.71) is fulfilled. Then, Equation (3.71) implies that the total width of an oscillator with a flat base will be equal, up to linear approximation, to the total width of an oscillator with curved base extensions (Fig. 3.23b): $\hat{B} = 3\,\mathrm{m} \cdot \sin\alpha = 0.30\,\mathrm{m}$; $B = \alpha'/\alpha \cdot 1.5\,\mathrm{m} \cdot \sin\alpha = 0.30\,\mathrm{m}$. This equal width correlates with the equal displacement capacities $u_\mathrm{C,c}$ of the center C that are listed in Table 3.6.

Equivalency I

A solitary rocking oscillator with an extended curved base ($\rho = \rho_\mathrm{c}$) responds equivalent, up to a linear approximation, to a rocking oscillator with a flat base.

General Case

In case that the radius of curvature of the extended base is larger than ρ_c the response behaviors will not be similar despite their equal capacity θ_c; Equation (3.55) no longer holds for $\rho > \rho_\mathrm{c}$ such that the remaining stiffness term '$2\,\theta\,\rho$' in Equation (3.67) precludes any coincidence of responses, as Figure 3.24 shows.

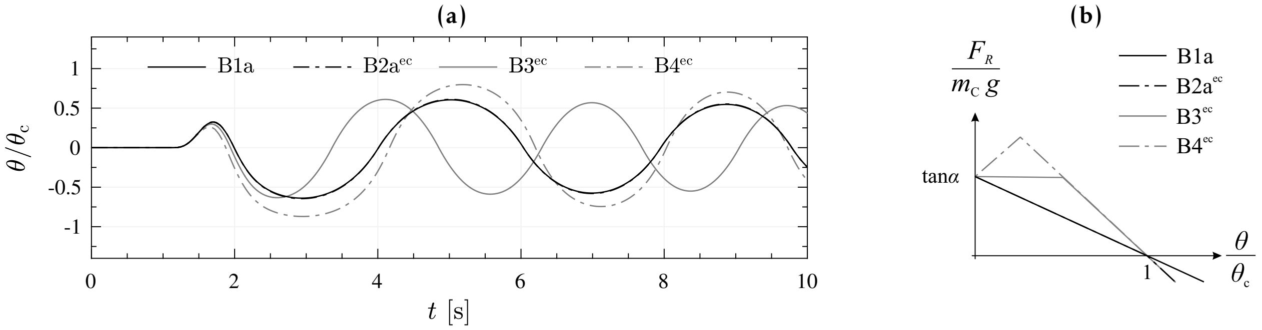

Figure 3.24: Oscillator comparison: B1a vs. B2a$^\mathrm{ec}$, B3$^\mathrm{ec}$, B4$^\mathrm{ec}$: (a) Tilt angle response time histories when subjected to an antisymmetric Ricker wavelet ($a_p = 0.28\ g$, $T_p = 1.02$ s); (b) Static nonlinear pushover response curves.

3.3.4 Similitude between Rolling-and-Rocking Oscillators

The comparison of the similitude parameters of the rocking and the rolling-and-rocking oscillators shows that the parameter ρ makes it impossible to explain the discovered equivalency. However, using Equation (3.68), the linearized version of Equation (3.55) makes the parameter ρ redundant, as it can be replaced by the two common parameters α and α' through

$$\alpha = \alpha' \cdot (1 - 2\,\rho_c)\,. \tag{3.72}$$

Then, the rolling motion of the curved oscillator is described by Equation (3.69), resulting in the following dimensionless similitude parameters:

$$\mathcal{F}\left(\frac{\theta}{\alpha'}, \frac{\alpha}{\alpha'}, \hat{p}\;t, \frac{\omega_p}{\hat{p}}, \hat{a}_p, c_r\right) = 0\,, \tag{3.73}$$

where

$$\hat{p}^2 = \frac{g}{R}\,\frac{1}{1+\lambda}\,\frac{\alpha}{\alpha'} = p^2\,\frac{\alpha}{\alpha'}\,. \tag{3.74}$$

Example 3.7: Similitude between a rolling and a rocking oscillator

Using Equation (3.69) the response histories of a rolling oscillator B1$^{\mathrm{ec}}$ and a rocking oscillator B2 are computed and compared. The details of the oscillators are listed in the following table:

Oscillator	R [m]	$\tan\alpha$	$\tan\alpha'$	λ	ρ	β	c_r	θ_c	$p \mid \hat{p}$ [s^{-1}]	a_p [g]	T_p [s]
B1$^{\mathrm{ec}}$	2.0	0.10	0.15	0.33	0.165	0.152	0.970	0.149	1.571	0.199	1.667
B2	1.5	0.10	-	0.36	-	-	0.971	0.100	2.193	0.199	1.194

In case (a) a FVA with $\theta_0 = 0.8\,\theta_c$, and in case (b) a RHA to a symmetric Ricker wavelet with $\hat{a}_p = 2$ and $\omega_p/\hat{p}_i = 2.4$ are preformed. Note that the only parameter that is set equal is α. There is a slight difference in the coefficient of restitution due to the different factor λ, but is has marginal effect.

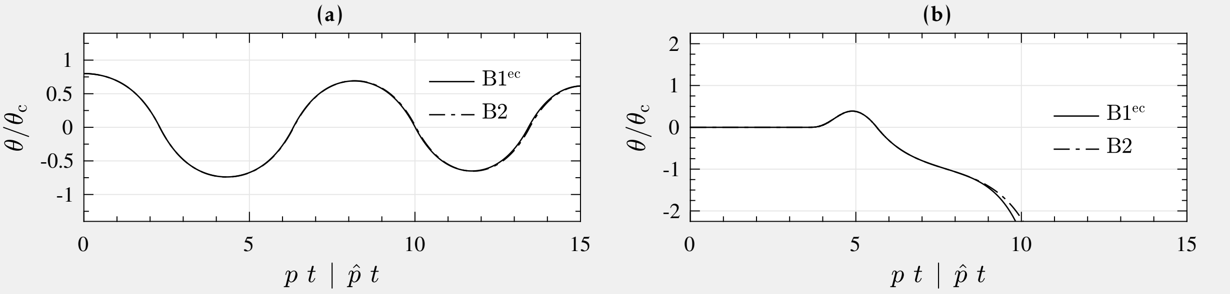

Figure 3.25: Response history comparison of a rolling oscillator B1$^{\mathrm{ec}}$ and a rocking oscillator B2: (a) FVA; (b) RHA.

3.4 Rolling-and-Rocking Frames

Rocking oscillators that were presented in the previous sections can be standalone objects like old artifacts or tombstones. Most of the time, however, they are arranged such that multiple oscillators combined support a single elevated object (*e.g.*, ancient temples). When rigid rocking oscillators are combined in-plane (2D) rocking frame structures as shown in Figure 3.26 are formed. Vassiliou [38] and Makris *et al.* citeMakris2013,Makris2015springer extended the rocking model of a solitary rigid rectangular oscillator, like Housner's block, to a rocking frame structure comprising N such rigid rectangular oscillators capped by a single rigid beam (Fig. 3.26b).

3.4.1 Rigid Frame Structure with Flat Based Oscillators

In this section, I revisit the array of free-standing oscillators capped with a freely supported rigid beam, and present it using the nomenclature chosen for this thesis. I use the abbreviation «F» (rocking **f**rame structure) for referencing to a frame structure with flat based oscillators.

Equation of Motion

The equation of motion for the frame structure shown in Figure 3.26b was derived by Makris & Vassiliou [39] (Eq. 2.21) and is restated here for completeness:

$$\ddot{\theta} = -\hat{p}^2 \cdot \left(\sin\left(\pm\alpha - \theta\right) + \frac{\ddot{u}_g}{g} \cos\left(\pm\alpha - \theta\right) \right), \tag{3.75}$$

where $\hat{p}$, the frequency parameter of the rocking frame, is now

$$\hat{p} = \sqrt{\frac{1 + 2\gamma}{1 + \lambda + 4\gamma}} \cdot \sqrt{\frac{g}{R}}. \tag{3.76}$$

The ratio γ of the mass of the cap-beam, m_B, divided by the mass of all N oscillators is still defined as

$$\gamma = \frac{m_\text{B}}{N\, m_\text{C}}. \tag{3.77}$$

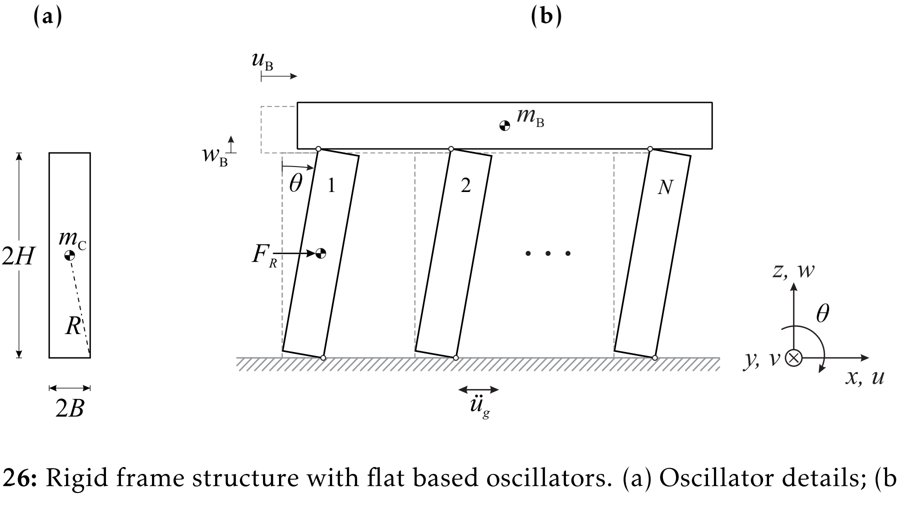

Figure 3.26: Rigid frame structure with flat based oscillators. (a) Oscillator details; (b) Model.

Uplift and Post-Uplift Behavior

The uplifting force of rocking frame structures is different from a solitary free-standing oscillator of equal slenderness. The additional weight of the cap-beam m_B lifts the initial resistance to

$$F_R = (1+2\gamma) N\, m_\mathrm{C}\, g \tan\alpha\,. \tag{3.78}$$

When the frame is dynamically excited, however, the uplifting acceleration is identical to the solitary oscillator, as is the rotation capacity. Figure 3.27 plots the pushover curve of frame structures comprising N identical oscillators.

The linearized post-uplift stiffness yields:

$$k^*_{rock} = \frac{k_{rock}}{(1+2\gamma)\, N\, g\, m_\mathrm{C}} = -1\,. \tag{3.79}$$

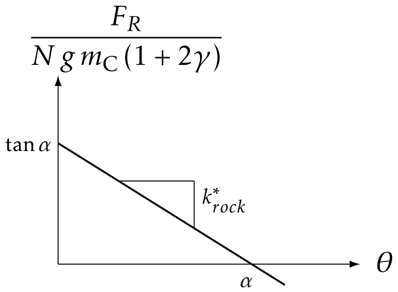

Figure 3.27: Static nonlinear pushover response curve of a rigid frame structure with flat based oscillators.

Coefficient of Restitution

The coefficient of restitution of the rocking frame is:

$$c_r = \left(1 - \frac{2\cdot(1+4\gamma)}{1+\lambda+4\gamma}\sin^2\alpha\right)^2\,. \tag{3.80}$$

Size Equivalency

One of the findings presented in [38, 39, 127] was the equivalency in response behavior between a rocking frame structure and a solitary rocking oscillator of the same slenderness as the oscillators of the frame, yet larger size. Given the size R of the oscillator of the frame, the corresponding larger size of the solitary rocking oscillator is $\hat{R}$, defined by Equation (2.24). A similar expression is found for the general case by comparing Equation (3.76) with Equation (3.13):

$$\hat{R} = \frac{1+\lambda+4\gamma}{\left(1+2\gamma\right)\cdot\left(1+\lambda\right)}\cdot R. \tag{3.81}$$

Figure 3.28 plots the size $\hat{R}$ according to Equation (3.81) for different mass distributions and shapes of the oscillators ($\lambda = \{0, 0.33, 0.40, 0.49, 1\}$). As discussed on page 30, the mass eccentricity factor λ can, theoretically, take values between 0 and 1. The case of $\lambda = 1$ would yield $\hat{R} = R$: there would be no size effect when a cap-beam is added to oscillators. For $\lambda = 0$ the size effect is the strongest: for $\gamma \longrightarrow \infty$ the equivalent size would be $\hat{R} = 2\cdot R$.

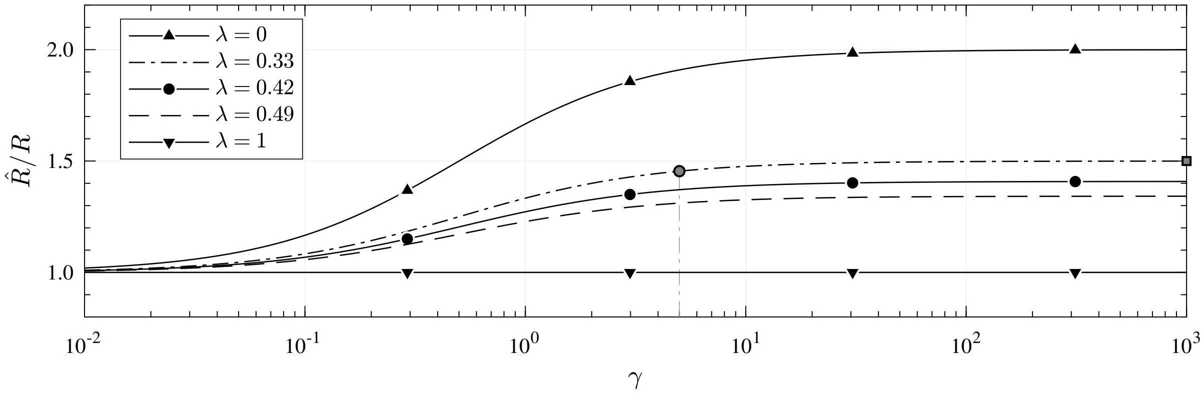

Figure 3.28: Equivalent size $\hat{R}$ of a solitary free-standing rigid oscillator as a function of the rotational inertia factor λ when compared to a rocking frame with weight ratio γ and size R.

Given the range of realistic values for λ ($0.33 \leq \lambda \leq 0.50$) and the assumption that the cap-beam is heavier than the supporting columns ($\gamma \geq 5$), the equivalent size $\hat{R}$ is more or less constant. Assume a frame with common rectangular solid oscillators ($\lambda = 1/3$) of size R, and a cap-beam mass ratio $\gamma = 5$. Then, the size of the equivalent solitary oscillator is $\hat{R} = 1.455 \cdot R$ (indicated with ●). If we now assume that the cap-beam is infinitely heavy ($\gamma \to \infty$), $\hat{R}$ would be $1.50 \cdot R$ (indicated with ■) which is only 3 % larger than what we get for $\gamma = 5$. For a frame where the oscillators are reinforced concrete columns (assuming the case $d_s/2H = 0.15$: $\lambda = 0.49$) the maximum equivalent size ($\gamma \to \infty$) becomes $\hat{R} = 1.342 \cdot R$.

Similitude Parameters

Applying dimensional analysis to the rocking frame structures yields the following dimensionless products:

$$\mathcal{F}\left(\frac{\theta}{\alpha}, \hat{p}\ t, \frac{\omega_p}{\hat{p}}, \hat{a}_p, c_r\right) = 0 . \tag{3.82}$$

where $\hat{p}$ is defined by Equation (3.76). Note that the dimensionless products are identical for the rocking frame with flat based oscillators and the solitary flat based oscillator. Apart from impacts (c_r might slightly differ), similitude can therefore be achieved. For the rocking frame, however, the space θ/α vs. $\hat{p}\ t$ has to be used while for the solitary oscillator it is θ/α vs. $p\ t$ (Fig. 3.29).

Example 3.8: Equivalent size of a rocking frame with reinforced concrete columns

Let us consider a rocking frame structure with $\gamma = 10$. The columns are 3 m tall, have a slenderness of $\tan\alpha = 0.1$, and are protected at the end with steel end plates of height $d_s = 12$ cm. The ratio $d_s/2H$ is computed to be 0.04, for which $\lambda = 0.422$ follows. Then, $\hat{R}$ is equal to $1.39 \cdot R$ which is 5.8 % lower than if we assume an evenly distributed mass. Hence, the additional rotational inertia due to the steel end plates generates a performance that is worse when compared to a frame comprising columns of equal heights but with evenly distributed mass.

Example 3.9: Similitude between a rocking frame and a rocking oscillator

Using the linearized version of Equation (3.75), which is identical to Equation (3.15) with the exception that $\hat{p}$ instead of p is used (for $\gamma = 0$ they are identical), the response histories of a rocking frame F1 and a rocking oscillators B2 are computed and plotted in Figure 3.29. The details of the oscillators are listed in the following table:

Oscillator	R [m]	$\tan\alpha$	λ	γ	c_r	$p \mid \hat{p}$ [s^{-1}]	a_p [g]	T_p [s]
F1	2.0	0.10	0.42	15	0.961	1.573	0.199	1.664
B2	3.0	0.15	0.35	-	0.936	1.556	0.298	1.682

In case (a) a FVA with $\theta_0 = 0.8\,\alpha$, and in case (b) a RHA to a symmetric Ricker wavelet with $\hat{a}_p = 2$ and $\omega_p/\hat{p}_i = 2.4$ are preformed. In this example, the coefficient of restitution is not fixed to a certain value on purpose. The responses are identical until the first impact occurs. Note that the parameters were selected randomly, similitude will work no matter what the values are.

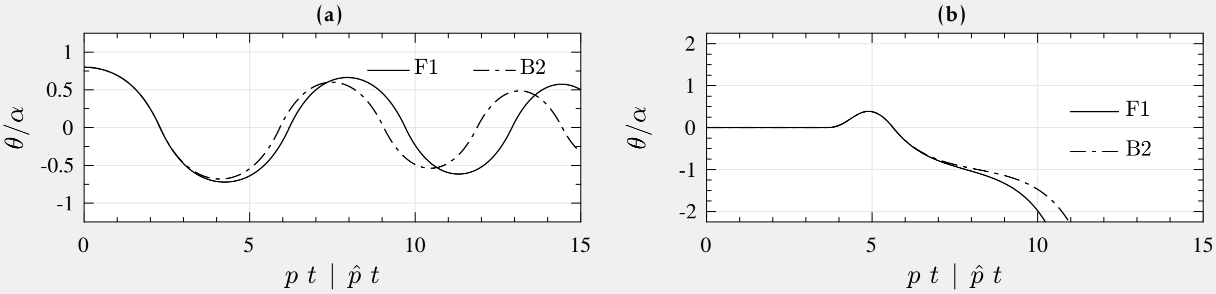

Figure 3.29: Response history comparison of rocking frame F1 and a rocking oscillator B2 (see Example 3.9 for oscillator details): (a) FVA; (b) RHA.

3.4.2 Rigid Frame Structure with Curved Based Oscillators

In this section, the oscillators of the rocking frame are replaced with oscillators where the base is extended with curved wedges. I derive the equations of motion, and compute the force–rotation behavior. The goal is to combine the beneficiary findings from the previous chapter with the advantages of a heavy cap-beam. I use the abbreviation «F$^{\text{ec}}$» from the words rolling-and-rocking frame structure with curved based oscillators.

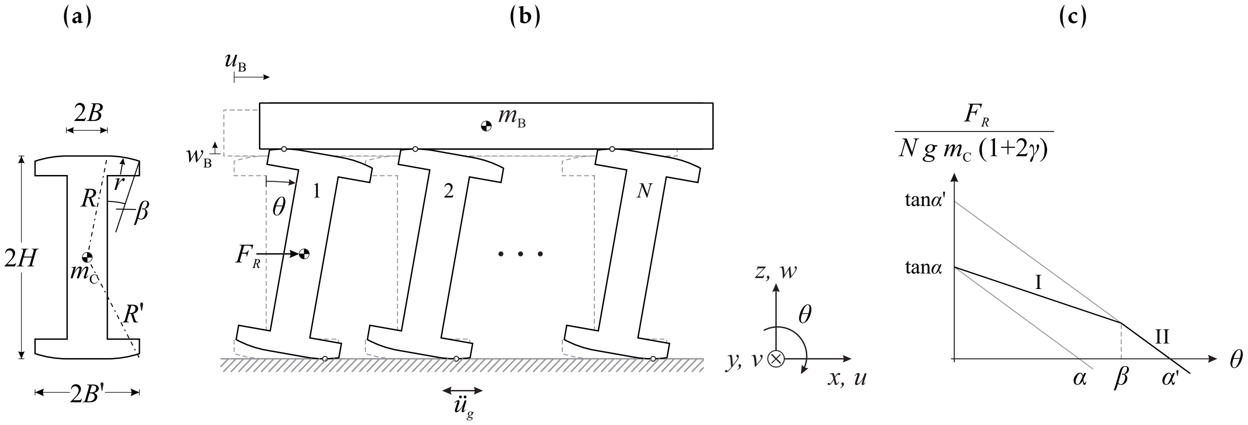

Figure 3.30: Rigid frame structure with curved based oscillators. (a) Oscillator details; (b) Model; (c) Static nonlinear pushover response curve.

Geometry

In order to derive the equations of motion for the frame in Figure 3.30b for both phase I and II the coordinates of the cap-beam mass m_B are needed. It is assumed that there is no sliding at the contact interface between the cap-beam and oscillator. The coordinates u_B and w_B at the top of the oscillator indicate the contact point between these two rigid objects, and are deduced from the coordinates of C as follows:

$$u_\mathrm{B} = 2\,u_\mathrm{C}, \tag{3.83}$$

$$w_\mathrm{B} = 2\,w_\mathrm{C}, \tag{3.84}$$

where the coordinates of C for phases I and II are given by Equations (3.46)–(3.47) and (3.51)–(3.52).

Equations of motion

The equation of motion for phase I becomes

$$\begin{aligned}
&\ddot{\theta}\cdot\Big(\lambda+(1+4\gamma)\cdot\Big(1+4\rho\cos\alpha\cdot\big(\cos(\pm\alpha-\theta)-\cos\alpha\big)+8\rho^2\cos^2\alpha\cdot\big(1-\cos\theta\big)\Big)\Big)=\\
&\quad-\dot{\theta}^2(1+4\gamma)\cdot\Big(2\rho\cos\alpha\sin(\pm\alpha-\theta)+4\rho^2\cos^2\alpha\sin\theta\Big)\\
&\quad-\frac{g}{R}(1+2\gamma)\cdot\Big(\sin(\pm\alpha-\theta)+2\rho\cos\alpha\sin\theta\Big)\\
&\quad-\frac{\ddot{u}_g}{R}(1+2\gamma)\cdot\Big(\cos(\pm\alpha-\theta)+2\rho\cos\alpha\big(1-\cos\theta\big)\Big),
\end{aligned}\tag{3.85}$$

and for phase II

$$\begin{aligned}
&\ddot{\theta}\cdot\Big(\lambda+(1+4\gamma)\cdot\Big(1+4\,\rho\,\cos\alpha\cdot\big(\cos(\alpha-\beta)-\cos\alpha\big)+8\,\rho^2\,\cos^2\alpha\cdot\big(1-\cos\beta\big)\Big)\Big)=\\
&\quad-\frac{g}{R}(1+2\gamma)\cdot\Big(\sin(\pm\alpha-\theta)+2\,\rho\,\cos\alpha\cdot\big(\sin(\pm\beta-\theta)+\sin\theta\big)\Big)\\
&\quad-\frac{\ddot{u}_g}{R}(1+2\gamma)\cdot\Big(\cos(\pm\alpha-\theta)+2\,\rho\,\cos\alpha\cdot\big(\cos(\pm\beta-\theta)-\cos\theta\big)\Big).
\end{aligned}\tag{3.86}$$

Setting $\rho = 0$ simplifies Equation (3.85) and (3.86) to one identical equation of motion equal to the one of the rocking frame with flat based oscillators (Eq. 3.75). For $\rho > 0$, no analytic simplification is possible. Linearization of Equations (3.85) and (3.86) with respect to α and θ yields

$$\ddot{\theta} = -\frac{1+2\gamma}{1+\lambda+4\gamma}\cdot\frac{g}{R}\cdot\left(\pm\,\alpha-\theta\cdot\big(1-2\,\rho\big)+\frac{\ddot{u}_g}{g}\right) \qquad \text{for phase I, and} \tag{3.87}$$

$$\ddot{\theta} = -\frac{1+2\gamma}{1+\lambda+4\gamma}\cdot\frac{g}{R}\cdot\left(\pm\,\alpha'-\theta+\frac{\ddot{u}_g}{g}\right) \qquad \text{for phase II,} \tag{3.88}$$

where the first two fractions are identical to the squared frequency parameter of the flat based rocking frame $\hat{p}$ according to Equation (3.76). Note the resemblance of Equation (3.87) with Equation (3.59), and of Equation (3.87) with Equation (3.61). We can, therefore, be confident that a similar condition to Equation (3.70) can be found for rocking frame structures with curved based oscillators, and that dimensionless similitude products can be identified.

3.5 Response Comparison of Free-Standing Frame Structures

3.5.1 Size Equivalency

By comparing Equations (3.59) and (3.61) with Equations (3.87) and (3.88) one can establish an equivalency, up to a linear approximation, between the solitary oscillator with an extended curved base and the frame supported by oscillators with extended curved bases: the response of the frame is equivalent to the response of a solitary oscillator with same properties, yet larger size.

The equivalent semi-diagonal is:

$$\hat{R} = \frac{1+\lambda+4\gamma}{(1+2\gamma)\cdot(1+\lambda)} \cdot R. \tag{3.89}$$

This size equivalency of a frame with extended curved based oscillators to a solitary oscillator with an extended curved base is identical to the size equivalency of a frame with non-extended oscillators to a solitary oscillator with no base extensions (Eq. 3.81).

Hence, following the same procedure as in Section 3.3.3, a to Equation (3.70) equivalent expression is found:

$$\hat{R} = \frac{1+\lambda+4\gamma}{(1+2\gamma)\cdot(1+\lambda)} \frac{\alpha'}{\alpha} \cdot R. \tag{3.90}$$

where $\hat{R}$ is the equivalent size of a solitary flat based rocking oscillator to a frame with curved based oscillators or to an oscillator ($\gamma = 0$) of size R, respectively. Note that for $\gamma = 0$ Equation (3.90) collapses to Equation (3.70).

For $\lambda = 1/3$ Equation (3.90) yields

$$\hat{R} = \frac{1+3\gamma}{1+2\gamma} \frac{\alpha'}{\alpha} \cdot R. \tag{3.91}$$

Equivalency II

A frame supported by rocking oscillators with extended curved bases ($\rho = \rho_c$) responds equivalent, up to a linear approximation, to a solitary rocking oscillator with an extended curved base ($\rho = \rho_c$) and appropriate size.

3.5.2 Similitude between Rolling-and-Rocking Frames and Oscillators

Following the procedure in Section 3.3.4, the following equation of motion for rolling-and-rocking frame structures with ρ_c is valid during the phase I (rolling):

$$\frac{\ddot{\theta}}{\alpha'} = -\frac{g}{R}\frac{1+2\gamma}{1+\lambda+4\gamma}\frac{\alpha}{\alpha'}\cdot\left(\pm 1-\frac{\theta}{\alpha'}+\frac{\ddot{u}_g}{g\,\alpha}\right). \tag{3.92}$$

The following dimensionless similitude parameters can be identified:

$$\mathcal{F}\left(\frac{\theta}{\alpha'},\frac{\alpha}{\alpha'},\hat{p}\,t,\frac{\omega_p}{\hat{p}},\hat{a}_p,c_r\right)=0\,, \tag{3.93}$$

where

$$\hat{p}^2=\frac{g}{R}\frac{1+2\gamma}{1+\lambda+4\gamma}\frac{\alpha}{\alpha'}\,. \tag{3.94}$$

Example 3.10: Similitude between rolling-and-rocking frames and oscillators

Using Equation (3.92) the response histories of rolling-and-rocking frames (F1$^{\text{ec}}$, F2) and rolling-and-rocking oscillators (B3$^{\text{ec}}$, B4) are computed and plotted. The details of the oscillators are listed in the following table:

Oscillator	R [m]	$\tan\alpha$	$\tan\alpha'$	λ	ρ	β	γ	θ_c	c_r	$p \mid \hat{p}$ [s^{-1}]	a_p [g]	T_p [s]
F1$^{\text{ec}}$	2.0	0.10	0.15	0.38	0.165	0.152	10	0.149	0.961	1.291	0.199	2.028
F2	2.5	0.10	-	0.34	-	-	15	0.100	0.961	1.408	0.199	1.859
B3$^{\text{ec}}$	3.0	0.10	0.15	0.36	0.165	0.152	-	0.149	0.971	1.268	0.199	2.064
B4	4.0	0.10	-	0.37	-	-	-	0.100	0.971	1.338	0.199	1.957

In case (a) a FVA with $\theta_0 = 0.8\,\alpha$, and in case (b) a RHA to a symmetric Ricker wavelet with $\hat{a}_p = 2$ and $\omega_p/\hat{p}_i = 2.4$ are preformed. In this example, the coefficient of restitution is not fixed to a certain value on purpose. The responses are identical until the first impact occurs. Note that the parameters were selected randomly, similitude will work no matter what the values are.

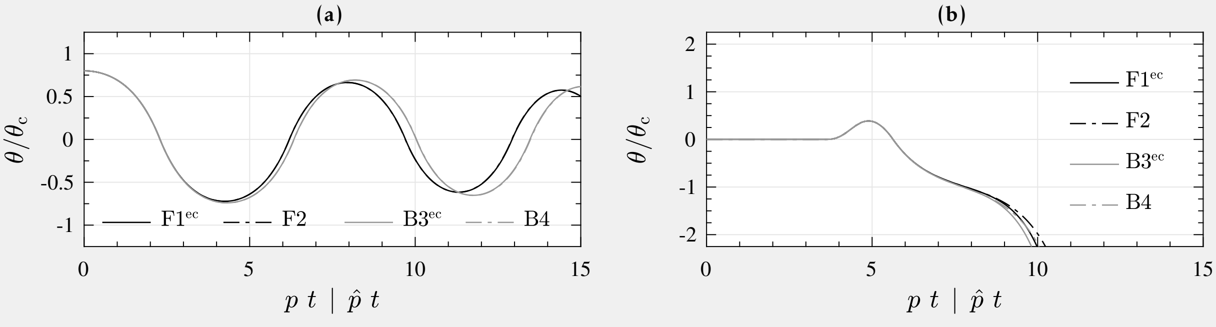

Figure 3.31: Response history comparison of two rolling-and-rocking frames (F1$^{\text{ec}}$, F2) and two rolling-and-rocking oscillators (B3$^{\text{ec}}$, B4): (a) FVA; (b) RHA.

3.6 Influence of Linearization

By linearization of the equations of motion of the different investigated systems it could be shown that similitude exists between them, *e.g.*, that the response between a rolling-and-rocking frame is similar to the response of a rolling-and-rocking oscillator (given that the curvature value ρ is the same).

In an effort to quantify the error that is introduced by this linearization, response history analyses are performed on the rolling-and-rocking oscillator B3$^{\mathrm{ec}}$ that was introduced in Example 3.10, comparing both the complete and the linearized solutions for: (a) small amplitudes ($\theta_{\max} \approx 0.2{\cdot}\theta_{\mathrm{c}}$), (b) moderate amplitudes ($\theta_{\max} \approx 0.5 \cdot \theta_{\mathrm{c}}$), and (c) amplitudes close to overturning ($\theta_{\max} \approx \theta_{\mathrm{c}}$).

Figure 3.32 shows different free vibration responses, and Figure 3.33 shows the different responses to symmetric Ricker wavelets with $T_p = 2.064\,\mathrm{s}$ and $a_p = \{0.130, 0.165, 0.185\}g$. The difference between the complete and the linearized solutions is small for the considered sizes and displacement magnitudes.

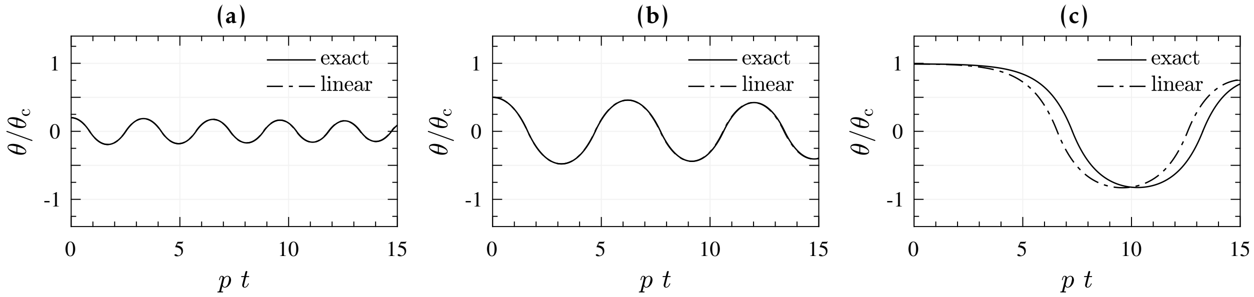

Figure 3.32: Free vibration response history comparison for the exact and the linearized equation of motion for the rolling-and-rocking oscillator B3$^{\mathrm{ec}}$: (a) Small amplitudes ($\theta_0 = 0.2 \cdot \theta_{\mathrm{c}}$); (b) Moderate amplitudes ($\theta_0 = 0.5 \cdot \theta_{\mathrm{c}}$); (c) Amplitudes close to overturning ($\theta_0 = 0.99 \cdot \theta_{\mathrm{c}}$).

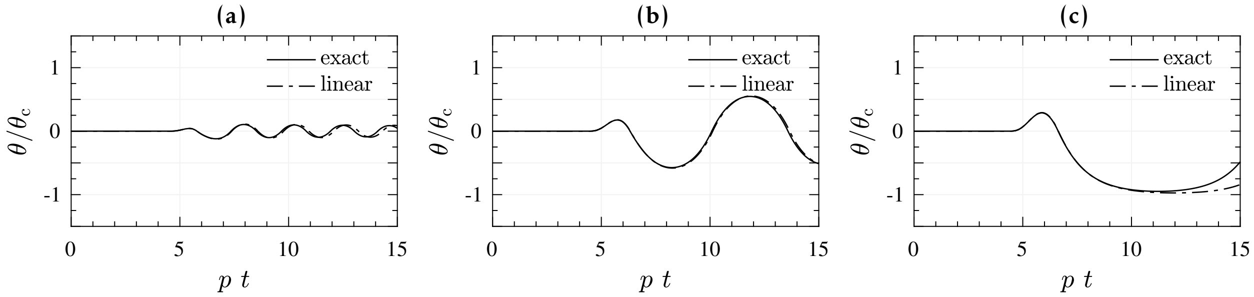

Figure 3.33: Response history comparison for the exact and the linearized equation of motion for the rolling-and-rocking oscillator B3$^{\mathrm{ec}}$: response to a symmetric Ricker wavelet ($T_p = 2.064\,\mathrm{s}$, $a_p = \{0.130, 0.165, 0.185\}g$): (a) Small amplitudes; (b) Moderate amplitudes; (c) Amplitudes close to overturning.

CHAPTER 4

PLANAR 2DOF ROCKING

In this chapter planar rocking systems that can be described with two degrees of freedom are discussed. Part of the material presented in this chapter has been published. At the ECCOMAS Congress on Crete the numerical model of the podium structures was briefly introduced [3], focusing, however, on the experimental part which is covered in Chapter 6. The numerical model was presented in more detail at the World Conference on Earthquake Engineering [4] that was held in Santiago de Chile, and in the later published journal article [5].

4.1 Introduction

In this chapter I present and discuss planar rocking systems that can be described with two degrees of freedom. A classical example of a MDOF planar rocking system is the multi-drum column where a rigid rocking column is modeled as more than one rigid element, *e.g.*, for ancient columns. Consequently, there are multiple degrees of freedom that have to be considered.

In this thesis, however, other kinds of planar MDOF rocking systems are being investigated, in particular:

Seismically isolated multistory structures
Multistory structures that are seismically isolated with a so called *kinematic bearing* (rocking elements in the ground floor) are the topic of the first part of this chapter (Sec. 4.2). I refer to such structures as *podium structures*: structures that extend the rocking frame with an additional degree of freedom, assigned to the elastic displacement of the superstructure.

4.2 Rocking Podium Structures

In this section I present the analytical investigation of the dynamics of rocking podium structures with an attached elastic oscillator atop. First, I define a class of rocking podium structures, followed by the formulation of the equations of rocking motion of such structures. After conducting a dimensional analysis of the equations of motion, they are solved for analytic pulse and recorded ground motion excitation to investigate the stability and maximum deformation demands and capacities of rocking podium structures.

4.2.1 Introduction

Structures fixed to the ground using foundation systems that prevent uplift and sliding dominate modern seismic design. However, next to the conventional base isolation where an additional soft layer is inserted between the foundation and the superstructure and is specially designed such that it can take most of the seismic displacement demand, another kind of base isolation evolved. Its concepts centers on allowing the structure to uplift from its foundation and rock in response to ground motion excitation.

Uplift serves as a mechanical fuse, limiting the forces transmitted to the structure and the foundation, while the energy of the input ground motion is dissipated through impacts at the rocking interfaces. Consequently, the seismic demands in the isolated superstructure are decreased, allowing for better-performing and safer structures. The size effect (larger rocking structures are more stable) and the lack of residual displacements are two remarkable dynamic properties of rocking structures.

Pioneering rocking structures have been investigated, designed, and built in New Zealand [93,94], Russia and the USSR [95], and the USA [96] in the 1970s. However, the concept of *kinematic bearings* where the columns of the entire bottom story of the structures are allowed to rock freely in response to earthquake ground motion excitation, effectively forming a *flexible story* [100] with the ability to return to its pre-excitation configuration, was mainly developed in Russia and the USSR. More than 400 buildings with such flexible stories were built in Russia over the past four decades [101]. The buildings performed well in earthquakes they were exposed to, and the ability of the columns to rock did not deteriorate over the years [101,102].

Notably, full-scale dynamic tests have been performed on real structures [103,104]. Figure 4.1 shows a three-story masonry building placed on a kinematic bearing story being constructed in Russia in 2008. This structure was tested in free rocking motion by applying an initial lateral displacement using hydraulic jacks. The concrete columns of the bottom story of such a rocking

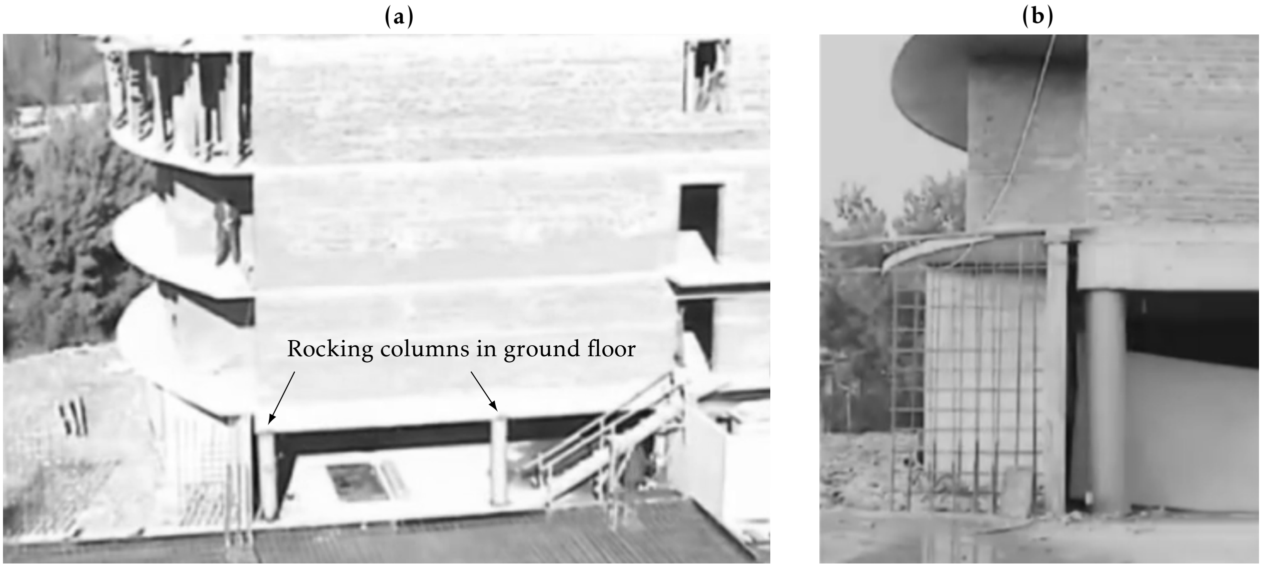

Figure 4.1: Full-scale dynamic tests of a rocking podium structure [103]: (a) 4-story masonry structure; (b) initial displacement of the kinematic bearing story column.

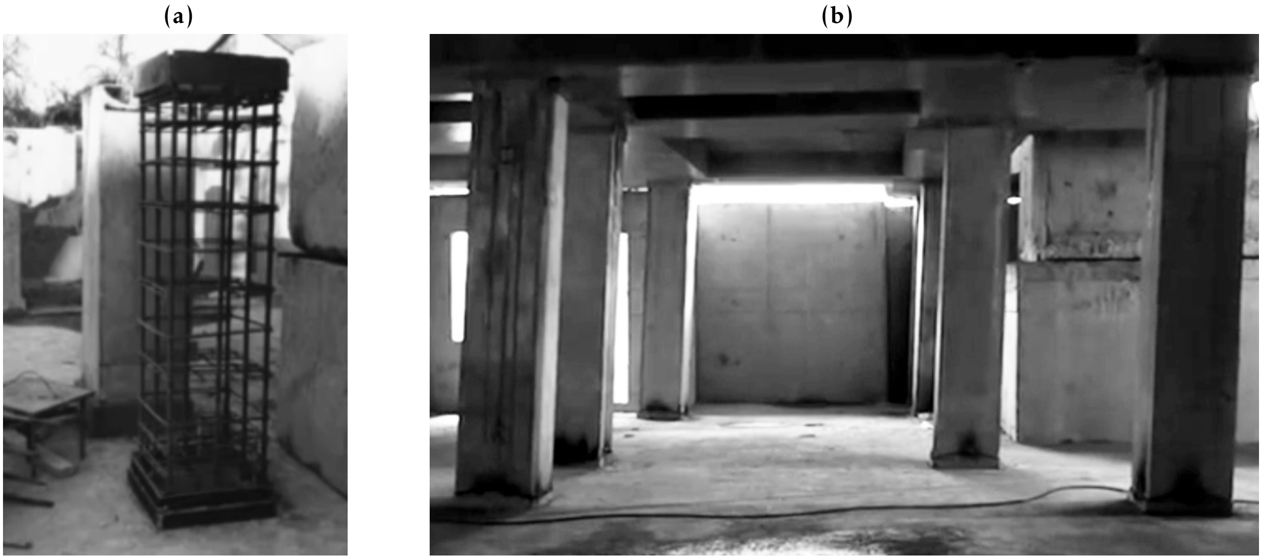

Figure 4.2: Rocking columns in bottom kinematic bearing story: (a) Completed and unfinished column [103]; (b) Initial displacement of a free rocking motion test [104].

structure are designed to uplift and sustain rocking motion during an earthquake event. The ends of the columns are protected by steel plates or caps to avoid concrete crushing when they uplift (Fig. 4.2a). Insuring that the kinematic bearing story does not collapse (overturn) in a design-basis earthquake and control of the forces in the superstructure is achieved by sizing the rocking columns (Fig. 4.2b). Design guidelines for such rocking structures were presented in the early 1970s in Polyakov's well-known textbook [95]. He suggested that:

i) that the superstructure on top of the flexible story behave as a rigid body, and

ii) that the dynamics of the flexible first story (the kinematic bearing ground floor) be described using an elastic fixed-base cantilever SDOF model.

A similar modeling approach for rocking structures was later suggested by Priestly, Evison, & Carr [105].

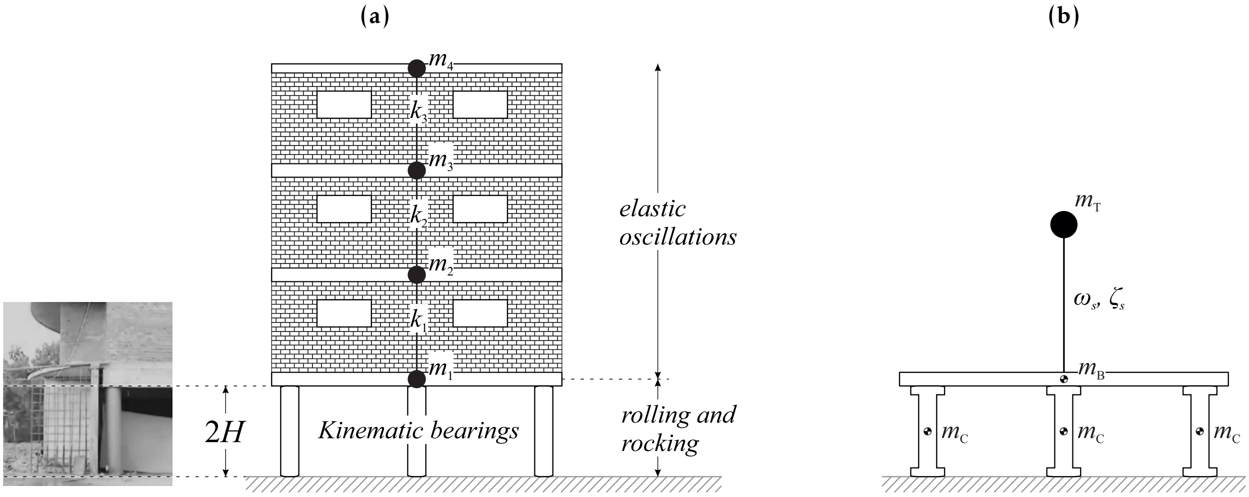

Figure 4.3: Rocking podium structure: (a) Masonry building isolated on a rocking ground floor [103]; (b) Dynamic model: initial position.

4.2.2 Dynamic Model

A multi-story superstructure built on a rocking first story, akin to the one shown in Figure 4.3a, is modeled as a rocking podium structure shown in Figure 4.3b. The dynamics of the superstructure are assumed to be adequately represented by a SDOF cantilever system. Thus, the rolling-and-rocking frame model described in Section 3.4 is extended by adding a deformable SDOF system fixed on top of the cap-beam of the rolling-and-rocking frame.

The following assumptions are made:

- The rocking first story is represented by a rolling-and-rocking frame structure described in Section 3.4. This means that:
    - it is assumed to be rigid;
    - given a curved base ($\rho > 0$), it experiences rolling (phase I) and rocking (phase II);
    - the horizontal displacement and vertical displacement of the rigid cap-beam are defined by Equation (3.83) and Equation (3.84), respectively. They are both functions of the first degree of freedom, the tilt angle θ;
    - the contact surfaces at the bottom and the top of the columns of the rolling-and-rocking podium frame do not allow any sliding and stay intact throughout the rocking motion (there is no crushing or permanent deformation of the contact surfaces).
- The SDOF system representing the multi-story structure on the rolling-and-rocking podium remains elastic. Its response, denoted with the second degree of freedom, u_T, is characterized by the stiffness k_s, the damping coefficient c_s, and the mass m_T, and is measured relative to the supporting ground (total displacement). They translate into other and independent system parameters, the fixed-base natural frequency ω_s and the viscous damping ratio ζ_s, as follows:

$$k_s/m_\mathrm{T} = \omega_s^2, \qquad c_s/m_\mathrm{T} = 2\zeta_s\omega_s. \tag{4.1}$$

- The superstructure mass m_T is lumped at the top and does not have any rotational inertia. Similarly, one could assume that m_T displaces only horizontally. The mass m_T is the sum of all story masses above the cap-beam: $m_\mathrm{T} = \sum_2^{n_s} m_i$ where n_s is the number of stories.
- The overturning moment exerted by the superstructure on the podium cap-beam is not large enough to cause uplift of the cap-beam (detachment of the beam from the columns).

The rocking podium structure is a 2DOF system where the motion of the rolling-and-rocking frame cap-beam with respect to the support is described by the displacement u_B (equivalently, tilt angle θ) and the motion of the superstructure mass m_T with respect to the cap-beam is described by the displacement u_T. A superstructure mass ratio is defined as

$$\eta = \frac{m_\mathrm{T}}{m_\mathrm{B}}. \tag{4.2}$$

Assuming that the weight of each story is roughly the same, η can be interpreted as the number of stories above the rocking podium frame.

Equation of Motion before Uplift and Uplift Criterion

Before uplift, the equation of motion of the superstructure on top of the rocking podium frame is

$$\ddot{u}_{\mathrm{T}} + 2\,\zeta_s\,\omega_s\,\dot{u}_{\mathrm{T}} + \omega_s^2\,u_{\mathrm{T}} = -\ddot{u}_g\,. \tag{4.3}$$

The podium frame does not move before uplift, removing its degree of freedom from consideration. The uplift criterion $\ddot{u}_g = \pm g\,\tan\alpha$ that was defined in Chapter 3 is modified by the presence of the superstructure on top of the cap-beam. Figure 4.4a shows the situation of the podium at incipient uplift (for uplift occurring towards the right side: $\theta > 0$). The lateral force V_s is the resulting shear force acting at the base of the SDOF oscillator.

$$V_s = k_s\,u_{\mathrm{T}} + c_s\,\dot{u}_{\mathrm{T}} = m_{\mathrm{T}} \cdot \left(\omega_s^2\,u_{\mathrm{T}} + 2\,\zeta_s\,\omega_s\,\dot{u}_{\mathrm{T}}\right). \tag{4.4}$$

The principle of virtual work for a positive $\ddot{u}_g$ and a virtual rotation of $-\delta\theta$ at incipient uplift is applied:

$$\delta\theta \cdot (B\,N\,m_{\mathrm{C}}\,g - H\,N\,m_{\mathrm{C}}\,g) + \delta\theta \cdot (2\,B\,m_{\mathrm{B}}\,g + 2\,B\,m_{\mathrm{T}}\,g) - \delta\theta \cdot 2\,H\,m_{\mathrm{B}}\,\ddot{u}_g + \delta\theta \cdot 2\,H\,V_s = 0\,. \tag{4.5}$$

Combining Equations (4.4) and (4.5) yields

$$\ddot{u}_g \cdot (2\,m_{\mathrm{B}} + N\,m_{\mathrm{C}}) = g\,\tan\alpha \cdot (2\,m_{\mathrm{B}} + 2\,m_{\mathrm{T}} + N\,m_{\mathrm{C}}) + \omega_s^2\,m_{\mathrm{T}}\,u_{\mathrm{T}} + 2\,\zeta_s\,\omega_s\,m_{\mathrm{T}}\,\dot{u}_{\mathrm{T}}\,. \tag{4.6}$$

Then, the rocking podium frame uplift thresholds for both positive and negative ground accelerations are

$$\ddot{u}_{g,up} = \pm g\,\tan\alpha + \frac{2\,\gamma\,\eta}{2\,\gamma + 1} \cdot \left(\pm g\,\tan\alpha + \omega_s^2\,u_{\mathrm{T}} + 2\,\zeta_s\,\omega_s\,\dot{u}_{\mathrm{T}}\right). \tag{4.7}$$

For rigid superstructures where $\left(\omega_s^2\,u_{\mathrm{T}} + 2\,\zeta_s\,\omega_s\,\dot{u}_{\mathrm{T}}\right) \rightarrow -\ddot{u}_g$ and for light superstructures where $\eta \rightarrow 0$, Equation (4.7) resolves to $\pm g\,\tan\alpha$.

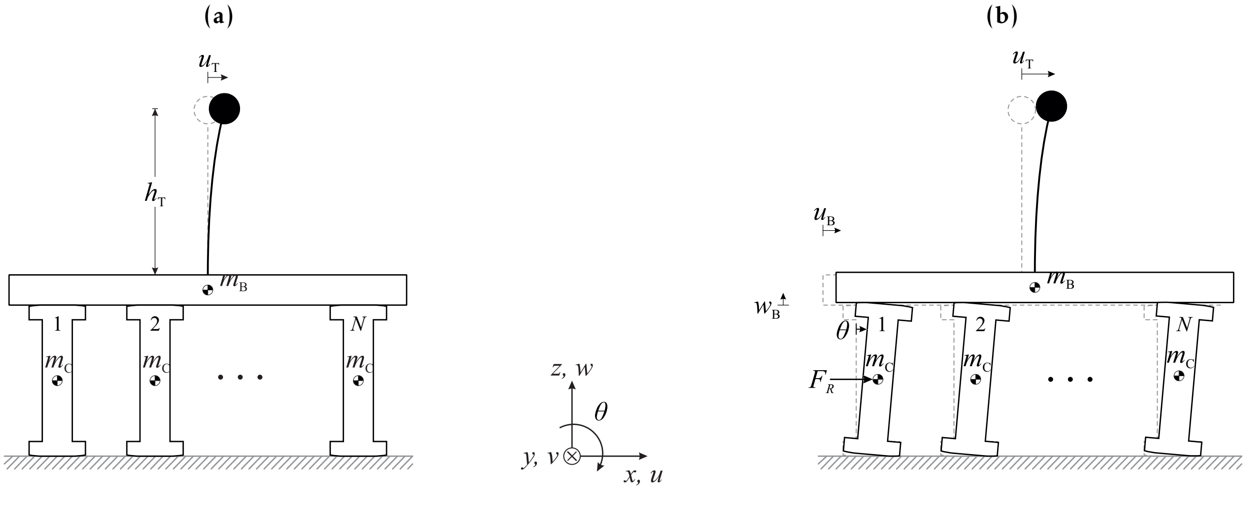

Figure 4.4: Dynamic model of a rolling-and-rocking podium structure: (a) Pure elastic oscillation of top mass m_{T}; (b) Mixed response in uplifted state.

Equations of Motion after Uplift

The Lagrangian formulation is used to derive the equations of motion of the 2DOF rolling-and-rocking podium structure after uplift. The equations of motion presented here are in a general form and allow application to all the rocking and rolling-and-rocking systems that have been presented in this thesis so far.

The equation of motion regarding the first degree of freedom, the tilt angle θ, is

$$\begin{aligned}\ddot{\theta}\cdot\Big(\lambda+(1+4\gamma)\,\frac{{u'_{\mathrm{B}}}^{2}+{w'_{\mathrm{B}}}^{2}}{4R^2}+4\gamma\,\eta\,\frac{{w'_{\mathrm{B}}}^{2}}{4R^2}\Big)&=\dot{\theta}^2\Big((1+4\gamma)\,\frac{u'_{\mathrm{B}}\cdot u''_{\mathrm{B}}+w'_{\mathrm{B}}\cdot w''_{\mathrm{B}}}{4R^2}+4\gamma\,\eta\,\frac{w'_{\mathrm{B}}\cdot w''_{\mathrm{B}}}{4R^2}\Big)\\&\quad-\frac{g}{R}(1+2\gamma+2\gamma\,\eta)\cdot\frac{w'_{\mathrm{B}}}{2R}-\frac{\ddot{u}_g}{R}(1+2\gamma)\cdot\frac{u'_{\mathrm{B}}}{2R}\\&\quad+4\gamma\,\eta\cdot\frac{u'_{\mathrm{B}}}{2R}\cdot\Big(\omega_s^2\,\frac{u_{\mathrm{T}}-u_{\mathrm{B}}}{2R}+2\zeta_s\,\omega_s\,\frac{\dot{u}_{\mathrm{T}}-\dot{u}_{\mathrm{B}}}{2R}\Big).\end{aligned}\tag{4.8}$$

The equation of motion for the second degree of freedom, the top mass elastic displacement u_{T}, is

$$\ddot{u}_{\mathrm{T}}+\omega_s^2\cdot(u_{\mathrm{T}}-u_{\mathrm{B}})+2\zeta_s\,\omega_s\cdot(\dot{u}_{\mathrm{T}}-\dot{u}_{\mathrm{B}})=-\ddot{u}_g\,.\tag{4.9}$$

The complete equations of motion of the rolling-and-rocking podium structure are specified in Appendix A.3.1. A comparison of Equations (4.3) and (4.9) shows that the displacement demand of the ground motion is now taken by both the rocking podium frame and the elastic superstructure.

In Equations (4.8) and (4.9) two different kind of derivatives are used: the notation $\dot{\square}$ denotes the time derivative $\frac{\mathrm{d}}{\mathrm{d}t}$ while the notation $\square'$ implies the partial derivative $\frac{\partial}{\partial\theta}$. This distinction is necessary because u_{B} is a function of θ, and

$$\dot{u}_{\mathrm{B}}=\frac{\mathrm{d}\,u_{\mathrm{B}}}{\mathrm{d}\,t}=\frac{\partial u_{\mathrm{B}}}{\partial\theta}\cdot\frac{\partial\theta}{\partial t}=u'_{\mathrm{B}}\cdot\dot{\theta}\,.\tag{4.10}$$

The equations present a similarity with several other problems of rocking–elasticity interaction [66, 70, 72, 128, 129]. For a rolling-and-rocking podium, the horizontal displacement and vertical displacement of the cap-beam are given by $u_{\mathrm{B}}=2\,u_{\mathrm{C}}$ and $w_{\mathrm{B}}=2\,w_{\mathrm{C}}$, where u_{C} and w_{C} are defined by Equations (3.46) and (3.47) for phase I (rolling) and by Equations (3.51) and (3.52) for phase II (rocking):

$${}^{\mathrm{I}}u_{\mathrm{B}}=2R\sin(\pm\alpha)-2R\sin(\pm\alpha-\theta)+2r\cdot\big(\theta-\sin\theta\big)\tag{4.11}$$

$${}^{\mathrm{I}}w_{\mathrm{B}}=2R\cos(\pm\alpha-\theta)+2r\cdot\big(1-\cos\theta\big)\tag{4.12}$$

$${}^{\mathrm{II}}u_{\mathrm{B}}=2R\sin(\pm\alpha)-2R\sin(\pm\alpha-\theta)+2r\cdot\big(\pm\beta-\sin(\pm\beta-\theta)-\sin\theta\big)\tag{4.13}$$

$${}^{\mathrm{II}}w_{\mathrm{B}}=2R\cos(\pm\alpha-\theta)+2r\cdot\big(\cos(\pm\beta-\theta)-\cos\theta\big)\tag{4.14}$$

Then, we get the following derivatives:

$$\frac{{}^{\mathrm{I}}u'_{\mathrm{B}}}{2R}=\frac{1}{2R}\,\frac{\partial\,{}^{\mathrm{I}}u_{\mathrm{B}}}{\partial\theta}=\cos(\pm\alpha-\theta)+2\rho\cos\alpha\cdot\big(1-\cos\theta\big)\tag{4.15}$$

$$\frac{{}^{\mathrm{I}}w'_{\mathrm{B}}}{2R}=\frac{1}{2R}\,\frac{\partial\,{}^{\mathrm{I}}w_{\mathrm{B}}}{\partial\theta}=\sin(\pm\alpha-\theta)+2\rho\cos\alpha\cdot\sin\theta\tag{4.16}$$

$$\frac{{}^{\mathrm{II}}u'_{\mathrm{B}}}{2R}=\frac{1}{2R}\,\frac{\partial\,{}^{\mathrm{II}}u_{\mathrm{B}}}{\partial\theta}=\cos(\pm\alpha-\theta)+2\rho\cos\alpha\cdot\big(\cos(\pm\beta-\theta)-\cos\theta\big)\tag{4.17}$$

Example 4.1: Deriving the equation of motion for the free-standing rigid block using Equation (4.8)

Equation (4.8) can even be used to derive the equation of motion of the rigid rocking block without extensions. For $\eta = \gamma = 0$, we get

$$\ddot{\theta} \cdot \left(\lambda + \frac{{u'_{\mathrm{B}}}^2 + {w'_{\mathrm{B}}}^2}{4R^2}\right) = \dot{\theta}^2 \left(\frac{u'_{\mathrm{B}} \cdot u''_{\mathrm{B}} + w'_{\mathrm{B}} \cdot w''_{\mathrm{B}}}{4R^2}\right) - \frac{g}{R} \cdot \frac{w'_{\mathrm{B}}}{2R} - \frac{\ddot{u}_g}{R} \cdot \frac{u'_{\mathrm{B}}}{2R},$$

where ${u'_{\mathrm{B}}}^2 + {w'_{\mathrm{B}}}^2 = 4R^2$ and $u'_{\mathrm{B}} \cdot u''_{\mathrm{B}} + w'_{\mathrm{B}} \cdot w''_{\mathrm{B}} = 0$. With

$$\frac{u'_{\mathrm{B}}}{2R} = \cos(\pm\alpha - \theta) \qquad \text{and} \qquad \frac{w'_{\mathrm{B}}}{2R} = \sin(\pm\alpha - \theta),$$

the equation resolves into the equation of motion of the free-standing rigid block (Eq. 3.11):

$$\ddot{\theta} \cdot (\lambda + 1) = -\frac{\ddot{u}_g}{R} \cdot \cos(\pm\alpha - \theta) - \frac{g}{R} \cdot \sin(\pm\alpha - \theta).$$

$$\frac{{}^{\mathrm{II}}w'_{\mathrm{B}}}{2R} = \frac{1}{2R} \frac{\partial\, {}^{\mathrm{II}}w_{\mathrm{B}}}{\partial\theta} = \sin(\pm\alpha - \theta) + 2\rho\cos\alpha \cdot \Big(\sin(\pm\beta - \theta) + \sin\theta\Big) \tag{4.18}$$

For example, the first term of Equation (4.8) for the rolling phase becomes:

$$\begin{aligned} \ddot{\theta} \cdot \Bigg(&\lambda + (1 + 4\gamma) \cdot \Big(1 + 4\rho\cos\alpha \cdot \big(\cos(\pm\alpha - \theta) - \cos\alpha\big) + 8\rho^2\cos^2\alpha \cdot \big(1 - \cos\theta\big)\Big) \\ &+ 4\gamma\eta \cdot \Big(\sin^2(\pm\alpha - \theta) + 4\rho\cos\alpha\, \sin(\pm\alpha - \theta)\, \sin\theta + 4\rho^2\cos^2\alpha\, \sin^2\theta\Big)\Bigg) = \ldots \end{aligned} \tag{4.19}$$

Impacts and Energy Dissipation

The proposed dynamic model of a rocking podium structure has two degrees of freedom. Thus, two equations are needed to determine the post-impact condition and, thereby, the energy dissipated at impact.

The model proposed by Housner [16] presumes that rocking column impacts are instantaneous and that the contact forces between the rocking column and the rocking surfaces are concentrated at the pivot points. Therefore, at the moment of impact, the pivot point instantaneously moves to the other edge of the column. This assumption has been previously used to calculate the coefficient of restitution in several rocking systems [39, 41, 130].

The aforementioned assumption results in CoAM for each column of the rocking podium frame during impact. Moreover, it is assumed that the elastic deformation of the superstructure is small compared with its size (height h_{T}), so CoAM is applied in the undeformed configuration of the rocking podium structure (Fig. 4.3b). This yields the first equation:

$$c_r = \frac{\dot{\theta}^2_{after}}{\dot{\theta}^2_{before}} = \left(1 - 2\sin^2\alpha \cdot \frac{1 + 4\gamma + 4\gamma\eta}{1 + \lambda + 4\gamma + 4\gamma\eta}\right)^2. \tag{4.20}$$

The second equation comes from the assumption that the horizontal velocity of the superstructure mass m_{T} does not change during impact:

$$\dot{u}_{\mathrm{T},after} = \dot{u}_{\mathrm{T},before}. \tag{4.21}$$

Equation (4.20) can be compared with the expressions for the coefficient of restitution of other, simpler, rocking systems. With $\eta = \gamma = 0$, for example, it yields exactly what Housner proposed for his rigid block, and with $\eta = 0$, its solution is equal to the expression of Makris and Vassiliou [39] for a rocking frame. Different impact assumptions have also been proposed for deformable rocking structures [66, 69, 70, 128].

Frequency in the Uplifted State

As has been shown both analytically [70, 72, 73, 131] and experimentally [67, 74, 76], the natural frequency of an uplifted structure, $\omega_{s,u}$, is larger than the fixed-base frequency ω_s of the same structure. This supports the assumption of a *rigid-body superstructure* found in Polyakov's book[1] [95].

The uplifted frequency can be computed through eigenfrequency analysis of the rocking podium structure:

$$|\,\mathbf{K} - \omega_{s,u}^2\,\mathbf{M}\,| = 0\,, \tag{4.22}$$

where **K** is the stiffness matrix and **M** is the mass matrix of the rocking podium structure. In the presence of damping, the aforementioned equation needs to be correct only if damping satisfies the Caughey–O'Kelly condition [74], which is not the case. However, since the superstructure remains elastic, the energy dissipated through its motion (its damping) is expected to be relatively small compared with the energy dissipated by the rocking of the podium frame and, therefore, Equation (4.22) is expected to give a good approximation of the uplifted frequencies. This was experimentally confirmed for other elastic uplifting systems [74, 76].

Linearizing the equations of motion of the rolling-and-rocking podium structure (Eqs. 4.8 and 4.9) and neglecting gravity yield the mass and stiffness matrices of the system:

$$\mathbf{M} = \begin{bmatrix} R\cdot\left(1+\lambda+4\gamma+4\gamma\eta\sin^2\alpha\right) & 0 \\ 0 & 1 \end{bmatrix}, \quad \mathbf{K} = \begin{bmatrix} 4R\gamma\eta\,\omega_s^2\cos^2\alpha & -2\gamma\eta\,\omega_s^2\cos\alpha \\ -2R\omega_s^2\cos\alpha & \omega_s^2 \end{bmatrix}. \tag{4.23}$$

Note that the fact whether the oscillators are curved or not does change the above matrices due to the applied linearization . Solving the eigenvalue problem (Eq. 4.22) gives

$$\omega_{s,u}^4\cdot\left(1+\lambda+4\gamma+4\gamma\eta\sin^2\alpha\right) - \omega_{s,u}^2\,\omega_s^2\cdot(1+\lambda+4\gamma+4\gamma\eta) = 0\,. \tag{4.24}$$

The eigenfrequency analysis reveals the two distinct mode shapes of the uplifted rocking podium structure: The first one is a rotation of the podium frame columns with a natural frequency of 0 Hz, a rigid body mode. The second one is the vibration of the elastic SDOF system when the rocking podium frame is uplifted (Fig. 4.4b). In the uplifted state, the natural eigenfrequency $\omega_{s,u}$ of the SDOF system is

$$\omega_{s,u} = \sqrt{\frac{1+\lambda+4\gamma\cdot(1+\eta)}{1+\lambda+4\gamma\cdot(1+\eta\sin^2\alpha)}}\cdot\omega_s\,. \tag{4.25}$$

---

[1] The first design guideline of Polyakov is to treat the superstructure as a rigid body.

Clearly, the natural frequency of the uplifted SDOF system, $\omega_{s,u}$, is larger than its fixed-base frequency ω_s. For heavy superstructures ($\eta \to \infty$) (*i.e.*, large number of stories), the amplification factor simplifies to $1/\sin\alpha$, which coincides with the solution of Yim and Chopra [131] for structures with foundation uplift.

Figure 4.5a plots the superstructure vibration frequency amplification factor for different values against the superstructure mass ratio for the three superstructure mass ratio values, effectively representing the number of stories above the rocking podium frame. It can be seen that the eigenfrequencies of superstructures with more stories experience larger amplification when the podium is uplifted. However, assuming that the fixed-base natural frequency of a building is given by the empirical relation $f_n = 10\,\mathrm{Hz}/n_s$, one can prove that the uplifted frequency of the superstructure decreases with increasing number of stories.

Since a planar model is used to represent the in-plane behavior of a 3D podium structure, the cap-beam represents the mass of a whole slab. Typically, this slab is much heavier than the total weight of the columns, so γ is expected to have a large value. Therefore, it is reasonable to assume that the eigenfrequencies of the superstructure when the podium is in the uplifted state are given by the limit of Equation (4.25) as $\gamma \to \infty$:

$$\omega_{s,u} = \sqrt{\frac{1+\eta}{1+\eta\,\sin^2\alpha}} \cdot \omega_s\,. \tag{4.26}$$

Figure 4.5b plots Equation (4.26) for different values of column slenderness α, assuming $\gamma = 10$.

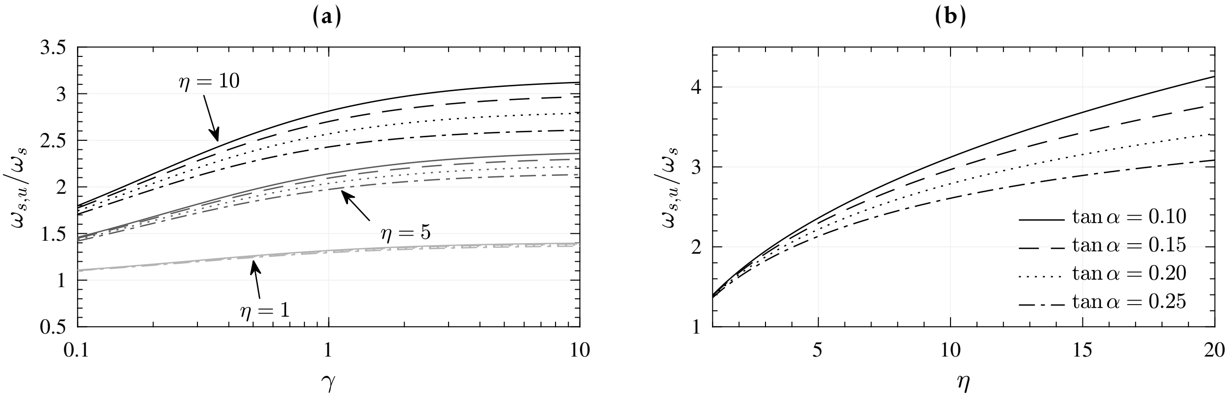

Figure 4.5: Amplification factor for the natural frequency ω_s of the elastic superstructure on a rocking podium frame in the uplifted (rocking) state: (a) Variation with respect to the beam bass ratio γ; (b) Variation with respect to the superstructure mass ratio η, given $\gamma = 10$.

Damping in the Uplifted State

As in [70,72,74,131], the assumption of viscous damping of the superstructure leads to a damping ratio in the uplifted state equal to

$$\zeta_{s,u} = \sqrt{\frac{1+\lambda+4\gamma\cdot(1+\eta)}{1+\lambda+4\gamma\cdot(1+\eta\,\sin^2\alpha)}} \cdot \zeta_s = S_r \cdot \zeta_s\,. \tag{4.27}$$

However, the results of experiments [76] show that uplifting of a deformable rocking column may not affect its damping. Therefore, it is reasonable to assume that the forces representing energy dissipation in the equation of motion of the superstructure are not proportional to the elastic velocity of the superstructure. However, since damping in the superstructure is expected to be small, [76] suggests to use viscous damping equal to ζ_s/S_r so that damping in the uplifted (amplified) state is equal to ζ_s.

4.2.3 Dimensional Analysis

This section examines the response of the rolling-and-rocking podium structure model shown in Figure 4.4 to an idealized acceleration pulse.

Equation of Motion for the Tilt Angle θ

In order to identify the dimensionless parameters the tilt angle equation of motion of the rolling-and-rocking podium is linearized with respect to θ and α. Linearization for phase I yields:

$$\begin{aligned}\ddot{\theta}\cdot\Big(\lambda+1+4\gamma\Big) = &-\frac{g}{R}(1+2\gamma+2\gamma\eta)\cdot\Big(\pm\alpha+\theta\cdot(2\rho-1)\Big)-\frac{\ddot{u}_g}{R}\Big(1+2\gamma\Big)\\ &+4\gamma\eta\cdot\left(\omega_s^2\left(\frac{u_\mathrm{T}}{2R}-\theta\right)+2\zeta_s\,\omega_s\left(\frac{\dot{u}_\mathrm{T}}{2R}-\dot{\theta}\right)\right).\end{aligned} \tag{4.28}$$

Reformulation gives:

$$\begin{aligned}\ddot{\theta} = &\overbrace{-\frac{1+2\gamma+2\gamma\eta}{\lambda+1+4\gamma}\,\frac{g}{R}\cdot\left(\pm\alpha+\theta\cdot(2\rho-1)+\frac{\ddot{u}_g}{g}\right)}^{\text{rigid response}}\\ &\underbrace{+\frac{4\gamma\eta}{\lambda+1+4\gamma}\cdot\left(\omega_s^2\left(\frac{u_\mathrm{T}}{2R}-\theta\right)+2\zeta_s\,\omega_s\left(\frac{\dot{u}_\mathrm{T}}{2R}-\dot{\theta}\right)+\frac{\ddot{u}_g}{2R}\right)}_{\text{elastic response}}.\end{aligned} \tag{4.29}$$

The response of the tilt angle θ has two components: i) a rigid response component, originating from the response of the rigid rolling-and-rocking frame (Eq. 3.87); and ii) an elastic response component, originating from the interaction with the superstructure mass degree of freedom u_T.

For rigid superstructures ($\omega_s \to \infty$) the elastic response disappears. Then, the response of the podium structure is identical to the response of a rigid rolling-and-rocking frame where, instead of γ, $\hat{\gamma} = \gamma\cdot(1+\eta)$ is used. If the superstructure is really soft ($\omega_s \to 0$) the response is comparable with a rigid rolling-and-rocking frame where an additional mass m_T is added on perfectly sliding bearings on top of the frame (the mass is only activated vertically but not horizontally).

Similar observations can be made for the equation of motion for phase II:

$$\begin{aligned}\ddot{\theta} = &\overbrace{-\frac{1+2\gamma+2\gamma\eta}{\lambda+1+4\gamma}\,\frac{g}{R}\cdot\left(\pm\alpha'-\theta+\frac{\ddot{u}_g}{g}\right)}^{\text{rigid response}}\\ &\underbrace{+\frac{4\gamma\eta}{\lambda+1+4\gamma}\cdot\left(\omega_s^2\left(\frac{u_\mathrm{T}}{2R}-\theta\right)+2\zeta_s\,\omega_s\left(\frac{\dot{u}_\mathrm{T}}{2R}-\dot{\theta}\right)+\frac{\ddot{u}_g}{2R}\right)}_{\text{elastic response}}.\end{aligned} \tag{4.30}$$

Dimensionless Parameters

Following the procedure in Section 3.3.4, the response of the tilt angle is a function of the following dimensionless similitude parameters:

$$\mathcal{F}\left(\frac{\theta}{\alpha'},\frac{\alpha}{\alpha'},\hat{p}\,t,\frac{\omega_p}{\hat{p}},\hat{a}_p,\frac{\omega_s}{\hat{p}},\eta,\zeta_s,c_r\right)=0\,, \tag{4.31}$$

where

$$\hat{p}^2=\frac{g}{R}\,\frac{1+2\gamma+2\gamma\eta}{\lambda+1+4\gamma}\,\frac{\alpha}{\alpha'}\,. \tag{4.32}$$

Range of Interest of the Dimensionless Parameters

- Column slenderness:

  Since $\tan\alpha$ controls the superstructure design forces, in order for the rocking podium structure to work as a useful seismic isolation system, α cannot be excessively large. Typically, slenderness values $\tan\alpha < 0.2$ are meaningful.

- Size-frequency parameter:

  Ideal candidates for rocking isolation, such as tall bridges and chimneys, can have a height reaching several tens of meters. However, in the model under study, typical rocking podium columns are expected to have a height of no more than 6 m. A value of $\omega_p/p = 8$ corresponds to a pulse period of 0.5 s for a 6 m tall column. Therefore, values of $\omega_p/p < 8$ will be examined.

- Mass ratio:

  For superstructure floors of equal mass, η corresponds to the number of floors. Superstructures with up to 10 floors (for rocking spectra) and up to five floors (for time history analysis) are analyzed. As previously explained, γ is expected to be large as it represents a slab-to-columns mass ratio. Figure 4.5a shows that the frequency amplification ratio has already saturated for $\gamma = 10$, so γ is set to equal to 10.

- Superstructure frequency:

  A lower bound for ω_s/p is derived by minimizing ω_s and maximizing p (*i.e.*, minimizing rocking column height). Therefore, a lower bound of ω_s/p is obtained by assuming a 10-story superstructure placed on a 3 m tall rocking podium. Then, the fundamental period of the superstructure is on the order of 1 s and $\omega_s/p \approx 3$.

- Superstructure damping ratio:

  The superstructure is intended to remain elastic during its response to design-basis excitation. Therefore, its fixed-base structural damping is expected to be no larger than 0.01. According to Section 4.2.2, $\zeta_s = 0.01/S_r$ is used. This way, the uplifted damping will be constant and equal to 0.01.

4.2.4 Response to Analytic Pulse Ground Motions

In this section the response of the rocking podium ($\rho = 0$) structure to analytical pulse ground motions is investigated. Figures 4.6 and 4.7 show the maximum rocking angle response spectra for antisymmetric and symmetric Ricker wavelet excitations. From left to right, the weight of the superstructure (*i.e.*, the number of stories), defined by Equation (4.2), is increased ($\eta = \{1, 5, 10\}$). From top to bottom, the natural period T_s of the superstructure SDOF model is increased from 0 s (rigid) to 0.95 s (deformable) ($\omega_s/p = \{\infty, 30, 6, 3\}$). The podium cap-beam-to-column mass ratio is chosen as $\gamma = 10$ as it was found that its further increase does not influence the response (Fig. 4.5, left). The column slenderness used to compute the rocking spectra is $\tan\alpha = 0.15$. Results of analyses for other slenderness values, not presented here because of space limits, show that the rocking podium spectra are not sensitive to this parameter. The mass eccentricity factor λ is set to 1/3 (uniformly distributed column mass). The lower x-axes of the spectra show the value of the pulse natural frequency ω_p normalized by p, which corresponds to the frequency parameter of a column with evenly distributed mass and semi-diagonal R, defined by Equation (3.13). To give a sense of the magnitude of the non-dimensional term ω_p/p, the pulse period, T_p, that corresponds to $p = 2.2\ \mathrm{s}^{-1}$ (column with $2H = 3$ m) is plotted on the top horizontal axis.

In order to test the second design guideline of Polyakov [95], that is, the rocking frame should be treated as a very flexible elastic structure (without any rocking elements); the spectra in Figures 4.6 and 4.7 also plot (white dashed lines) the pulse acceleration that would cause a displacement of the system (measured at the top of the rocking columns) equal to the column total width ($2B$) and would, therefore, cause collapse. This design guideline is consistent to what [65,132,133] propose.

Figure 4.8 plots the minimum overturning acceleration spectra for both symmetric and antisymmetric Ricker wavelet excitations. It shows that the interaction between the rocking podium frame and the elastic superstructure follows similar trends as the ones observed in [70,72].

1. For low values of ω_p/p (small height of the rocking podium frame or low-frequency pulses), the deformability of the superstructure has a detrimental effect on the stability of the system, while the opposite holds for large values of ω_p/p.
2. For low values of ω_p/p, the deformability of the superstructure clearly decreases the acceleration needed to cause uplift: $\ddot{u}_{g,up} < g\tan\alpha$.
3. The effects of the superstructure deformability become negligible for $\omega_s/p > 6$. For 3 m tall columns, this value of ω_s/p corresponds to a structural period, T_s, equal to 0.48 s.
4. The weight of the superstructure has only a marginal influence on the system stability. Based on these findings, the first Polyakov [95] guideline (to treat the superstructure of rocking podium structures as a rigid body) is reasonable, at least for superstructures with natural periods shorter than 0.48 s (for a rocking column height equal to 3 m). For values of $\omega_p/p < 1.8$, the second Polyakov guideline (modeling the rocking story as a very flexible elastic oscillator) is conservative. However, for larger values of ω_p/p (corresponding to pulse periods smaller than about 1.6 s for 3 m tall columns of the rocking frame), analytic pulse analysis suggests that this assumption become non-conservative and should clearly be avoided.

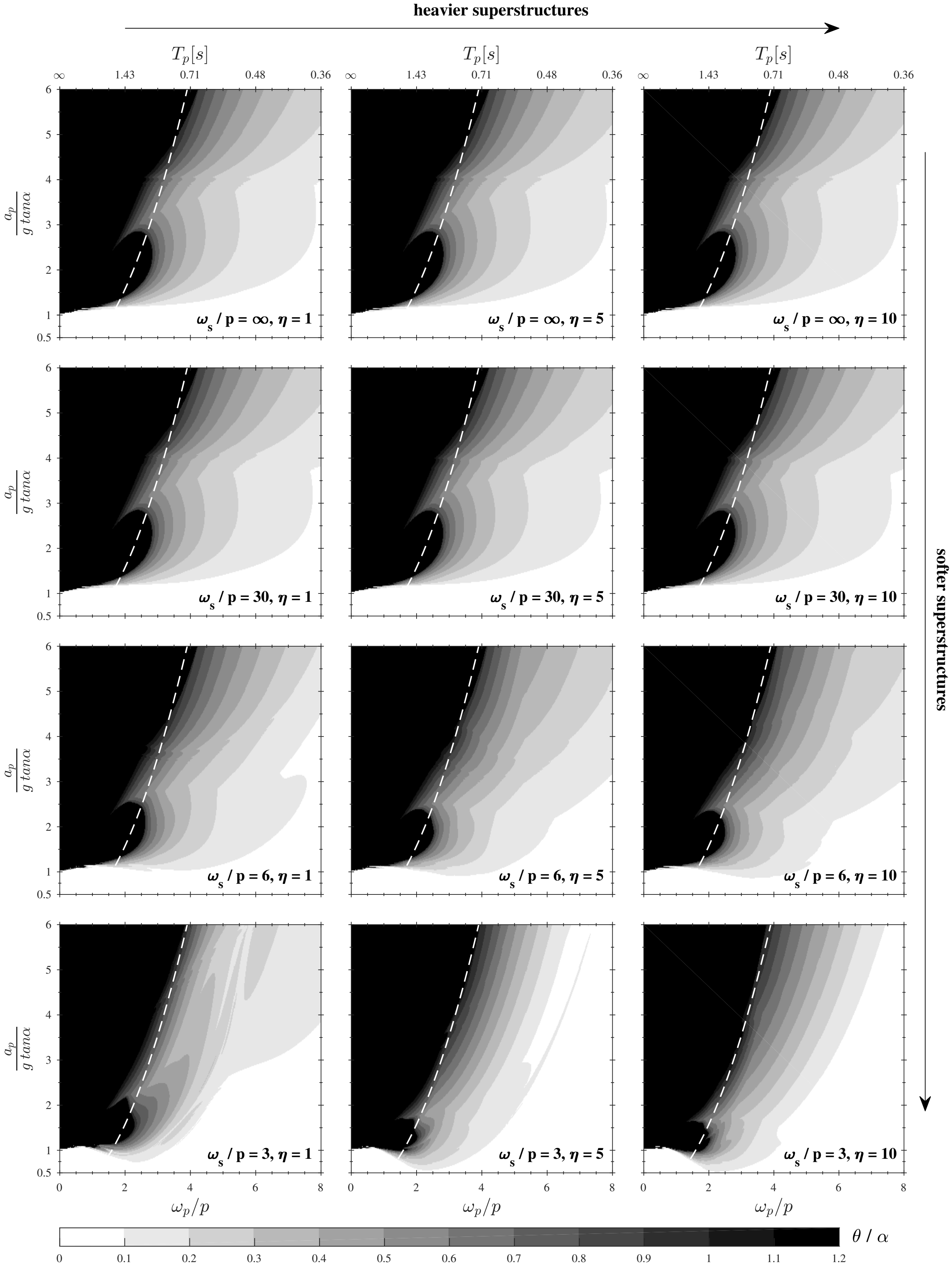

Figure 4.6: Rocking spectra (maximum base rotation, θ/α) of a rocking podium structure with $\gamma = 10$ and different values of ω_s/p (∞, 30, 6, 3) and η (1, 5, 10) subjected to an antisymmetric Ricker wavelet. The white dashed line indicates Polyakov's overturning acceleration.

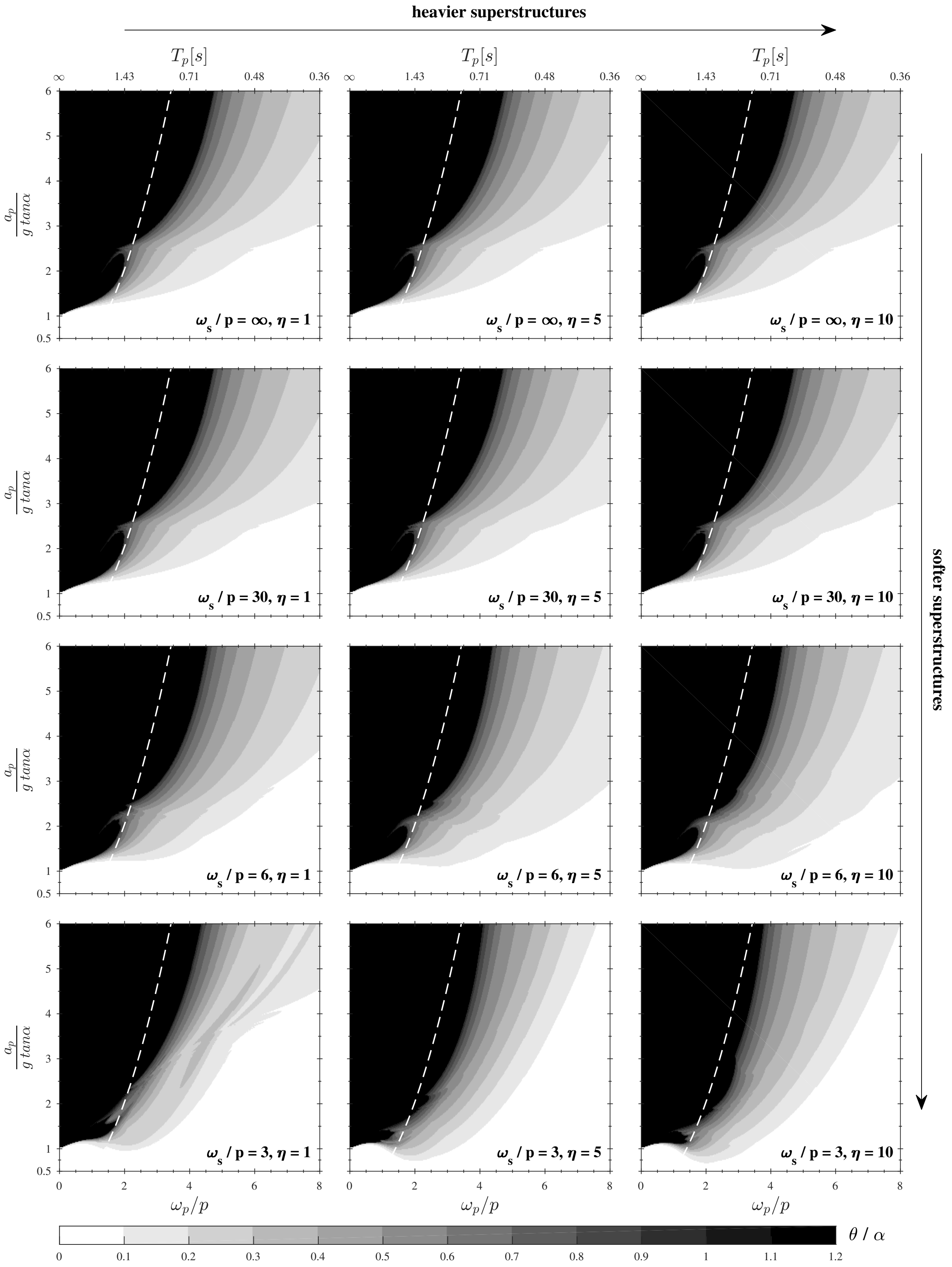

Figure 4.7: Rocking spectra (maximum base rotation, θ/α) of a rocking podium structure with $\gamma = 10$ and different values of ω_s/p (∞, 30, 6, 3) and η (1, 5, 10) subjected to a symmetric Ricker wavelet. The white dashed line indicates Polyakov's overturning acceleration.

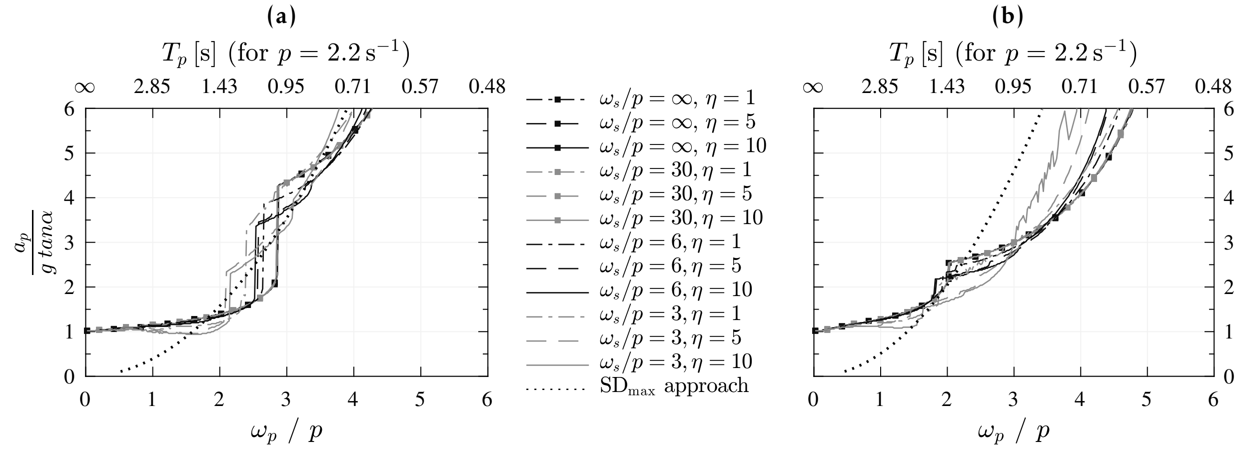

Figure 4.8: Overturning spectra for a rocking podium structures subjected to Ricker wavelets: (a) Anti-symmetric Ricker; (b) Symmetric Ricker.

4.2.5 Response to Recorded Ground Motions

Recorded ground motions might or might not contain acceleration pulses. Even in the case of pulselike ground motions, the pulse itself cannot entirely describe the overturning potential of the ground motion [79]. Therefore, the analysis presented in the previous section provides only qualitative conclusions. In order to further explore the stability of rocking podium structures and to further check the validity of the design rules of thumb proposed by Polyakov [95], the model presented is excited with recorded ground motions.

A model with a 3 m tall rocking frame that supports either a one-story ($\eta = 1$, $T_s = 0.1$ s) or a five-story ($\eta = 5$, $T_s = 0.5$ s) superstructure. In order to have different displacement capacities of the rocking columns, models with column slenderness of $\tan\alpha = 0.15$ (used for Ricker pulse analyses) as well as $\tan\alpha = 0.10$ and $\tan\alpha = 0.20$ are analyzed. According to Polyakov's design guidelines [95], a rocking column is stable as long as the maximum of ground motion elastic displacement spectrum, $\mathrm{SD}_{\max}$, is smaller than the width of the column $2B$ (*e.g.*, $2B = 0.60$ m for $\tan\alpha = 0.20$). A viscous damping ratio of 2% was used to compute the ground motion elastic displacement spectra. This should not be confused with the superstructure damping. It is the viscous damping of Polyakov's equivalent linear system that is intended to approximate the damping of the rocking story.

Tables 4.1 and 4.2 show the recorded ground motions from the Next Generation Attenuation (NGA) [134] database that were used to investigate the response of rocking podium structures for pulse-like (group A) and non-pulse-like (group B) ground motions. The records are chosen such that $\mathrm{SD}_{\max}$ values, shown in the last column of the tables, vary sufficiently to cover different displacement capacities ($2B$ either 0.30 m, 0.45 m, or 0.60 m) of the podium structure columns.

In general, the maximum spectral displacement approach proposed by Polyakov [95] leads to a conservative design. Figure 4.9 compares the maximum displacement at the top of the rocking podium columns $u_{\mathrm{B,max}}$ computed in the ground motion response history analyses using the proposed rocking podium structure model to the maximum elastic spectral displacement for each of the 21 x 6 = 126 conducted analyses, both normalized by $2B$.

Table 4.1: Pulse-like ground motions used for the seismic response analysis.

No.	Earthquake	Year	Station	NGA file	PGA [g]	$\mathrm{SD}_{\mathrm{max}}$ [m]
A1	Parkfield	1966	C #2/065	00029L	0.48	0.46
A2	San Fernando	1971	Pacoima Dam/164	00077L	1.23	1.06
A3	San Salvador	1986	Geotech Invest Center/180	00568T	0.48	0.36
A4	Whittier Narrows	1987	LB-Orange Ave/010	00645L	0.26	0.14
A5	Spitak	1988	Gukasian/000	00730L	0.20	0.31
A6	Loma Prieta	1989	Oakland, outer Harbor Wharf/000	00783L	0.29	0.33
A7	Erznican	1992	Erzincan/NS	00821L	0.52	0.94
A8	Erznican	1992	Erzincan/EW	00821T	0.50	0.85
A9	Landers	1992	Yermo Fire Station/270	00900L	0.24	1.19
A10	Landers	1992	Yermo Fire Station/360	00900T	0.15	0.70
A11	Northridge	1994	Jensen Filter Plant Gen BLDG/022	00983L	0.56	1.25
A12	Kobe	1995	Takarazu/000	01119L	0.69	0.77
A13	Kobe	1995	Takarazu/090	01119T	0.69	0.55

Table 4.2: Non-pulselike ground motions used for the seismic response analysis.

No.	Earthquake	Year	Station	NGA file	PGA [g]	$\mathrm{SD}_{\mathrm{max}}$ [m]
B1	Imperial Valley	1940	Imperial Valley/180	00006L	0.31	0.37
B2	Imperial Valley	1940	Imperial Valley/270	00006T	0.21	0.64
B3	San Fernando	1971	Pacoima Dam/254	00077T	1.16	0.36
B4	San Salvador	1986	Geotech Invest Center/090	00568L	0.87	0.46
B5	Whittier Narrows	1987	LB-Orange Ave/280	00645T	0.15	0.07
B6	Spitak	1988	Gukasian/090	00730T	0.18	0.18
B7	Loma Prieta	1989	Oakland, outer Harbor Wharf/270	00783T	0.27	0.46
B8	Northridge	1994	Jensen Filter Plant Gen BLDG/292	00983T	1.04	0.70

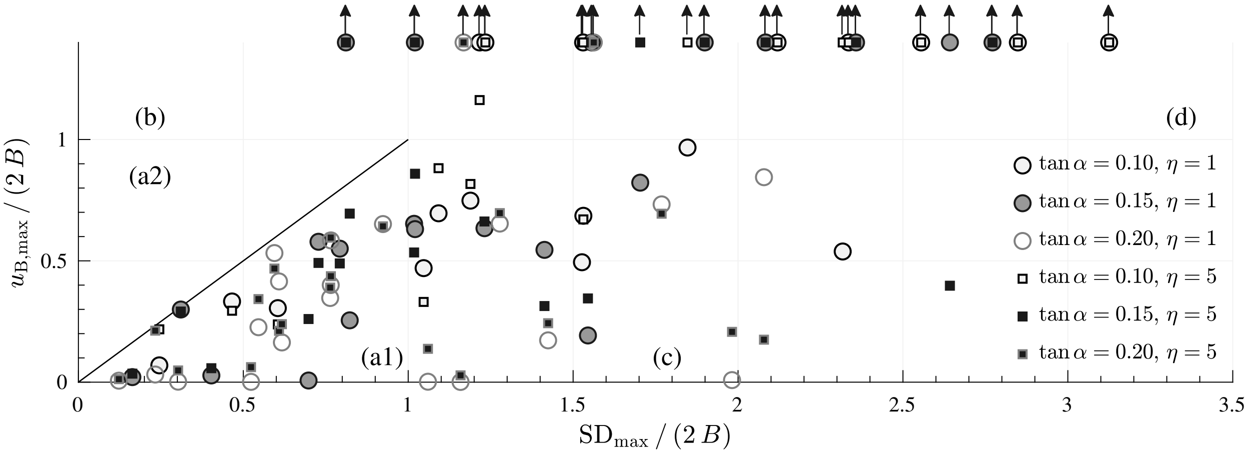

Figure 4.9: Results of earthquake ground motion response history analyses: Maximum top column displacement $u_{\mathrm{B,max}}$ vs. maximum elastic spectral displacement $\mathrm{SD}_{\mathrm{max}}$.

The plotted results are divided into four areas: (a), (b), (c), and (d). According to [95], $\mathrm{SD}_{\mathrm{max}} > 2B$ corresponds to overturning. Hence, the space where a design is even considered is represented by the areas (a) and (b). Points above the $u_{\mathrm{B,max}}/2B = 1$ line correspond to overturning according to the rocking podium model ((b) + (d)), while points right of the $\mathrm{SD}_{\mathrm{max}}/2B = 1$ line correspond to overturning according to the maximum elastic spectral displacement ((c) + (d)).

For points below the diagonal (a1), the $\mathrm{SD}_{\mathrm{max}}$ approach is conservative, while the opposite holds for points above the diagonal (a2). There are many ground motions for which the $\mathrm{SD}_{\mathrm{max}}$ approach predicts overturning while the rocking podium structure model does not (points inside (c)). However, out of 126 response history analyses, there were only two false-negative (*i.e.*, unconservative) overturning predictions (◉ at $\mathrm{SD}_{\mathrm{max}}/2B = 0.8$). The transverse-direction record of the 1986 San Salvador earthquake (No. A3) overturns both rocking podium buildings ($\eta = 1$ and $\eta = 5$) with columns with a slenderness of $\tan\alpha = 0.15$ in a RHA. However, Polyakov's $\mathrm{SD}_{\mathrm{max}}/2B = 0.36\ \mathrm{m}/0.45\ \mathrm{m} = 0.80 < 1$ criterion indicates the buildings should survive this earthquake ground motion.

In contrast to the responses to analytic pulse ground motions, the responses of the rocking podium structures to recorded ground motions are more sensitive to the column slenderness parameter. It seems that the high-frequency incoherent component of the ground motion is oftentimes able to induce column uplift and initiate the rocking motion earlier. This observation parallels the conclusion for elastic rocking structures with similar column sizes [69].

The ground motion analysis results also reveal that the $\mathrm{SD}_{\mathrm{max}}$ approach gives conservative results in a larger range of pulse frequencies than the analytical pulse analysis shows. Namely, analytical pulse analysis predicts that the $\mathrm{SD}_{\mathrm{max}}$ approach is unconservative for $\omega_p/p > 1.8$ (*i.e.*, for 3 m tall rocking podium frame columns, the approach is unconservative for pulses with pulse period $T_p < 1.6$ s, see Figure 4.8). However, the Erzincan (No. A7) and the Northridge (No. A11) pulses have frequencies on the order of 0.9 s and 0.5 s, respectively, and still, the maximum elastic spectral displacement approach is conservative. It seems that, for the ground motions used, the incoherent high-frequency component of the ground motion increased (Fig. 4.8) more than it increased the overturning potential of the ground motion.

Influence of Superstructure Period

On the basis of the rocking spectra of a rocking podium structure with 10 stories ($\eta = 10$) subjected to an antisymmetric Ricker wavelet in Figure 4.6 the influence of the superstructure period is investigated. The goal is to quantify the error that originates from the first design guideline of Polyakov to treat the superstructure as rigid. For $\eta = 10$, amplifications of the uplifted frequency should theoretically be in the order of 2.5–3.0 (Fig. 4.5), reducing the oscillation amplitudes in the superstructure considerably. Note that this quantification depends on the selected base system, here the 3 m tall column in the bottom story, as well as the number of additional stories considered.

Comparing the spectra next to each other is difficult, as they are very similar to each other. Hence, relative rocking spectra are generated, where the underlying spectrum is the rigid case ($T_s = 0$ s), and plotted in Figure 4.10.

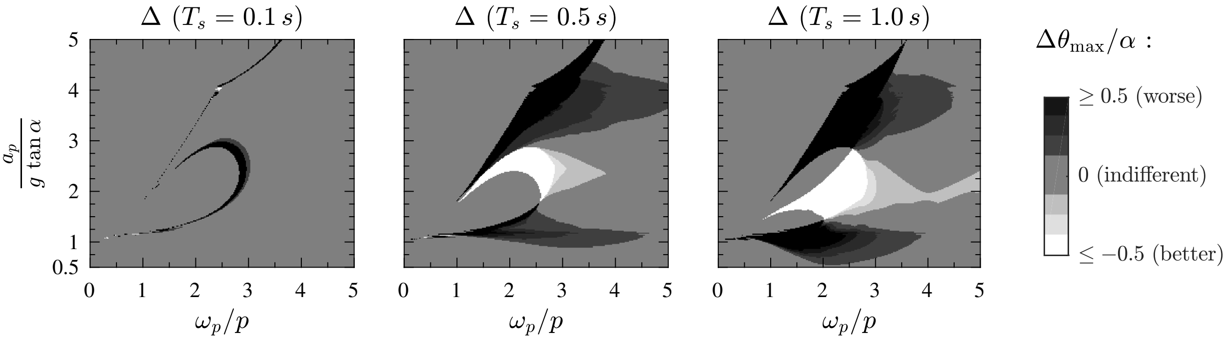

Figure 4.10: Relative rocking spectra: comparison of elastic (T_s = 0.1 s, 0.5 s, 1.0 s) superstructure vs. a rigid superstructure (T_s = 0 s).

For the case of $T_s = 0.1$ s there is almost no difference to be noticed. The spectrum for $T_s = 0.5$ s on the other hand has more colored areas and, thus, differs more from the rigid case. The minim acceleration is lowered marginally. The area of overturning with 1 impact reduced in size (brighter part in the middle of the spectrum), and in return, the overturning area without impact enlarged (darker part in the top part of the spectrum).

The most significant difference can be seen in the spectrum for $T_s = 1.0$ s. Clearly, there is an amplification in the response that leads to a significantly lower minimum overturning acceleration line when the pulse frequency ω_p is between $1\,p$ and $2\,p$ (corresponds to pulse periods T_p between 1.4 s and about 2.9 s), and between $2p$ and $4p$ the maximum tilt angle is increased at low acceleration amplitudes ($a_p \approx g\tan\alpha$). The amplification in the elastic response of the oscillator atop can lead to an early uplift of the columns in the ground level (where a totally rigid system would remain at standstill) if the superstructure period T_s is larger than 0.5 s.

4.2.6 Conclusions

Rocking podium structures comprise a superstructure anchored on top of a rigid slab supported by freestanding columns that can uplift and undergo rocking motion in response to sufficiently strong ground motion excitation. A dynamic model that describes the in-plane seismic response of such structures (Fig. 4.4) was derived and presented in this chapter. This model was used to analyze the seismic response of a wide range of rocking podium structures to analytical pulse and recorded ground motion excitations. The computed responses indicate that rocking podium structures remain stable under ground motion excitation and that the rule-of-thumb guidelines of Polyakov [95] are conservative in most of the cases examined.

The question is: “What kind of structures need to be base isolated?”. The answer is mostly that stiff structures which attract forces (in case of a seismic event the stiffness creates large inertia forces) need to be isolated. To add, in many cases their displacement capacity is lower when compared to softer structures. The case of a four story masonry structure, discussed in the introduction of this chapter, is a case example. Masonry structures are rather stiff and exhibit low ductility. Hence, they are predestined for an isolation of such kind. The equivalent seismic forces acting on the superstructure are controlled by the dimensions of the rocking podium columns.

Chapter 5

Three-Dimensional MDOF Rocking

In this chapter the simplest 3D rocking model is examined: a cylinder rocking and wobbling exclusively above the initial position of its base, without sliding or rolling out. In this sense, the investigated model is a direct extension of Housner's model, which also constrains the rocking body to restore to its original position.

Part of the material presented in this chapter has been published. The undamped model was presented in 2017 at the World Conference on Earthquake Engineering that was held in Santiago de Chile, Chile [6]. The extended damped model was published as a journal article in Earthquake Engineering & Structural Dynamics in 2017 [7].

Burger & Egger analyzed the rocking and rolling response of a rigid cylinder on a rigid base, and visualized the response in a graphical user interface (GUI) [12]. Burger extended this topic in his Master thesis to a damped model [13].

5.1 Introduction

Often the dynamic models used in the research are multiple degree-of-freedom (MDOF) models and assume unbounded 3D motion. They involve stepping or rolling rigid rocking bodies out of their initial position. This behavior results to residual deformations. Thus, these models are suitable for equipment but not for structural components designed to uplift.

In this chapter the simplest 3D rocking model is examined: a cylinder rocking and wobbling (rolling unsteadily) exclusively above the initial position of its base, without sliding or rolling out (*i.e.*, a 3D inverted pendulum). This simplified 3D bounded rocking and wobbling motion model is developed because, if rocking is to be used for seismic response modification, no residual displacement or rolling out of the body would be acceptable.

Such motion constraints could be implemented, for example, as a recess around the cylindrical column or via methods presented by Mashal *et al.* [135]. The accuracy of the model depends on how efficiently the constraints are implemented. The model investigated herein is much simpler and computationally cheaper than the MDOF models, thereby allowing for extensive parametric studies and probabilistic seismic analysis. Two versions of the model are developed and compared: one without (Section 5.2) and one with damping (Section 5.3).

5.2 Undamped Bounded Free-Standing Rigid Cylinder

The axially symmetric cylinder shown in Figure 5.1 is the extension from two- to three-dimensional motion of the rigid rocking block. The cylinder has a total mass m_{C}, a radius B and a total height $2H$. Its semi-diagonal is denoted with R and its slenderness with $\alpha = \mathrm{atan}(B/H)$. To compute the dynamic response the following assumptions are made:

a) The cylinder is considered rigid and homogeneous.

b) The contact between the cylinder and the supporting plane is point-wise (at T).

c) The cylinder is constrained not to roll out of its initial position.

d) The friction between the cylinder and the supporting plane surface is sufficiently large to prevent sliding.

e) The supporting plane surface is assumed completely rigid.

f) No damping mechanism is considered.

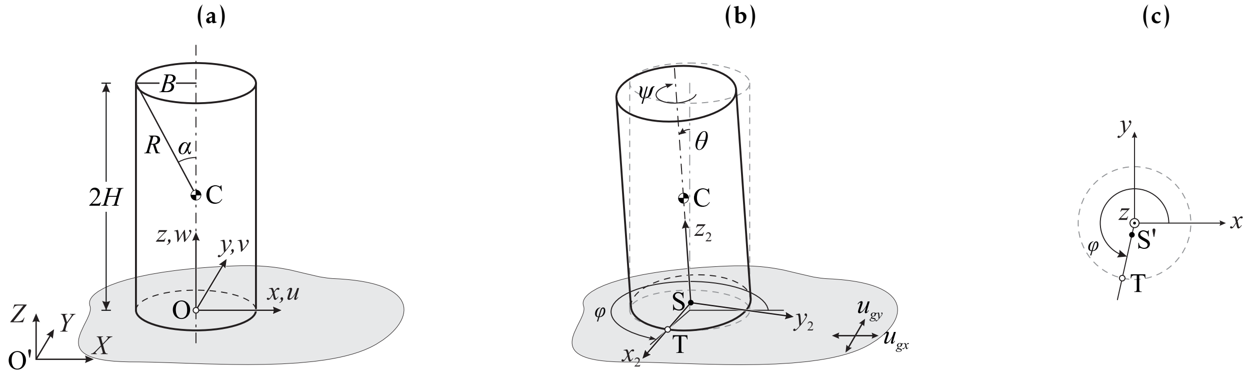

Figure 5.1: Undamped Bounded Free-Standing Rigid Cylinder: (a) Geometry; (b) DOF 1: θ, DOF 2: φ; (c) Position of T.

5.2.1 Euler Angles

The following coordinate systems are used: X,Y,Z is the inertial reference frame; x,y,z originates at the center of the bottom of the cylinder, O, and has the same orientation as X,Y,Z; $\tilde{x},\tilde{y},\tilde{z}$ originates at S and follows the rotations of the cylinder. At rest, all three coordinate systems have the same orientation, and the last two coincide. To describe the position of the cylinder when moving the so called 3-2-3 Euler angles are used:

> The Euler angles are three angles introduced by Leonhard Euler to describe the orientation of a rigid body with respect to a fixed coordinate system. [136]

Here, these three angles are φ, θ, and ψ; and the fixed coordinate system is X,Y,Z. The first angle, φ, is equal to the rolling angle and describes the first of three Euler transformations: a rotation around the axis z. This leads to a new coordinate system x_1,y_1,z_1. The second angle, θ, is equal to the cylinder tilt angle and describes the second Euler transformation: a rotation around the axis y_1. This leads to the new coordinate system x_2,y_2,z_2. The third angle, ψ, describes the third Euler transformation: a rotation around the axis z_2. This leads to the new coordinate system x_3, y_3, z_3. Since it is assumed that the friction between the cylinder and the foundation is large enough to prevent sliding, it can be proven that $\psi = -\varphi$, leaving only two angles necessary to describe the cylinder's position.

5.2.2 Degrees of Freedom

Given the aforementioned assumptions, the model of the undamped bounded free-standing rigid cylinder has two active degrees of freedom, as listed in Table 5.1.

Table 5.1: Undamped bounded free-standing rigid cylinder: degrees of freedom.

DOF	Name	Variable	Definition
1	Tilt angle	θ	It defines the amount the cylinder has tilted when compared to the initial position. It ranges from 0 to $\pi/2$.
2	Rolling angle	φ	It determines the location of the contact point between the cylinder and the supporting plane (Point T), and ranges from 0 to 2π ($\varphi = \pi$ will yield the same location of the contact point T as $\varphi = 3\pi$ or $\varphi = -\pi$ would).

5.2.3 Reference Frame

In order to derive the equations of motion of the cylinder, the translational and rotational motion of the center of mass of the cylinder should be tracked, relative to the inertial reference frame X, Y, Z. Referring to Figure 5.1, the position vector of the center of mass, C, is:

$$\boldsymbol{r}_{\mathrm{O'C}} = \boldsymbol{r}_{\mathrm{O'O}} + \boldsymbol{r}_{\mathrm{OS}} + \boldsymbol{r}_{\mathrm{SC}} . \tag{5.1}$$

The components of the position vector are:

$$\boldsymbol{r}_{\mathrm{O'O}} = u_{gx} \cdot \mathbf{i}_X + u_{gy} \cdot \mathbf{i}_Y + 0 \cdot \mathbf{i}_Z , \tag{5.2}$$

$$\boldsymbol{r}_{\mathrm{OS}} = d_x \cdot \mathbf{i}_x + d_y \cdot \mathbf{i}_y + d_z \cdot \mathbf{i}_z , \tag{5.3}$$

$$\boldsymbol{r}_{\mathrm{SC}} = 0 \cdot \mathbf{i}_{x,3} + 0 \cdot \mathbf{i}_{y,3} + H \cdot \mathbf{i}_{z,3} , \tag{5.4}$$

where $\mathbf{i}$ are the unit vectors of each coordinate system, and u_{gx} and u_{gy} are the two horizontal components of the earthquake ground motion excitation. The unit vectors are related through the following transformations:

$$\begin{bmatrix} \mathbf{i}_X \\ \mathbf{i}_Y \\ \mathbf{i}_Z \end{bmatrix} = \mathbf{I} \cdot \begin{bmatrix} \mathbf{i}_x \\ \mathbf{i}_y \\ \mathbf{i}_z \end{bmatrix} \quad \text{and} \quad \begin{bmatrix} \mathbf{i}_x \\ \mathbf{i}_y \\ \mathbf{i}_z \end{bmatrix} = \boldsymbol{A}_1 \cdot \boldsymbol{A}_2 \cdot \boldsymbol{A}_3 \cdot \begin{bmatrix} \mathbf{i}_{x,3} \\ \mathbf{i}_{y,3} \\ \mathbf{i}_{z,3} \end{bmatrix} , \tag{5.5}$$

where $\mathbf{I}$ is the unit matrix and $\boldsymbol{A}_1$, $\boldsymbol{A}_2$ and $\boldsymbol{A}_3$ are the rotation matrices that correspond to the Euler angles:

$$\boldsymbol{A}_1 = \begin{bmatrix} \cos\varphi & -\sin\varphi & 0 \\ \sin\varphi & \cos\varphi & 0 \\ 0 & 0 & 1 \end{bmatrix} , \quad \boldsymbol{A}_2 = \begin{bmatrix} \cos\theta & 0 & \sin\theta \\ 0 & 1 & 0 \\ -\sin\theta & 0 & \cos\theta \end{bmatrix} , \quad \boldsymbol{A}_3 = \begin{bmatrix} \cos\varphi & \sin\varphi & 0 \\ -\sin\varphi & \cos\varphi & 0 \\ 0 & 0 & 1 \end{bmatrix} . \tag{5.6}$$

With reference to Equations (5.5) and (5.6), vector $\boldsymbol{r}_{BS}$ can be written in X, Y, Z coordinates as:

$$\boldsymbol{r}_{\mathrm{SC}} = H\cos\varphi\sin\theta\cdot\mathbf{i}_X + H\sin\varphi\sin\theta\cdot\mathbf{i}_Y + H\cos\theta\cdot\mathbf{i}_Z, \tag{5.7}$$

or, in vector coordinates:

$$\boldsymbol{r}_{\mathrm{SC}} = H\cdot\begin{bmatrix}\cos\varphi\sin\theta\\ \sin\varphi\sin\theta\\ \cos\theta\end{bmatrix}. \tag{5.8}$$

With reference to Equation (5.3) and Figure 5.1, d_x, d_y and d_z are:

$$d_x = B\cos\varphi\cdot\left(1-\cos\theta\right), \qquad d_y = B\sin\varphi\cdot\left(1-\cos\theta\right), \qquad d_z = B\cdot\sin\theta, \tag{5.9}$$

and $\boldsymbol{r}_{\mathrm{OS}}$ becomes:

$$\boldsymbol{r}_{\mathrm{OS}} = B\cdot\begin{bmatrix}\cos\varphi\cdot\left(1-\cos\theta\right)\\ \sin\varphi\cdot\left(1-\cos\theta\right)\\ \sin\theta\end{bmatrix}. \tag{5.10}$$

Therefore, Equation (5.1) can be written in X, Y, Z coordinates as:

$$\boldsymbol{r}_{\mathrm{O'C}} = \begin{bmatrix}u_{gx}\\ u_{gy}\\ 0\end{bmatrix} + B\cdot\begin{bmatrix}\cos\varphi\cdot(1-\cos\theta)\\ \sin\varphi\cdot(1-\cos\theta)\\ \sin\theta\end{bmatrix} + H\cdot\begin{bmatrix}\cos\varphi\sin\theta\\ \sin\varphi\sin\theta\\ \cos\theta\end{bmatrix}. \tag{5.11}$$

5.2.4 Equations of Motion

To derive the equations of motion via the Lagrangian method described in Appendix A.2 the kinetic energy T and the potential energy V need to be computed. The kinetic energy T of the rigid cylinder in Figure 5.1a is equal to the sum of the translational kinetic energy and the rotational kinetic energy. The translational kinetic energy T_{trans} is associated with the absolute velocity of the center of the mass, and is:

$$T_{trans} = \frac{1}{2}m_{\mathrm{C}}\cdot\dot{\boldsymbol{r}}_{\mathrm{O'C}}^{\mathrm{T}}\cdot\dot{\boldsymbol{r}}_{\mathrm{O'C}}. \tag{5.12}$$

The rotational kinetic energy T_{rot} is associated with the rotational velocity of the cylinder and can be calculated by

$$T_{rot} = \frac{1}{2}\boldsymbol{\omega}^{\mathrm{T}}\cdot\mathbf{I}\cdot\boldsymbol{\omega}, \tag{5.13}$$

where $\mathbf{I}$ is the moment of inertia tensor of the cylinder about its principle axes going through the center of the mass C. $\mathbf{I}$ is given by $\mathbf{I} = \mathrm{diag}(I_x, I_y, I_z)$ where I_x, I_y and I_z are calculated with respect to the x_3, y_3, z_3 coordinate system:

$$I_x = I_y = \frac{3B^2+4H^2}{12}\cdot m_{\mathrm{C}} = I_1, \tag{5.14}$$

$$I_z = \frac{B^2}{2}\cdot m_{\mathrm{C}} = I_2. \tag{5.15}$$

Due to the rotational symmetry of the cylinder I_x and I_y are identical. The angular velocity of the cylinder is given by the three Eulerian angle rotations mentioned in Section 5.2.1. Thus, the angular velocity is the sum of three rotations and can be written as

$$\boldsymbol{\omega} = \dot{\varphi} \cdot \mathbf{i}_{z,1} + \dot{\theta} \cdot \mathbf{i}_{y,2} - \dot{\varphi} \cdot \mathbf{i}_{z,3}\,. \tag{5.16}$$

With Equation (5.5) and (5.6) the angular velocity can be expressed with respect to X, Y, Z:

$$\boldsymbol{\omega} = \dot{\theta} \cdot \begin{bmatrix} -\sin\varphi \\ \cos\varphi \\ 0 \end{bmatrix} - \dot{\varphi} \cdot \begin{bmatrix} \cos\varphi \sin\theta \\ \sin\varphi \sin\theta \\ \cos\theta - 1 \end{bmatrix}. \tag{5.17}$$

Applying the Lagrange equations to the rigid cylinder (Fig. 5.1) yields:

$$\begin{aligned} &\ddot{\theta} \cdot \left(I_1^* + H^2 + B^2\right) + \dot{\varphi}^2 \sin\theta \cos\theta \cdot \left(I_2 - I_1 + B^2 - H^2\right) - \dot{\varphi}^2 \sin\theta \cdot \left(I_2 + B^2\right) \\ &\quad + \dot{\varphi}^2 BH \cdot \left(\cos^2\theta - \sin^2\theta - \cos\theta\right) \\ &\quad = -g \cdot \left(B\cos\theta - H\sin\theta\right) - \ddot{u}_{gx} \cos\varphi \cdot \left(B\sin\theta + H\cos\theta\right) - \ddot{u}_{gy} \sin\varphi \cdot \left(H\cos\theta + B\sin\theta\right) \end{aligned} \tag{5.18}$$

$$\begin{aligned} &\ddot{\varphi} \cdot \left(\left(I_1^* + I_2^* + B^2 + H^2\right) \cdot \sin^2\theta - 2\cos\theta \cdot \left(I_2^* + B^2\right) \cdot \left(1 - \cos\theta\right)\right) + 2\ddot{\varphi} BH \sin\theta \cdot \left(1 - \cos\theta\right) \\ &\quad + 2\dot{\varphi}\dot{\theta} \sin\theta \cdot \left(I_2^* + B^2 + \left(I_1^* - I_2^* - B^2 + H^2\right) \cdot \cos\theta + BH\sin\theta\right) \\ &\quad + 2\dot{\varphi}\dot{\theta} BH \cos\theta \cdot \left(1 - \cos\theta\right) \\ &\quad = \left(B \cdot \left(1 - \cos\theta\right) + H\sin\theta\right) \cdot \left(\ddot{u}_{gx} \sin\varphi - \ddot{u}_{gy} \cos\varphi\right) \end{aligned} \tag{5.19}$$

where, using $R = \sqrt{H^2 + B^2}$ and $\tan\alpha = B/H$,

$$I_1^* = \frac{I_1}{m_C} = \frac{3B^2 + 4H^2}{12} = \frac{R^2\left(3 + \cos^2\alpha\right)}{12}, \tag{5.20}$$

$$I_2^* = \frac{I_2}{m_C} = \frac{B^2}{2} = \frac{R^2 \sin^2\alpha}{2}. \tag{5.21}$$

Using the above expression, Equations (5.18) and (5.19) respectively rewrite to:

$$\begin{aligned} &\ddot{\theta} R \frac{15 + \cos^2\alpha}{12} + \dot{\varphi}^2 R \sin\theta \cos\theta \cdot \left(\frac{5}{4}\sin^2\alpha - \frac{4}{3}\cos^2\alpha\right) - \frac{3}{2}\dot{\varphi}^2 R \sin\theta \sin^2\alpha \\ &\quad + \dot{\varphi}^2 R \cos\alpha \sin\alpha \cdot \left(\cos^2\theta - \sin^2\theta - \cos\theta\right) \\ &\quad = -g\sin(\alpha - \theta) - \cos(\alpha - \theta) \cdot \left(\ddot{u}_{gx} \cos\varphi + \ddot{u}_{gy} \sin\varphi\right) \end{aligned} \tag{5.22}$$

$$\begin{aligned} &\ddot{\varphi} R \cdot \left(\frac{4 + \sin^2\alpha}{3} \sin^2\theta + \left(1 - \cos\theta\right) \cdot \left(\sin 2\alpha \sin\theta - 3\sin^2\alpha \cos\theta\right)\right) \\ &\quad + \dot{\varphi}\dot{\theta} R \sin 2\alpha \cdot \left(\cos\theta \cdot \left(1 - \cos\theta\right) + \sin^2\theta\right) \\ &\quad + \dot{\varphi}\dot{\theta} R \sin\theta \cdot \left(3\sin^2\alpha + \left(\frac{8}{3}\cos^2\alpha - \frac{5}{2}\sin^2\alpha\right) \cdot \cos\theta\right) \\ &\quad = \left(\sin\alpha - \sin(\alpha - \theta)\right) \cdot \left(\ddot{u}_{gx} \sin\varphi - \ddot{u}_{gy} \cos\varphi\right) \end{aligned} \tag{5.23}$$

5.2.5 Uplift Condition

Uplift occurs when the total ground acceleration $\ddot{u}_g^{\varphi}$ with the direction φ exceeds the value $g\tan\alpha$:

$$\ddot{u}_g^{\varphi} = \sqrt{\ddot{u}_{gx}^2 + \ddot{u}_{gy}^2} \geq g\,\tan\alpha\ . \tag{5.24}$$

The direction of uplift is along the D'Alembert inertia force vector at the instant of uplift, and is given by the angle φ_0:

$$\varphi_0 = \arccos\left(\frac{-\ddot{u}_{gx}}{\sqrt{\ddot{u}_{gx}^2 + \ddot{u}_{gy}^2}}\right). \tag{5.25}$$

5.2.6 Impact Treatment

Unlike the equations used to describe the 2D rocking problem (which are non-smooth as they have to treat impact) the equations presented herein are smooth: the tilt angle θ is always positive, and the change of contact point is a continuous function of the rolling angle φ. There is no instantaneous impact and, therefore, no need to treat impact like the 2D case, but the numerical results presented in the following sections show that a very rapid (but continuous) change of the pivot point may occur.

However, by setting $\ddot{\varphi} = \dot{\varphi} = 0$ and $\ddot{u}_{gx} = \ddot{u}_{gy} = 0$ in Equation (5.18) the response of the cylinder is planar, and therefore non-smooth, and one recovers the equation of the planar free vibration rocking motion of a cylinder:

$$\ddot{\theta}\,I_0 + g\,m_C\,R\cdot\sin(\alpha-\theta) = 0\,, \tag{5.26}$$

where I_0 is the moment of inertia of the cylinder around a point on the circumference of its base. Analogously to the 2D case can the frequency parameter p be determined:

$$p^2 = \frac{g\,m_C\,R}{I_0} = \frac{12}{15+\cos^2\alpha}\,\frac{g}{R}\,. \tag{5.27}$$

Note that the equations of motion (Eqs. 5.22 and 5.23) derived in this section can only be numerically applied to the 3D problem when one can be sure that a 3D rocking and wobbling motion is initiated and no non-smooth impact will occur: this is achieved via a non-zero initial spin, $\dot{\varphi}_0$, in the case of free vibration, and via applying a two-horizontal-component ground excitation in the case of an earthquake excitation. Such initiation resembles numerical analysis of buckling using a second-order geometry method, where one needs to apply an initial imperfection in order to observe buckling.

5.2.7 Wobbling Period

Using Equation (5.22) without the ground motion excitation, and assuming a constant cylinder tilt angle $\theta > 0$ ($\ddot{\theta} = \dot{\theta} = 0$), one obtains the angular velocity $\dot{\varphi}_0$ of the cylinder and the corresponding wobbling period as a function of the title angle θ:

$$\dot{\varphi}_0 = \frac{T_w}{2\pi}\,, \tag{5.28}$$

where

$$T_{\mathrm{w}} = \frac{2\pi}{p}\sqrt{-\frac{\begin{pmatrix}\sin\theta\cos\theta\cdot\left(\frac{5}{4}\sin^2\alpha-\frac{4}{3}\cos^2\alpha\right)-\frac{3}{2}\sin\theta\sin^2\alpha\\ +\cos\alpha\,\sin\alpha\cdot\left(\cos^2\theta-\sin^2\theta-\cos\theta\right)\end{pmatrix}}{\sin\left(\alpha-\theta\right)\cdot\frac{15+\cos^2\alpha}{12}}}. \tag{5.29}$$

Figure 5.2 plots the cylinder wobbling period, T_{w}, normalized with respect to the cylinder frequency parameter p (Eq. 5.27) against the normalized tilt angle of the cylinder for different values of cylinder slenderness $\tan\alpha$. The Euler's Disk case is represented by $\tan\alpha = 1\,000$. The normalized period of a 2D rocking block, as derived by Housner [16], is also depicted. The analogy between 2D rocking and 3D bounded wobbling is evident. Note that Housner's derivation is linearized and holds only for small values of the slenderness angle α (then it is also independent of the exact value of α).

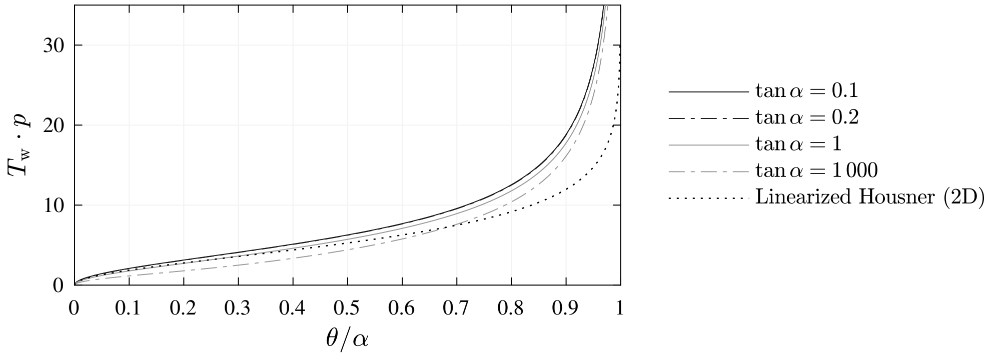

Figure 5.2: Wobbling period: tilt angle relation for rocking and wobbling cylinders of different slenderness.

5.3 Damped Bounded Free-Standing Rigid Cylinder

For MDOF systems the damping matrix is often assumed to be mass and stiffness proportional, to facilitate uncoupled modal response analysis. This approach emerged from the necessity to model the decay of motion without having to solve systems of nonlinear ODEs, which is oftentimes impossible to do analytically.

Nowadays, the increase of computational power allows for solving numerically the equations of motion and, therefore, for using different energy dissipation models that might better describe the nature of the diminishing response of a moving structure. On the other hand, the use of Rayleigh damping to describe energy dissipation in rocking structures (2D or 3D) has been shown to be inadequate to describe the decay of the response and difficult to calibrate ([137] and references therein). Therefore, Rayleigh damping is avoided, and a different method, based on [137], is suggested hereafter.

If it is the variation of the contact force that causes energy to be dissipated from the rocking and wobbling rigid cylinder, it is reasonable to model this content using a linear spring in parallel with a linear viscous damper at the contact point (Fig. 5.3b). The viscous damper dissipates energy only

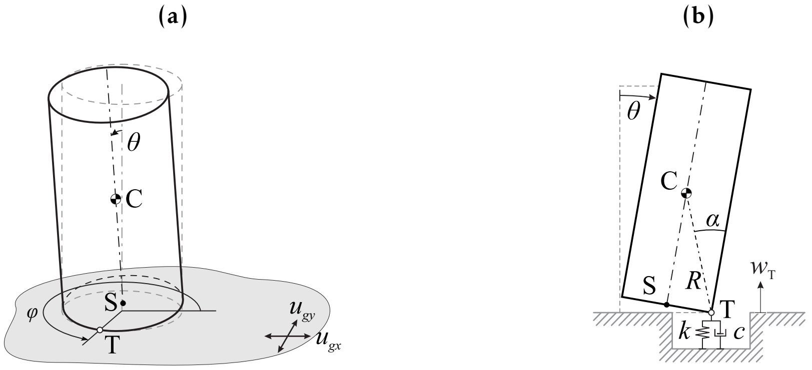

Figure 5.3: Degrees of freedom of damped bounded free-standing rigid cylinder: (a) DOF 1: θ, DOF 2: φ: (b) DOF 3: w_T.

when the contact point moves up and down and dissipates more energy when the point moves faster. This model is not to be confused with Winkler springs [138]: the contact is pointwise, and the spring and the dashpot are associated with the contact point, not distributed across the support surface. Note that the spring and the dashpot are not used to describe the compressibility of the ground but are merely utilized to dissipate energy during the rolling and wobbling motion of the rigid cylinder on a rigid surface.

5.3.1 Degrees of Freedom

To account for energy dissipation, a damping mechanism is added to the existing model. As shown in Figure 5.3b, a spring and dashpot system is introduced underneath T. Both the spring and the dashpot are fixed to the rigid support surface below. However, since the contact point T is moving with changing rolling angle φ inside the X-Y-plane, the influence is restricted to vertical movement (Z-axis only). The spring stiffness is denoted with k and the damping coefficient is introduced as c.

By introducing a spring and dashpot system, a third degree of freedom is added to the system: the vertical deformation w_T of the point T. Position $w_T = 0$ corresponds to a static equilibrium position of a titled cylinder, where the deformation of the contact point spring under the cylinder self-weight is equal to $w_{st} = (m_C g)/k$.

5.3.2 Properties of Spring and Dashpot

The implemented mechanism can be described with the spring stiffness k and the dashpot coefficient c. Assuming $\ddot{\theta} = \dot{\theta} = 0$, the cylinder with mass m_C undergoes a vertical damped harmonic oscillation whose equation of motion is given by:

$$\ddot{w}_T + 2\,\zeta\,\omega_n\,\dot{w}_T + \omega_n^2\,w_T = 0\,, \tag{5.30}$$

$$\omega_n = \sqrt{\frac{k}{m_C}}\,, \quad \text{and} \quad \zeta = \frac{c}{2\,m_C\,\omega_n} = \frac{c}{c_{cr}}\,, \tag{5.31}$$

where ω_n is the natural oscillation frequency of the undamped system and ζ is the damping ratio. By changing the value of the parameter ζ in Equation (5.31) one is able to regulate the damping behavior, as listed in Table 5.2.

Table 5.2: Damped harmonic oscillator behavior for different damping ratios ζ.

Damping ratio	System behavior
$\zeta > 1$: overdamped	The system returns to steady state without oscillating. Larger values of ζ lead to a slower return to equilibrium.
$\zeta = 1$: critically damped	The system returns to steady state as quickly as possible without oscillating (although overshoot can occur).
$\zeta < 1$: underdamped	The system oscillates with a slightly lower frequency $\tilde{\omega}_n = \omega_n \sqrt{1-\zeta^2}$ than the undamped case with the amplitude gradually decreasing to zero.

Note that ω_n and ζ are not independent parameters from each other. Nevertheless, this notation is commonly used and will hereafter be referred to as the *damping parameters*. In order to study the influence of these parameters on the overall damping behavior of a cylinder, the loss of energy per cycle needs to be quantified. Unlike in 2D case where the energy decrease manifests itself at impact (via the coefficient of restitution c_r and the loss of kinetic energy) there is no such straightforward way to compute the energy loss in the 3D case. Therefore, damping in the 3D case is investigated via a parameter study, discussed in more detail in Section 5.4.4.

Initially, the parameters are set to the following values:

$$\omega_n = 200\,\mathrm{rad/s}, \quad \text{and} \quad \zeta = 0.5. \tag{5.32}$$

5.3.3 Equations of Motion

Referring to Equation (5.11), the position vector of the center of mass, C, for the damped system is updated to:

$$\boldsymbol{r}_{\mathrm{O'C}} = \begin{bmatrix} u_{gx} \\ u_{gy} \\ 0 \end{bmatrix} + b \cdot \begin{bmatrix} \cos\varphi \cdot (1-\cos\theta) \\ \sin\varphi \cdot (1-\cos\theta) \\ \sin\theta \end{bmatrix} + H \cdot \begin{bmatrix} \cos\varphi \sin\theta \\ \sin\varphi \sin\theta \\ \cos\theta \end{bmatrix} + \begin{bmatrix} 0 \\ 0 \\ w_{\mathrm{T}} \end{bmatrix}. \tag{5.33}$$

The Lagrange equation of motion for the third degree of freedom is

$$\frac{\mathrm{d}}{\mathrm{d}t}\left(\frac{\partial L}{\partial \dot{w}_{\mathrm{T}}}\right) - \frac{\partial L}{\partial w_{\mathrm{T}}} + \frac{\partial D}{\partial \dot{w}_{\mathrm{T}}} = 0. \tag{5.34}$$

Note that the dissipated energy D is related to the vertical velocity $\dot{w}_{\mathrm{T}}$ and can be written as:

$$D = \frac{1}{2} c \cdot \dot{w}_{\mathrm{T}}^2, \tag{5.35}$$

which is known as Rayleigh's dissipation function [139]. The equation of motion for the rolling angle, φ, given by Equation (5.23), remains unchanged when damping is introduced. However, the equation of motion for the tilt angle, θ, given by Equation (5.22), is now:

$$\begin{aligned} &\ddot{\theta} R \frac{15+\cos^2\alpha}{12} + \dot{\varphi}^2 R \cos\alpha \sin\alpha \cdot \left(\cos^2\theta - \sin^2\theta - \cos\theta\right) \\ &\quad + \dot{\varphi}^2 R \sin\theta \cos\theta \cdot \left(\frac{5}{4}\sin^2\alpha - \frac{4}{3}\cos^2\alpha\right) - \frac{3}{2}\dot{\varphi}^2 R \sin\theta \sin^2\alpha \\ &\quad = -(g + \ddot{w}_{\mathrm{T}}) \cdot \sin(\alpha-\theta) - \cos(\alpha-\theta) \cdot \left(\ddot{u}_{gx}\cos\varphi + \ddot{u}_{gy}\sin\varphi\right). \end{aligned} \tag{5.36}$$

The equation of motion for the third degree of freedom, w_{T}, is given by

$$\ddot{w}_{\mathrm{T}} + 2\,\zeta\,\omega_n\,\dot{w}_{\mathrm{T}} + \omega_n^2\,w_{\mathrm{T}} = \dot{\theta}^2\,R\cos(\alpha-\theta) - \ddot{\theta}\,R\sin(\alpha-\theta)\,. \tag{5.37}$$

5.4 Free Vibration Response

The aforementioned equations are implemented in Matlab following the procedure described in Appendix B, and solved numerically. Then, the free rocking and wobbling responses of undamped and damped ($2H = 3$ m and $\tan\alpha = 0.2$) rigid cylinders from three initial conditions (θ_0 [rad], $\dot{\theta}_0$ [rad/s], ϕ_0 [rad], $\dot{\phi}_0$ [rad/s]) are computed and compared against each other. Three characteristic response motions of a rigid cylinder can be identified:

1. Quasi-Rocking
2. Pure Wobbling
3. Combined Free-Rocking and Wobbling

5.4.1 Quasi-Rocking

For a very small initial spin (Fig. 5.4), the cylinder changes its pivot point rapidly (but smoothly, as the solution is continuous). This is the quasi-rocking response mode. The term 'quasi' is used because this numerical test confirms the experimentally observed [42,56] and theoretically proven result [84] that the planar motion of a cylinder is unstable: an initial angle of turn as low as $\dot{\varphi} = 10^{-8}$ rad/s induces a clear out-of-plane motion. Therefore, the change of pivot point is defined by an angle of turn, slightly smaller than π, which compares well with the prediction of [85]. Indeed, [85] gives an angle of turn equal to

$$\Delta\varphi = \pi\sqrt{\frac{I_1^* + R^2\cos^2\alpha}{I_1^* + R^2}} = \pi\sqrt{\frac{3 + 13\cos^2\alpha}{15 + \cos^2\alpha}} = 3.095\,, \tag{5.38}$$

while the numerical calculations give a slightly lower value: at every impact the spin angle φ is instantaneously increased by $\Delta\varphi = 3.058$ (Fig. 5.4a, undamped case).

The abrupt change of the pivot point generates large vertical forces at the contact point (in the limit case, they become infinite and the spinning motion tends to an impact). Clearly, damping exists. Therefore, this quasi-impact mechanism is one source of damping of the rocking and wobbling motion of a rigid cylinder. Unless there is a fracture of the surfaces in contact, energy dissipation is mainly due to radiation damping [140]. As Figures 5.4a and 5.4b show, the contact force appears as a spike, quasi-impact, at every rapid change of the contact point. During the change of pivot point, a jump in the tilt velocity, $\dot{\theta}$, is observed. This is not a discontinuity (since the equations are smooth) but rather a rapid change of φ. This rapid but continuous change of pivot point does not appear in the 2D problem because unlike in the 3D model is θ not always positive but changes sign with changing pivot points. The closer the motion to pure rocking is, the larger become the spikes. In the limit case of instantaneous impact (Housner's assumption for the 2D rocking problem), the impact force becomes a Dirac function. The variation of the contact force generates

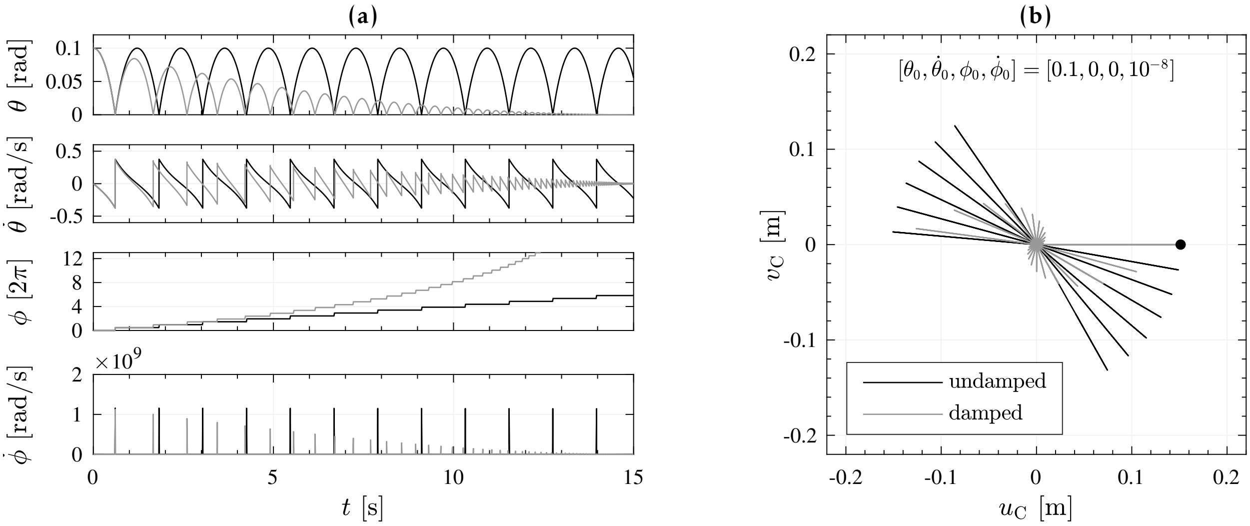

Figure 5.4: Free vibration response comparison for different initial conditions for a undamped and damped ($\omega_n = 200$ rad/s, $\zeta = 0.5$) cylinder of size $2H = 3$ m and slenderness $\tan\alpha = 0.2$.

intense vibrations in the support (be it an infinite half-space or a real-world support) that lead to the gradual decay of motion.

5.4.2 Pure Wobbling

For every cylinder geometry and each tilt angle, there exists a unique initial spin velocity $\dot{\varphi}_0$ that can generate the response during which the tilt angle stays constant and the cylinder wobbles without rocking. This is the pure wobbling response mode. Figure 5.5 plots the response of a rigid cylinder for an initial spin defined through Equations (5.29) and (5.28):

$$T_{\text{wobb}} = 2.88 \text{ s}, \tag{5.39}$$

$$\dot{\varphi}_0 = 2.18 \text{ rad/s}. \tag{5.40}$$

Note the constant spin velocity $\dot{\varphi}$ in Figure 5.5a, compared with the infinite peaks in the quasi-rocking response mode. It is also worth noting that since the tilt angle stays constant, the tilt

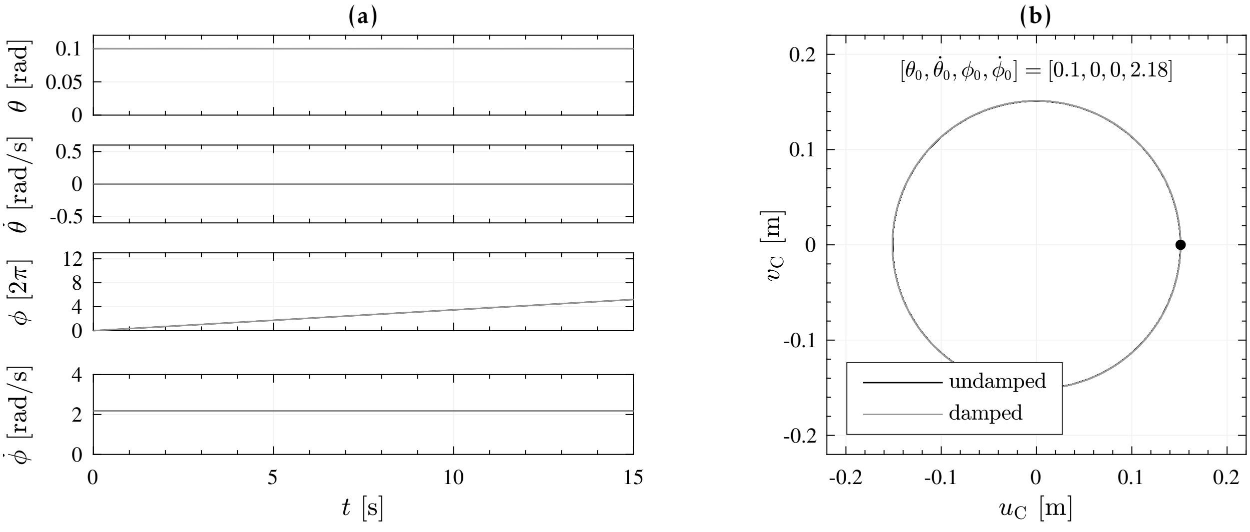

Figure 5.5: Free vibration response comparison for different initial conditions for a undamped and damped ($\omega_n = 200$ rad/s, $\zeta = 0.5$) cylinder of size $2H = 3$ m and slenderness $\tan\alpha = 0.2$.

acceleration, $\ddot{\theta}$, is zero, and hence, the vertical force at the contact point is constant and equal to the weight of the cylinder.

The energy dissipated by a rigid cylinder undergoing a pure wobbling motion on a rigid surface is very small. A spinning coin or the Euler's Disk offers empirical proofs of this statement. There is an open debate on whether this energy dissipation originates from air viscosity [141] or friction [142], but there is a consensus that the amount of dissipated energy is small compared with the kinetic and potential energy quantities in the dynamic system.

5.4.3 Combined Free-Rocking and Wobbling

Figure 5.6 plots the response of a rigid cylinder due to a combination of the two pure response modes previously discussed. Even though the two pure response modes interact, the tilt angle never comes close to zero. The change of pivot point is too slow for any energy to be dissipated.

Note that the term 'modes' does not refer to modes of vibration resulting from modal analysis but rather identifies distinct types of rigid cylinder response.

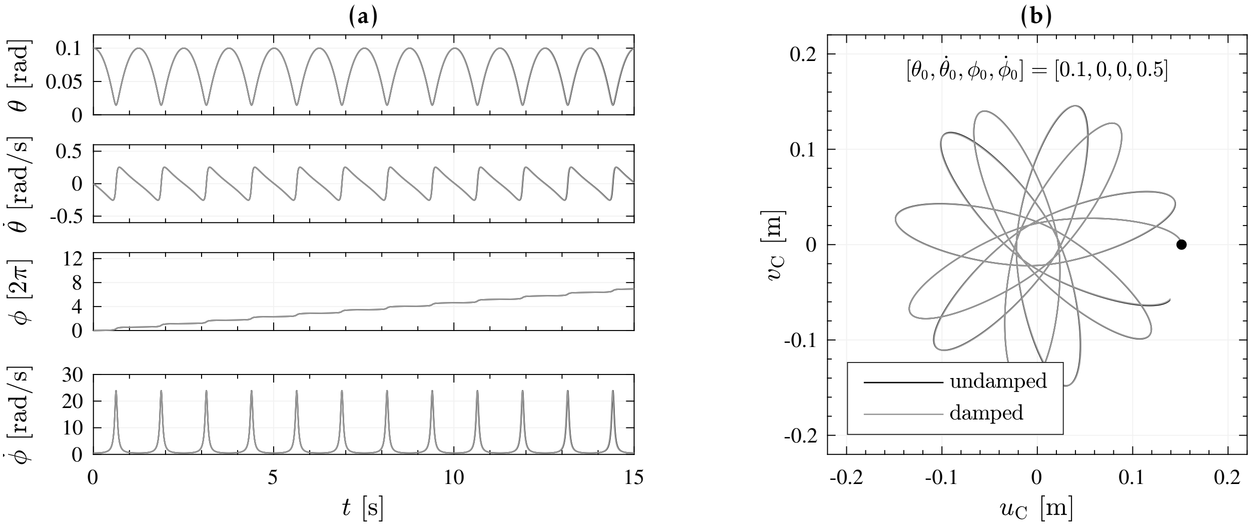

Figure 5.6: Free vibration response comparison for different initial conditions for a undamped and damped ($\omega_n = 200$ rad/s, $\zeta = 0.5$) cylinder of size $2H = 3$ m and slenderness $\tan\alpha = 0.2$.

5.4.4 Numerical Damping

The free rocking and wobbling responses of differently damped ($2H = 3$ m and $\tan\alpha = 0.2$) rigid cylinders for the quasi-rocking case ($\theta_0 = 0.1$ rad, $\dot{\theta}_0 = 0$ rad/s, $\phi_0 = 0$ rad, $\dot{\phi}_0 = 1\mathrm{e}-08$ rad/s). The two sets of parameters listed in Table 5.3 are chosen to examine the effect of the damping

Table 5.3: Sets of parameters chosen to examine the effect of the numerical damping.

Set	ND-1	ND-2
Parameters	$\omega_n = 200$ rad/s, $\zeta = \{0.05,\ 0.5,\ 5\}$	$\omega_n = \{20,\ 200,\ 2000\}$ rad/s, $\zeta = 0.5$

parameters. The first set, ND-1, investigates the effect that different damping ratios ζ have on the response. The set ND-2 examines varying damping damping frequencies ω_n.

Figure 5.7 plots the quasi-rocking responses of the oscillator for the subset ND-1. The plots overlap, indicating that the proposed 3D bounded rocking and wobbling motion model is not sensitive to the values of the damping ratio of the contact point spring and dashpot system for as long as the spring is stiff enough to represent a rigid support. In this case $\omega_n = 200\,\text{rad/s}$ is stiff enough.

The quasi-rocking responses of the oscillator for the subset ND-2 are shown in Figure 5.8. What happens if the support becomes softer can be seen in Figure 5.8 for the case $\omega_n = 20\,\text{rad/s}$: there is a slight delay in the response as the transition from one pivot point to the other takes more time.

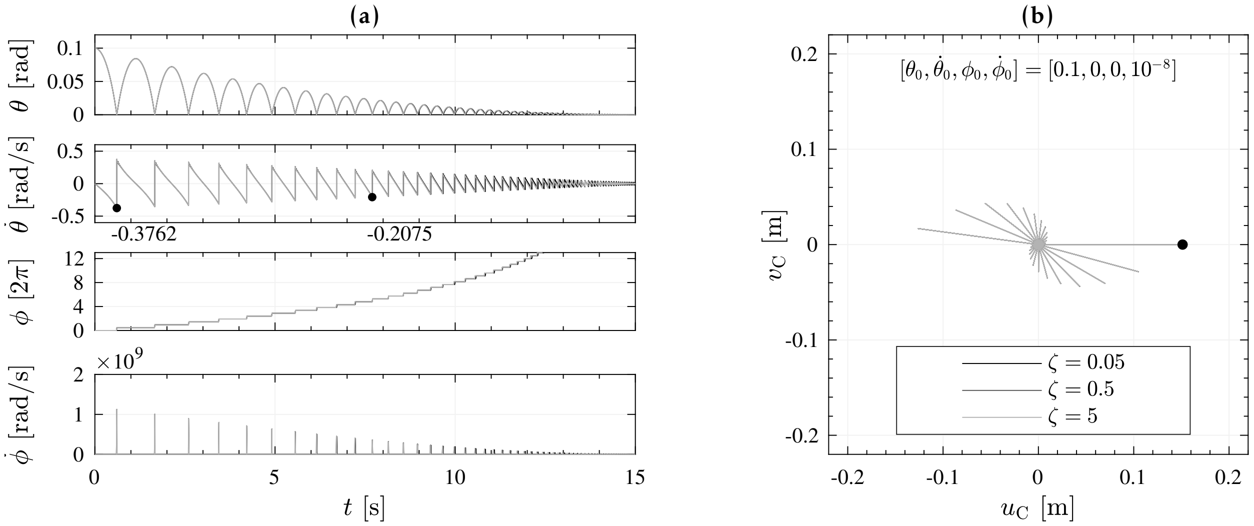

Figure 5.7: Free vibration response comparison of a rigid cylinder ($2H = 3$ m, $\tan\alpha = 0.2$) for different damping conditions (Set ND-1).

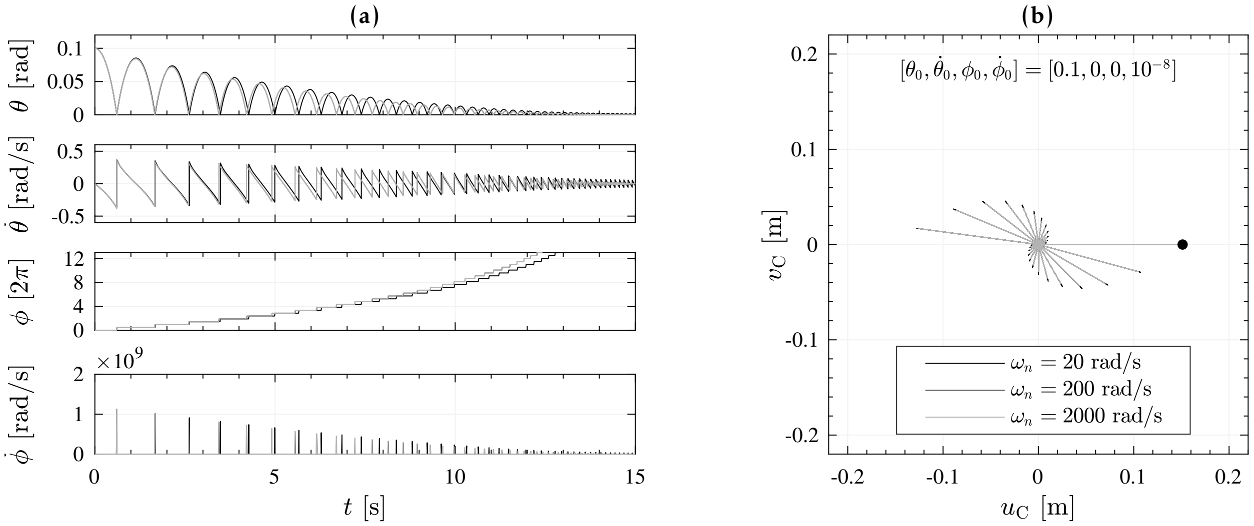

Figure 5.8: Free vibration response comparison of a rigid cylinder ($2H = 3$ m, $\tan\alpha = 0.2$) for different damping conditions (Set ND-2).

Analogy to 2D Rocking Impacts

This perhaps counterintuitive outcome that the damping parameters do not affect the response is similar to the observations of the 2D rocking response in [137] and is related to the fact that the impacts in rocking motion are not central. Nevertheless, the proposed model succeeds in dissipating energy during motions that tend to pure rocking. In fact, applying Housner's approach for a rigid cylinder (Eq. 2.15) with $I_0 = I_1$ according to Equation (5.14) would give a coefficient of restitution equal to

$$\sqrt{c_r} = \frac{\dot{\theta}_{\text{after}}}{\dot{\theta}_{\text{before}}} = 1 - \frac{\sin^2\alpha}{\frac{5}{8} + \frac{1}{24}\cos^2\alpha} = 0.9422. \tag{5.41}$$

Calculating the coefficient of restitution (the support surface is assumed rigid) from the first ten impacts shown in 5.7a yields

$$\sqrt{c_r} = \sqrt[10]{\frac{0.2075}{0.3762}} = 0.9422. \tag{5.42}$$

The two values are equal to four significant digits.

Sensitivity of Damping Parameters

Therefore, the response of the 3D bounded rocking cylinder is not sensitive to the exact values of the spring and dashpot properties of the damped model even when the response includes quasi-rocking behavior and virtually instantaneous changes of the contact point occur. In the cases where the change of pivot point is not quasi-instantaneous (Fig.s 5.5 and 5.6), there is zero damping and the responses of the damped and undamped model are identical.

Therefore, for further investigation on 3D cylinders with a damping mechanism the initially selected damping parameters will be kept: $\omega_n = 200$ rad/s and $\zeta = 0.5$.

5.5 Ground Motion Response

5.5.1 Time history response comparison

When the analysis of the undamped and damped free rocking and wobbling response of a free-standing 3D bounded rigid cylinder is extended to earthquake excitation, the response of the two models (damped and undamped) is going to be similar if wobbling motion dominates the response (*i.e.*, quasi-impacts do not occur, and the amount of dissipated energy is very small). If, however, quasi-impacts occur, the damped model is going to dissipate non-negligible amounts of energy and the solutions from the two models will start to diverge.

To test the aforementioned statement, the support surface of a rigid cylinder with $2H = 3$ m and $\tan\alpha = 0.2$ is excited bidirectionally using the two horizontal components of the recorded ground motion records listed in Table 5.4. The records were acquired via the NGA database [134] and scaled such that the peak ground acceleration, $\ddot{u}^{\varphi}_{g,\max}$ according to Equation (5.24), is $0.30\,g$ and therefore equal to 1.5 times the uplifting acceleration $g\tan\alpha$. The two components

Table 5.4: Bidirectional ground motion records used to compute the 3D ground motion response of a cylinder: records downloaded via the NGA database (unfiltered).

Earthquake (Year)	Station (NGA file)	Direction	$\ddot{u}_{g,\max}$ [g]	Scaling	$\theta_{\max}^{\text{undamped}}$ [rad]	$\theta_{\max}^{\text{damped}}$ [rad]
San Fernando	Pacoima Dam	x: 164° (L)	1.226	0.198	0.010	0.007
(1971)	(00077)	y: 254° (T)	1.159			
Loma Prieta	Oakland, Outer Harbor	x: 000° (L)	0.287	0.898	0.156	overturn
(1989)	Wharf (00783)	y: 270° (T)	0.269			
Landers	Yermo Fire Station	x: 270° (L)	0.245	1.215	overturn	overturn
(1992)	(00900)	y: 360° (T)	0.151			
Tabas	Tabas	x: LN (L)	0.836	0.350	overturn	overturn
(1978)	(00143)	y: TR (T)	0.852			
El Centro	Imperial Valley	x: 180° (L)	0.313	0.943	overturn	overturn
(1914)	(00006)	y: 270° (T)	0.215			
Kobe	Takarazuka	x: 000° (L)	0.693	0.394	0.120	0.118
(1995)	(01119)	y: 090° (T)	0.694			
Whittier Narrows	LB-Orange Ave	x: 010° (L)	0.255	1.172	0.106	0.106
(1971)	(00645)	y: 280° (T)	0.149			

longitudinal (L) and transverse (T) are rotated such that two independent components X and Y result. Apart from scaling and rotation into its principal directions, no other modifications or filters were applied. By scaling the records to the same level of peak ground accelerations, the influence of other ground motion parameters will become apparent. Such scaling of a single recorded ground motion is not ideal as it may produce unrealistically strong ground motions. Nevertheless, the present study adopts this scaling model, and will also be applied in the section that discusses seismic performance rocking spectra.

The ground motion responses are grouped according to the observed response behaviors. Note that this is always with respect to the applied scaling level. It might very well be that the response behavior looks different at a different level of scaling.

San Fernando

The first group consists of only one record, the San Fernando ground motion with an applied scaling factor of 0.198. Although the earthquake is scaled to 1.5 times the uplifting acceleration, the ground motion is barely able to induce tilting angles, as Figure 5.9 displays. A reason for this could be that the PGA of the record (shown in Figure C.3) happens towards the end of the recording.

Loma Prieta, Landers, and Tabas

The second group comprises the strong ground motion records Loma Prieta, Landers, and Tabas. The responses of the damped and undamped cylinders to these records are plotted in Figures 5.10, 5.11, and 5.12. The earthquakes, scaled by 0.898, 1.215, and 0.350 respectively, overturn the

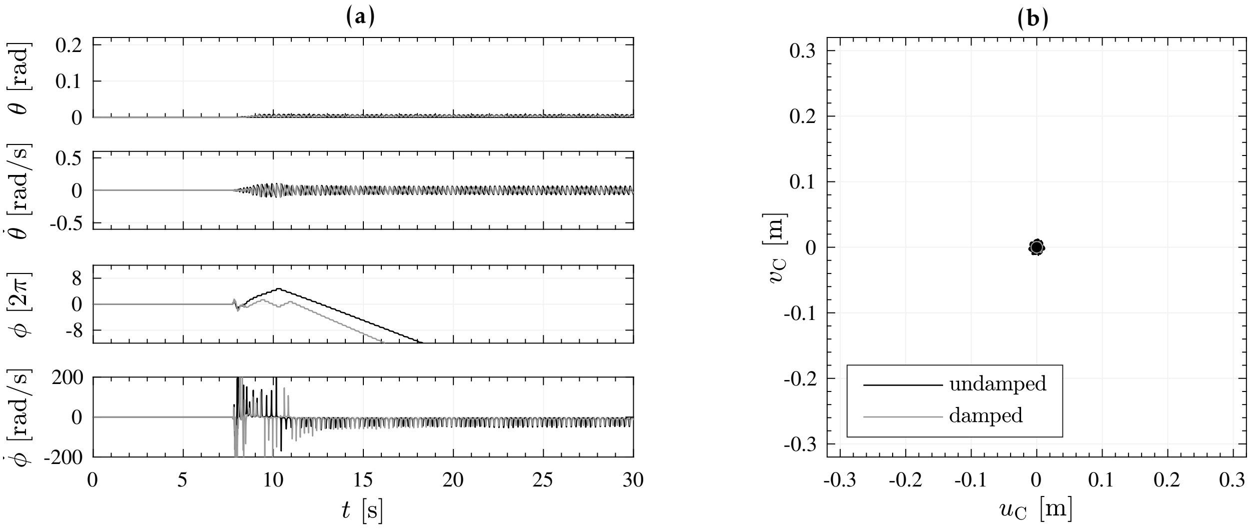

Figure 5.9: San Fernando ground motion record (scaled by 0.198): Time history response comparison for the damped and undamped model of a cylinder with $2H = 3$ m and $\tan\alpha = 0.2$.

cylinder within seconds after uplift occurs: from the instant of uplift until overturning (defined as a tilt angle $\theta = 1.5\,\alpha$) about 3–5 s elapse. An exception is the Loma Prieta record: here only the damped model is brought to overturning. The damped and the undamped model start to diverge after a quasi-impact at $t = 16.6$ s. In the end, the difference becomes so large that one overturns while the other does not. For the seven investigated and to $0.3\,g$ scaled records this is the only case where the two models contradicted each other (Tab. 5.4).

El Centro, Kobe, and Whittier Narrows

The third and last group consists of the records El Centro, Kobe, and Whittier Narrows. Figure 5.13 plots the response time histories for the 1940 El Centro earthquake with an applied scaling factor of 0.943. Both the undamped and damped model uplift at $t = 2.07$ s, and their responses coincide during the first 18 s. Then, stronger quasi-impacts occur: the cylinder is tilted beyond 0.1 rad and starts to tilt back towards the center. At the following quasi-impact a rapid change of pivot point takes place (low values of θ accompanied with high spin velocities $\dot{\varphi}$). It is at this point where the damped and the undamped model start to diverge. Ultimately, both simulations will overturn.

Both the Kobe (scaled by 0.394) and the Whittier Narrows (scaled by 1.172) record induce rocking and wobbling motion with one large pulse. After that, the response is basically unaffected by the ground excitation and performs a motion encountered in Figures 5.14 and 5.15. Visible in the plots of the orbits of the center of cylinder mass the cylinder never return back to the center. This means that no impact-like events occur, resulting in the observed behavior.

Observations

Studying the three-dimensional model under earthquake excitation showed that the implementation of damping can have a big influence on the response of individual cases. Whether damping influences a specific single case or not mainly depends on the way the cylinder responds to the ground motion. If it contains a high amount of rolling and wobbling motion damping is less effective. On the other hand, if the cylinder responds in a way that leads to multiple impact-like

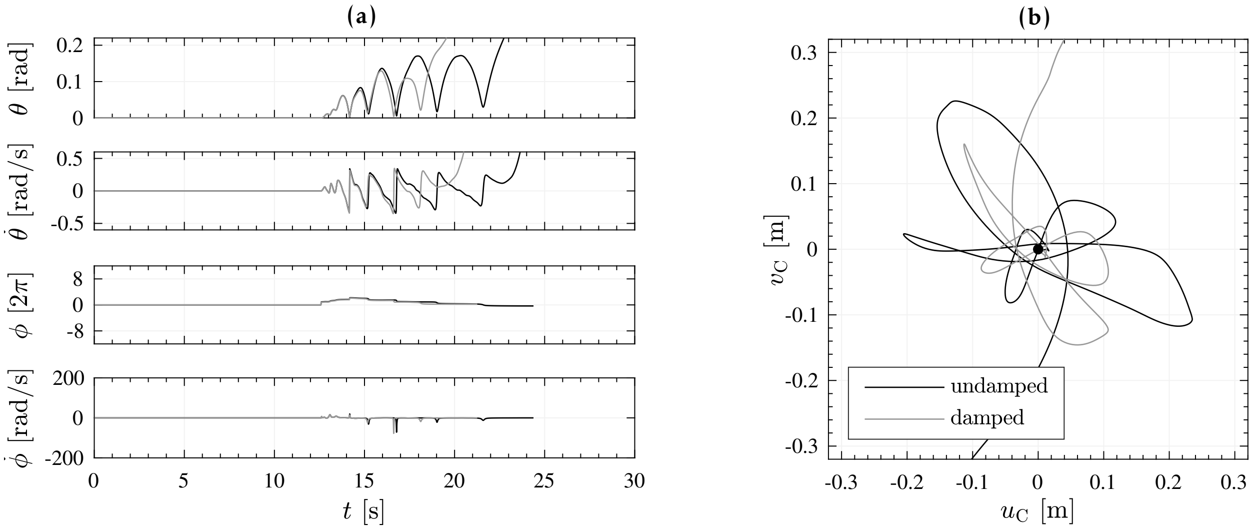

Figure 5.10: Loma Prieta ground motion record (scaled by 0.898): Time history response comparison for the damped and undamped model of a cylinder with $2H = 3$ m and $\tan\alpha = 0.2$.

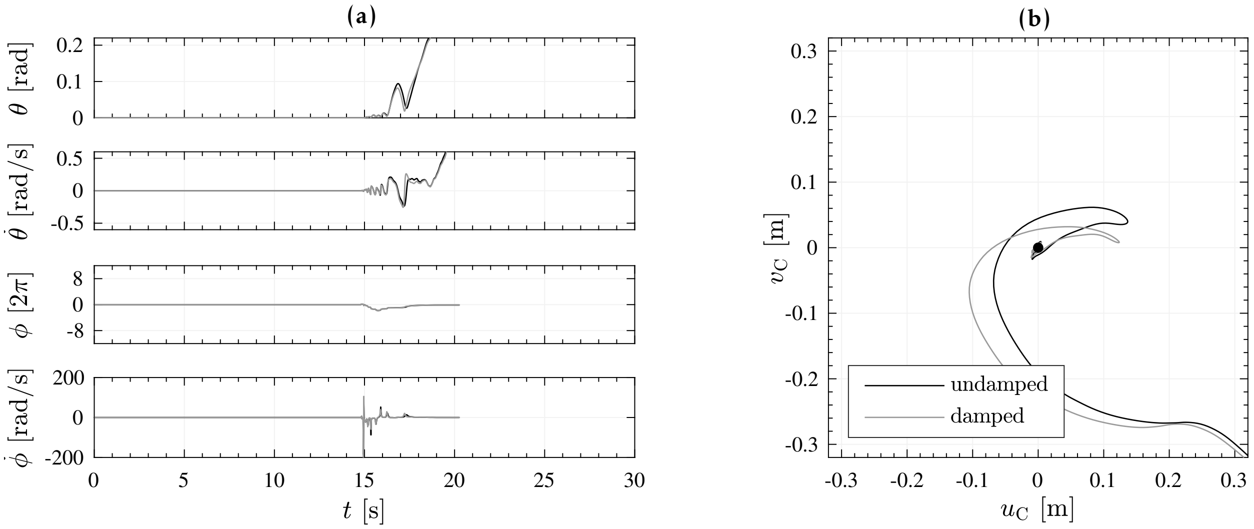

Figure 5.11: Landers ground motion record (scaled by 1.215): Time history response comparison for the damped and undamped model of a cylinder with $2H = 3$ m and $\tan\alpha = 0.2$.

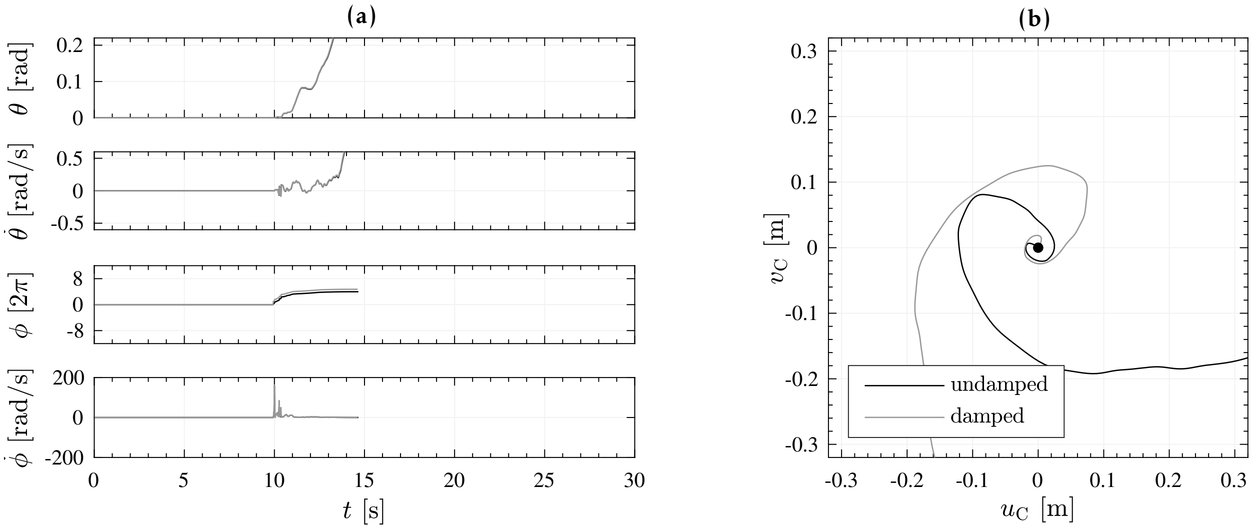

Figure 5.12: Tabas ground motion record (scaled by 0.350): Time history response comparison for the damped and undamped model of a cylinder with $2H = 3$ m and $\tan\alpha = 0.2$.

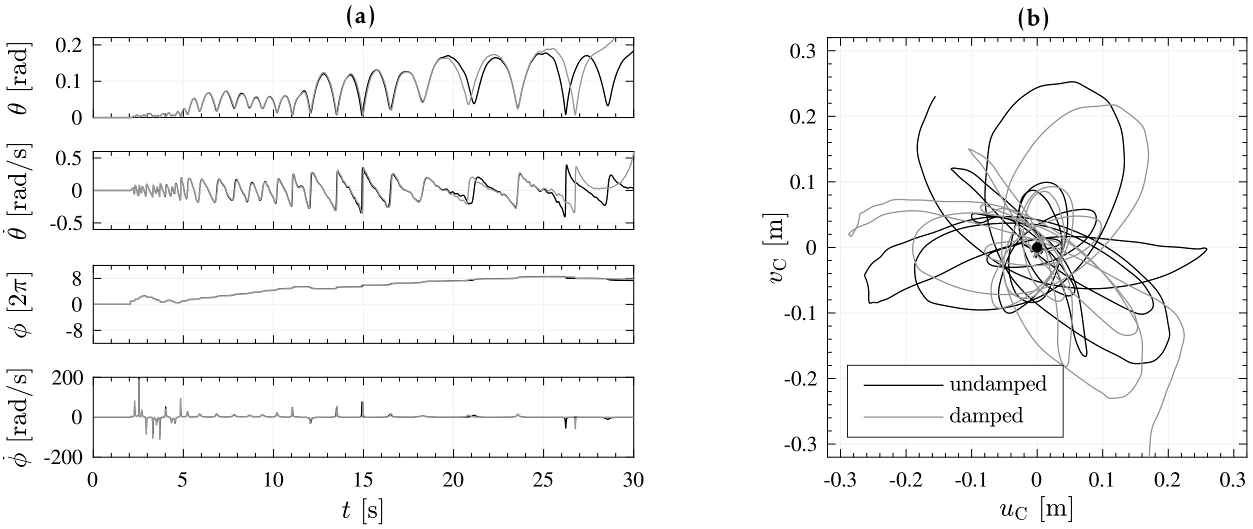

Figure 5.13: El Centro ground motion record (scaled by 0.943): Time history response comparison for the damped and undamped model of a cylinder with $2H = 3$ m and $\tan\alpha = 0.2$.

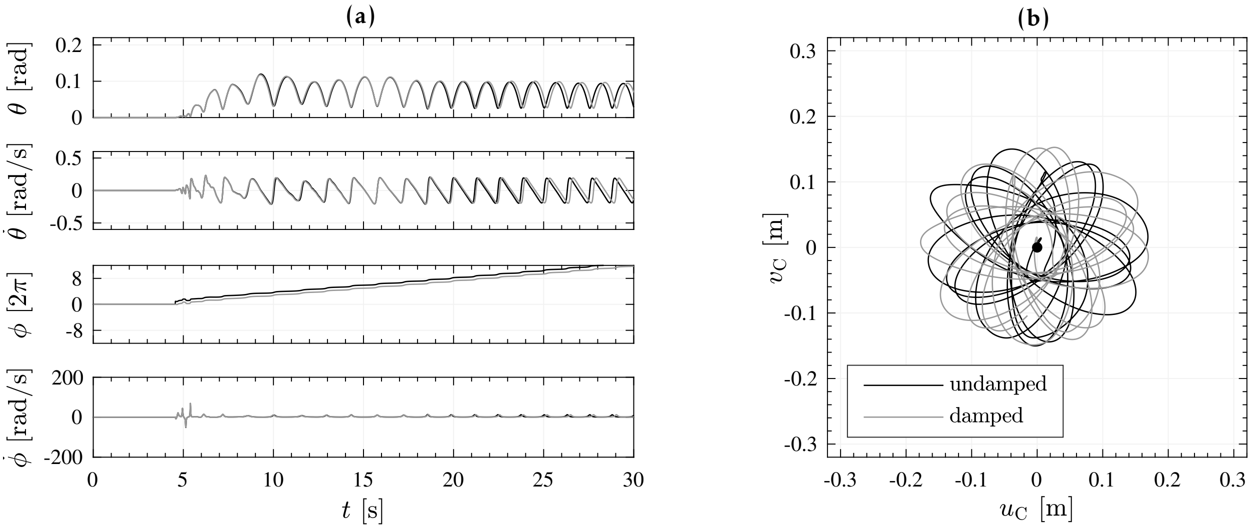

Figure 5.14: Kobe ground motion record (scaled by 0.394): Time history response comparison for the damped and undamped model of a cylinder with $2H = 3$ m and $\tan\alpha = 0.2$.

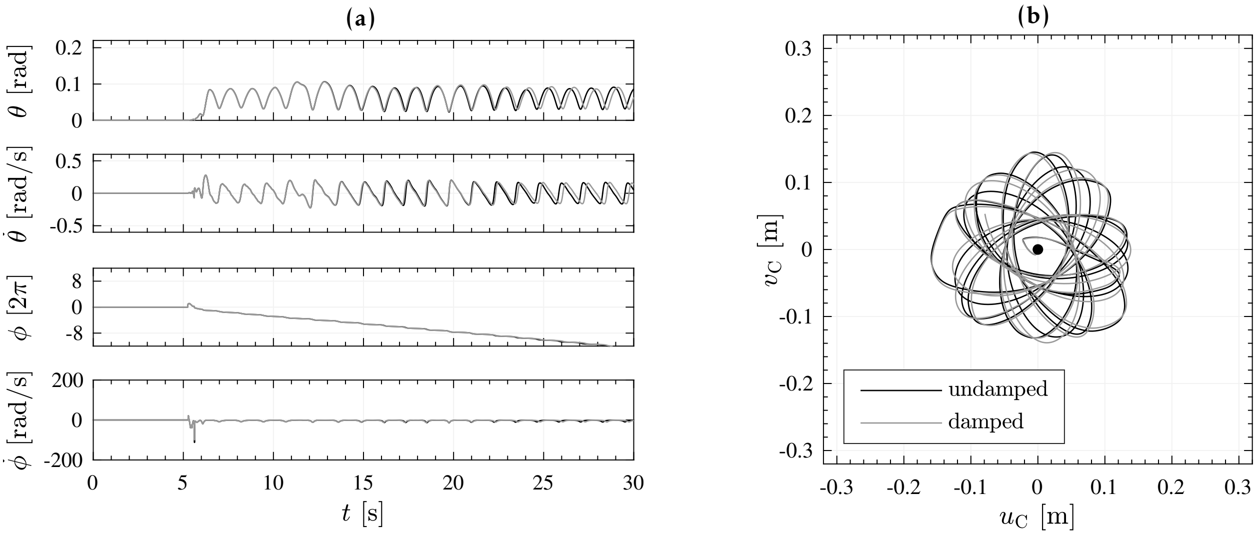

Figure 5.15: Whittier Narrows ground motion record (scaled by 1.172): Time history response comparison for the damped and undamped model of a cylinder with $2H = 3$ m and $\tan\alpha = 0.2$.

events damping affects the outcome significantly. In these cases the implemented damping affects the spin velocity at the quasi-impacts. In doing so already small changes in the spin velocity can lead to a totally different response. Hence, it is possible that the implementation of damping results in entirely different outcomes. In many cases, however, is the effect of damping marginal to not even noticeable.

5.5.2 Spectral response comparison

Rocking Response and Relative Rocking Response Spectra

As encountered before (Fig. 5.10) the behavior of the rocking system due to a ground motion excitation can be quite arbitrary. Small changes, *e.g.*, in geometry, can significantly influence a single outcome. To better grasp the effect such little changes might have, 3D rocking spectra are computed. The abscissa plots the semi-diagonal R of the cylinder. The left ordinate shows the ground motion scaling with respect to the uplifting acceleration,

$$\frac{\ddot{u}^{\varphi}_{g,\max}}{g\tan\alpha}, \tag{5.43}$$

while the right ordinate shows the actual ground motion scaling factor denoted 'EQ-Scaling'. The response tilt angle, $\theta_{\max}$, is normalized with the respective slenderness α.

Figure 5.16a shows response spectrum for an undamped cylinder with $\tan\alpha = 0.2$ for the El Centro ground motion and compares it to the damped model in Figure 5.16b (brighter areas indicate where the outcome of the damped model was better and, *vice versa*, for darker areas). Again, the difference between the damped and the undamped model is small. Only a few single dots with black or white color indicate certain cases where the outcome is completely different (*e.g.*, black: no overturning for the undamped while the damped model does overturn).

Figure 5.17 shows the relative rocking response spectra for the same cylinder when excited by the other six ground motion records listed in Table 5.4.

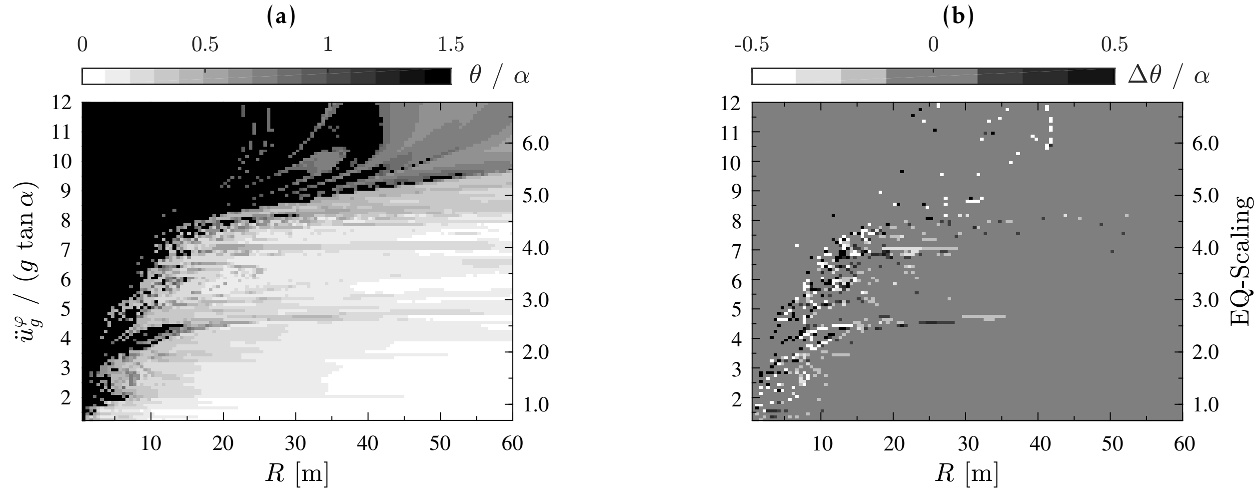

Figure 5.16: Rocking response spectra of a cylinder with $\tan\alpha = 0.2$ for El Centro ground motion: (a) Undamped response model; (b) Relative spectrum of damped vs. undamped model (light color: damped model performs better).

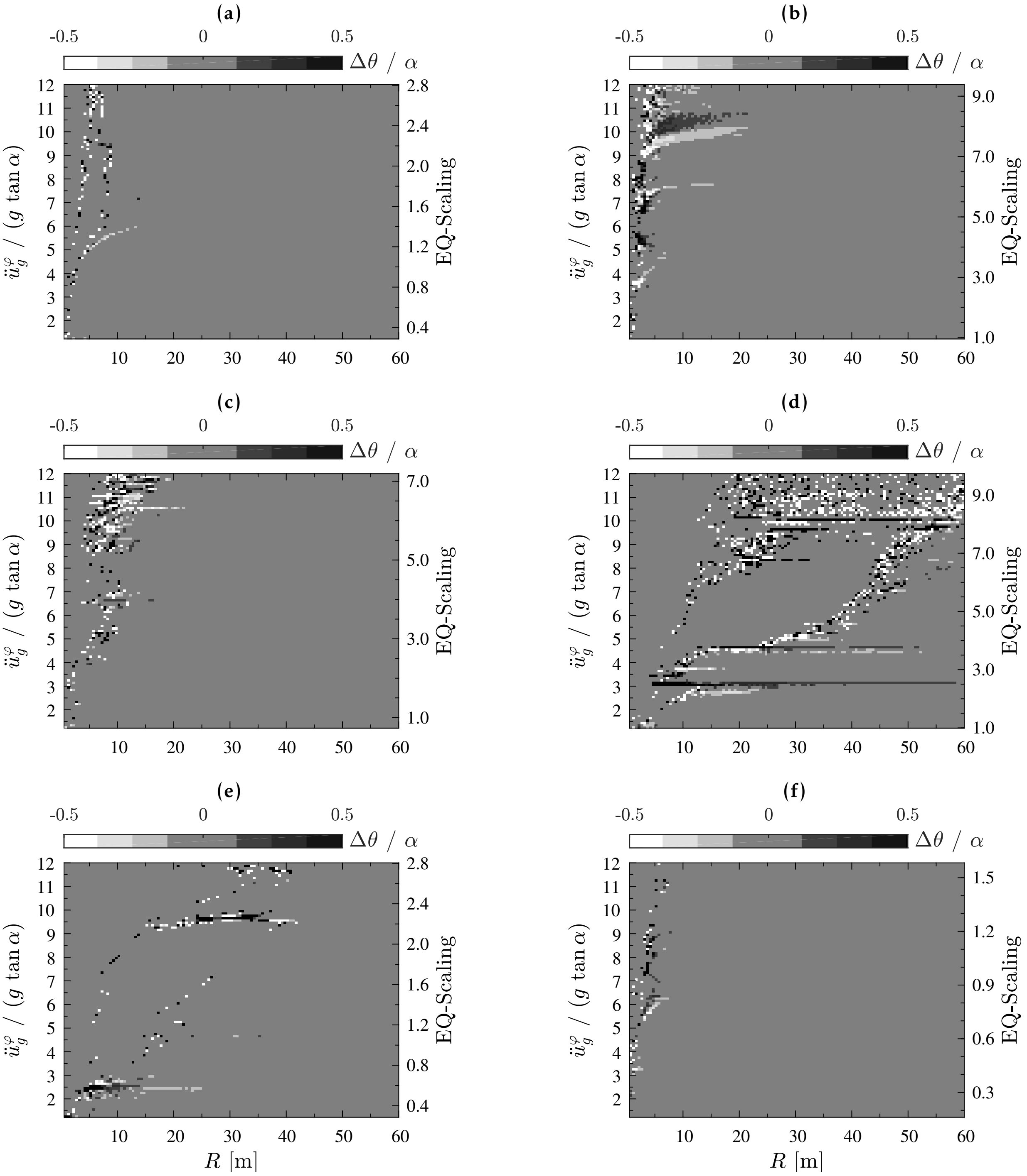

Figure 5.17: Relative spectra of damped vs. undamped model for different recorded ground motions listed in Table 5.4 (see Figure 5.16 for color scale): (a) Kobe; (b) Whittier Narrows; (c) Loma Prieta; (d) Landers; (e) Tabas; (f) San Fernando.

Note the different appearance the spectra have: the records of Landers and Tabas seem to be similar to the El Centro record in the sense that they lead to a similar overturning behavior of the 3D rocking cylinder where overturning still occurs for cylinders with considerable sizes (semi-diagonal $R \geq 30$ m). It is clear that the assumption of complete rigidity for theses sizes will no longer be meaningful but for the purpose of comparison it is acceptable. In comparison, the shape of the spectra of the records Loma Prieta, Kobe, San Fernando, and Whittier Narrows are much narrower: overturning will only occur for cylinders with a semi-diagonal $R \leq 10$ m.

Characteristic Ground Motion Parameters

In a effort to investigate the source of these spectral differences between types of earthquakes, characteristic ground motion parameters are computed. The selected parameters are listed and briefly described in Table 5.6. The corresponding computed values for the investigated strong ground motion records, which are scaled such that $\ddot{u}_{g,\max}^{\varphi} = 0.30\,g$, are specified in Table 5.5.

It seems that there is correlation between the shape of the response spectra shown in Figure 5.17 and the bracketed duration T_d of the respective ground motion. The parameter CAV is directly linked to T_d and, consequently, shows the same correlation. The parameter I_a is computed by integrating the absolute acceleration of time and, therefore, shows a similar trend. The duration of the ground motion significantly influences the 3D rocking response of a rigid cylinder. If after an occurred uplift the ground continues to shake for an extended time, the cylinder struggles not to overturn. The reason for this is that the implemented damping mechanism only dissipates little energy. Hence, the longer the ground motion is, the more kinetic energy will build up in the system, resulting in larger tilt angles and spin velocities. At one point, the oscillator can no longer absorb the additional energy, and overturns. The predominant frequency as well as the rms acceleration seem to have no significant influence on the response.

Table 5.5: Bidirectional ground motion records used to compute the 3D ground motion response of a cylinder: ground motion parameters computed for the records scaled such that $\ddot{u}_{g,\max}^{\varphi} = 0.30\,g$.

Earthquake	EQ-Scaling	f_{pred} [Hz]	T_d [s]	CAV [g s]	a_{rms} [g]	I_a [g s]
El Centro	0.943	1.489	28.82	1.271	0.581	0.159
Loma Prieta	0.899	1.392	8.76	0.633	0.760	0.083
Kobe	0.394	2.173	3.57	0.463	0.988	0.057
Landers	1.216	0.684	24.18	1.213	0.605	0.145
Tabas	0.351	1.587	20.34	1.075	0.647	0.139
Whittier Narrows	1.173	1.270	7.50	0.585	0.796	0.078
San Fernando	0.198	2.417	8.86	0.478	0.558	0.045

5.6 Conclusions

A two-degree-of-freedom model (three when damping is included) that describes the 3D dynamic behavior of a free-standing rigid cylindrical column that can uplift, rock, and wobble with the constraint that it does not slide or roll out of its original position (*i.e.*, an inverted pendulum) was developed. It is the simplest 3D extension of the 2D Housner rigid-body rocking model.

Damped vs. Undamped Cylinder

Two versions of the model were developed: an undamped one and a damped one. The latter is equipped with a damping mechanism such that the responses of a uniaxially excited 3D model and the 2D Housner model match well. It was found that the 3D motion of a free-standing rigid cylinder is dominated by wobbling, making the responses of the damped and undamped models

Table 5.6: Characteristic strong ground motion parameters.

Name	Parameter	Definition
Predominant frequency	f_{pred}	The predominant frequency is defined as the frequency corresponding to the maximum value of the Fourier amplitude spectrum. To avoid the influence of individual spikes the predominant frequency is obtained from a smoothed spectrum.
Bracketed duration	T_d	The bracketed duration is defined as the time between the first and last exceedances of a threshold acceleration, usually $0.05\,g$. The duration of strong ground motion can have a strong influence on earthquake damage.
Cumulative absolute velocity	CAV	The cumulative absolute velocity has been found to correlate well with structural damage potential. It is simply the area under the absolute accelerogram: $$\mathrm{CAV} = \int_0^{T_d} \lvert a(t)\rvert \, d\,t. \tag{5.44}$$
Root mean square acceleration	a_{rms}	The *rms acceleration* is a single parameter that includes the effects of the amplitude and the frequency content of a strong motion record. It is defined as $$a_{rms} = \sqrt{\frac{1}{T_d}\int_0^{T_d} \lvert a(t)\rvert^2 \, d\,t}. \tag{5.45}$$
Arias intensity	I_a	The *Arias intensity* is closely related to the rms acceleration. It is defined as $$I_a = \frac{\pi}{2\,g}\int_0^{\infty} \lvert a(t)\rvert^2 \, d\,t. \tag{5.46}$$

essentially identical. Therefore, the simpler undamped model of the rocking and wobbling 3D motion of a bounded free-standing rigid cylinder can be used with confidence if only a damping mechanism in the support surface is considered. Other damping mechanisms such as the rolling friction or air resistance were neglected.

Correlated Ground Motion Characteristics

In the second part of this chapter ground motion characteristics were investigated in an effort to find correlation between such parameters and the destructiveness of a ground motion record, interpreted from the overturning spectra. The comparison of the characteristic quantities of each ground motion showed that the bracketed duration, T_d, the cumulative absolute velocity, CAV, as well as the arias intensity, I_a, correlate well with the observed overturning capabilities. However, further and deeper investigations into this topic are necessary in order to evaluate these observations.

Nonetheless, the duration of the ground motions, represented by T_d, majorly affects the overturning probability, and raises the question of an appropriate damping mechanism. Without damping, long lasting ground motions will eventually overturn any cylinder where uplift was induced.

CHAPTER 6

EXPERIMENTAL CAMPAIGN

In this chapter experimental tests that were performed with the aim of validation of selected models presented and numerically investigated in Chapters 3 and 4 are presented. Part of the material presented in this chapter has been published. The rocking podium structure (Section 6.3) model was presented in 2016 the ECCOMAS Congress on Crete [3]. The extensive experimental study on Housner's rocking block (Section 6.4.4) was published as a journal article in Earthquake Engineering & Structural Dynamics in 2018 [9].

In most cases the experiments were conducted with the help of ETH students as part of their master program. Studemann & Jost were involved with the execution of the tests performed on rocking oscillators, rocking frames, and rocking podium structures [14]. Blöchinger & Wellauer performed a series of free vibration rolling-and-rocking tests on the rigid oscillator in the ETH laboratory [10]. Finally, Strand performed a series of 600 shaking table rocking response tests on the rigid rocking oscillator (i.e., Housner's block) [15].

6.1 Introduction

6.1.1 Numerical vs. Experimental Testing

When performing numerical analyses any outcome can be reproduced since the initial conditions are numerically defined (unless a random number generator is used to modify certain parameters such as adding white noise to an acceleration signal). The only factors that could affect the numerical results are the selected values of the relative and absolute tolerance for the numerical solver. The standard values used for the ODE solvers (see Section B.1) in my calculations with MATLAB were:

$$\mathrm{RelTol} = 10^{-12}, \qquad \mathrm{AbsTol} = 10^{-12}. \tag{6.1}$$

The numerical stability of the response makes it possible to investigate small changes of parameter values, *e.g.*, the damping values used for the damped 3D rocking cylinder. In my opinion, the representation in MATLAB is the cleanest way to model any rocking problem.

If one tries to validate a numerical rocking model one single test will not suffice because of secondary effects due to small changes in the boundary conditions as well as the initial conditions. For example, in MATLAB I always assumed the initial tilt angle to be $\theta_0 = 0$ rad, and stay constant until uplift occurs. However, as experimental results showed, this could not be verified in the experiments, or only up to a certain level of accuracy.

Therefore, when performing experimental testing, an adequate test procedure needs to be defined where a) either as many tests as needed are performed that one single outcome (be it an outlier) does not affect the overall response behavior, or where b) experiments are repeated numerous times with the same initial laboratory conditions. In that sense, applying method a) to experimental testing of rocking structures is comparable to a random process and should be evaluated as such: from a probabilistic standpoint. If method b) is applied the same test can be repeated until the same or similar response behavior occurs such that the results are trustworthy and can be used for reproducing single cases.

6.1.2 Prototype Scaling

Engineering models are used to study complex problems. Usually, these models are smaller than the final design, but not always. The use of scaled models allows testing of a design prior to building, and in many cases such tests are a critical step in the development process.

Model and Prototype The laboratory built systems are often thought as *model*(m) while the system built the beyond laboratory frame is called *prototype*(p).

6.1.3 Time Scaling of Ground Motion Signals

If the size of the model $R_{(m)}$ is different from the prototype size $R_{(p)}$ the ground motion signals have to be scaled in the time domain according to similitude theory. Consider a ground acceleration time history with a given PGA and a time increment Δt. Note that this signal could be represented by Fourier series with amplitudes $a_{p,i}$ and frequencies $\omega_{p,i}$. From dimensional analysis we know that the response of a rocking system is a function of the following parameters (among others):

$$\mathcal{F}\left(p\,t, \frac{\omega_p}{p}\right), \tag{6.2}$$

where p is inverse proportional to the root of the oscillator size R:

$$p \propto \frac{1}{\sqrt{R}}. \tag{6.3}$$

If the goal is to have similitude between the model (m) and the prototype (p) the nondimensional time, $\tau = p\,t$, needs to be identical in both cases:

$$p_{(m)}\,\Delta t_{(m)} \overset{!}{=} p_{(p)}\,\Delta t_{(p)} \tag{6.4}$$

Hence, it follows:

$$\Delta t_{(m)} = \Delta t_{(p)}\,\frac{p_{(p)}}{p_{(m)}} = \Delta t_{(p)}\,\sqrt{\frac{R_{(m)}}{R_{(p)}}}. \tag{6.5}$$

The above condition implies that the input signal, in this case the ground motion time history with a given recording time step $\Delta t_{(p)}$, is scaled in time according to the root of the size ratio between the model and the prototype. Therefore, for a model smaller than the prototype ($R_{(m)} < R_{(p)}$ and $p_{(m)} > p_{(p)}$), the ground motion signal needs to be run faster during the experiment. This corresponds to an increase of $\omega_{p(m)}$ such that the second term of Equation (6.2), as expected, also achieves similitude. Analytical ground motion pulses such as the Ricker wavelets are therefore scaled in time by increasing their dominant cyclic frequency: $\omega_{p(m)} > \omega_{p(p)}$.

6.2 Laboratory Equipment and Setup

In this section the laboratory equipment that was used to execute the tests and record measurements is described. The main focus lies on the following equipment:

1. Accelerometers
2. Shaking table
3. NDI camera system

6.2.1 Accelerometers

During the experiments in the IBK laboratory acceleration time histories were recorded using the device LIS344ALH, an ultra compact consumer low-power three-axis linear accelerometer able to measure acceleration $\pm 2g / \pm 6g$. The accelerometers were glued to the shaking table (Fig. 6.1). To guarantee redundancy, a minimum of two devices were placed on the shaking table for capturing the occurring acceleration, a necessity for the numerical model. Experience showed that this decision was indeed a good one.

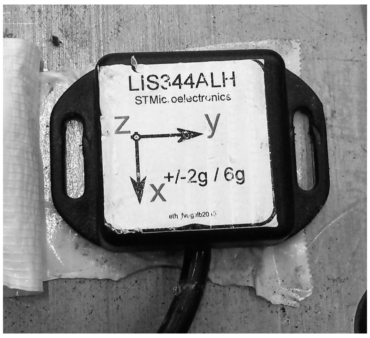

Figure 6.1: Accelerometer.

6.2.2 Uniaxial Shaking Table in the IBK Laboratory

The rocking response of the specimens was induced by a dynamic excitation of its support. This was achieved by placing the specimen on top of the uniaxial ETH shaking table in the IBK laboratory [143] (Fig. 6.2a). The shaking table platform is a stiff steel box on roller bearings actuated using a servo-hydraulic actuator to move only in one horizontal direction.

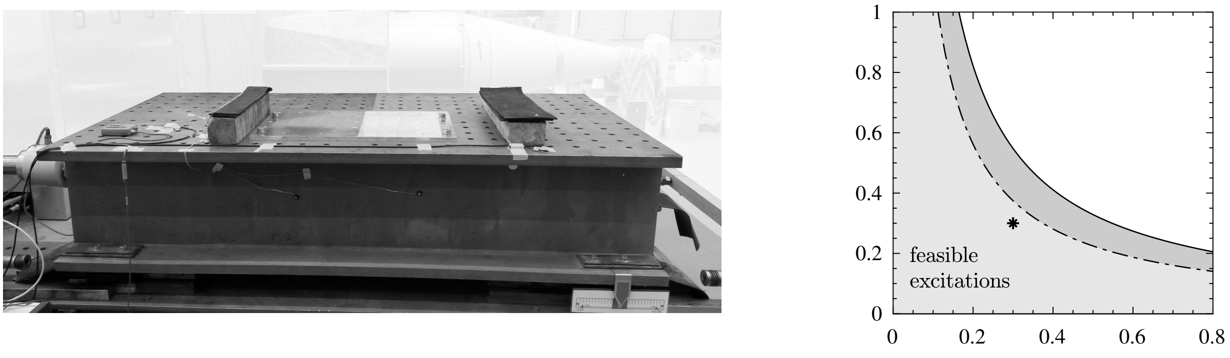
(a)

(b)

Figure 6.2: ETH 1-D shaking table: (a) Laboratory setup; (b) Motion limits.

Limitations of Shaking Table Actuator

The stroke of the shaking table is geometrically limited at 250 mm and the maximum possible velocity is capped at 220 mm/s due to oil flow limitation (using the 2.1 l/s valve). In addition, the controller of the servo-hydraulic actuator does not allow it to stop and stand still in order to avoid friction effects when the motion continues. Instead the actuator oscillates around a target value with an amplitude in the order of 0.10 mm and a main frequency of about 1.5 Hz–2.0 Hz.

The rather low values for the stroke and the maximum velocity of the shaking table fairly reduce the range of application. Figure 6.2b plots the limitation lines corresponding to the symmetric and antisymmetric Ricker wavelets in the space a_p vs. T_p of the respective analytical pulse. The asterisk represents an antisymmetric Ricker wavelet with $a_p = 0.3g$ and $T_p = 0.3$ s. Although this motion is not very strong the feasible range is almost fully exploited with $v = 176$ mm/s. Since the velocity is linearly dependent on a_p and also T_p, a maximal increase of 25% of either of the two is possible ($T_p = 0.375$ s given $a_p = 0.3g$, and *vice versa*). Note that these limits are theoretical values.

Acceleration vs. Displacement Signals

When computing the numerical time history response the ground motion acceleration time history is applied directly to the system as an external force (acceleration × mass). In the laboratory, however, this is not possible. The controller of the shaking table only handles displacement (position) commands. Hence, the ground motion acceleration has to be converted into a displacement by double integration.

Unfortunately, the shaking table reproduced the command motions with different degrees of accuracy during the tests, depending on the characteristics of the motion and numerous factors associated with the state of the shaking table. As an example, Figure 6.3 plots the both acceleration and displacement signal of the afore discussed antisymmetric Ricker ($a_p = 0.3g$, $T_p = 0.3$ s) and compares it with the measured signal in the laboratory. Even though the measured displacement signal looks decent, its corresponding acceleration signal, measured with accelerometers, is far from ideal. Instead of $0.3g$ a PGA of $0.5g$ occurs. Additionally, the shaking table controller struggles to follow the displacement signal and tries to compensate, resulting in overshooting accompanied with high accelerations. At $t = 0.8$ s the pulse should theoretically have ceased, but we still measure acceleration above $0.3g$.

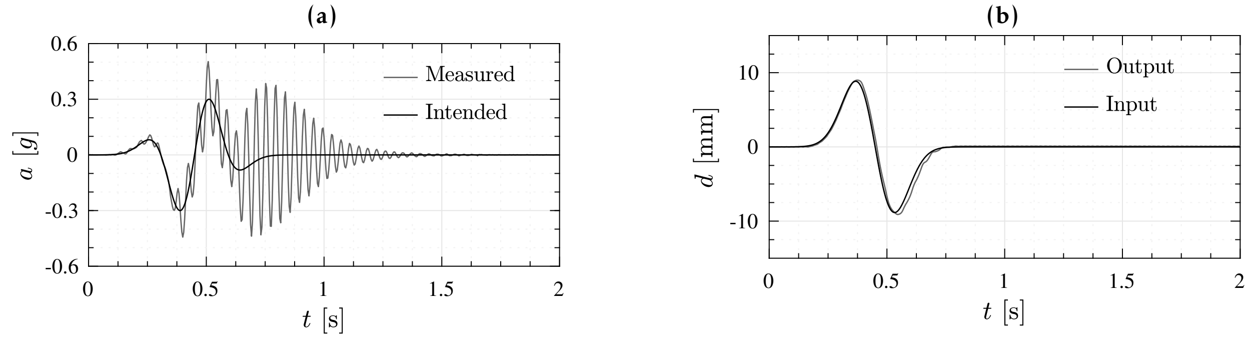

Figure 6.3: Discrepancies between shaking table in- and output: (a) Acceleration signals; (b) Displacement signals.

Tuning of the Shaking Table Controller

The proportional–integral–derivative (PID) shaking table controller can be tuned such that these effects are minimized. The PID controller continuously calculates the error value $\varepsilon(t)$ as the difference between the desired and the measured process variable setpoints and applies a correction based on proportional (P), integral (I), and derivative (D) terms (hence the name PID). However, this tuning needs to be done before every test (*i.e.*, when a different ground motion signal is used) and with the specimen atop. For tests that can be repeated this procedure might work, but is very time consuming (up to five runs are necessary to optimally tune the controller).

A higher value of K_P leads to a better match between the input and the measured displacement, but is accompanied with higher accelerations (Fig. 6.3a) that, in extreme cases, result in reaching the force limit and immediate shutdown of the actuator ($F_\mathrm{max} = 100\,\mathrm{kN}$). Note that the measured acceleration signals form the basis (input) of the numerical MATLAB model. Therefore, the shaking table was tuned to reproduce realistic accelerations at the expense of accurately represented displacements.

Depending on the incentive for a certain experimental study, this fact could jeopardize it entirely. In the experimental campaign discussed in this thesis, however, this was not the case. Nonetheless, certain observed discrepancies between the experimental and numerical results can definitely be attributed to this anomaly.

6.2.3 Spatial Position Tracking System

In order to track the spatial position of selected points on the specimens during the tests an Optotrak Certus System, manufactured by Northern Digital Inc. [144], was used (Fig. 6.4a). It uses active infrared-emitting diodes as markers and a trinocular camera system to determine the position of the markers (Fig. 6.4). The built-in tools of the Optotrak Certus System software are able to measure angles, either in 2D or 3D, between lines defined by two markers. Other output parameters can be defined, *e.g.*, to show the out-of-plane behavior of the specimen or to measure the slip of the specimens. The main components of a typical setup for the NDI in the laboratory are listed in Table 6.1 and illustrated in Figure 6.4b.

According the manufacturer, at minimal distance (1.5 m away from the markers) the field of vision of the position sensor is 0.5 m wide and 0.9 m high, given it is horizontally aligned (Fig. 6.4a). At maximal distance (7 m) the area increases to 3.0 m × 4.2 m. In between, the increase is almost linear. The accuracy of the system has been determined in previous experiments in the IBK laboratory [76]. In the plane parallel to the camera's eyes (x-y-plane) the accuracy is about 0.02 mm. Out-of-plane (z-direction), the accuracy is about 0.10 mm. The system's sampling frequency is 4'600 Hz. However, depending on the number of markers in use, the overall sampling frequency drops. Using n markers simultaneously the maximum possible sampling frequency f_sampling of the system can be calculated with Equation (6.6).

$$f_\mathrm{sampling} = \frac{4'600\,\mathrm{Hz}}{\mathrm{n} + 1.3}, \qquad \text{(using software 12 or higher)} \tag{6.6}$$

Table 6.1: Main components of the NDI setup in the laboratory.

No.	Name	Function
1	Primary position sensor	The position sensor (= camera) detects infrared light emitted from markers within a specific range enabling motion tracking of objects.
2	Secondary position sensor	A second position sensor can be used in parallel if necessary, *i.e.*, for larger objects or surfaces that are hidden from the primary position sensor.
3	System control unit (SCU)	The SCU controls the operation of the position sensor and attached strobers. It is also processes the information collected by the position sensor and sends it to the host computer.
4	Marker strober	This device is controlled by the SCU. It is responsible for activating and deactivating the markers.
5	Marker	The marker is an infrared light emitting diodes that is tracked by the position sensor when activated by the strober. Three or more markers can be defined as a rigid body (optimizing the measurement accuracy).
6	Cable to host PC	Connects the SCU with the host computer.


(a) (b)

Figure 6.4: NDI, Optotrak Certus HD [144]: (a) Primary position sensor (No. 1); (b) Laboratory setup.

In the performed tests in the present thesis, between three and 16 markers were used simultaneously, resulting in maximum possible sampling frequencies between 1’150 Hz and 270 Hz. In the end, the sampling frequency was coordinated with the sampling frequencies of other measuring devices (*i.e.*, the accelerometers and the shaking table controller) to simplify the post-processing of the collected data, resulting in sampling ratio of $f_{\text{sampling}} = 250\,\text{Hz}$.

6.2.4 Setup in the ETH Laboratory

Figure 6.5 shows and Figures 6.6 and 6.7 illustrate how the different devices and equipment were arranged in the IBK laboratory. In the following, I briefly explain how one experiment with shaking table excitation was typically performed:

1. Load the command file (desired input displacement) into the shaking table controller
2. Prepare the specimen for testing
3. Start the recording at the NDI host PC
4. Start the recording at the measurement PC
5. Execute the previously loaded command file in the controller PC
6. Record videos or take pictures of the ongoing experiments (optional)
7. Stop the recordings at the NDI host and measurement PCs
8. Save the recordings with the specific name defined in the laboratory journal

The above described procedure takes about 3–5 minutes for an actual test duration of only about 10 s. By recording a common empty channel in all the different measurement and recording devices the first step towards synchronization was made. However, because the signals are not of digital nature the offset could not easily be determined. Hence, a switch with a 1.5 V battery was connected to the empty channel such that at a random point during the recordings one triggering would suffice to enable synchronization.

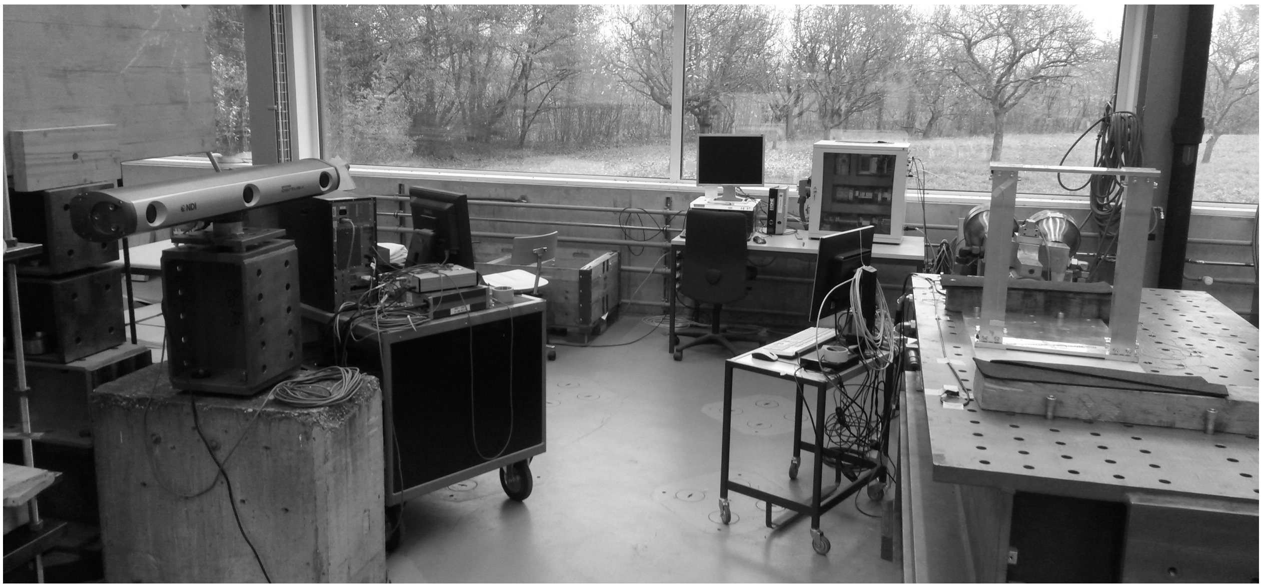

Figure 6.5: Test setup in the IBK laboratory.

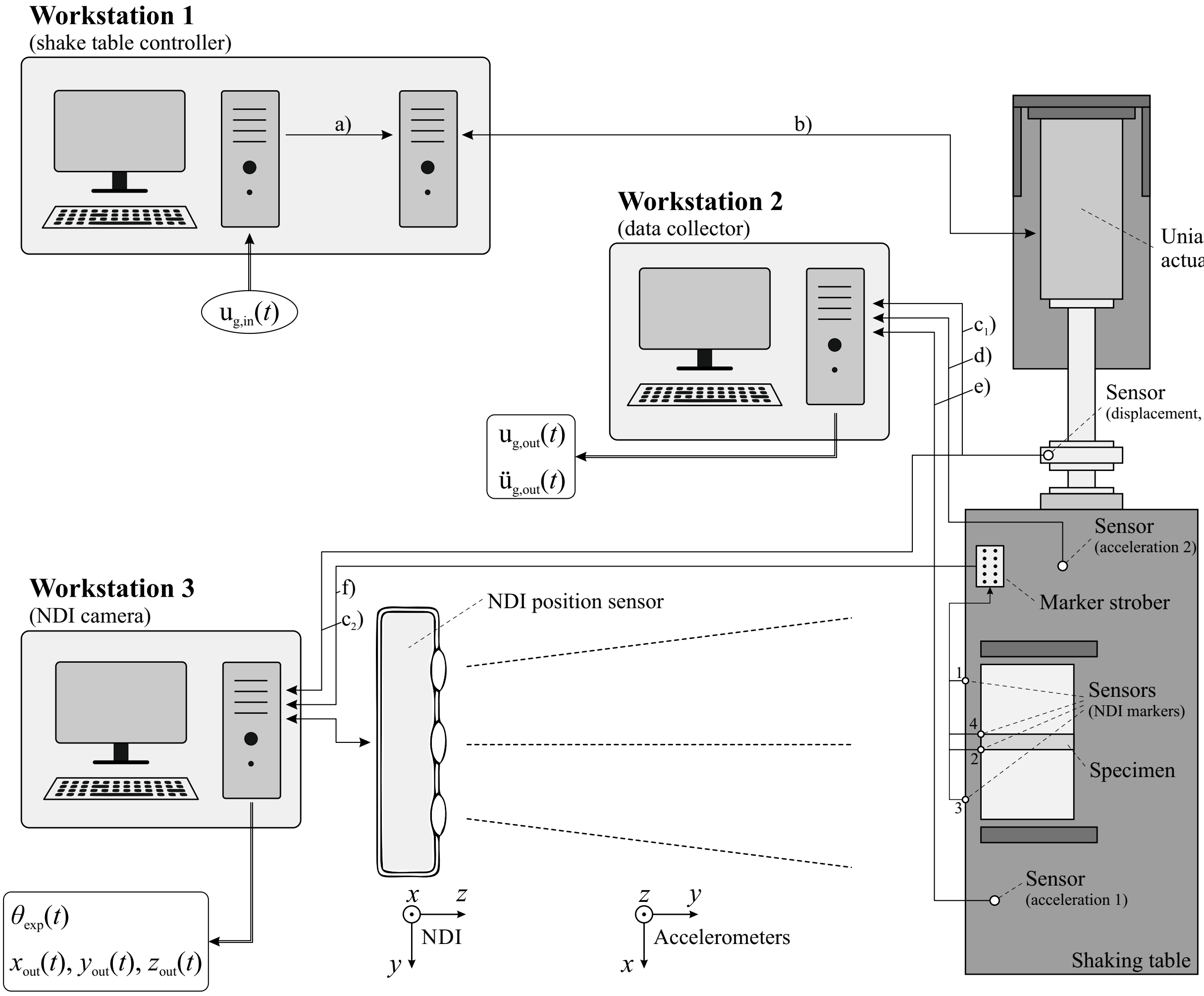

Figure 6.6: Schematic overview of the laboratory setup (top view).

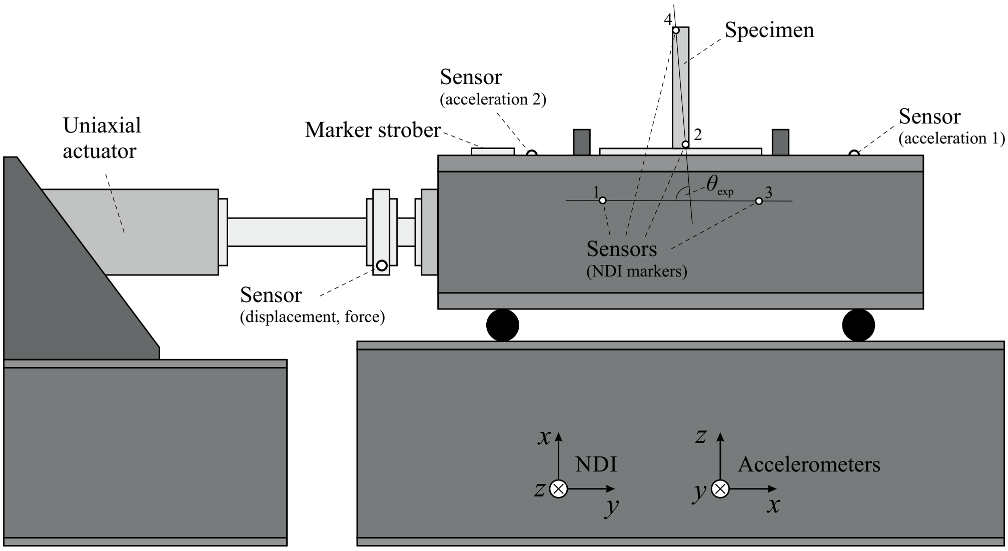

Figure 6.7: Schematic overview of the laboratory setup (side view).

6.3 Podium Structure

The first experiments that I planned in the framework of this thesis were aimed at validating the planar model of the rocking podium structure (developed in Chapter 4) as it is shown in Figure 6.8a.

6.3.1 First Modeling Attempt

In 2014 tests on the setup shown in Figure 6.8b were performed with the help of the Master students Bellagamba and Crettaz. Unfortunately, the test results were unsatisfactory and could not be used to validate the dynamic model developed. Neither the uplifting time nor the response behavior (θ_{max}) could be reproduced with confidence. In addition, in more than a few cases not even overturning could be predicted.

There were many reasons as to why the structure behaved like this. But, I will focus on the main lessons learned:

- Accuracy:

  It is essential that every part that is involved in the dynamic test, *e.g.*, the rocking column or the beam, is produced with the highest accuracy possible. Right angles need to be 90°, and planes should be planar. This also includes that model parts supposedly equal are constructed as such. For example, the result of a dynamic test should not depend on the arrangement of the rocking columns.

- Materials:

  The used materials need to be selected with care. As it is most likely not possible to achieve similitude for all material properties (density, Young's modulus, *etc.*), one has to define certain criteria and choose materials according to them. In the presented case the wood plates deformed quite a bit under pointwise loads (that appear at the contact point of the rocking column). This had an effect on the uplifting force (lower stiffness), on the inherent damping, and so on. Therefore, the wood that was used proved to be inappropriate.

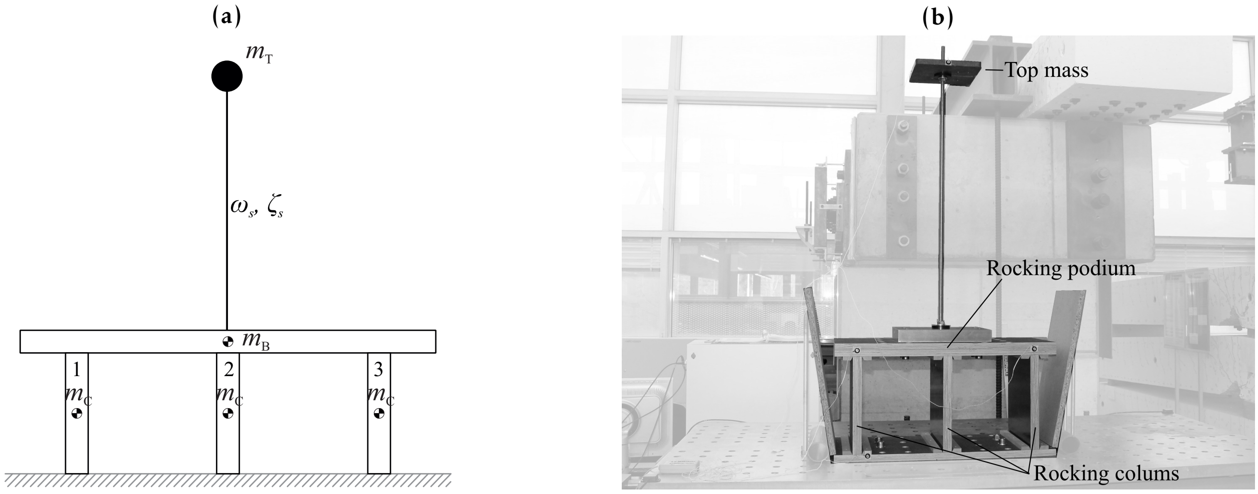

Figure 6.8: Experimental testing of rocking podium structures: (a) Dynamic model; (b) Experimental setup (1^{st} attempt).

- Modeling:

  In the process of designing an experimental setup one has to make sure that the assumptions made for the numerical model will hold in an experimental test. For example, if sliding is precluded in the numerical model, either of the following precautions, or a combination of them, have to be taken to guarantee it during the experiments:

  - The friction coefficient in the laboratory needs to be large enough by using a certain material.
  - If the impact mechanism is not or only marginally affected, it is also possible to use additional layers such as sandpaper [76].
  - Additional parts can be used to prevent sliding mechanically such as shear bolts or sliding restrainers (used in this case).

  Similarly, the out-of-plane motion of the top mass was underestimated. Although the specimens were excited uniaxially, the top mass oscillation became bidirectional after some time. Hence, using only one rod for the elastically modeled superstructure was a mistake. This discovery was used to optimize other ongoing rocking tests inside the IBK laboratory (the out-of-plane stiffness was increased enforcing the motion to stay in-plane [76]).

- Successive testing:

  It is recommended that the testing program starts with the simplest configuration possible and is gradually upgraded. This ensures that the difference between the measurements and the numerical model can be attributed to the according source of error. Naturally, this is a lot more time consuming. For the experimental setup under investigation, the entire setup was merely tested in its final configuration, making it impossible to correctly correlate possible sources of error with their impact on the response.

6.3.2 Second Modeling Attempt

One year after attempt 1 another series of experiments were carried out with the aim of validating the planar model of the rocking podium structure. Taking into account all the afore discussed learned lessons, I had designed a new experimental setup, illustrated in Figure 6.9. The material mainly used was aluminum alloy[1].

The elastic superstructure was designed such that its weight and its oscillation frequency could be modified separately. Furthermore, the system's out-of-plane stiffness was increased to enforce planar motion only. The aluminum plates were fabricated on a computer numerically controlled (CNC) machine in the IBK laboratory, ensuring evenness with minimal error. The base plate was fixed to the shake table and acted as the rigid support surface. The rest of the aluminum was ordered from an external vendor as extruded profiles with different shapes (I, L, and □). In order to allow for replacements or improvements during the testing campaign, the specimen was screwed together. The elastic SDOF superstructure was fixed to the aluminum plate positioned on top of

---

[1] EN AW-6060: $\rho_{\mathrm{Al}} = 2.71\,\mathrm{g/cm^3}$, $E_{\mathrm{Al}} = 70\,\mathrm{GPa}$

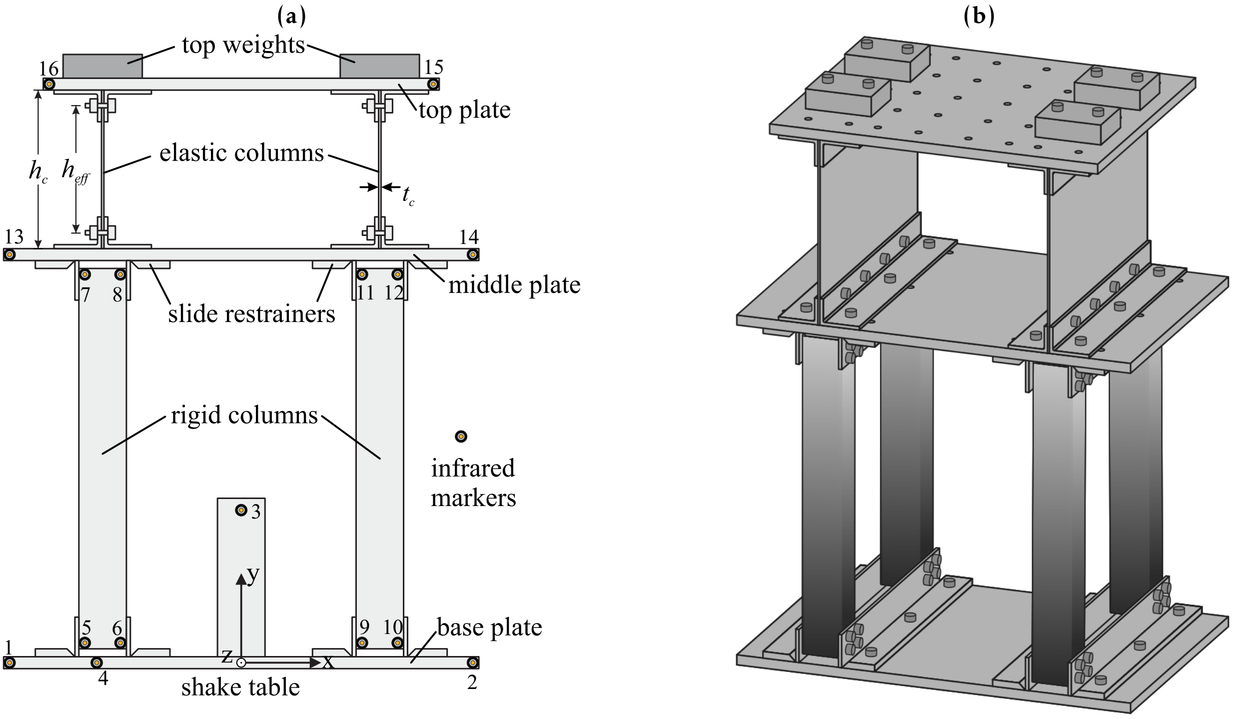

Figure 6.9: Design of experimental setup: (a) Front view (with locations of the infrared markers); (b) 3D rendering.

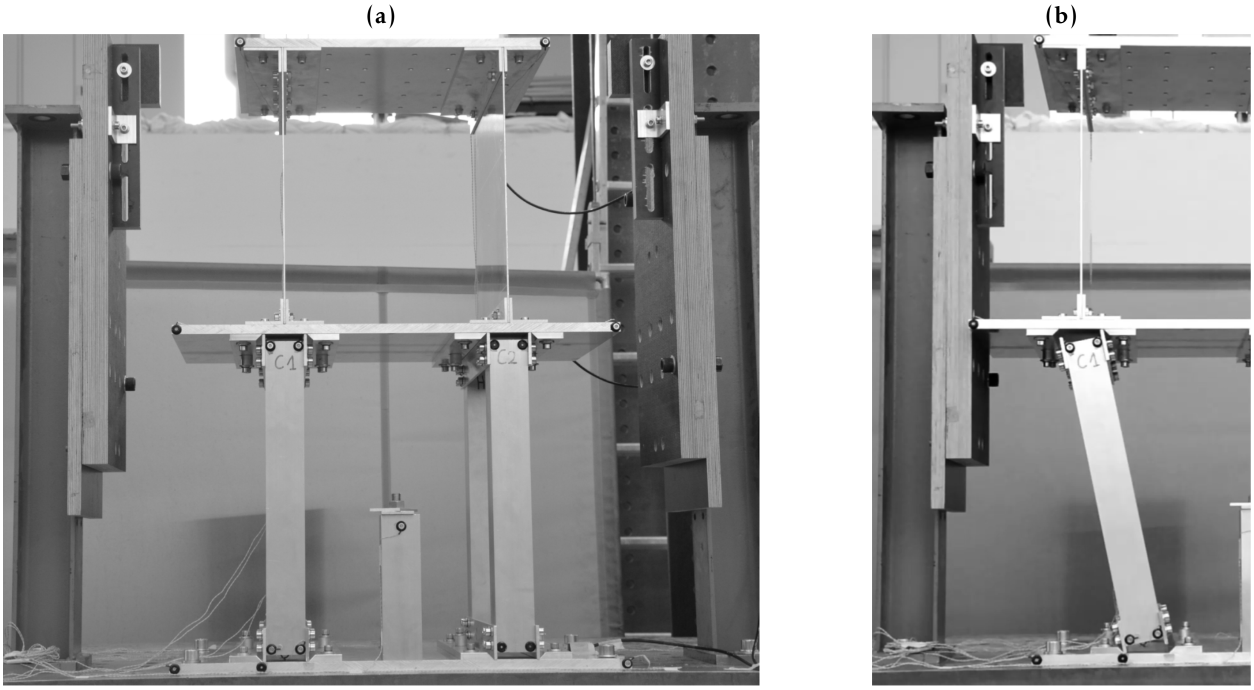

Figure 6.10: Experimental setup in the IBK laboratory at ETH Zurich: (a) Front view; (b) Overturned specimen.

the rocking columns. It comprises two elastic columns, the top plate, the top weights, and the connecting L-sections.

Figure 6.10 shows the experimental setup in the IBK laboratory at ETH Zurich. Note that to prevent the podium structure from collapsing completely, safety barriers were fixed onto the shaking table (beams on the left in Figure 6.10).

6.3.3 Dimensions and Weights

Many combinations are possible with this setup. It was designed in this way to allow for numerous testing with different parameters. The experiments described in this section, however, were performed with one specific setup only which will be described in details in the following sections.

Rocking Frame

The rocking frame (RF) that forms the rocking floor comprises two identical rocking columns, denoted with RC, that consist of numerous aluminum parts. The total height of the rocking column is $2H = 500\,\text{mm}$ and the total width is $2B = 69.7\,\text{mm}$, resulting in a slenderness of $\tan\alpha = 0.1394$ and a size of $R = 252.4\,\text{mm}$. Each of the two rocking columns consist of two identical 480 mm tall extruded hollow □-profiles (60 mm× 60 mm× 4 mm), four rectangular sheets (400 mm× 50 mm× 5 mm), two at the bottom and two at the top, and 32 screws (M8) to connect everything into one rocking column stiff enough to be modeled as rigid.

During rocking motion, the rocking columns are assumed to rotate around the outer edges of the rectangular sheets. Total weight of one rocking column adds up to

$$m_\text{C} = 3.94\,\text{kg}\,. \tag{6.7}$$

Note that due to the symmetry the columns orientation is not of concern. The rotational inertia of the column around the center of mass, I_C, is numerically computed at a value of $130'316\,\text{kg mm}^2$, implying that $\lambda = 0.519$. The exact value is determined in a later step by performing a free vibration analysis.

The cap-beam of the rocking frame is an aluminum plate with dimensions 700 mm× 400 mm× 15 mm. In total four slide restrainer, made by chamfering one edge of a rectangular sheet, are installed on the lower side of the beam plate. They prevent sliding of the columns along the plate, but also serve as a overturning protection because the columns are blocked from moving sideways extensively. On the upper side of the beam, four L-shaped profiles (60 mm× 40 mm × 5 mm) are used to connect the elastic columns of the superstructure. Including 50% of the superstructure's elastic column masses, this leads to a total mass of the cap-beam of

$$m_\text{B} = 17.05\,\text{kg}\,. \tag{6.8}$$

Superstructure

The superstructure comprises the top aluminum plate (500 mm × 400 mm × 15 mm), the additional weights if added (15.84 kg in total), four of the afore mentioned L-shaped profiles, and two aluminum sheets (441 mm × 400 mm × 3 mm) representing the elastic columns. Its total weight, excluding 50% of column masses, is

$$m_\text{T} = 27.52\,\text{kg}\,. \tag{6.9}$$

The connections of the column sheets to the top and cap-beam plate are assumed rigid. Hence, the superstructure period can be computed with:

$$k_s = 2 \cdot 12 \frac{E_a I_c}{h_{eff}^3}, \tag{6.10}$$

$$T_s = 2\pi \cdot \sqrt{\frac{m_{\mathrm{T}}}{k_s}}. \tag{6.11}$$

The effective or the net height h_{eff} of the column is defined as the distance between the screws and bolts at the bottom and top of the elastic column (Fig. 6.9a). For the present column it follows:

$$h_{eff} = 401\ \mathrm{mm}, \tag{6.12}$$

$$I_c = \frac{(3\ \mathrm{mm})^3 \cdot 400\ \mathrm{mm}}{12} = 900\ \mathrm{mm}^4. \tag{6.13}$$

Then, the stiffness k_s and the superstructure period T_s can be computed:

$$k_s = 24 \cdot \frac{70\,\mathrm{GPa} \cdot 900\ \mathrm{mm}^4}{(401\ \mathrm{mm})^3} = 23.45\,\mathrm{kN/m}, \tag{6.14}$$

$$T_s = 2\pi \sqrt{\frac{27.52\ \mathrm{kg}}{23.45\,\mathrm{kN/m}}} = 0.215\ \mathrm{s}. \tag{6.15}$$

Note that the value of T_s corresponds to the fixed base natural period. The experimentally measured value of T_s was 0.222 s (about 3% error).

Following the theory of Section 4.2.2 the dimensionless mass ratios can be computed:

$$\gamma = \frac{m_{\mathrm{B}}}{N m_{\mathrm{C}}} = \frac{17.05\ \mathrm{kg}}{2 \cdot 3.94\ \mathrm{kg}} = 2.164, \tag{6.16}$$

$$\eta = \frac{m_{\mathrm{T}}}{m_{\mathrm{B}}} = \frac{27.52\ \mathrm{kg}}{17.05\ \mathrm{kg}} = 1.614. \tag{6.17}$$

6.3.4 Similitude Analysis

The above mentioned model dimensions were chosen so that it reproduces, as closely as possible, a typical full size prototype podium structure. The main laboratory constraint was the size of the model, which resulted in a scaling down of the rocking column height by a factor of 6 (given that a typical floor would have a height of 3.0 m). To maintain similitude, the excitation frequency (or the ground motion history time step Δt) needs to be scaled accordingly. As discussed in Section 6.1.3, the resulting time scaling factor becomes $\sqrt{6}$.

The fundamental vibration of the prototype superstructure was targeted to be in the range between 0.5 s and 0.6 s, chosen as typical for a 5-story masonry building. The measured value of 0.222 s corresponds to a fundamental period of 0.544 s for the prototype.

The uplifted period $T_{s,up}$ was measured during the experiments to be 0.145 s which is 1.53 times smaller than the fixed-base natural period of 0.222 s. This confirms the amplification that one gets using Equation (4.25), namely:

$$f_{s,up} = 1.52 \cdot f_s. \tag{6.18}$$

Slightly unfortunate was the selected combination of the superstructure height h_c and weight m_T. Considering that the period of the superstructure was selected for a 5-story masonry building, the weight ratio η would need to be in the order of 4–5. However, it is only 1.61. In retrospect, a better combination could have been used where h_c was smaller and m_T was larger.

6.3.5 Calibration Tests of Sub Assemblies

Free vibration rocking motion tests were performed to determine the exact values of the rotational inertia I_C (λ) and the coefficient of restitution c_r of the rocking column and the rocking frame.

Frequency Parameter

The frequency parameter p can be back-calculated from a free vibration test data using the nonlinear relationship between the rocking period T_R and the frequency parameter p (Eq. 2.8), repeated here for convenience:

$$T_R = \frac{4}{p}\cosh^{-1}\left(\frac{1}{1-\frac{\theta_0}{\alpha}}\right),$$

where θ_0 is the maximum tilt angle for a rocking response half-cycle of duration $T_R/2$. The influence of decreasing values for θ_0 over time was accounted for by a polynomial regression. The resulting frequency parameter values over 15 response half-cycles were averaged to obtain the measured frequency parameter value p. With the individual definition of p for the column or the frame, λ can be derived. Note that λ was back-calculated from the free vibration test of the column and was fixed at this value (it could also be computed from the free vibration test of a frame).

Coefficient of Restitution

The coefficient of restitution in free rocking motion was derived by relating the total pre- and post-impact energies of the specimen. Thus, it needed to be calibrated for both cases. The analytical definition of the coefficient of restitution is the ratio of the angular velocities squared after and before impact. The underlying assumption that energy is only dissipated at impact was adopted for the experimental back-calculation. Furthermore, the potential energy was assumed to be zero at impact. Then, the coefficient of restitution is equivalent to the ratio of kinetic energies after and before impact. Applying energy conservation, c_r yields:

$$c_{r\mathrm{emp}} = \frac{E_{\mathrm{p},i+1}}{E_{\mathrm{p},i}}, \tag{6.19}$$

where E_p is defined according to Equation (2.10) and θ, again, is the respective maximum tilt angle θ_0 in that rocking response half-cycle.

Back-Calculation from Free Vibration Tests

The free vibration test were performed on the still standing shaking table having, as close as possible, identical conditions. In total ten free vibration tests were performed on the rocking

Figure 6.11: Calibration tests of sub assemblies: (a) Rocking column; (b) Rocking frame.

columns (five for the left, and five on the right column) and seven on the rocking frame. In case of the frame, also different weight ratios γ were considered ($\gamma = \{1.682,\ 3.692\}$).

Figure 6.11a shows the free vibration test 005 of column RC2, and Figure 6.11b the test 006 of the rocking frame with $\gamma = 3.692$ right before they were started. The columns or the frames, respectively, were tilted upto a tilt angle θ_0 that was randomly chosen, and then tied to the left overturning blockage safety barrier. To guarantee similar starting conditions the specimens' motion was initiated by burning the retaining cord.

Rocking Column

From the experimental data displayed in Figure 6.12 the mentioned parameters were back-calculated to be:

$$p = 5.018\,\mathrm{s}^{-1} \quad \rightarrow \quad \lambda = 0.54, \tag{6.20}$$

$$c_{r\mathrm{emp}} = 0.9417. \tag{6.21}$$

The previously computed analytical value of 0.519 undervalued the excentric little masses (*e.g.*, screws and bolts). The error with respect to the total inertia ($\lambda + 1$) around the pivot point O is 1.3%. The theoretical value of the restitution coefficient is $c_{r\mathrm{th}} = 0.9514$. Thus, the experimental setup loses roughly 1% more energy at impact than analytically computed when assuming CoAM.

Figure 6.12 also displays the response obtained using the numerical model (Eq. 3.12) with the frequency parameter p and the coefficient of restitution c_r obtained from response measurements. Notably, the two response histories compare well for more than 10 rocking cycles.

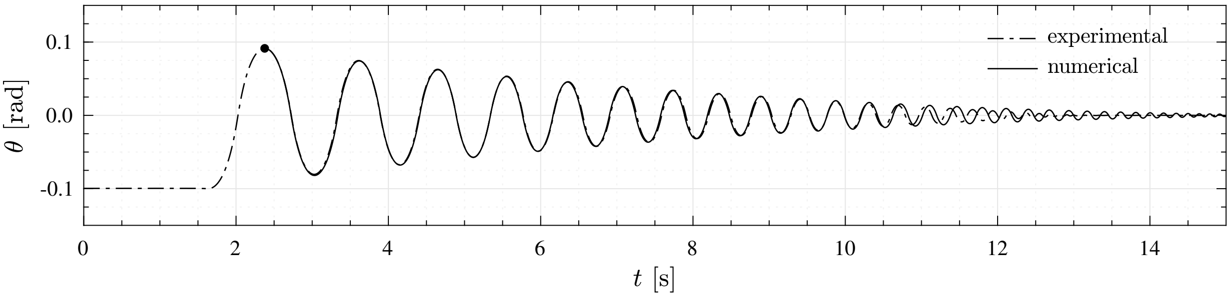

Figure 6.12: Calibration of column.

Rocking Frame

From the experimental data displayed in Figures 6.13 and 6.14 the coefficient of restitution for the frame was back-calculated to be:

$$\gamma = 1.682 : \begin{cases} c_{r\text{emp}} & = 0.9528 \\ c_{r\text{th}} & = 0.9300 \end{cases} \tag{6.22}$$

$$\gamma = 3.692 : \begin{cases} c_{r\text{emp}} & = 0.9537 \\ c_{r\text{th}} & = 0.9276 \end{cases} \tag{6.23}$$

Hence, the experimental setup of the frame loses on average about 2.5% less energy at impact than analytically computed when assuming CoAM. This decrease in energy dissipation, when comparing with singular columns, is attributed to the fact that the impact (in the case of the frame four different interfaces experience impacting) happens less instantaneously but rather distributed over a short time δt. Consequently, the energy loss decreases. This fact becomes more apparent towards the end of the motion, as the plots in Figures 6.13 and 6.14 indicate. Nevertheless, during the first up to eight rocking cycles the numerical and the experimental responses match well.

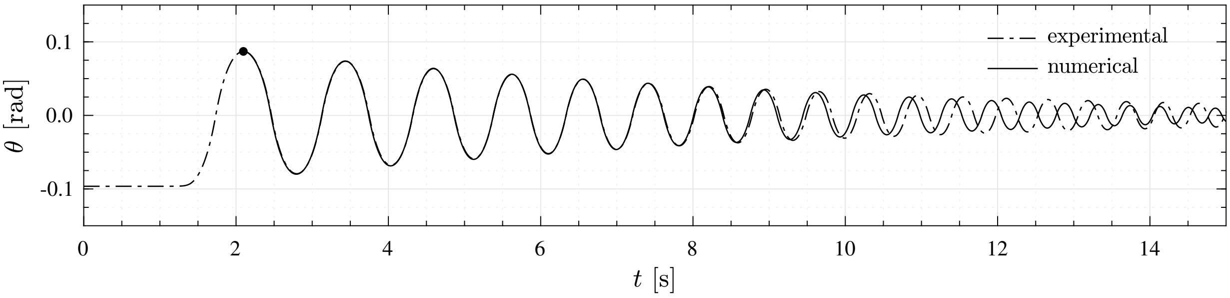

Figure 6.13: Calibration of frame ($\gamma = 1.682$).

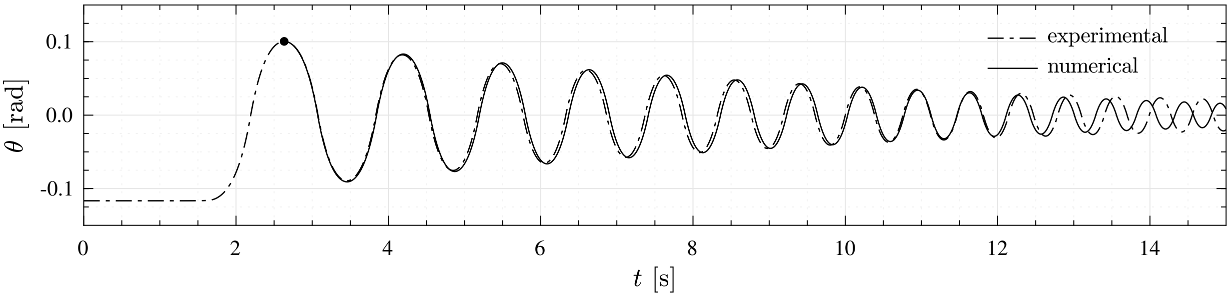

Figure 6.14: Calibration of frame ($\gamma = 3.692$).

6.3.6 Excitation

The final setup of the specimen shown in Figure 6.10 was tested using 12 different symmetric and 12 different antisymmetric Ricker wavelets. The Ricker wavelets had acceleration amplitudes of $a_p = \{0.20,\ 0.25,\ 0.30\}g$ and pulse periods of $T_p = \{0.20,\ 0.30,\ 0.40,\ 0.50\}$ s. At the Prototype scale these values correspond to periods of $\{0.49,\ 0.74,\ 0.98,\ 1.23\}$ s. For three (No. 8, 11, and 12) out of the 24 different Ricker wavelets the shake table would reach its motion limits (Fig. 6.2b), namely the velocity limit of 220 mm/s (Fig. 6.15).

Table 6.2: List of tests with Ricker wavelet excitation.

Antisymmetric Ricker (□)						Symmetric Ricker (•)					
No.	a_p [g]	T_p [s]	No.	a_p [g]	T_p [s]	No.	a_p [g]	T_p [s]	No.	a_p [g]	T_p [s]
1	0.20	0.20	7	0.25	0.40	13	0.20	0.20	19	0.25	0.40
2	0.20	0.30	8	0.25	0.50	14	0.20	0.30	20	0.25	0.50
3	0.20	0.40	9	0.30	0.20	15	0.20	0.40	21	0.30	0.20
4	0.20	0.50	10	0.30	0.30	16	0.20	0.50	22	0.30	0.30
5	0.25	0.20	11	0.30	0.40	17	0.25	0.20	23	0.30	0.40
6	0.25	0.30	12	0.30	0.50	18	0.25	0.30	24	0.30	0.50

For the present study this did not pose any problems as the acceleration and displacement output of the shake table was measured in all tests and was subsequently used as input for the numerical model for comparison.

Table 6.2 lists the 24 tests with Ricker wavelets, numbered for reference.

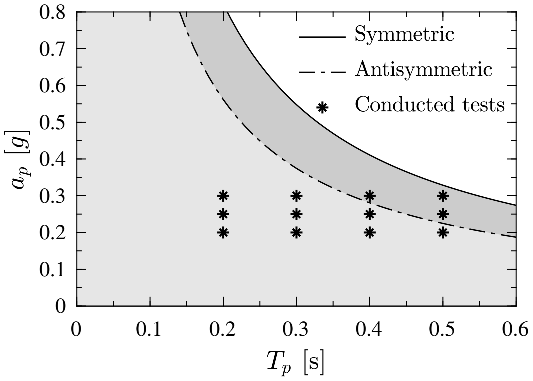

Figure 6.15: Shake table motion limits.

6.3.7 Experiment Outcomes and Comparison with Numerical Results

The objective of the experimental campaign was to validate the analytic model of a rocking podium structure presented in the Section 4.2. The specimen was tested against 12 different symmetric and antisymmetric Ricker pulses. For the numerical solution, the measured shaking table (*i.e.*, ground) acceleration was used as input.

Table 6.3: Comparison of computed and measured superstructure deformation u_T–u_B [mm]. Overturning occurred in tests is highlighted in bold font.

	Antisymmetric Ricker (□)					Symmetric Ricker (•)			
	experimental		numerical			experimental		numerical	
No.	$\theta_{\max}$ [α]	$u_T - u_B$ [mm]	$\theta_{\max}$ [α]	$u_T - u_B$ [mm]	No.	$\theta_{\max}$ [α]	$u_T - u_B$ [mm]	$\theta_{\max}$ [α]	$u_T - u_B$ [mm]
1	0.093	5.028	0.096	6.057	13	0.060	4.614	0.052	4.315
2	0.245	6.476	0.256	5.510	14	0.198	5.923	0.118	6.529
3	0.558	8.270	0.567	7.234	15	0.285	8.138	0.283	6.683
4	**1.571**	**5.829**	**1.571**	**4.486**	16	0.500	8.511	0.407	7.912
5	0.122	5.927	0.133	5.846	17	0.079	5.540	0.066	4.398
6	0.292	8.788	0.308	7.611	18	0.250	6.575	0.232	6.311
7	0.497	8.629	0.674	5.704	19	0.456	8.336	0.343	7.009
8	**1.571**	**3.392**	**1.571**	**4.414**	20	0.591	7.745	0.572	8.753
9	0.132	6.461	0.152	6.242	21	0.111	6.690	0.082	5.376
10	0.287	7.831	0.344	7.060	22	0.356	8.345	0.266	6.696
11	0.478	8.546	0.607	7.092	23	0.688	8.017	0.498	7.293
12	0.709	8.438	**1.571**	**3.770**	24	**1.571**	**5.325**	0.832	6.310

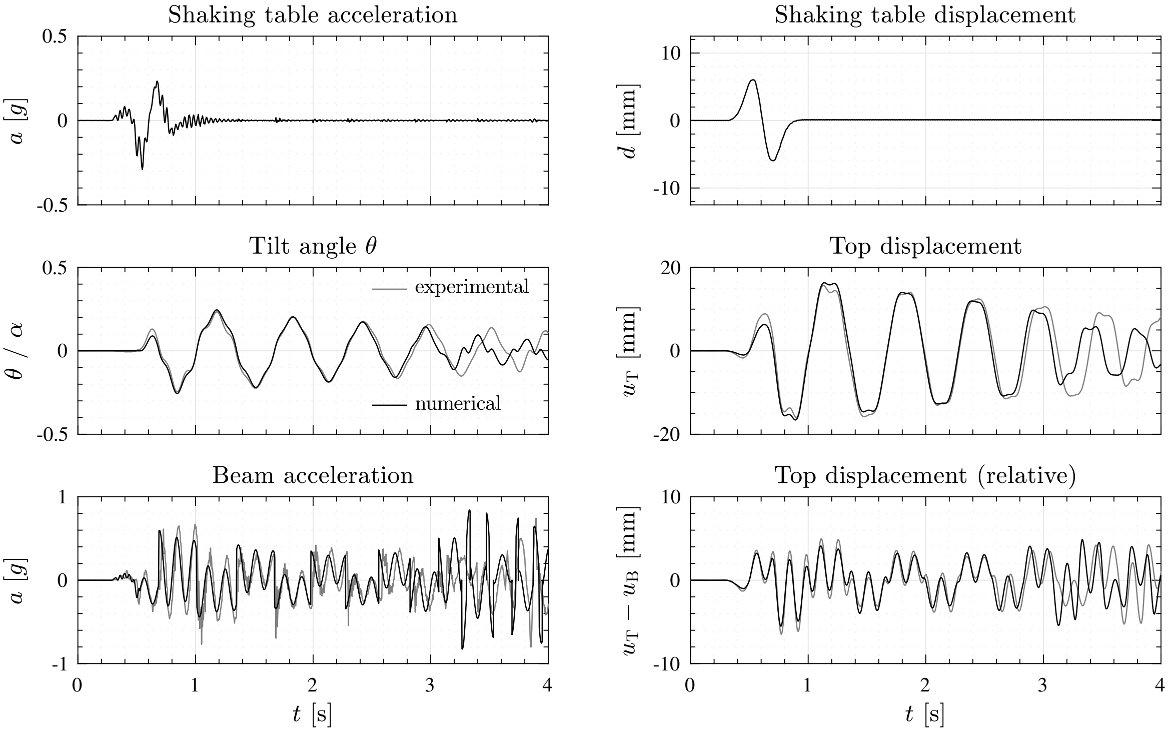

Figure 6.16: Response comparison (Test No. 2).

Figures C.6–C.29 that are added in Appendix C (page 166ff) compare the numerical and experimental time histories of the normalized tilt angle, θ/α, the absolute and relative top mass displacement, u_T and $u_T - u_B$, and the accelerations of the ground and beam. An instancing plot showing the response comparison of test No. 2 is plotted in Figure 6.16. Notably, the two responses match well. Even though some tilt angle time histories were captured very well by the numerical solution, it is generally difficult to predict the entire time history correctly. Unlike elastic systems, the *period* of rocking oscillators strongly depends on their amplitude of vibration. In turn, the amplitude depends on the energy dissipated at each impact. Therefore, any error introduced grows larger, since the solution goes out of phase with the experiment. This confirms the observations of many researchers and suggests that a stochastic (rather than a deterministic) treatment of the rocking problem should be employed.

Nevertheless, for analytic pulses, where the maximum tilt angle occurs in the beginning of the time history, the matching in terms of tilt angle maxima is generally good, even though the

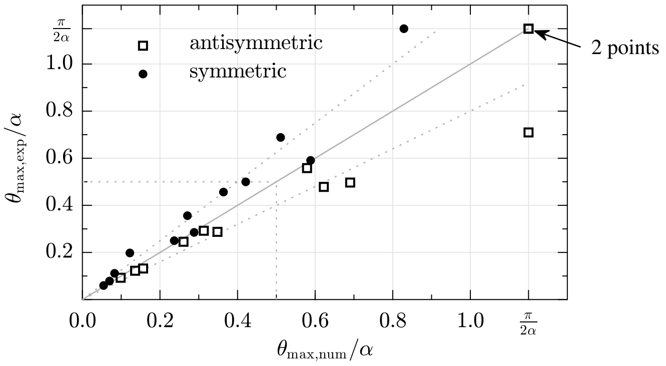

Figure 6.17: Comparison of computed and measured maximum normalized tilt angle θ/α.

shake table controller was not able to enforce a clear pulse motion. Figure 6.17 demonstrates this match by comparing the maximum tilt angles. For small absolute tilt angles ($\theta/\alpha < 0.5$) the results compare better. As the tilt angles increase, the negative post-uplift stiffness of the rocking structure affects the highly nonlinear behavior more and more, leading to larger discrepancies between the computed and measured maximum tilt angles.

The maximum superstructure deformation ($u_\mathrm{T} - u_\mathrm{B}$) is also captured quite well, with an average error of 8% (Tab. 6.3). The tests with bold font were not taken into account because in these tests either the numerical and/or the experimental model overturned.

6.3.8 Observations

A typical test response is one where the frame uplifts and rocks without overturning, without out-of-plane motion, or stepping or sliding on the rocking surface, and where the superstructure elastic oscillator vibrates in its uplifted frequency $f_{s,up}$.

The following deviations in specimen response were observed:

- Sliding:

  Two different types of sliding were observed.

  One type was sliding occurring at every impact during rocking and the other type was sliding occurring when there was no rocking. The amount of sliding during the rocking motion was small, and very difficult to detect in measured data (the transition from one edge of the rocking column to the other was usually fast and clear).

  The other type was sliding while the columns were not rocking which was significantly larger and could be detected in measurements. Such sliding occurs because the still-vibrating SDOF superstructure excites the podium frame, causing the relatively light columns to overcome friction at their bases and slide. Restrainers were placed near the column bases to keep such sliding to a minimum (< 0.3 mm) for small and light specimens tested in this study.

- Out-of-plane movement:

  The large number of rocking interfaces (two rocking columns with four rocking edges each) accompanied by unnoticeable but still present imperfections and asymmetry caused small out-of-plane movements during a few tests, accumulating to 2 mm in the worst case.

- High-frequency content of the top mass:

  The recorded motions of the top mass have a pronounced high frequency component. This component is attributed to the rocking impacts. It cannot be captured by the analytic model since the impacts excite higher modes of vibration which are not taken into account in the analytic model.

- Gap opening (detachment of the frame):

  The overturning moment during the tests caused a gap opening between the frame and the supporting column as illustrated in Figure 6.18. This is assumed to be caused by the overturning moment of the superstructure mass which was not considered in the analytical model. Hence, this source of error could very well lead to a large difference throughout the entire motion. Whether or not this occurred during was not easy to determine and additional data processing is needed.

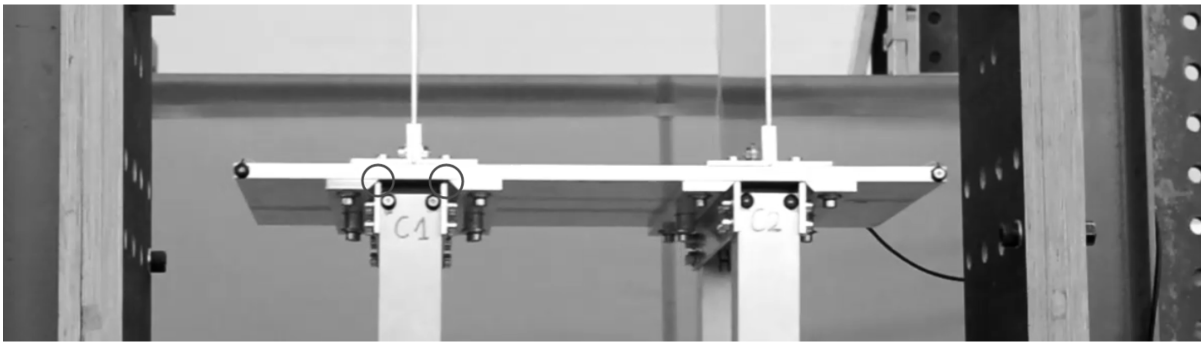

Figure 6.18: Gap opening during test No. 3.

- Edges of Rocking Column:

  The designed rocking columns were not easy to screw together accurately. The bottom and the top sheets (*i.e.*, the rocking edges of the column) should form a plane. It is well known, that four points (two from each 'line') over-determine a plane and one has to be very precise when assembling it in order to avoid double impacting which will happen if the two edges are somehow skew. In addition, being unsupported at midspan, the 5 mm thin sheets deformed and made the columns wider in the middle. To avoid this unwanted effect, the edges were carved in the area where no loads have to be carried (Fig. 6.19).

Figure 6.19: Carved edges of the rocking column.

6.4 Modified Rigid Columns

Based on the observations that were made for the rigid columns of the podium structure setup, the columns were once again modified to improve precision and extend their range of application. So far, the rocking columns only consisted of columns with flat bases. Now, the bases were extended to also be curved to test the introduced model in Section 3.2.4: a rigid column with a curved base.

In this section the experimental redesign and implementation of such columns is presented, and then experimentally validated by performing free vibration and shaking table tests.

6.4.1 Specimen

In the subsequent section, the improved flat model of the rocking column is extensively tested (600 tests were performed) against ground motions excitations of synthetic nature.

The core structure of the columns presented in the preceding section was kept as is, that is, the hollow □-profiles. However, the rest was replaced and improved. A specimen «RC» consists of two columns «C», two link plates «L», four exchangeable bases «F» (column **f**eet), and four cubic blocks «CB», all made of aluminum alloy[1] (Fig. 6.20). The specific part details (*i.e.*, technical drawings) of the main parts can be found in the Appendix D as listed in Table 6.4.

Again, two linked columns were used to avoid out-of-plane motion. The exchangeable *bases* at the top of the column are a) for possible use in a rocking frame configuration, and b) to have

---

[1] EN AW-6060: $\rho_{\mathrm{Al}} = 2.71\,\mathrm{g/cm^3}$, $E_{\mathrm{Al}} = 70\,\mathrm{GPa}$

Table 6.4: Main parts of the modified rigid column.

No.	Part	Technical drawing	No.	Part	Technical drawing
1	Base	Appendix D.1.3 (page 184ff)	3	Column	Appendix D.1.4 (page 187)
2	Linking plate	Appendix D.1.1 (page 183)	4	Block	Appendix D.1.2 (page 184)

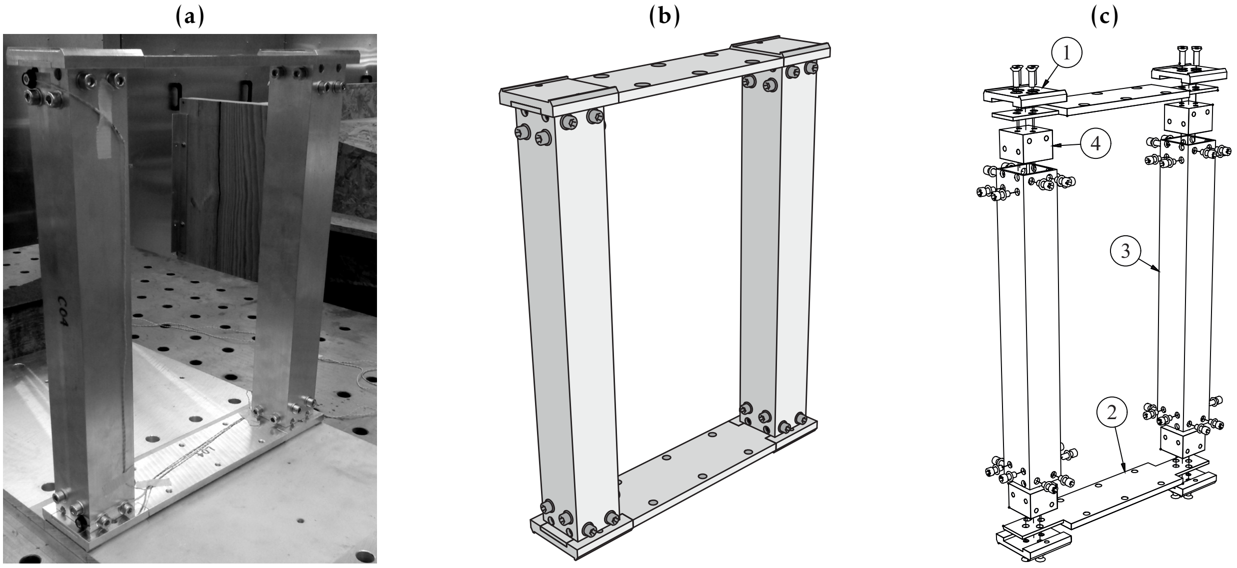

Figure 6.20: Redesign rigid rocking column: (a) Specimen; (b) 3D rendering; (c) 3D rendering (exploded).

a symmetrical specimen. Note that symmetry is not a necessary condition but it simplifies the laboratory work. If the column were not symmetric, two rotational inertia factors λ would need to be computed and/or experimentally validated.

6.4.2 Geometric Characteristics

The total height of the rocking column setup is again $2H = 500$ mm. The horizontal projection of the curved feet ($2 \cdot (B_{\text{curved}} + B)$) is identical in all specimens and equal to 150 mm, resulting in $\tan\alpha' = 150/500 = 0.30$. Two groups of specimens are examined: One with a flat base equal to $2B = 50$ mm (F01–F04: $\tan\alpha = 0.10$) and one with a flat base equal to $2B = 75$ mm (F05–F08: $\tan\alpha = 0.15$). In each group, four different setups are tested: flat (without extensions), $r = 125$ mm, $r = 250$ mm, and $r = 500$ mm (these curvatures correspond to a negative, zero, and positive post-uplift stiffness, respectively).

The different bases of the specimens are illustrated in Figure 6.22 and are summarized (together with the specimen masses) in Table 6.5. Note that the critical curvature according to Equation (3.55) is $\rho_c = 0.333$ for the bases F01–F04 and $\rho_c = 0.250$ for the bases F05–F08. Hence, for F07 ρ is equal to ρ_c and for F02 $\rho < \rho_c$.

The bases were manufactured in the physics laboratory at ETH Zurich. The bases F01 and F06 are shown in Figure 6.21.

Table 6.5: Geometric characteristics of the different investigated bases of the modified rigid column.

	$2H$	$2B$	R	b	$2B'$	$\tan\alpha$	$\tan\alpha'$	r	ρ	β	θ_c	m	Drawing
	[mm]	[mm]	[mm]	[mm]	[mm]	[–]	[–]	[mm]	[–]	[–]	[–]	[kg]	Figure (page)
F01	500	50	251.2	-	50	0.10	-	-	-	-	0.100	0.162	D.3 (184)
F02	500	50	251.2	50	150	0.10	0.30	125	0.25	0.412	0.197	0.329	D.4 (184)
F03	500	50	251.2	50	150	0.10	0.30	250	0.50	0.201	0.297	0.293	D.5 (185)
F04	500	50	251.2	50	150	0.10	0.30	500	1.00	0.100	0.294	0.310	D.6 (185)
F05	500	75	252.8	-	50	0.15	-	-	-	-	0.149	0.164	D.7 (185)
F06	500	75	252.8	37.5	150	0.15	0.30	125	0.25	0.305	0.291	0.289	D.8 (186)
F07	500	75	252.8	37.5	150	0.15	0.30	250	0.50	0.151	0.295	0.304	D.9 (186)
F08	500	75	252.8	37.5	150	0.15	0.30	500	1.00	0.075	0.293	0.311	D.10 (186)

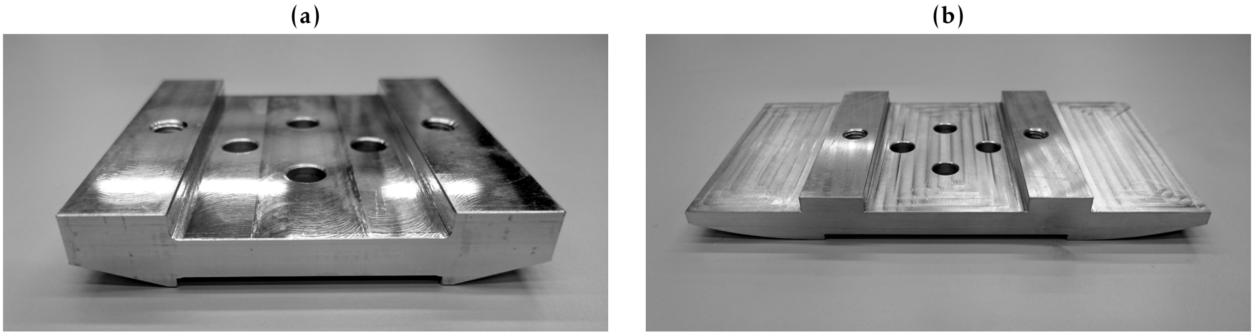
(a)

(b)

Figure 6.21: Specimen components of the modified rigid column: (a) Base F01; (b) Base F06.

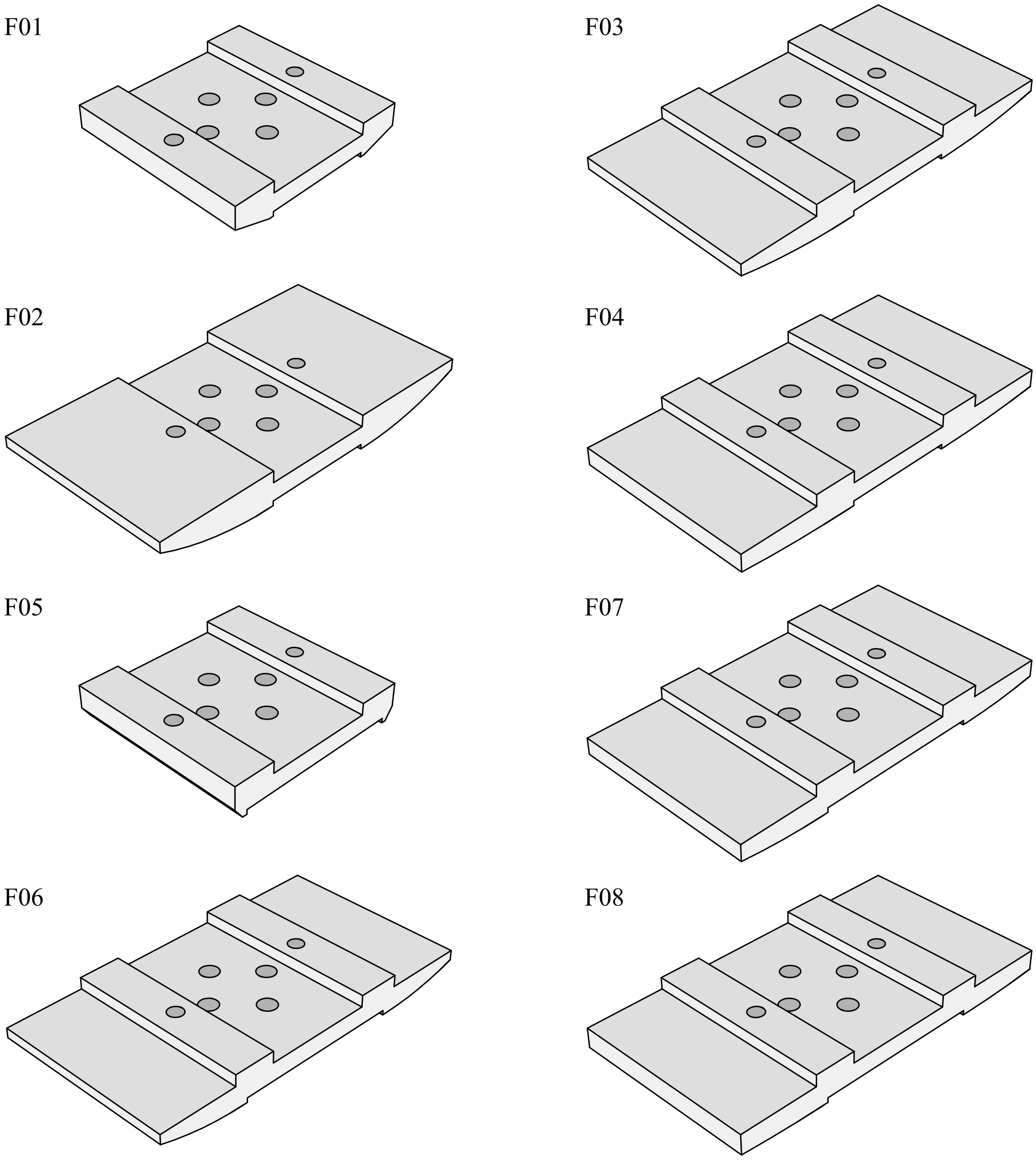

Figure 6.22: 3D illustration of the different investigated bases of the modified rigid column.

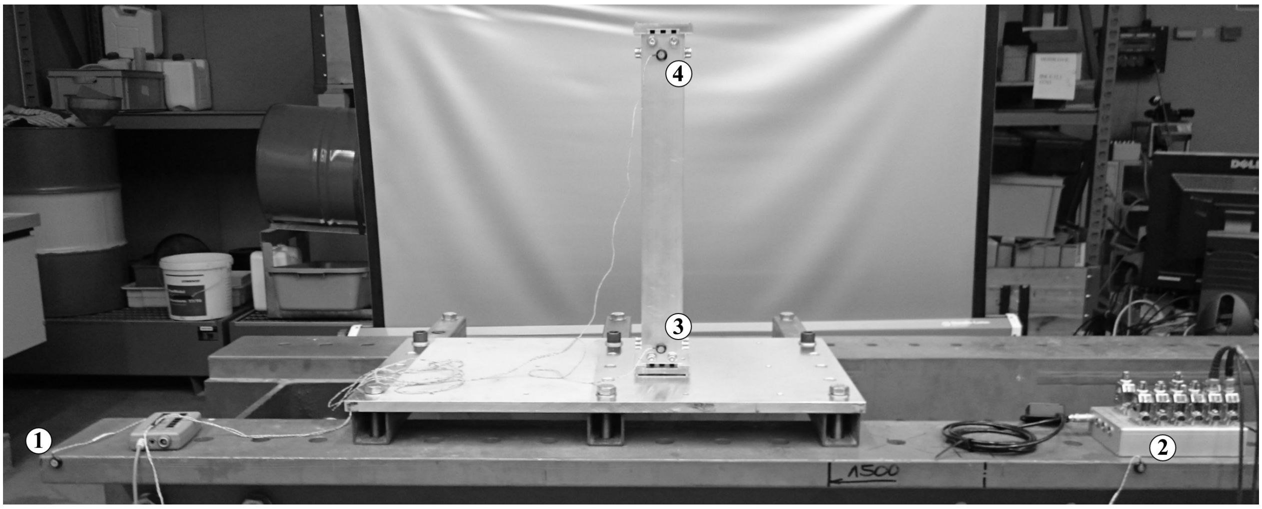

Figure 6.23: Test setup for free vibration test of the modified rigid columns.

6.4.3 Free Vibration Tests

Experimental Setup

Since only free vibration tests were performed the setup was mounted onto a rigid beam in a separate room in the IBK laboratory. The flat base was taken from the rocking podium structure experiment series (Fig. 6.23). Four NDI markers were placed on the setup; two on the rocking column and two at the base, as far apart as possible from each other to minimize the measuring error. The NDI software calculates the planar (if a plane can be defined) and the 3D angle between the two lines 1–2 and 3–4 and directly saves it. This makes post-processing of the data much easier. In this experiment the sampling frequency was selected to be 500 Hz since only four markers were used simultaneously.

Results and Comparison with Numerical Model

Each specimen (F01–F08) was tested three times so that in total 24 tests were performed. Found in the Appendix C, Figures C.30–C.37 plot the time histories of the normalized tilt angle, θ/α. Three time histories are plotted in each plot:

a) the experiment results,

b) the numerical solution with the theoretical (Housner) coefficient of restitution, and

c) the numerical solution with an empirical coefficient of restitution. The empirical coefficient of restitution was obtained from the first 10 motion cycles assuming that energy dissipation takes place only at impact.

As an example, the time history comparisons of specimen F01 are plotted here:

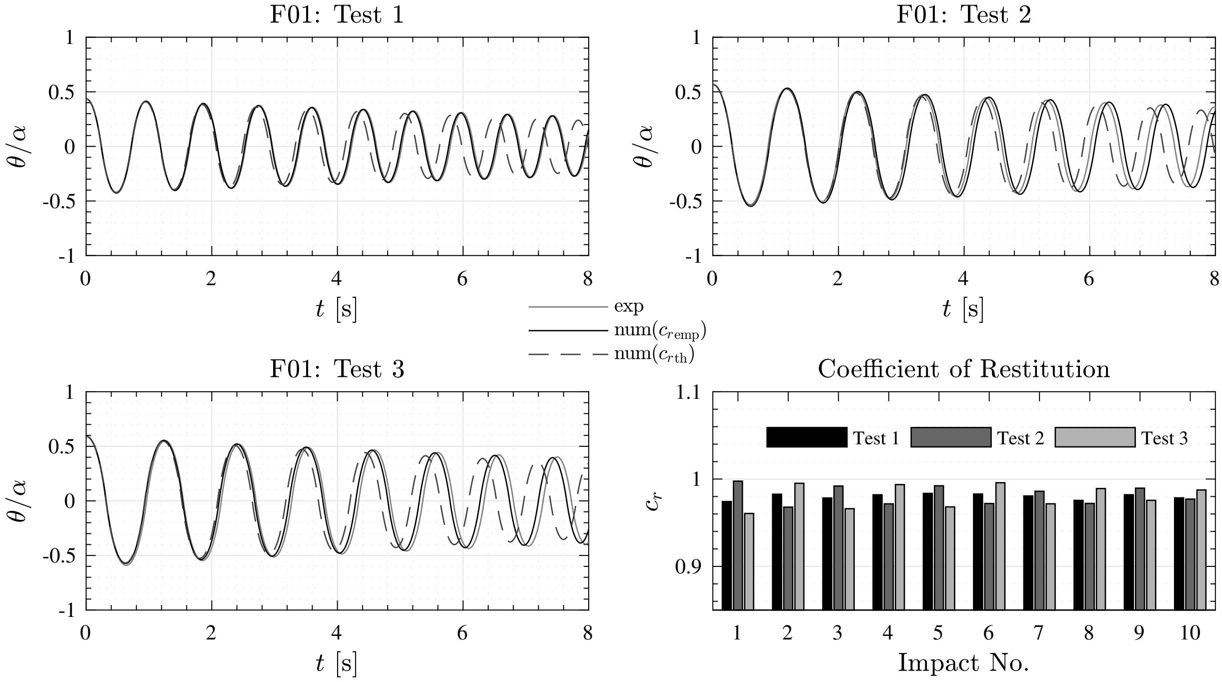

Figure 6.24: Specimen F01: Free vibration tests.

Observations

1) Housner's assumptions give a good estimate of the coefficient of restitution. For example, in Setup F01 the experimental value is $\sqrt{c_{r\mathrm{emp}}} = 0.990$ while Housner assumptions would give $\sqrt{c_{r\mathrm{th}}} = 0.988$. In terms of normalized energy loss per impact, the empirical coefficient would give $1 - c_{r\mathrm{emp}} = 1.94\%$ while Housner would give $1 - c_{r\mathrm{th}} = 2.36\%$.

2) The experimentally computed coefficient of restitution is influenced by the side from which impact occurs. In some tests, especially for specimens F05 and F08 the difference between the left and the right side was more than 10%. This indicates the difficulty in manufacturing completely symmetric specimens as well as measurement inaccuracies.

3) Housner-like coefficients of restitution slightly overestimate energy dissipation for the specimens without extensions (Specimens F01 and F05). In an effort to explore the source of this deviation, one has to explore Housner's assumptions:

   (a) the impact is instantaneous, and

   (b) all the impact forces are concentrated on the new pivot point.

   Assumption (a) allows for the typical assumption that the non-impact forces (in this case the weight) can be neglected during the application of CoAM. Assumption (b) leads to CoAM applied about the new pivot point. Otherwise, the CoAM should be applied about the point where the resultant of the impact forces is acting. Since the bodies are rigid, the impact is expected to be instantaneous (and the weight is expected to be much smaller than the impact forces), at least for relatively large velocity impacts.

   On the other, hand back-calculations for Specimen F01 show that the slight difference between the experimentally observed and the Housner coefficient of restitution means that the point of action of the force should be 0.2 mm away from the new pivot point. Missing the point of application of the resultant of the impact forces by only 0.2 mm (which corresponds to 0.4% of the base width) shows that Housner assumptions are valid and reasonable.

4) The addition of the curved wedges reverses the situation: Housner assumptions underestimate the energy loss consistently. It seems that the addition of the wedges shifts the point of action of the impact forces away from the axis of symmetry, hence increasing the energy dissipation. However, apart from stating that qualitative result, it is impossible to quantify the increase.

5) In general, the coefficient of restitution decreases (implying a larger damping ratio) for low velocity impacts. This explains why a rocking block does not need infinite number of impacts to stop, as Housner assumptions would predict, and is consistent with the results presented in [67]. Evidently, for smaller velocity impacts, the weight of the specimen is not negligible when compared to the impact forces and Housner's assumption (a) does not hold: the weight contributes to the impulse-momentum equation and slows down the motion.

6) Even though the coefficient of restitution is predicted relatively well, in many cases the numerical solutions diverge from the experimental data (*e.g.*, become out of phase). Unlike

elastic viscously-damped systems (where the period and the damping are only loosely related — $\omega_d = \omega_n \sqrt{1-\zeta^2}$) the 'period' of a rocking column (*i.e.*, twice the time interval between two impacts) strongly depends on damping. This is attributed to the dependence of the period on the amplitude of vibration (hence on the coefficient of restitution).

The above observation explains the difficulties in predicting the seismic response of a rigid block to a specific time history [76] and urges for a stochastic treatment of the rocking problem. It is evident that if deviations of 0.2 mm in the prediction of the location of the impact point (an error of 0.4% of the flat part of the foundation) lead to different time history results, then, the deterministic treatment of the rocking problem is impossible.

Conclusions

Curved base extensions are added to the flat base of a rocking rigid column in order to increase its overturning stability without significantly increasing the base moment. The equation of motion was derived and validated against free-vibration tests. It is shown that the theoretical values for the coefficient of restitution are numerically close to the experimentally obtained values. However, the response of the block is so sensitive to the exact coefficient of restitution value that a deterministic calculation of the response to a ground motion becomes practically impossible.

6.4.4 Shake Table Testing

A series of shaking table tests was conducted to measure the in-plane response of a virtually rigid rocking specimen to earthquake-like ground motion excitation. In this section the experimental specifications are discussed. The statistical evaluation of the test results, however, is conducted in the next chapter.

Specimen Details

The specimen that was used for the test series is identical to the setup F05 of the preceding section discussing free vibration responses. The specimens depth of 400 mm was chosen in order to keep the rocking motion in plane. The base has a total width of 82 mm, but the effective rocking width (distance between the pivot points O and O') is only 75 mm resulting in an effective slenderness of $\tan\alpha = 75\,\text{mm}/500\,\text{mm} = 0.15$. The rocking specimen had a total weight of 3.94 kg. Its eigenperiod, corresponding to both columns bending in phase out of the specimen's plane was measured to be 0.04 s (the Fourier spectrum analysis showed the peak response at 25 Hz). The base plates were machined such that the width of the base in contact with the support is 2 mm (Fig. D.7). This was done to make the impact zone as close to a point as possible, thus, simulating Housner's assumptions, yet wide enough to avoid damage during the repeated tests.

Recent research examined Housner's assumption regarding the point of action of the impact forces on a rigid rocking block with a flat base by either trying to determine the exact point of action of the impact forces [145] or by treating the location of the impact forces as a random variable [146]. The model examined here represents structures that are designed to rock, meaning that their contact with the support surface is designed such that the pivot points are well defined and the impact forces are concentrated as close to the corner as possible to decrease the uncertainty concerning the position of the impact forces. However, even if the pivot points are well defined and the coefficient of restitution is accurately estimated using measured data, the response of a rocking specimen is so sensitive to the initial conditions and the contact surface imperfections that the outcomes of individual experiments are often not repeatable, as seen in the preceding section. Further investigation of contact surface stiffness and imperfection effects on rocking motion are available in [147, 148].

Frequency Parameter and Coefficient of Restitution

Using the procedure described in Section 6.3.5 the frequency parameter and restitution coefficient are determined from a free vibration test.

$$p = 4.8883\ \mathrm{s}^{-1} \quad \rightarrow \quad \lambda = 0.6235, \tag{6.24}$$

$$c_{r\mathrm{emp}} = 0.9532. \tag{6.25}$$

Figure 6.25 plots the measured free rocking response of the specimen and the response obtained using the numerical model (Eq. 3.12) with the frequency parameter p and the coefficient of restitution $c_{r\mathrm{emp}}$ obtained from response measurements. Notably, the two response histories compare well for more than 20 rocking cycles. The measured and the Housner restitution coefficient differ by less than 1%:

$$c_{r\mathrm{th}} = 0.9465. \tag{6.26}$$

However, as shown in the next chapter, even such small discrepancies between the numerical model and the experimentally tested specimen lead to large errors in predicting the response of the rocking specimen to ground motion excitation.

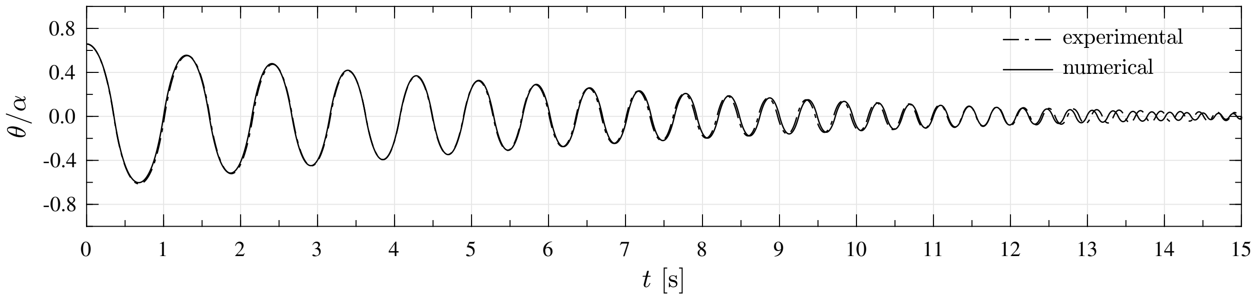

Figure 6.25: Free rocking response: comparison between measured response of the rocking specimen and the response computed using the numerical model.

Synthetic Ground Motion Ensembles

In order to constrain the uncertainty of the ground motion excitation, the ensemble of ground motions used in the shaking table tests and the subsequent numerical model response analyses was synthesized using a spectral version of the Rezaeian and Der Kiureghian stochastic ground motion model [149–152]. This model generates ground motion records from a stochastic model based on a set of parameters of engineering significance (namely, the predominant spectral content, the energy content, and duration). It has been shown [150] that the elastic response spectra of the synthetic motions are statistically compatible with the response spectrum of the original motion. Therefore, hereby, the generated synthetic motions are defined as target-spectrum-consistent. Observe that in this context, 'target-spectrum-consistent ground motions' should not be confused with other synthetic ground motions models which generate motions starting from a given response spectrum.

Two recorded ground motions, the longitudinal component of the 1940 El Centro Array #9 record (Fig. 6.26a) and the transverse component of the 2003 Lefkada record (Fig. 6.27a), were used as the *seed* ground motions. Two ground motion ensembles, each with one hundred synthetic ground motions, were generated from the two seed ground motions.

The individual ground motion and ensemble mean elastic pseudo-acceleration and displacement spectra are shown in Figure 6.26b-c for the 1940 El Centro seed motion, and in Figure 6.27b-c for the 2003 Lefkada seed motion. The Rezeian and Der Kiureghian model succeeds in producing synthetic ground motions with elastic response spectra similar to those of the recorded seed ground motions. The displacement spectra are also plotted because several researchers reported that the peak elastic spectral displacement is a good measure of the overturning potential of a ground motion [65, 132, 133].

Elastic response spectrum compatibility guarantees that the responses of the same elastic structure to the ground motions in the generated ensemble will be statistically similar. However, this does not guarantee that structures that respond inelastically, such as rocking structures, will have similar responses to individual ground motions in the generated ensemble. In fact, Vassiliou *et al.* [7] have shown that ground motions with identical elastic spectra can have very different rocking responses and rocking spectra. A stochastic model to generate ground motions with the same overturning potential does not exist. In this study, a stochastic method to generate ground motions with similar elastic response spectra was adopted as the best-available precondition for a statistical comparison of the numerical and experimental rocking oscillator responses.

Scaling of the Ground Motion Ensemble

The response of a rocking oscillator is affected by the size of the oscillator [16]: larger rocking structures excited by the same ground motion are more stable. As discussed in Section 6.1.3, changing the size of the rocking oscillator affects its response the same as changing the squared frequency of the ground motion excitation in the opposite direction. Hence, the time step Δt of the vector of the generated ground motions is scaled according to Equation (6.5) to facilitate an experimental investigation. Three different prototype rocking oscillators, with heights $2H$ equal to 5 m, 10 m, and 20 m, were tested.

Given that in the specimen height $2H$ is 0.5 m, the ground motions in the two synthetic ensembles were time-scaled a factor of $\sqrt{10}$, $\sqrt{20}$, and $\sqrt{40}$, respectively. The elastic response spectra of the time-scaled ground motions in the two generated ensembles are shown in Figures 6.26(d,g,j) for the 1940 El Centro seed motion and in Figures 6.27(d,g,j) for the 2003 Lefkada seed ground

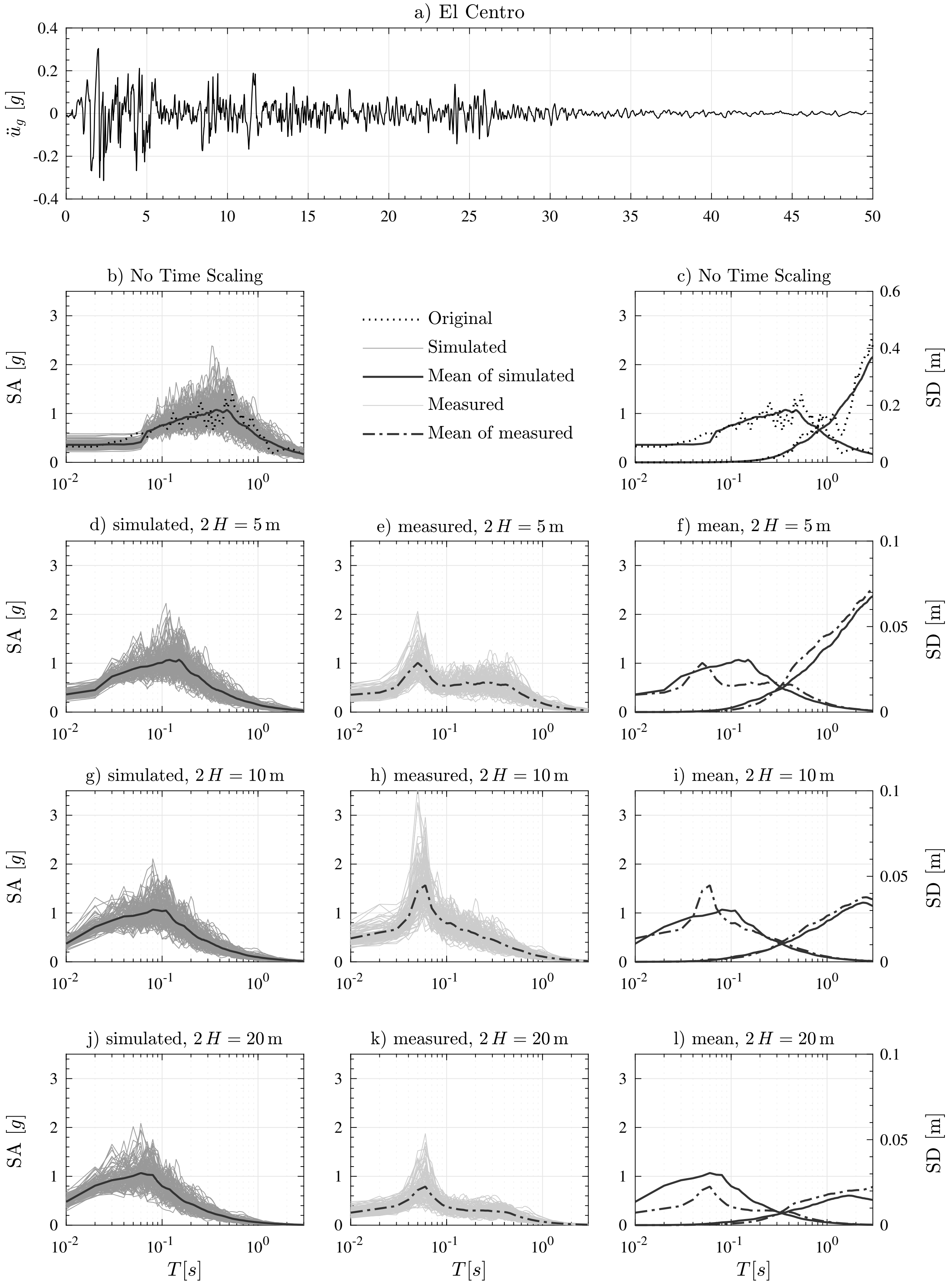

Figure 6.26: a) 1940 El Centro recorded ground motion; b) Pseudo-acceleration elastic response spectra of unscaled motions; c) Mean pseudo-acceleration and displacement elastic response spectra of the original and the simulated ground motions; d-l) Response spectra of the time-scaled simulated ground motions and their shake table realizations.

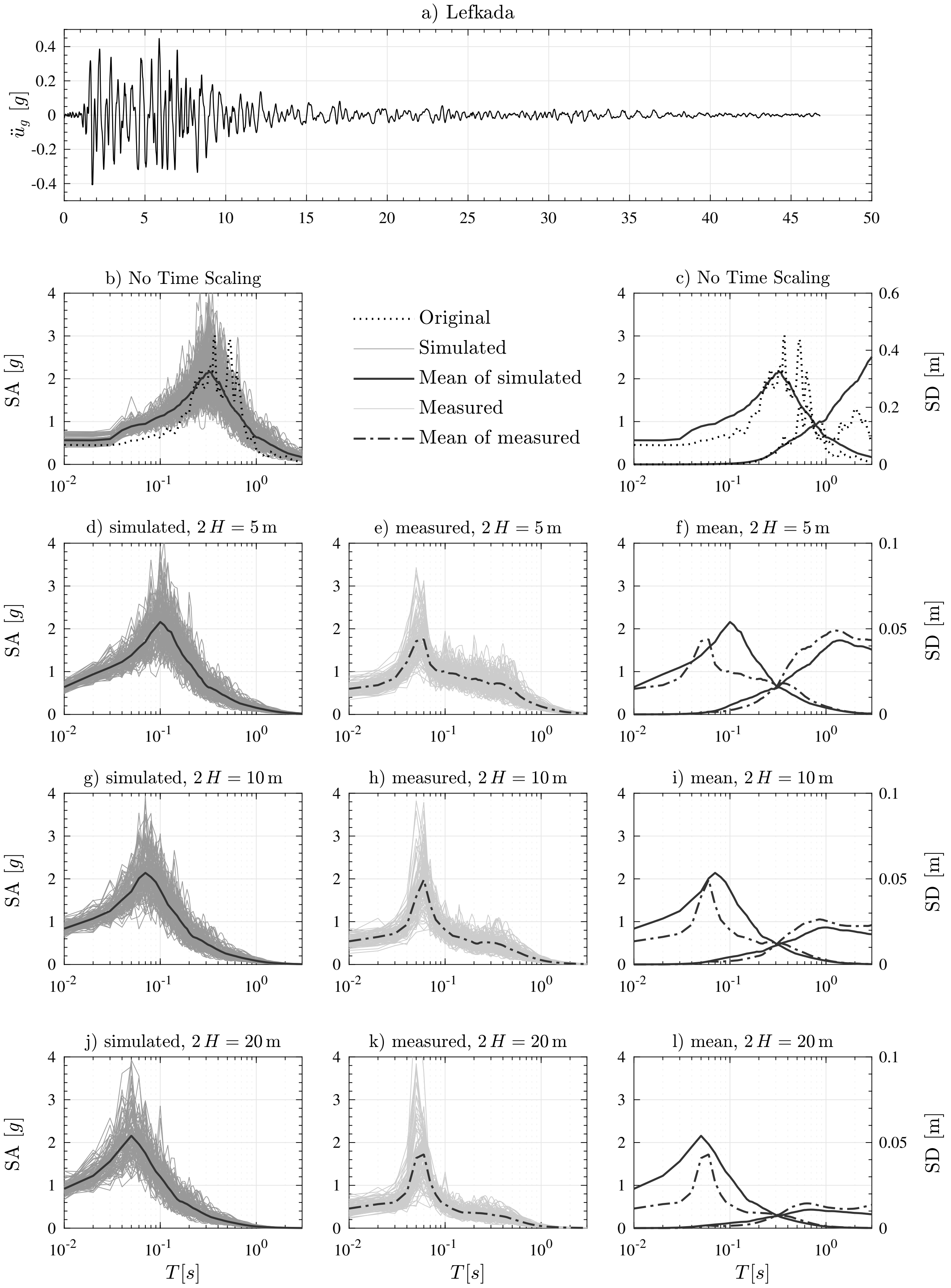

Figure 6.27: a) 2003 Lefkada recorded ground motion; b) Pseudo-acceleration elastic response spectra of unscaled motions; c) Mean pseudo-acceleration and displacement elastic response spectra of the original and the simulated ground motions; d-l) Response spectra of the time-scaled simulated ground motions and their shake table realizations.

motion: the shift of the maximum amplitudes towards shorter vibration periods, consistent with the ground motion time scaling, is evident.

As the ETH shaking table used to conduct the rocking response tests is not perfect, the dynamics of the table further modifies the motion that is applied at the base of the rocking specimen. The elastic response spectra of the applied and measured ground motions are shown Figures 6.26 and 6.27. The mean pseudo-acceleration response spectra in Figures 6.26 and 6.27 reveal an amplification of the ground motions in the shaking table resonance frequency range as well as the inability of the shaking table to reproduce the high-frequency ground motion components, particularly for the $2H = 20$ m prototype rocking oscillator.

For consistency, the measured (as-applied) ground motions are used as excitation to compute the response of the numerical model of the rocking oscillator.

Deterministic Rocking Response History Comparison

Figure 6.28 compares the tilt angle time histories of rocking oscillators with heights $2H$ equal to 5 m, 10 m, and 20 m, obtained in shaking table tests to the tilt angle time histories obtained using numerical models excited by the same measured (as-applied) time-scaled ground motions randomly picked from the ensembles (one for El Centro and one for Lefkada). Two numerical models, one with the 1963 Housner restitution coefficient (Eq. 6.26) and the other with a restitution coefficient measured in free rocking tests (Eq. 6.25) were run. In some cases the two models are capable of matching the measured response time history but, generally, they fail to do so. More disturbingly, neither model correctly predicts the occurrence of overturning, nor do the models provide an accurate estimate of the maximum attained tilt angle of the rocking oscillator.

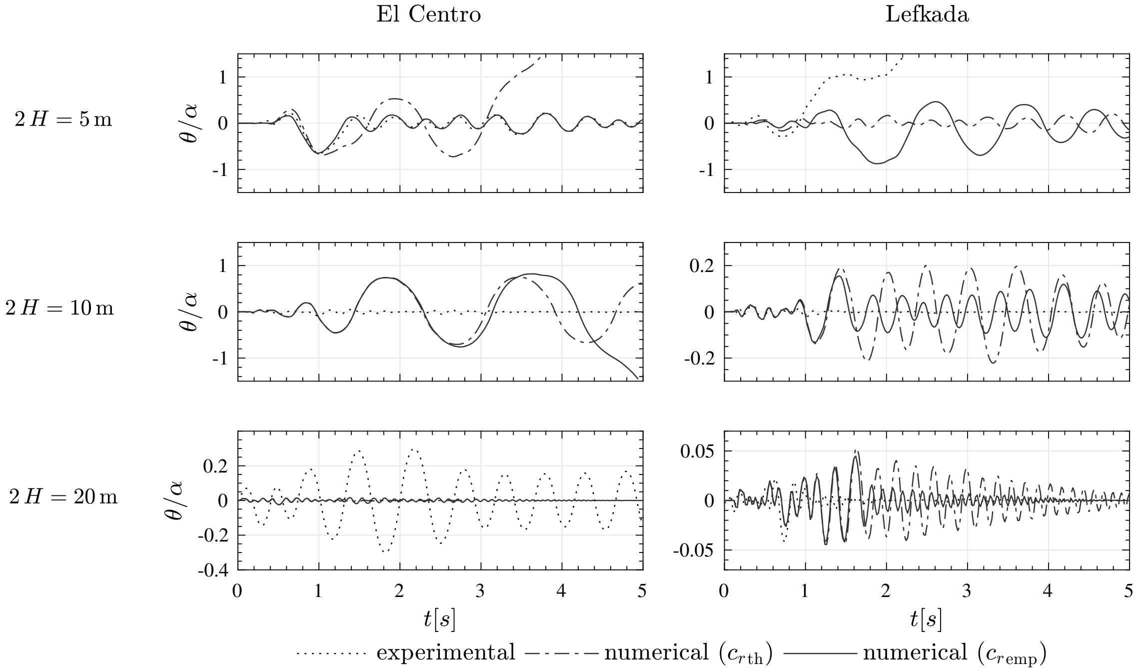

Figure 6.28: Deterministic comparison of the tilt angle response time histories to time-scaled recorded 1940 El Centro and 2003 Lefkada target-spectrum-consistent ground motions obtained from an experiment and from two numericical models.

It should be noted that large scaling factors (*e.g.*, for a height $2H = 20\,\mathrm{m}$ in the prototype scale) lead to heavy scaling of the ground motion. Consequently, the finite deformability of the specimen could also be a source of error. However, the same lack of ability of rocking models to describe shake table experiments has been reported by other researchers that have used true scale or slightly scaled models (*e.g.*, [67, 109]).

Figures 6.29 and 6.30 compare the normalized maxima of the tilt angle time histories, θ/α, obtained in shaking table tests, to the corresponding maxima of the numerical models (using the measured coefficient of restitution, $c_{r\mathrm{emp}}$) for all ground motions and all heights $2H$. Even though there is a trend, it can be seen clearly that the error is large in most cases.

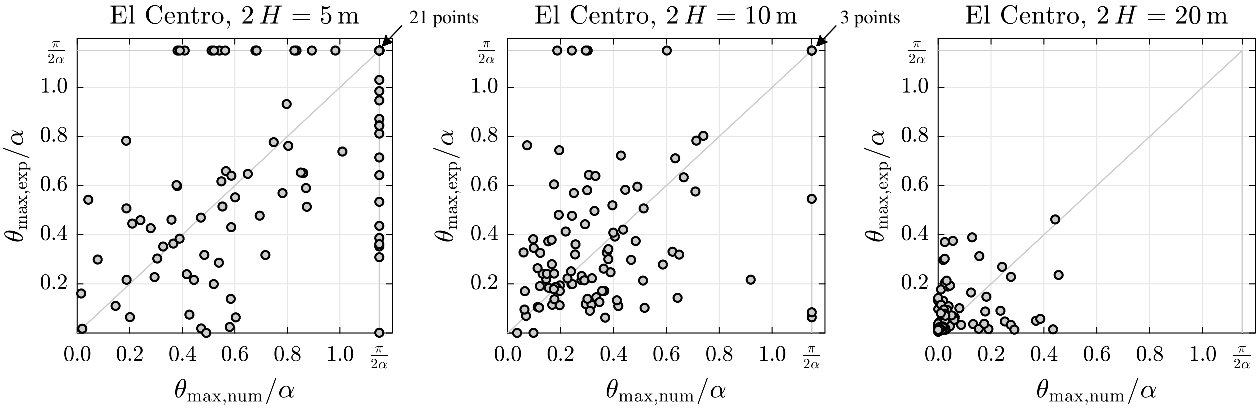

Figure 6.29: Comparison between the normalized maxima of the tilt angle time histories for the 1940 El Centro synthetic ground motion ensemble: experimental vs. numerical ($c_{r\mathrm{emp}}$).

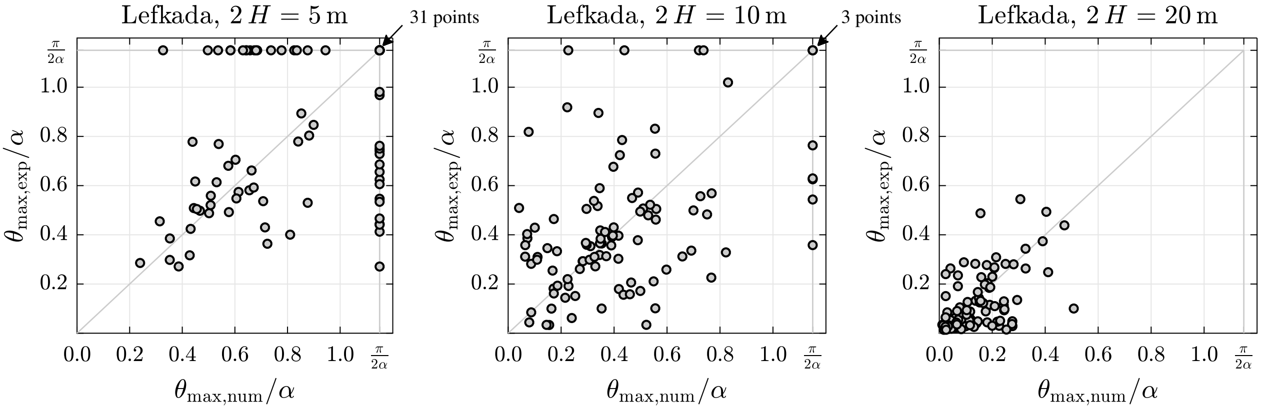

Figure 6.30: Comparison between the normalized maxima of the tilt angle time histories for the 2003 Lefkada synthetic ground motion ensemble: experimental vs. numerical ($c_{r\mathrm{emp}}$).

CHAPTER 7

PROBABILISTIC INVESTIGATION

In this chapter the probabilistic investigation of the 600 performed shaking table test on Housner's rocking model is presented. The exposition of the topic was done by M. Broccardo and is presented in the subsequent sections for completeness. The material presented in this chapter has been published as listed in Table 7.1.

Table 7.1: Probabilistic investigation: publication list.

Year	Title	Published in	Ref.
2017	Probabilistic Validation of the Housner Rocking Model	COMPDYN, Rhodes	[8]
2018	Is rocking motion predictable?	Earthquake Engng Struct Dyn	[9]

7.1 Statistical Comparison of Rocking Response Quantities

The experimental response data were obtained by conducting a total of 600 shaking table rocking oscillator response tests (text execution is described in the preceding chapter, Section 6.4.4). The response of rocking oscillators with total heights $2H$ of 5 m, 10 m, and 20 m, respectively, excited by each one of the hundred ground motions in the two target-spectrum-consistent ensembles was recorded. A numerical model (Eq. 3.12) was made for each prototype size and two restitution coefficient values, one measured and one theoretically computed. An array of 1200 time history analyses, one for each synthetic target-spectrum-consistent ground motion, was done.

The responses of the tested and the numerically modeled rocking oscillators are compared in terms of the maximum rocking tilt angle $\theta_{\max}$, obtained in response to the same measured (as-applied) ground motion excitation. In numerical simulations, a rocking block is declared to have statically overturned when its maximum tilt angle exceeds the slenderness of the block (*i.e.*, the center of the block mass moves over the pivot point), and dynamically overturned when its maximum tilt angle reaches $\pi/2$ (*i.e.*, 90°).

7.1.1 Explanatory Data Analysis

Following Yim *et al.* [22], the maximum tilt angle $\theta_{\max}$ normalized by the rocking block slenderness α data from the shaking table tests and from response analyses using numerical models with the 1963 Housner model and the measured coefficient of restitution values are arranged in ascending order and plotted in the form of empirical cumulative distribution functions (CDFs) in Figures 7.1 and 7.2. This plot shows the probability that the maximum tilt angle of a rocking oscillator is smaller or equal to a specific value of $\theta_{\max}/\alpha$.

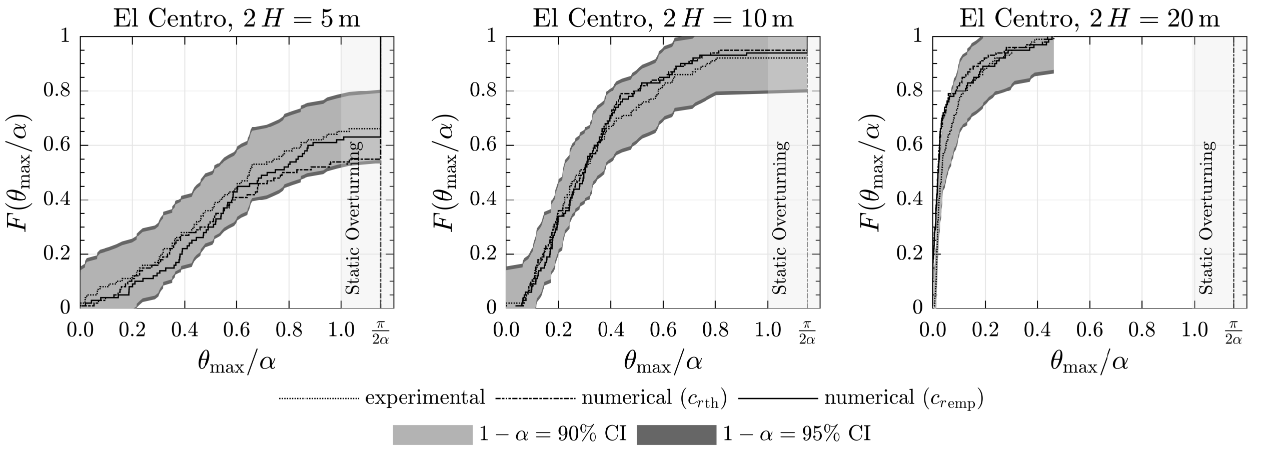

Figure 7.1: Cumulative distribution functions of the normalized maximum tilt angle $\theta_{\max}/\alpha$ for the 1940 El Centro synthetic ground motion ensemble.

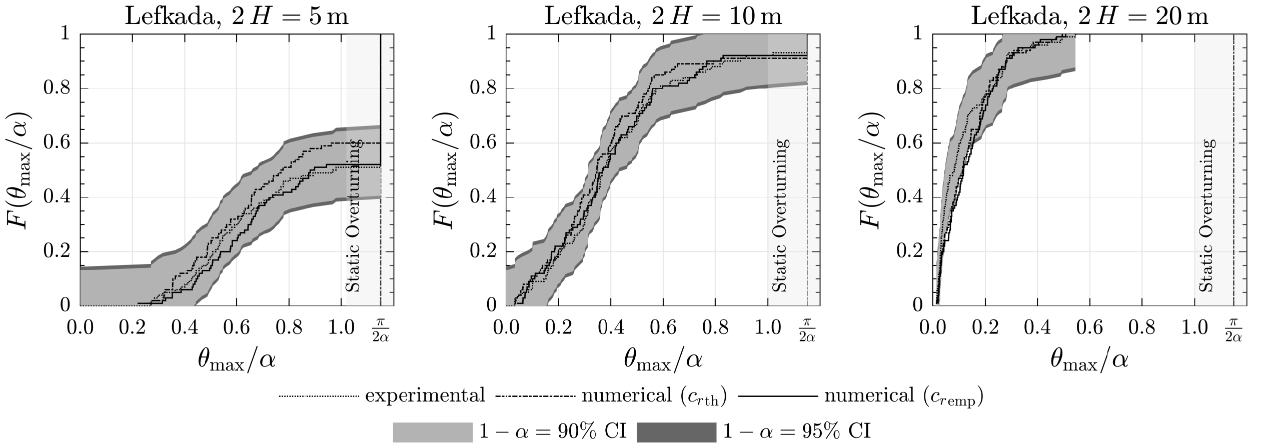

Figure 7.2: Cumulative distribution functions of the normalized maximum tilt angle $\theta_{\max}/\alpha$ for the 2003 Lefkada synthetic ground motion ensemble.

Table 7.2: Comparison of the rocking oscillator maximum tilt angle relative errors from the prototype tests and the numerical model with the measured coefficient of restitution.

		El Centro			Lefkada		
$2H$		θ_{num} [α]	θ_{exp} [α]	$\Delta\theta/\theta_{\text{exp}}$ [−]	θ_{num} [α]	θ_{exp} [α]	$\Delta\theta/\theta_{\text{exp}}$ [−]
5 m	25th percentile	0.430	0.360	0.194	0.600	0.550	0.091
	50th percentile	0.710	0.650	0.092	0.880	0.970	−0.093
	75th percentile	OT	OT	-	OT	OT	-
	CM	0.507	0.462	0.097	0.611	0.575	0.063
	CSD	0.246	0.268	-	0.172	0.176	-
10 m	25th percentile	0.180	0.170	0.059	0.220	0.260	−0.154
	50th percentile	0.300	0.280	0.071	0.370	0.370	0
	75th percentile	0.430	0.510	−0.157	0.550	0.540	0.019
	CM	0.311	0.310	0.003	0.369	0.385	−0.042
	CSD	0.181	0.199	-	0.200	0.211	-
20 m	25th percentile	0.005	0.018	−0.722	0.060	0.032	0.875
	50th percentile	0.019	0.033	−0.424	0.117	0.081	0.444
	75th percentile	0.051	0.095	−0.463	0.208	0.180	0.156
	CM	0.065	0.079	0.177	0.143	0.121	0.182
	CSD	0.108	0.098	-	0.109	0.118	-

OT: overturn, CM: conditional mean, CSD: conditional standard deviation, $\Delta\theta = \theta_{\text{num}} - \theta_{\text{exp}}$

In the same graph, the 90% and 95% nonparametric confidence intervals (CI) [153] are reported for the experimental CDF. A CI of 90% for the experimental empirical CDF means that if the experiments were performed with a different ensemble of hundred simulated ground motions there is a 90% probability that the new empirical CDF would be contained in the CI. Observe that the $\theta_{\max}/\alpha$ CDFs for the rocking blocks with 5 m and 10 m total heights have a 'jump' (*i.e.*, a discontinuity greater than 0.01) at $\theta_{\max}/\alpha = \pi/(2\,\alpha)$. These cases correspond to the overturning of the rocking oscillator.

Consequently, there is a finite probability mass associated with these CDF discontinuities, which is the probability of the overturning event. It follows that the CDF is a mixed CDF, comprising rocking oscillator non-overturning and overturning events:

$$F\left(\frac{\theta_{\max}}{\alpha}\right) = (1 - p_{\mathrm{o}})\,\overline{F}\left(\frac{\theta_{\max}}{\alpha}\right) + p_{\mathrm{o}}\;\mathcal{H}\left(\frac{\theta_{\max}}{\alpha} - \frac{\pi}{2\alpha}\right) \tag{7.1}$$

where $\mathcal{H}(\bullet)$ is the Heaviside function, $\overline{F}(\bullet)$ is a continuous CDF conditional to the non-overturning event set, and p_{o} is the probability of overturning. Table 7.2 reports the $\theta_{\max}/\alpha$ percentiles of the empirical F and the conditional mean and standard deviation values of the empirical $\overline{F}$.

The following conclusions are drawn from the data in Figures 7.1 and 7.2 and from Table 7.2:

- There is no systematic bias between the experimentally obtained empirical CDFs and numerically obtained empirical CDF. The non-exceedance probability obtained from the numerical models is larger than that obtained from prototype tests for some values of the normalized tilt angle and smaller for others (Figures 7.1 and 7.2). The same pattern emerges from the percentile data in Table 7.2.
- The numerical CDF curves for the $2H = 5$ m and the $2H = 10$ m rocking oscillators are well inside the confidence intervals (CIs) of the experimental CDFs. The exception are the numerical CDFs for the $2H = 20$ m rocking oscillators where both numerical CDFs are outside the 90% and 95% CIs for small values of normalized tilt angles. In the context of earthquake engineering, these data indicate that the 1963 Housner numerical models (with the theoretical as well as with the measured restitution coefficient) can predict the statistical distribution of the maximum response of a rocking oscillator with sufficient accuracy.
- The ground motion variability, even within a single target-spectrum-consistent ground motion ensemble, overshadows both the numerical model error and the chaotic behavior arising from the large sensitivity of the rocking oscillator. Ground motion uncertainty is expected to be even more dominant when the source and site variability is included.
- Figure 7.3 plots the relative distance between the numerical and experimental CDFs. 'Distance' refers to the Kolmogorov distance of the two CDFs, that is their vertical distance. The relative distance generally decreases as the tilt angle approaches the static overturning limit (Fig. 7.3). The relative distances are larger for the $2H = 20$ m rocking oscillator and for smaller tilt angles. Decrease of numerical model accuracy for taller rocking oscillators can be attributed to two factors: 1) the maximum tilt angles are small and close to the measurement error of the NDI system equal to $0.0053\,\alpha$; and 2) to represent a $2H = 20$ m rocking oscillator

prototype using the 0.5 m tall specimen, similitude dictates a time-scaling of the ground motion by $\sqrt{40} = 6.32$. Such scaling significantly increases the frequency content and this increases the error of the 1963 Housner model introduced by assuming that the rocking body is rigid. In fact, the eigenperiod of the specimen is 0.04 s. Scaling back to the $2H = 20$ m prototype level gives it an eigenperiod of 0.25 s, indicating that the deformability of the rocking oscillator cannot be neglected and that the rocking oscillator should be modeled as deformable, not rigid [66, 67, 72, 76, 109].

- For both ground motion sets and for $2H = 5$ m and $2H = 10$ m rocking oscillators, the maximum error in predicting the 25th, the 50th, and the 75th percentile of the tilt angle $\theta_{\max}$ is 19.4% (Tab. 7.2, El Centro, $2H = 5$ m), with most other relative distance values less than 10%.
- The relative distance is lower when the experimentally measured coefficient of restitution is used in place of the 1963 Housner theoretical value. The distance between the two numerical models is more pronounced for the smallest ($2H = 5$ m) rocking oscillator.
- A comparison between the probabilities of overturning when the Housner coefficient of restitution and when the measured coefficient of restitution are used reconfirms the 1980 finding of Yim *et al.* [22]: "From a probabilistic point of view, the coefficient of restitution influences the response [...] to a much lesser degree than the other system parameters."
- Finally, the shake table tests have experimentally validated Housner's proposition that larger tall slender structures are exceptionally stable. This can be seen clearly in Figures 7.1 and 7.2 where 100% of the $2H = 20$ m cases never reached a normalized rotation of greater than $0.5\,\alpha$ and $0.6\,\alpha$ for the El Centro and Lefkada sets of ground motions, respectively.

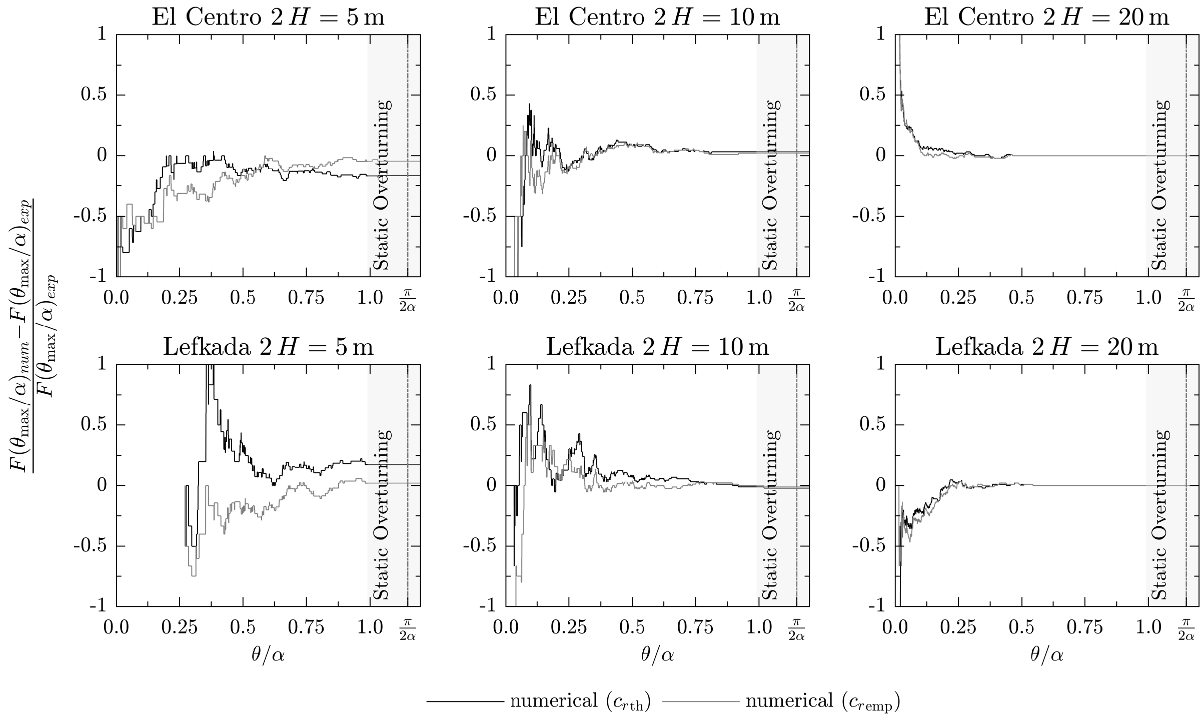

Figure 7.3: Relative distance (*i.e.*, relative error) in estimating the maximum rocking oscillator tilt CDFs.

7.2 Statistical Testing of Numerical Model Quality

The exploratory data analysis, presented above, indicates that the 1963 Housner numerical model can be used to predict the probability of overturning of a rigid rocking oscillator, and the probability distribution of the maximum tilt angle of a rigid rocking oscillator that does not overturn. These two engineering hypotheses are formally tested to determine whether there is statistical evidence against the use of numerical models to obtain a probabilistic characterization of the $\theta_{\max}/\alpha$. In specific, this section performs two hypothesis testing: the first hypothesis test tests the *overturning predictability* via a test of equal proportions, the second hypothesis test tests the conditional CDF $\overline{F}(\theta_{\max}/\alpha)$ via the classical two-sample Kolmogorov-Smirnov test [154–156].

The tests starts by randomly dividing the entire test set into two statistically independent subsets D_1 and D_2. Given the two subsets, the test statistics for the two proposed hypothesis tests are computed with the corresponding p-value. In the test of equal proportion the test statistic is the difference between the two proportions of overturning event, while in the two-sample Kolmogorov-Smirnov test the statistic test is the maximum distance between the two CDF conditional to the not overturning event.

The null hypothesis H_0 is rejected when the p-value is lower than a given statistical significance value α_s. A fairly large value of statistical significance of 0.1 is used to allow for a nuanced qualification of null hypothesis validity using an evidence classification scale shown in Table 7.3. Note: the computed p-values *do not* represent the probability that H_0 is true. A detailed explanation of the two hypothesis testing procedure can be found in [153].

Table 7.3: Evidence classification p-value scale [153].

p-value	Evidence	p-value	Evidence
< 0.01	Very strong against H_0	0.05 – 0.10	Medium-weak against H_0
0.01 – 0.05	Strong against H_0	> 0.10	Small or none against H_0

7.2.1 Test of Equal Proportion

The ability of the 1963 Housner numerical model to predict the probability of overturning of a rigid rocking oscillator p_o (Eq. 7.1) is tested using the experimental and numerical response data obtained for the two target-spectrum-consistent ground motion ensembles created from the 1940 El Centro and the 2003 Lefkada recorded ground motions. The proportions test is limited to the data for the $2H = 5$ m and $2H = 10$ m rocking oscillators because the $2H = 20$ m rocking oscillator did not experience overturning. The probability of overturning is computed by counting the number of overturn events in the considered set of rocking oscillator experimental or numerical response evaluations.

The proportions test is performed in three stages as follows:

1. $H_0 : p_{oD_1}^{ex} = p_{oD_2}^{ex}$ vs. $H_1 : p_{oD_1}^{ex} \neq p_{oD_2}^{ex}$, where $p_{oD_1}^{ex}$ and $p_{oD_2}^{ex}$ are the experimentally estimated probability of overturning. The null hypothesis H_0 is that the probability of overturning of

a rigid rocking oscillator obtained from shaking table experiments converges to some, yet unknown, value. If this hypothesis is rejected, there is strong evidence that the probability of overturning of a rigid rocking oscillator does not converge. This is interpreted as sign of probabilistic unpredictability.

2. $H_0 : p_{oD_1}^{ex} = p_{oD_2}^{nH}$ vs. $H_1 : p_{oD_1}^{ex} \neq p_{oD_2}^{nH}$, where $p_{oD_2}^{nH}$ is the estimated probability of overturning for the numerical model with the Housner coefficient of restitution. The null hypothesis H_0 is that the probability of overturning of a rigid rocking oscillator obtained from shaking table experiments is matched by the probability of overturning computed using the 1963 Housner numerical model with a theoretically computed coefficient of restitution. If this hypothesis is rejected, there is strong evidence that this numerical model cannot predict the probability of overturning of a rigid rocking oscillator, *i.e.*, that this numerical model is a poor proxy of the physical phenomenon.
3. $H_0 : p_{oD_1}^{ex} = p_{oD_2}^{nm}$ vs. $H_1 : p_{oD_1}^{ex} \neq p_{oD_2}^{nm}$, where $p_{oD_2}^{nm}$ is the estimated probability of overturning for the numerical model with the experimentally measured coefficient of restitution. The null hypothesis of Stage 3 follows the line of reasoning of Stage 2.

The computed p-values for the three proportions test stages are listed in Table 7.4. They show that, for the two generated target-spectrum-consistent ground motion ensembles, there is no evidence against the hypothesis that the probability of overturning of a rigid rocking oscillator is predictable, and there is no evidence against the hypothesis that the 1963 Housner numerical model with the measured restitution coefficient is a good predictor of the probability of overturning of a rigid rocking oscillator. On the other hand, the 1963 Housner numerical model with a theoretically computed coefficient of restitution may fail to correctly predict the probability of overturning of a rigid rocking oscillator (here, there is moderately weak evidence for this for the 10 m rocking oscillator and the 1940 El Centro ground motion ensemble). These conclusions corroborate the engineering observations made in Section 7.1.1.

Table 7.4: Computed p-values for the three proportions tests of the ability of the 1963 Housner numerical model to predict the probability of overturning of a rigid rocking oscillator. The shaded cell indicates a p-value smaller than 0.1.

	1940 El Centro		2003 Lefkada	
	$2H = 5$ m	$2H = 10$ m	$2H = 5$ m	$2H = 10$ m
Stage 1	0.40	0.46	0.32	0.70
Stage 2	0.099	1.00	0.69	0.29
Stage 3	0.29	0.69	0.32	0.46

7.2.2 Two-Sample Kolmogorov-Smirnov Test

The ability of the 1963 Housner numerical model to predict the CDF conditional to the non-overturning event of the maximum tilt angle of a rigid rocking oscillator ($\overline{F}$ in Eq. 7.1) is tested. Two such distributions are computed for each randomly generated response subset D_1 and D_2 pair and compared using the two-sample Kolmogorov-Smirnov goodness of fit test [154–156].

The two-sample Kolmogorov-Smirnov test is a non-parametrical statistical test if two empirical CDFs are samples from a common underlying, but yet unknown, CDF.

The proportions test is performed in three stages as follows:

1. $H_0 : \overline{F}^{ex}_{D_1} = \overline{F}^{ex}_{D_2}$ vs. $H_1 : \overline{F}^{ex}_{D_1} \neq \overline{F}^{ex}_{D_2}$ where $\overline{F}^{ex}_{D_1}$ and $\overline{F}^{ex}_{D_2}$ are the experimentally estimated conditional CDFs. The null hypothesis H_0 is that the CDF of the maximum tilt angle of a rigid rocking oscillator obtained from shaking table experiments converges to some, yet unknown, CDF. If this hypothesis is rejected, there is strong evidence that the tilt angle CDF of a rigid rocking oscillator does not converge. This is interpreted as sign of probabilistic unpredictability.
2. $H_0 : \overline{F}^{ex}_{D_1} = \overline{F}^{nH}_{D_2}$ vs. $H_1 : \overline{F}^{ex}_{D_1} \neq \overline{F}^{nH}_{D_2}$ where $\overline{F}^{nH}_{D_2}$ is the empirical conditional CDF for the numerical model with the Housner coefficient of restitution. The null hypothesis H_0 is that the CDF of the maximum tilt angle of a rigid rocking oscillator obtained from shaking table experiments is matched by the CDF of the maximum tilt angle computed using the 1963 Housner numerical model with a theoretically computed reinstitution coefficient. If this hypothesis is rejected, there is strong evidence that this numerical model cannot predict the CDF of the maximum tilt angle of a rigid rocking oscillator, *i.e.*, that this numerical model is a poor proxy of the physical phenomenon.
3. $H_0 : \overline{F}^{ex}_{D_1} = \overline{F}^{nm}_{D_2}$ vs. $H_1 : \overline{F}^{ex}_{D_1} \neq \overline{F}^{nm}_{D_2}$ where $\overline{F}^{nm}_{D_2}$ is the empirical conditional CDF for the numerical model with the experimentally measured coefficient of restitution. The null hypothesis of Stage 3 follows the line of reasoning of Stage 2.

The computed p-values for the three proportions test stages for the two target-spectrum-consistent ground motion ensembles are listed in Table 7.5.

Table 7.5: Computed p-values for the three proportions tests of the ability of the 1963 Housner numerical model to predict the CDF of the maximum tilt angle of a rigid rocking oscillator. The shaded cells indicate p-values smaller than 0.1.

	1940 El Centro			2003 Lefkada		
	$2H = 5$ m	$2H = 10$ m	$2H = 20$ m	$2H = 5$ m	$2H = 10$ m	$2H = 20$ m
Stage 1	0.40	0.89	0.68	0.62	0.20	0.24
Stage 2	0.17	0.99	0.017	0.07	0.58	0.017
Stage 3	0.14	0.99	0.032	0.62	0.34	0.009

Stage 1: Only small or no evidence against the hypothesis that the CDF (conditional on non-overturning) of the maximum tilt angle of a rigid rocking oscillator is probabilistically predictable for all the oscillator sizes.

Stage 2: Medium to weak evidence against the hypothesis that the 1963 Housner numerical model with the theoretical coefficient of restitution is a good predictor for $2H = 5$ m and $2H = 10$ m cases. However, for the $2H = 20$ m case, there is strong evidence against the hypothesis.

Stage 3: Small or no evidence against the hypothesis that the 1963 Housner numerical model with the measured coefficient of restitution is a good predictor for $2H = 5$ m and $2H = 10$ m cases. However, there is very strong evidence against the hypothesis for the $2H = 20$ m case.

These conclusions corroborate the engineering observations made in Section 7.1.1.

7.3 Conclusions

An experimental campaign has been designed to obtain observations of rocking motions to be compared with those obtained from numerical simulations. To constrain the uncertainty in the excitation, a stochastic model was used to generate two synthetic ground motions ensembles that match the physical characteristics of two recorded ground motions. These two ensembles were used in the numerical analyses and in the tests. The prototype response data were obtained by conducing 600 shaking table rocking oscillator response tests. The numerical model response data were obtained using the 1963 Housner model with measured and with theoretically computed restitution coefficient. Cumulative probability distributions of the maximum tilt of the rocking oscillator prototype and the rocking oscillator numerical models (that differ in the restitution coefficient) were compared first. The CDFs produced by the numerical models are within the 90% and the 95% of the confidence interval bounds of the experimental CDFs when the modeled structure is stiff enough to be assumed rigid.

These findings indicate that the Housner 1963 model can be used to predict the probability distribution of the maximum tilt angle of a rigid rocking oscillator, which is a mixed probability distribution comprising overturning and non-overturning events. Therefore, there is substantial *engineering* evidence for drawing the following conclusion: "The Housner 1963 model can predict the statistics of the response of a rocking oscillator subject to a given stochastic ground motion model when the modeled structure is stiff enough to be assumed rigid."

This conclusion was formally tested to determine whether there is *statistical* evidence against it. Specifically, two hypothesis test were performed: a test of equal proportions to test the 'overturning predictability,' and a two-sample Kolmogorov-Smirnov test to test the conditional CDF to the not-overturning event. The results of tests show that when the modeled structure is stiff enough to be assumed rigid, there is no statistical evidence against the above drawn conclusion.

CHAPTER 8

CONCLUSIONS AND OUTLOOK

8.1 Conclusions

Although rocking has been a subject of research for more than a century and it is present in our daily life, it is still a form of motion that — compared to other types of motions — has not been studied as extensively. Yet, the relatively small number of studies point to the remarkable characteristics of rocking structures that can be used very effectively to mitigate the harmful effects of earthquake ground motions.

In practice, compared to conventional design, very few structures exist where rocking is used to reduce the seismic demand: the idea of not fixing a structure to the ground leaves engineers that are unaware of the system's capabilities anxious because it is unusual and it contradicts the conventional design. The response of rocking objects is highly nonlinear due to the negative post-uplift stiffness. It can be solved analytically or with the use of modern finite-element software only with significant effort: the software struggles with systems that exhibit negative stiffness because common solution methods will not converge or simply will not work. The lack of relatively simple rocking structure design models, as opposed to complex response simulation models, deters from widespread use of rocking structures in earthquake engineering practice. It is this gap between the huge possibilities that the rocking design methodology offers and the lacking acceptance in the engineering community as well as the missing design solutions that motivated the work presented in this thesis the most.

This thesis aimed to develop and test a design concept that is applicable to buildings, bridges and tall slender structures such as wind turbines and chimneys. The main characteristic of this design concept is to let such structures uplift and engineer the post-uplift stiffness of the system, ranging from positive to negative, by making the structures roll before they start to rock. Hence, the findings presented in this thesis challenge the usual practice of anchoring the structures to the foundation to fully transmit the internal forces induced by earthquakes and other loads to the underlying soil, and the widely established belief that structures should have a positive post-yield stiffness to remain stable.

To do this, the behavior of rocking structures in various configurations and with different modeling assumptions has been studied extensively in this thesis for the free vibration response as well as the response induced by ground excitation. Starting with the Housner model, numerous SDOF rocking models were analyzed. It could be shown that, given certain preconditions, the responses of these models are similar, *e.g.*, the rocking response of a rocking frame can be reproduced with the simple rocking model of a solitary rigid block. One of the major issues of rocking, the lacking capacity, was addressed by extending the oscillator with curved bases without jeopardizing the force mitigation effect that rocking has. Design recommendations for such curved bases are proposed with respect to the following to parameters: 1) the uplifting force (via $\tan\alpha$), and 2) the needed (or desired) displacement capacity of the base column (θ_c).

The planar extension of these models to 2DOF allowed the investigation of podium structures where a second (elastic) degree of freedom is added to represent a superstructure possibly isolated on a rocking ground floor (= kinematic bearing). A dynamic model that describes the response of such structures was derived and presented, and was used to analyze the seismic response of a wide range of rocking podium structures to analytical pulse and recorded ground motion excitations. The computed responses indicate that rocking podium structures remain stable under ground motion excitation and that the rule-of-thumb guidelines of Polyakov are conservative in most of the cases examined. However, assuming the superstructure to be rigid is shown to be a justifiable assumption given that is not a flexible system, *e.g.*, a steel frame, making the primary response of the podium structure, the horizontal displacement of the column top of the ground floor, a SDOF problem. The equivalent seismic forces acting on the superstructure are controlled by the dimensions of the rocking podium columns. Determining the magnitude of these forces requires more accurate models of the rocking podium and the superstructure and is the focus of ongoing research.

A three-dimensional 2DOF model (3DOF when damping is included) that describes the dynamic behavior of a free-standing rigid cylindrical column that can uplift, rock, and wobble with the constraint that it does not slide or roll out of its original position (*i.e.*, an inverted pendulum) was developed next. It is the simplest 3D extension of the 2D Housner rigid-body rocking model. It was found that the 3D motion of a free-standing rigid cylinder is dominated by wobbling, making the responses of the damped and undamped models essentially identical. Therefore, the simpler undamped model of the rocking and wobbling 3D motion of a bounded free-standing rigid cylinder can be used with confidence if only a damping mechanism in the support surface is considered. Other damping mechanisms such as the rolling friction or air resistance were neglected. The ground motion analyses (using bidirectional records) showed that long lasting records exhibit more overturning potential. However, this fact was attributed to the low to nonexistent effect of the implemented damping mechanism.

The experimental campaign was used to successfully verify and validate the developed analytical models. Additionally, numerous shaking table tests were performed whose data were used in a probabilistic study investigating the statistical predictability of the response of a rigid rocking oscillator subject to a given stochastic ground motion model.

8.2 Summary of Each Chapter

Chapter 1 The first chapter presents a basic introduction into the world of rocking. The rocking concept is compared with the more common conventional seismic isolation concept. A small literature review on rocking is added where the rocking structures are divided into groups, *e.g.*, large rocking objects, 3D rocking objects, *etc.*

Chapter 2 In Chapter 2 specific topics from available literature are discussed in detail. The incentive behind this is to present the most related literature to the work presented in this thesis. Starting with Housner's block, free vibration and ground excited rocking motion is introduced and the equation of motion is derived. Important rocking motion parameters such as the frequency parameter p, the rocking period T_R, or the coefficient of restitution c_r, are explained. In addition, CoAM, one of the underlying assumptions when finding the analytical expression for c_r, is explained.

Following closely the work of Housner, the spectral approach of Zhang & Makris is explained subsequently. Rocking spectra are presented for a sinusoidal acceleration pulse where unsafe and safe ares within the spectra and their dependency on the oscillator's size R and on the pulse frequency ω_p are discussed. Then, the analytical model of a rocking frame, developed by M. Vassiliou, and its discovered size equivalency to a singular rocking column, are presented.

Lastly, a brief introduction to topic of dimensional analysis and similitude theory is given. Similitude is not only important in the context of experimental studies where the observed dimensions have to be scaled appropriately but also when comparing different rocking models.

Chapter 3 The third chapter discusses the planar (rolling and) rocking motion of SDOF systems where the only active degree of freedom is the tilt angle θ. First, solitary oscillators are examined. The factor λ, representing the mass distribution within a rocking oscillator, is introduced and the frequency parameter p is redefined with dependancy on λ, which was proven to be beneficial in the experimental campaign. Realistic values of mass distribution factors, caused by asymmetric geometry or different materials, are discussed subsequently.

Then, the model of the simple rigid rocking oscillator introduced by Housner is modified by extending its base with a) flat and b) curved wedges. The effect of this is an increased capacity (the center of the oscillator can displace more until failure occurs, *i.e.*, until it overturns). The equations of motion are derived for both a) and b). In case b) the additional parameter attributed to the curvature of the extended base mainly defines the tilting response of the oscillator. A response comparison of free-standing rigid oscillators shows that extending the base results in a decrease of the overturning area (with respect to the rocking spectra). In addition, unlike in the case of increasing size, no evidence is found that a positive post-uplift stiffness generally results in a better response behavior than a zero or negative post-uplift stiffness. In fact, the rocking oscillators with extended curved bases seem to be equally safe no matter what the curvature value ρ is, except, when it is lower than the critical curvature denoted with ρ_c.

Examining the linearized equations of motion reveals that similitude can be achieved between an extended curved based and a non-extended oscillator, given that the curvature value ρ of the curved extensions is equal to the aforementioned critical value ρ_c. The only difference originates from the coefficient of restitution which, assuming CoAM, depends on the slenderness α. Exemplary this fact is illustrated in various examples where the responses of a curved extended and a flat non-extended oscillator are compared in the nondimensional space θ/θ_c vs. $p\ t$.

Second, the analytical approach is extended to (rolling and) rocking frame structures. Similar as to the solitary oscillators, similitude between rocking frame structures can be achieved with respect to the linearized equations of motion given that the curvature value of the curved extended oscillators of the frame structure is ρ_c. The only difference originates from the coefficient of restitution.

Chapter 4 In Chapter 4 the planar rocking motion is extended to two degrees of freedom. The additional degree of freedom widens the range of rocking systems that can be investigated. One extension would be the elastic solitary rocking column. In this chapter, however, another model is investigated. Applying the isolation effect that rocking has, and being motivated by interesting rocking motion tests performed in Russia, a model was developed where an elastic structure, *e.g.*, a multi-story apartment building with masonry walls, is isolated on a rocking frame structure. In this thesis, such structures are referred to as *rocking podium structures*.

The equations of motion before and after uplift are derived, as well as an expression for the uplifting criterion which depends on the actual elastic deflection of the superstructure. It is shown analytically that the eigenfrequency of the superstructure is amplified in the uplifted state (*i.e.*, during rocking motion) where the main influencing parameters are the superstructure mass and the column slenderness. This amplification can very well be in the order of 3–5 and, therefore, significantly 'stiffen' the superstructure.

The developed analytical model is then used to test the postulated design guidelines by Polyakov [95] for rocking structures where the superstructure is assumed completely rigid. It is shown that the assumption of rigidity is justifiable for structures that are already stiff by nature, *e.g.*, masonry or reinforced concrete buildings (as opposed to an oscillating steel frame) such that their response behavior can be approximated by the SDOF rocking frame model (where the total weight of the cap-beam is increased accordingly). However, Polyakov's second design rule-of-thumb, that the demand for podium structures can be computed using the elastic response spectra, is found to be conservative.

Chapter 5 In the fifth chapter the rocking motion is extended to the three-dimensional space. In the first part, the equations of motion for the simplest 3D rocking model, a cylinder rocking and wobbling exclusively above the initial position of its base and without sliding or rolling out, are derived. By analyzing the response behavior of such cylinders, three characteristic response motions are identified: wobbling, quasi-rocking, and a combination of the two.

After implementing a simple damping mechanism at its base, the effect of damping is investigated for each of these response motions (which can be enforced using the respective initial conditions) as well as bidirectional ground motion excitation. It is found that, when compared to the undamped model, damping in the way it is implemented only affects the response when quasi-impacts occur.

A spectral response comparison showed that certain ground motion characteristics affect the response behavior noticeably while others do not. However, the presented 3D rocking model barely dissipates energy, such that longer ground motion records with moderate accelerations are more likely to cause overturning as opposed to short and high acceleration ground motion records. In reality, however, damping is expected to be present, *e.g.*, due to imperfections, even if the cylinder only performs a pure wobbling motion. Therefore, the found correlation needs to be treated with care until a more sophisticated model of the 3D rocking cylinder is used to either validate or reject this statement as it was done in 2D by Giouvanidis & Dimitrakopoulos [157].

Chapter 6 In Chapter 6 the experimental investigations that were performed in the framework of this thesis are presented and discussed. First, the main laboratory equipment such as accelerometers, shaking table, and NDI Optotrak-Certus system, are introduced and a typical test setup and test procedure for shaking table experiments are presented. In order to perform such tests a minimum of three computers in simultaneous use are needed to execute commands, control the actuator, record all measurements, *etc.* However, when free vibration tests are performed, only the NDI host PC is needed.

Second, the experimental investigation of the rocking podium structure is presented. Major design, modeling, and test execution issues are presented which were discovered during the first experimental study. These issues made a numerical and experimental model comparison meaningless and, therefore, the model needed a makeover. Hence, a second and improved model is introduced where only aluminum EN AW-6060 is used for structural model components (steel was used for additional weights). It is shown that accurate model calibration is crucial for the post-processing of rocking experiment data. The podium structure setup was tested in a series 24 shaking table experiments showing relatively good results. Only in two cases did the numerical and experimental model differ significantly (one model predicted overturning while the other did not, or *vice versa*). However, this fact only occurs when the model is close to overturning and minor differences between the models such as sliding effects, out-of-plane movement, gap opening, *etc.*, can have a significant effect on the test outcome.

Third, the rocking column setup is modified to allow testing of oscillators with extended curved bases. The redesigned rigid rocking column is presented in detail for eight different configurations (two flat and six curved models). The test results of a total of 24 performed free vibration tests are presented. It is shown that the developed analytical model for oscillators with curved bases works very well. In the following, one of the flat model setups was used for a series of 600 shaking table experiments that formed the data of the probabilistic investigation discussed in Chapter 7.

Chapter 7 Chapter 7 tries to probabilistically validate the rocking model of Housner (non-extended rigid oscillator). Two seed ground motions (El Centro and Lefkada) were used to create synthetic ground motion ensembles comprising 100 to the seed ground motion similar (in terms of defined characteristics) records. The rigid rocking oscillator model with a flat base (described in Chapter 6) is subjected to these two ensembles for prototype sizes of $2H = \{5\text{ m}, 10\text{ m}, 20\text{ m}\}$. This leads to three different time scaling factors, resulting in a total of 600 experiments. The corresponding numerical data consist of 1'200 time history analyses (two different restitution coefficient values were used).

No systematic bias between the experimentally and numerically obtained empirical mixed CDFs could be identified, and the data indicate that the Housner model can predict the statistical distribution of the maximum response, which is a mixed probability distribution comprising overturning and non-overturning events, with sufficient accuracy. This indication is formally tested to determine whether there is statistical evidence against it. Specifically, two hypothesis test are performed: a test of equal proportions to test the *overturning predictability*, and a two-sample Kolmogorov-Smirnov test to test the conditional CDF to the not-overturning event. The results of the tests show that when the modeled structure is stiff enough to be assumed rigid, there is no statistical evidence against it and one can conclude:

"The Housner 1963 model can predict the statistics of the response of a rocking oscillator subject to a given stochastic ground motion model when the modeled structure is stiff enough to be assumed rigid."

8.3 Outlook

8.3.1 Elastic Oscillators

The developed model of the rolling-and-rocking oscillator is assumed to be rigid. It is clear that in reality this is not the case, but the question is: «How much is the introduced error?» From a certain size of the oscillator (or a certain scaling factor in the experiments), the present elasticity cannot be neglected anymore. This fact could be noticed very well during the probabilistic investigation of rocking experiments of a rigid rocking block. For the $2H = 20$ m experiments, where a scaling factor of $\sqrt{6}$ was used, uplift could not be captured well: the CDF of the experimental model lay outside the confidence interval bounds.

Furthermore, rigidity was assumed to be true for reinforced concrete columns with a total height $2H \leq 6$ m. However, if one intends to apply the model to other larger objects such as bridge piers or rocking chimneys, elasticity will influence the response more and more with increasing height.

Hence, in these cases a model that includes elasticity should be used.

8.3.2 Rocking Podium Structures

During the experimental tests of the rocking podium structure, accelerometers were placed not only on the shaking table to measure the acceleration that was applied to the numerical model afterwards but also on the cap-beam and on the top mass. During the occurred impacts, high acceleration peaks were noticed in the acceleration time history of the cap-beam and the top mass. This fact has previously been shown both experimentally [69, 72, 74] and numerically [137, 158].

The occurred acceleration peaks were well above the uplifting acceleration level and could cause significantly larger than assumed forces in the superstructure. Hence, the force mitigation attributed to the kinematic bearing (rocking ground floor) is questionable. Note however that the experimental setup was designed to be as close to the numerical model as possible. The latter assumes the impact happens instantaneously and that the pivot points are only located at the edges of the flat base of the column. This assumption, originating from the CoAM, that is applied to the numerical model was enforced in the experiments via its design. As a result, impacts are accompanied by large vertical forces acting on the new pivot point, leading to significant vibrations that spread within the entire experimental setup.

In opposition to this finding stand the observations made from various real size experiments performed in Russia [103, 104] where rocking podium structures were released into free vibration showing a significant decrease of amplitude over a short period of time. This indicates that at prototype scale damping is more prominent (it affects the response of the rocking podium structure more than at model scale). Hence, in order to investigate damping effects, experiments should be carried out where a) the size of the setup is closer to the prototype size, and where b) more realistic materials are used (*e.g.*, reinforced concrete and steel).

8.3.3 3D Rocking Motion

The experimental campaign was limited to planar rocking models with up to two degrees of freedom. On one hand, there is the shaking table in the IBK laboratory: it only allows for uni-axial excitation and, therefore, makes it theoretically impossible to test a perfectly symmetric 3D specimen such as a rocking cylinder. On the other hand, a 3D rocking model will behave unpredictable. As shown in this thesis, the two-dimensional rocking model is sensitive to initial conditions and small imperfections which, for a bystander, might look just like a random process. I expect that extending rocking experiments to 3D would exponentially increase effects that lead to said impression. Nevertheless, the following topics with respect to 3D rocking motion remain to be investigated:

1. verification and validation of the 3D motion rigid cylinders,
2. development of a model for 3D motion of flexible rocking bodies,
3. development of a model for 3D motion of a podium structure.

APPENDIX A

THEORETICAL SUPPLEMENTS

A.1 Ricker Wavelets

The second derivative of the Gaussian distribution, $\exp\left(t^2/2\right)$, known in the seismological literature as the 'symmetric Ricker' wavelet [125, 126], given by Equation (A.1), has often been used to approximate the pulses contained in pulse-like ground motions. The value of the pulse period $T_p = 2\pi/\omega_p$ maximizes the Fourier spectrum of the symmetric Ricker wavelet.

Similarly, Equation (A.2) is the scaled third derivative of the Gaussian distribution, also referred to as the 'antisymmetric Ricker' wavelet, in which factor β is equal to 1.38011 [159] to enforce that the function maximum is equal to a_p. The symmetry point/axis of the respective wavelet is given by t_m.

$$a_p(t) = -a_p\left(1 - \frac{2\pi^2(t-t_m)^2}{T_p^2}\right)\exp\left(-\frac{1}{2}\frac{2\pi^2(t-t_m)^2}{T_p^2}\right), \tag{A.1}$$

$$a_p(t) = -\frac{a_p}{\beta}\left(\frac{4\pi^2(t-t_m)^2}{3\,T_p^2} - 3\right)\frac{2\pi(t-t_m)}{\sqrt{3}T_p}\exp\left(-\frac{1}{2}\frac{4\pi^2(t-t_m)^2}{3\,T_p^2}\right). \tag{A.2}$$

When a_p is preset with a '−' the first part of the wavelets exhibit a positive acceleration.

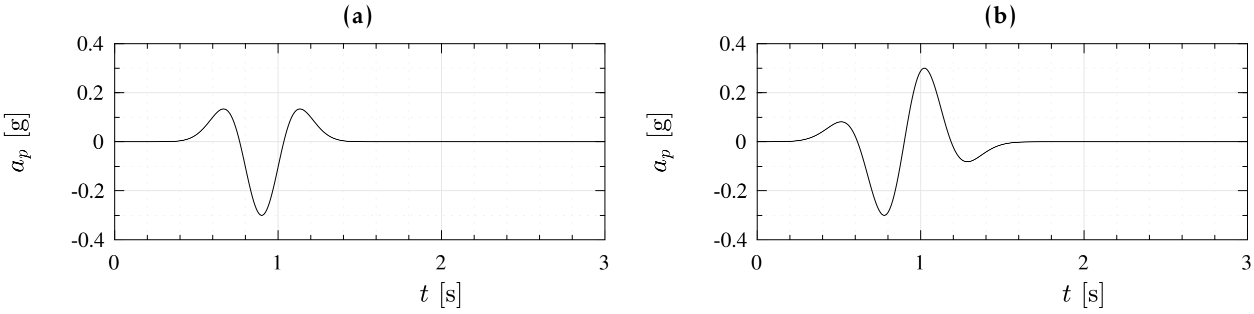

Figure A.1: Ricker wavelets with $a_p = 0.3\,g$ and $T_p = 0.6$ s: (a) Symmetric; (b) Antisymmetric.

A.2 Lagrangian Equations

The equations of motion of a n-dimensional rocking problem are derived by applying Lagrange's equations of the second kind or the *Euler–Lagrange* equations of motion. The equations are:

$$\frac{\mathrm{d}}{\mathrm{d}t}\left(\frac{\partial L}{\partial \dot{q}_i}\right) - \frac{\partial L}{\partial q_i} + \frac{\partial D}{\partial \dot{q}_i} = 0 \qquad (i = 1, 2, \ldots, n), \tag{A.3}$$

where q_i is one of the n independent coordinates, L is the Lagrangian and D the dissipated energy of the rocking system. The Lagrangian itself is defined as the difference between the kinetic energy T and the potential energy V, or

$$L = T - V\,. \tag{A.4}$$

A.3 Equations of Motion

A.3.1 Rolling-and-Rocking Podium Structure

Phase I

$$
\begin{aligned}
&\ddot{\theta}\cdot\Big(\lambda+(1+4\gamma)\cdot\Big(1+4\rho\cos\alpha\cdot\big(\cos(\pm\alpha-\theta)-\cos\alpha\big)+8\rho^2\cos^2\alpha\cdot\big(1-\cos\theta\big)\Big)\\
&\quad+4\gamma\eta\cdot\Big(\sin^2\big(\pm\alpha-\theta\big)+4\rho\cos\alpha\,\sin(\pm\alpha-\theta)\,\sin\theta+4\rho^2\cos^2\alpha\,\sin^2\theta\Big)\Big)\\
&=-\dot{\theta}^2\cdot\Big((1+4\gamma)\cdot\Big(2\rho\cos\alpha\sin(\pm\alpha-\theta)+4\rho^2\cos^2\alpha\sin\theta\Big)\\
&\qquad-2\gamma\eta\cdot\Big(\sin(\pm2\alpha-2\theta)-4\rho\cos\alpha\,\sin(\pm\alpha-2\theta)-4\rho^2\cos^2\alpha\,\sin(2\theta)\Big)\Big)\\
&\quad-\frac{g}{R}(1+2\gamma+2\gamma\eta)\cdot\Big(\sin(\pm\alpha-\theta)+2\rho\cos\alpha\sin\theta\Big)\\
&\quad-\frac{\ddot{u}_g}{R}(1+2\gamma)\cdot\Big(\cos(\pm\alpha-\theta)+2\rho\cos\alpha\big(1-\cos\theta\big)\Big)\\
&\quad+\frac{2\gamma\eta\omega_s}{R}\cdot\Big(\cos(\pm\alpha-\theta)+2\rho\cos\alpha\big(1-\cos\theta\big)\Big)\cdot\Big(\omega_s\cdot\big(u_{\mathrm{T}}-u_{\mathrm{B}}\big)+2\zeta_s\cdot\big(\dot{u}_{\mathrm{T}}-\dot{u}_{\mathrm{B}}\big)\Big)
\end{aligned}
\tag{A.5}
$$

Phase II

$$
\begin{aligned}
&\ddot{\theta}\cdot\Big(\lambda+(1+4\gamma)\cdot\Big(1+4\rho\,\cos\alpha\cdot\big(\cos(\alpha-\beta)-\cos\alpha\big)+8\rho^2\,\cos^2\alpha\cdot\big(1-\cos\beta\big)\Big)\\
&\quad+4\gamma\eta\Big(\sin^2(\pm\alpha-\theta)+4\rho\,\cos\alpha\,\sin(\pm\alpha-\theta)\big(\sin\theta+\sin(\pm\beta-\theta)\big)\\
&\qquad+4\rho^2\,\cos^2\alpha\,\big(\sin^2\theta+2\,\sin(\pm\beta-\theta)\sin\theta+\sin^2(\pm\beta-\theta)\big)\Big)\Big)\\
&=\dot{\theta}^2\cdot\Big(2\gamma\eta\cdot\Big(\sin(\pm2\alpha-2\theta)-4\rho\cos\alpha\,\big(\sin(\pm\alpha-2\theta)-\sin(\pm\alpha\pm\beta-2\theta)\big)\\
&\qquad-4\rho^2\cos^2\alpha\,\big(\sin(2\theta)+2\,\sin(\pm\beta-2\theta)-\sin(\pm2\beta-2\theta)\big)\Big)\Big)\\
&\quad-\frac{g}{R}(1+2\gamma+2\gamma\eta)\cdot\Big(\sin(\pm\alpha-\theta)+2\rho\,\cos\alpha\cdot\big(\sin(\pm\beta-\theta)+\sin\theta\big)\Big)\\
&\quad-\frac{\ddot{u}_g}{R}(1+2\gamma)\cdot\Big(\cos(\pm\alpha-\theta)+2\rho\,\cos\alpha\cdot\big(\cos(\pm\beta-\theta)-\cos\theta\big)\Big)\\
&\quad+\frac{2\gamma\eta\omega_s}{R}\cdot\Big(\cos(\pm\alpha-\theta)+2\rho\cos\alpha\,\big(\cos(\pm\beta-\theta)-\cos\theta\big)\Big)\cdot\Big(\omega_s\cdot\big(u_{\mathrm{T}}-u_{\mathrm{B}}\big)+2\zeta_s\cdot\big(\dot{u}_{\mathrm{T}}-\dot{u}_{\mathrm{B}}\big)\Big)
\end{aligned}
\tag{A.6}
$$

APPENDIX B

IMPLEMENTATION IN MATLAB

In this chapter I briefly discuss the procedure to numerically solve the equations of motion using MATLAB [160]. It may be mentioned here that several descriptions or examples presented subsequently were obtained from the MathWorks documentation [161].

B.1 Ordinary Differential Equation (ODE)

An ordinary differential equation (ODE) contains one or more derivatives of a dependent variable, x, with respect to a single independent variable, t, usually referred to as time. The notation used here for representing derivatives of x with respect to t is $\dot{x}$ for a first derivative, $\ddot{x}$ for a second derivative, and so on. The order of the ODE is equal to the highest-order derivative of x that appears in the equation, *e.g.*, the following 2nd order ODE, $\mathcal{G}_1$:

$$\mathcal{G}_1 : \ddot{x} - 9x + 8 . \tag{B.1}$$

B.1.1 Basic ODE solvers in MATLAB

The ODE solvers in MATLAB solve initial value problems with a variety of properties. The solvers can work on stiff or nonstiff problems, problems with a mass matrix, differential algebraic equations (DAEs), or fully implicit problems. Here, only solvers for stiff and nonstiff problems will be discussed. The rocking block initially is infinitesimally stiff. Once rocking is initiated, the problem behaves nonstiff (post-uplift stiffness is mostly negative for rocking problems).

`ode45` performs well with most ODE problems and should generally be your first choice of solver. However, `ode23` and `ode113` can be more efficient than `ode45` for problems with looser or tighter accuracy requirements.

Some ODE problems exhibit stiffness, or difficulty in evaluation. Stiffness is a term that defies a precise definition, but in general, stiffness occurs when there is a difference in scaling somewhere in the problem. For example, if an ODE has two solution components that vary on drastically different time scales, then the equation might be stiff. You can identify a problem as stiff if nonstiff solvers (such as `ode45`) are unable to solve the problem or are extremely slow. If you observe that a nonstiff solver is very slow, try using a stiff solver such as `ode15s` instead. When using a stiff solver, you can improve reliability and efficiency by supplying the Jacobian matrix or its sparsity pattern.

Table B.1: ODE solvers implemented in Matlab.

Solver	Problem Type	Accuracy	Solver	Problem Type	Accuracy
`ode45`	Nonstiff	Medium	`ode15s`	Stiff	Low to Medium
`ode23`		Low	`ode23s`		Low
`ode113`		Low to High	`ode23t`		Low
`ode15i`	Fully implicit	Low	`ode23tb`		Low

Table B.1 provides general guidelines on when to use each of the different solvers.

B.1.2 Solving ODEs in Matlab

In an initial value problem, the ODE is solved by starting from an initial state. Using the initial condition, x_0, as well as a period of time over which the answer is to be obtained, (t_0, t_f), the solution is obtained iteratively. At each step the solver applies a particular algorithm to the results of previous steps. At the first such step, the initial condition provides the necessary information that allows the integration to proceed.

The final result is that the ODE solver returns a vector of time steps $t = \left[t_0, t_1, t_2, \ldots, t_f\right]$ as well as the corresponding solution at each step $x = \left[x_0, x_1, x_2, \ldots, x_f\right]$.

Relevant Parameters of ODE Solvers

Via the option `odeset` various input parameters of the ODE solvers, that significantly influence the output, can be set. A selection of these parameters, that seem important for the rocking problem, are mentioned in the following.

`'AbsTol'` Absolute error tolerance

This tolerance is a threshold below which the value of the solution becomes unimportant. If the solution $|x|$ is smaller than `AbsTol`, then the solver does not need to obtain any correct digits in $|x|$. For this reason, the value of `AbsTol` should take into account the scale of the solution components. If `AbsTol` is a vector, then it must be the same length as the solution. If `AbsTol` is a scalar, then the value applies to all solution components.

`'RelTol'` Relative error tolerance

This tolerance measures the error relative to the magnitude of each solution component. Roughly speaking, it controls the number of correct digits in all solution components, except those smaller than the absolute tolerance `AbsTol`.

At each simulation step i, the solver estimates the local error e in the state j of the simulation. The solver reduces the size of time step i until the error of the state satisfies:

$$|\mathrm{e}(i,j)| \leq \max\Big(\mathrm{RelTol} \cdot |x(i,j)|,\ \mathrm{AbsTol}(i,j)\Big) \tag{B.2}$$

Thus, at state values of larger magnitude, the accuracy is determined by `RelTol`. As the state values approach zero, the accuracy is controlled by `AbsTol`. The correct choice of values for `RelTol` and `AbsTol` varies depending on the problem.

The default values may work for first trials of the simulation. As you adjust the tolerances, consider that there are trade-offs between speed and accuracy:

- If the simulation takes too long, you can increase (or loosen) the values of `RelTol` and `AbsTol` at the cost of some accuracy.
- If the results seem inaccurate, you can decrease (or tighten) the relative tolerance values by dividing with 10^N, where N is a real positive number. But this tends to slow down the solver.
- If the magnitude of the state values is high, you can decrease the relative tolerance to get more accurate results.

`'Events'` Event function

The event function specified by the function handle must have the general form `[value, isterminal, direction] = myEventsFcn(t,x)`. `value`, `isterminal`, and `direction` are vectors whose i^{th}element corresponds to the i^{th}event function.
If you specify an events function, you can call the ODE solver with three extra output arguments as `[t, x, te, xe, ie] = odeXY (odefun, tspan, x0, options)`. The three additional outputs returned by the solver correspond to the detected events:

- `te`: is a column vector of the times at which events occurred.
- `xe`: is the solution value corresponding to the event times in `te`.
- `ie`: are indices into the vector returned by the events function. The values indicate which event the solver detected.

Alternatively, you can call the solver with a single output as `sol = odeXY (odefun, tspan, x0, options)`. In this case, the event information is stored in the structure as `sol.te`, `sol.xe`, and `sol.ie`.

`'InitialStep'` Suggested initial step size

`InitialStep` sets an upper bound on the magnitude of the first step size that the ODE solver tries. If you do not specify an initial step size, then the solver bases the initial step size on the slope of the solution at the initial time point, `tspan(1)`. If the slope of all solution components is zero, then the solver might try a step size that is too large. If you are aware that this is occurring, or if you want to be sure that the solver resolves important behavior at the beginning of the integration, then use `InitialStep` to provide a suitable initial step size.

`'MaxStep'` Maximum step size

`MaxStep` sets an upper bound on the size of any step taken by the solver. If the ODE has periodic behavior, for example, then setting `MaxStep` to a fraction of the period ensures that the solver does not enlarge the step so much that it steps over an area of interest.

- Do not use `MaxStep` just to obtain more output points, as it can significantly slow down the integration. Instead, use the Refine option to compute additional points at low computational cost.

- Do not use `MaxStep` to increase the accuracy of the solution. If the solution is not accurate enough, then reduce the value of `RelTol` and use the solution to determine a suitable value for `AbsTol`.
- Avoid using `MaxStep` to make sure the solver does not step over some behavior that occurs only once in the integration interval. If you know the time at which the behavior occurs, then break the interval into two pieces and call the solver twice. If you do not know the time at which the change occurs, try reducing `RelTol` and `AbsTol`. Use `MaxStep` only as a last resort in this case.

`'Refine'` Solution refinement factor

This scalar specifies a factor by which the number of output points should increase in each step.

- If the refinement factor is 1, then the solver returns solutions only at the end of each step.
- If the refinement factor is $n > 1$, then the solver subdivides each step into n smaller intervals and returns solutions at each point.

The default value for most solvers is 1, but `ode45` uses a default of 4 to compensate for large step sizes. The extra values produced by the refinement factor are computed by means of continuous extension formulas. These are specialized formulas used by the ODE solvers to obtain accurate solutions between computed time steps without significant increase in computation time.

State Space Formulation

The equations of motion need to be transformed into the state space formulation before they can be implemented into MATLAB, *i.e.*, a single expression for $\ddot{x}$ is needed. For $\mathcal{G}_1$ one gets

$$\mathcal{G}_1 : \; \ddot{x} = 9x - 8 . \tag{B.3}$$

An equation of motion in the form of $\mathcal{G}_2$, for example, defined as

$$\mathcal{G}_2 : \; \ddot{x} - \cos \ddot{x} , \tag{B.4}$$

could not be solved numerically with the basic ODE solvers implemented in MATLAB. For every degree of freedom, q_i, a 2-dimensional state space vector

$$\boldsymbol{x} = [\, q_i \quad \dot{q}_i \,] \tag{B.5}$$

can be derived. Taking the time derivative of $\boldsymbol{x}$ yields:

$$\dot{\boldsymbol{x}} = [\, \dot{q}_i \quad \ddot{q}_i \,] = [\, \boldsymbol{x}(2) \quad \ddot{q}_i \,] , \tag{B.6}$$

where $\ddot{q}_i$ is the state space representation of the equation of motion of the degree of freedom q_i, *e.g.*, Equation B.3.

For n degrees of freedom the vector $\boldsymbol{x}$ is extended such that it becomes $2n$-dimensional. Note that the state space representation and thus the numerical implementation presented herein is only possible if the equations of motion can be decoupled.

B.1.3 Selection of Appropriate ODE Solver for Rocking Systems

Once the state space formulation is deduced, the EOM can be implemented numerically. Various ordinary differential equation (ODE) solvers are provided by Matlab, as listed in Table B.1. However, their suitability depends on the respective numerical problem at hand (*i.e.*, nonstiff, stiff, needed tolerances, *etc.*).

To find the best suited solver for rocking problems, the following three solvers are compared against each other with respect to the computation time t_{ode} for three different planar rocking problems (FVA, RHA for a pulse ground motion, and RHA for the recorded El Centro ground motion) for a rigid oscillator ($R = 1.50$ m, $\tan\alpha = 0.15$, $\lambda = 0.33$, $c_r = 0.90$) and different tolerances `AbsTol` and `RelTol`:

`ode45`	Generally, `ode45` should be tried first.
`ode23`	For systems with moderate stiffness, or when crude tolerances are used, `ode23` might be more efficient than `ode45`.
`ode113`	For strict tolerances, or when the ODE function is expensive to evaluate, `ode113` might be more efficient than `ode45`.

Note that for the rigid rocking problem nonstiff ODE solvers should be used. The stiff solvers either could not solve the EOM well or ran into tolerance issues. The exact solutions of the above mentioned problems are plotted in Figure B.1.

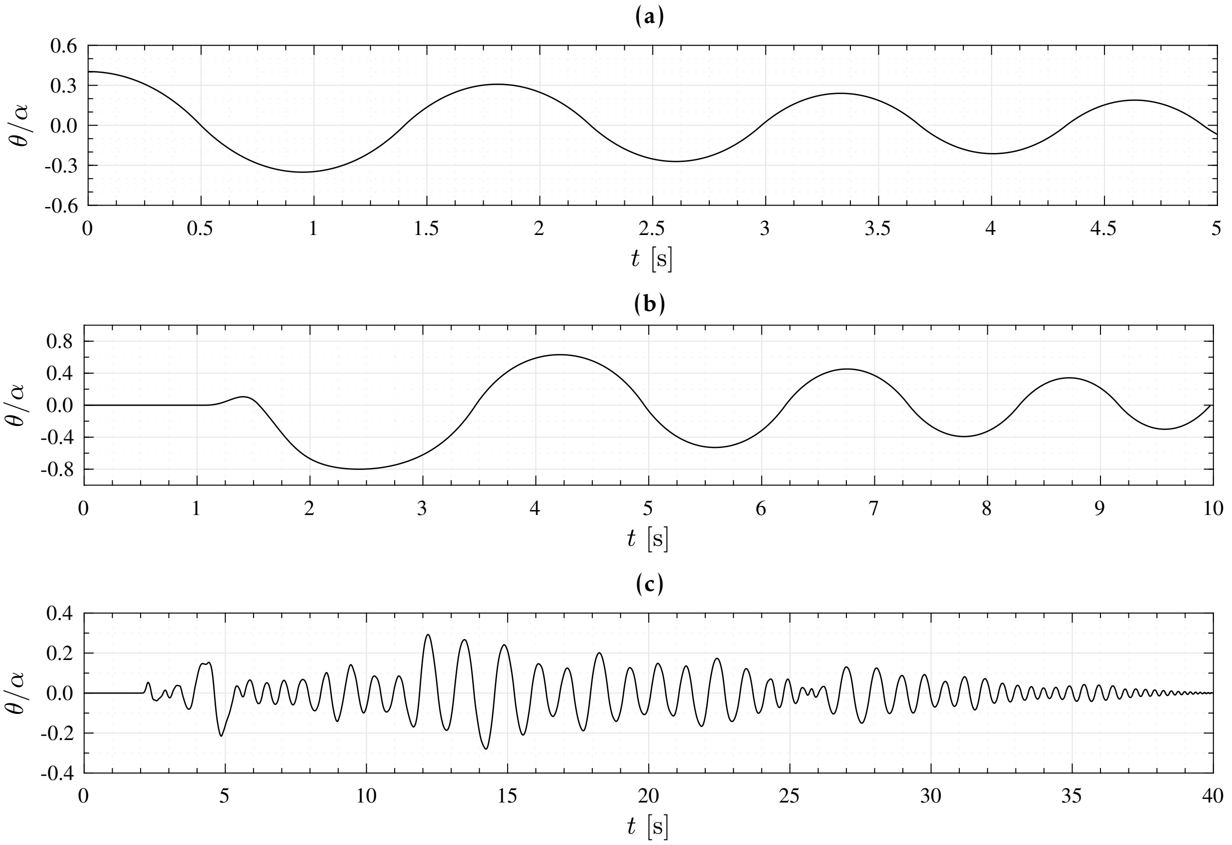

Figure B.1: Exact solutions for a rigid oscillator ($R = 1.50$ m, $\tan\alpha = 0.15$, $\lambda = 0.33$, $c_r = 0.90$): (a) FVA; (b) RHA for an antisymmetric Ricker ($a_p = 0.25\,g$, $T_p = 0.9$ s); (c) RHA for the El Centro ground motion record.

B.1.4 Comparison of ODE Solvers

The individual computation times t_{ode} are visualized in Figure B.2. They were computed using an Intel Core i7-7600U processor (@2.80GHz with boost to 3.90GHz) and 20 GB of DDR4 Ram (2400MHz). Note that there is practically no difference in computation times between the solvers `ode45` and `ode113`. However, with respect to accuracy of the results, there are differences. Figure B.3 plots the error developing for each of the investigated solvers over time for the RHA of the El Centro ground motion record. Clearly, `ode45` diverges more and earlier from the exact solution than the two other solvers `ode23` and `ode113`, given that the set tolerances are identical. Besides, for strict tolerances of RelTol = AbsTol = 10^{-12}, `ode45` still deviates significantly.

In terms of accuracy, `ode23` and `ode113` are roughly the same. For tolerances of RelTol = AbsTol = 10^{-12} the divergence of the computed solutions from the exact solution is negligible. But, while `ode113` finishes the computation in 27 s does it take `ode23` twice as much: 54 s.

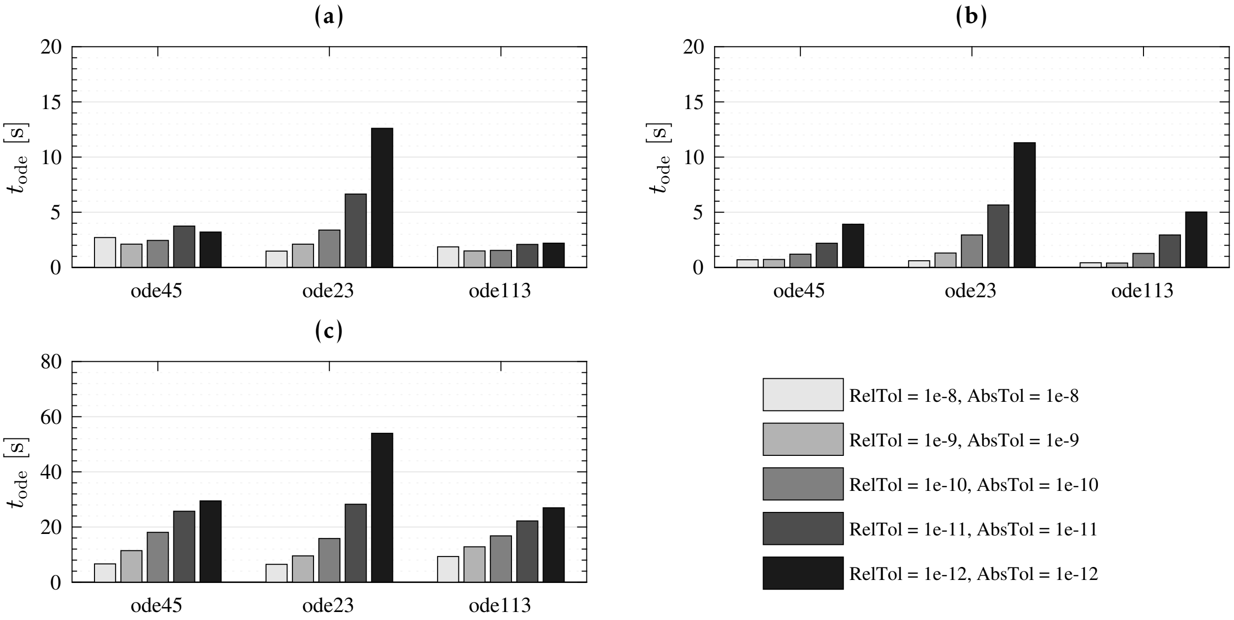

Figure B.2: ODE comparison: computation time of the ODE solvers for varying tolerances when computing the response of a rigid oscillator ($R = 1.50\,\mathrm{m}$, $\tan\alpha = 0.15$, $\lambda = 0.33$, $c_r = 0.90$): (a) FVA ($\theta_0 = 0.4\,\alpha$); (b) RHA (antisymmetric Ricker); (c) RHA (El Centro).

B.1.5 ODE Solver Recommendation

The comparison of the different ODE solvers revealed that the planar rocking problem was found to be solved the fastest by the solvers `ode45` and `ode113`, and with the most accuracy by the solvers `ode23` and `ode113`. Hence, it is recommended to use `ode113` with tolerances in the order of 10^{-11} to 10^{-12} for planar rocking problems. Not that for FVA and RHA for analytical pulse ground motions, the tolerances can be lowered significantly, to about 10^{-08}.

For the 3D rocking problem which does not need to treat impact, `ode45` performed about the same as `ode113`.

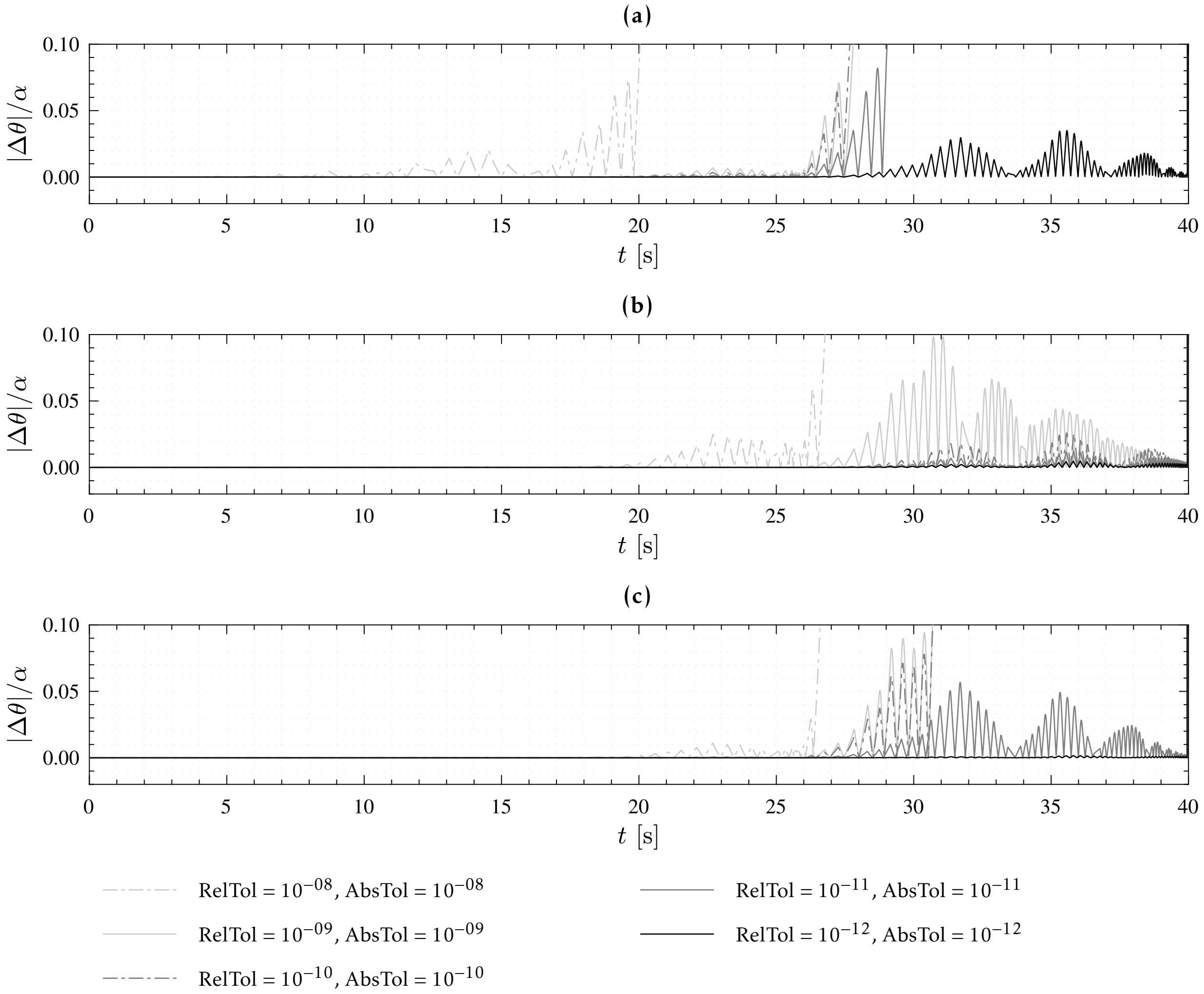

Figure B.3: ODE comparison: difference between ODE solvers and exact solution for varying tolerances when computing the response of a rigid oscillator ($R = 1.50$ m, $\tan\alpha = 0.15$, $\lambda = 0.33$, $c_r = 0.90$) subjected to the 1940 El Centro ground motion: (a) ode45; (b) ode23; (c) ode113.

B.2 Matlab Structure

To illustrate how the rocking problem was solved numerically in Matlab a specific example of a `.m`-file is discussed here. The presented Matlab file `SDOF_rigid_rocking.m` is able to compute the rocking response of rigid SDOF rocking oscillators.

B.2.1 Main File

```
function data = SDOF_rigid_rocking(geometry,model,analysis,inp)
  %% data = SDOF_rigid_rocking('geometry','model','analysis',input)
  % This script will calculate the time history response of the tile angle
  % theta and other rocking response quantites for either the free vibration
  % or the response history analysis.

  %% INPUT
  % geometry  = 'flat' | 'flat_ext' | 'curved'
  % model     = 'column' | 'frame'
  % analysis  = 'RA' | 'FVA'
  %              RA: Response time history Analysis
  %              FVA: Free Vibration time history Analysis
  % input: struct containing
  % ag      [g]       vector
  % ag_t    [s]       vector
  % R       [m]       value
  % alpha   [rad]     value
  % lambda  [-]       value
  % c_rest  [-]       value     // optional input
  % th_0    [rad]     value     // optional input
  % th_d_0  [rad/s]   value     // optional input
  % gamma   [-]       value     // optional input (frame)
  % rho     [-]       value     // optional input (curved)
  % beta    [-]       value     // optional input (curved)
  % alpha_p [-]       value     // optional input (curved)
  % comp = 'exact' | 'linear'   // optional input (default 'exact')
  % ode  = 'ode45' | 'ode23' | 'ode113' | 'ode15s' | 'ode23s' | ...
  %        'ode23t' | 'ode23tb' // optional input (default 'ode113')

  %% OUTPUT
  % data.t            [s]
  % data.theta        [rad]
  % data.theta_d      [rad/s]
  % data.theta_dd     [rad/s2]
  % data.theta_max    [rad]
  % data.par:         used parameters

  %% LOCAL PARAMETERS
  try
    par.g       = 9.807;
    par.R       = inp.R;
    par.alpha   = inp.alpha;
    par.lambda  = inp.lambda;
    if isequal(model,'frame')
      par.gamma   = inp.gamma;
    elseif isequal(model,'column')
      par.gamma   = 0;
      % for the single column the same script will be used as would be
      % used for the frame, with the difference that gamma = 0
    elseif isequal(model,'podium')
      par.gamma   = inp.gamma;
      par.eta     = inp.eta;
      par.Ts      = inp.Ts;
      par.zeta    = inp.zeta;
    else
      error('Missing input: model');
    end
    if isequal(geometry,'curved')
      par.rho     = inp.rho;
      par.beta    = inp.beta;
      par.alpha_p = inp.alpha_p;
      if par.rho == 0
        geometry  = 'flat';
      end
```

```
  elseif isequal(geometry,'flat_ext')
    par.alpha_p = inp.alpha_p;
  end
catch
  error('Missing input: parameters');
end

%% LOCAL EXCITATION
global excitation
try
  if isequal(analysis,'RA')
    % fprintf('Response Analysis.\n');
    excitation.t  = inp.ag_t;
    excitation.ag = inp.ag * par.g;
  elseif isequal(analysis,'FVA')
    % fprintf('Free Vibration Analysis.\n');
    excitation.t  = [0; 20];
    excitation.ag = [0; 0];
  end
catch
  error('Missing input: analysis');
end
time.start  = excitation.t(1);
time.end    = excitation.t(end);
time.dt     = excitation.t(2) - excitation.t(1);

%% INITIAL CONDITIONS
try
  inp.th_0;
  % fprintf('You have selected \x3b8_0 = %.3f [rad].\n',inp.th_0);
  par.th_0 = inp.th_0;
catch
  inp.th_0 = 0;
end
try
  inp.th_d_0;
  % fprintf('You have selected \x3b8_d_0 = %.3f [rad/s].\n',inp.th_d_0);
  par.th_d_0 = inp.th_d_0;
catch
  inp.th_d_0 = 0;
end
% fprintf('\n');

%% COEFFICIENT OF RESTITUTION
try
  inp.c_rest;
  par.c_rest = inp.c_rest;
catch
  par.c_rest = c_rest(par);
end
par.eps = sqrt(par.c_rest);

%% COMPUTATION
if ¬isfield(inp,'ode')
  inp.ode.type = 'ode113'; % default
elseif ¬isfield(inp.ode,'type')
  inp.ode.type = 'ode113'; % default
end
try
  inp.comp;
  if strcmp(inp.comp,'linear')
    par.comp = 'linear';
    fprintf('Computation with LINEARIZED equation of motion and MATLAB solver ...
        %s.\n',inp.ode.type);
  else
    par.comp = 'exact';
    fprintf('Computation with EXACT equation of motion and MATLAB solver ...
        %s.\n',inp.ode.type);
  end
catch
  par.comp = 'exact';
  fprintf('Computation with EXACT equation of motion and MATLAB solver %s.\n',inp.ode.type);
end

%% MORE PARAMETERS
if strcmp(par.comp,'linear')
  if strcmp(geometry,'flat_ext')
    par.ug_up = par.g * par.alpha_p;
```

```
    par.p     = sqrt((1+2*par.gamma)/(1+par.lambda+4*par.gamma)) * sqrt((par.g)/(par.R));
  else
    par.ug_up = par.g * par.alpha;
    par.p     = sqrt((1+2*par.gamma)/(1+par.lambda+4*par.gamma)) * sqrt((par.g)/(par.R));
  end
else
  if strcmp(geometry,'flat_ext')
    par.ug_up = par.g * tan(par.alpha_p);
    par.p     = sqrt((1+2*par.gamma)/(1+par.lambda+4*par.gamma)) * sqrt((par.g)/(par.R)) ...
        * ...
      sqrt((4*cos(par.alpha_p)*cos(par.alpha))/(cos(par.alpha_p)^2 + 3*cos(par.alpha)^2));
  else
    par.ug_up = par.g * tan(par.alpha);
    par.p     = sqrt((1+2*par.gamma)/(1+par.lambda+4*par.gamma)) * sqrt((par.g)/(par.R));
  end
end

%% STARTING CONDITIONS
state.overturn  = false;
state.uplift    = false;
state.stopped   = false;
state.impacts   = 0;
% Until uplift happens, theta and theta_dot are 0. If there is no uplift,
% all elements are 0.
clear yout tout
% yout will be the result from the numerical solver from matlab. The first
% column will give the angle of rotation theta of the block and the second
% column will give the velocity of the angle of rotation theta.
% initialize vectors
tout = zeros(10^5,1);
yout = zeros(10^5,2);
index = 1;
yout(index,:) = [inp.th_0, inp.th_d_0];
if (abs(inp.th_0) > 0 ||abs(inp.th_d_0) > 0)
  state.uplift = true;
end

%% SOLVER
while (tout(index) < time.end-0.05 && state.overturn == false && state.stopped == false)
  [f, fe] = get_ode(geometry,state);
  options = get_ode_options(fe,inp.ode);
  % timerange where the solver has to get a solution for...
  timerange = [tout(index) excitation.t(end)];
  % y0 = starting conditions for the solver
  y0 = yout(index,:);
  % Execute the solver
  switch inp.ode.type
    case 'ode45'
      options.Refine = 4;
      [t,y,¬,¬,ie] = ode45(f,timerange,y0,options,par,geometry);
    case 'ode23'
      [t,y,¬,¬,ie] = ode23(f,timerange,y0,options,par,geometry);
    case 'ode113'
      [t,y,¬,¬,ie] = ode113(f,timerange,y0,options,par,geometry);
    case 'ode15s'
      [t,y,¬,¬,ie] = ode15s(f,timerange,y0,options,par,geometry);
    case 'ode23s'
      [t,y,¬,¬,ie] = ode23s(f,timerange,y0,options,par,geometry);
    case 'ode23t'
      [t,y,¬,¬,ie] = ode23t(f,timerange,y0,options,par,geometry);
    case 'ode23tb'
      [t,y,¬,¬,ie] = ode23tb(f,timerange,y0,options,par,geometry);
  end
  % Output accumulation from different loops
  % t: time vector
  % y: 1st column: theta
  % y: 2nd column: theta_dot
  l = length(t);
  tout(index:index+l-1) = t;
  yout(index:index+l-1,:) = y;
  if t(end) < time.end
    % Events: 'uplift' | 'overturn' | 'impact' | 'rolling/rocking'
    % ie(end) == 1 || 2:        'uplift to the right | left'
    % ie(end) == 3:             'overturn'
    % ie(end) == 4:             'impact'
    % ie(end) == 5:             'rolling -> rocking'
    % ie(end) == 6:             'rocking -> rolling'
    switch ie(end)
```

```
        case 1      % 'uplift to the right'
          % fprintf('Uplift to the right (\x3b8 > 0) at t = %.3f s.\n',...
          %   tout(index+l-1,1));
          state.uplift = true;
        case 2      % 'uplift to the left'
          % fprintf('Uplift to the left (\x3b8 < 0) at t = %.3f s.\n',...
          %   tout(index+l-1,1));
          state.uplift = true;
        case 3      % 'overturn'
          % fprintf('Overturn at t = %.3f s.\n',tout(index+l-1,1));
          state.overturn = sign(y(end,1))*(state.impacts+1);
          state.stopped = true;
        case 4      % 'impact'
          yout(index+l-1,1) = 0;
          yout(index+l-1,2) = par.eps * y(end,2);
          % fprintf('Impact at t = %.3f s.\n',te(end));
          % fprintf('Impact at t = %.3f s, \x3b8_d = %.5f.',...
          %   tout(index+l-1,1), yout(index+l-1,2));
          state.impacts = state.impacts + 1;
          % Check if rocking motion stops after the last impact
          theta_v_limit = 0.0005; % rad/s
          if (abs(yout(index+l-1,2)) < theta_v_limit)
            ag = get_ag(t(end));
            % check for direct re-uplift due to ground motion
            if abs(ag) < par.ug_up
              state.uplift = false;
              yout(index+l-1,2) = 0;
              % fprintf(' Rocking motion stopped.');
            end
          end
          % fprintf('\n');
        case 5      % 'rolling -> rocking'
          % fprintf('Rolling -> Rocking at t = %.3f s, \x3b8 = %.4f, ...
          %   \x3b8_d = %.5f.\n',tout(index+l-1,1), yout(index+l-1,1),...
          %   yout(index+l-1,2));
        case 6      % 'rolling -> rocking'
          % fprintf('Rocking -> Rolling at t = %.3f s, \x3b8 = %.4f, ...
          %   \x3b8_d = %.5f.\n',tout(index+l-1,1), yout(index+l-1,1),...
          %   yout(index+l-1,2));
        otherwise
          error('No event found.\n');
      end
    end
    index = index+l-1;
  end
  tout          = tout(1:index,1);
  theta_out     = yout(1:index,1);
  theta_out_d   = yout(1:index,2);
  data.t        = tout;
  data.theta    = theta_out;
  data.theta_d  = theta_out_d;
  data.theta_dd = zeros(numel(tout),1);
  for i = 1:length(tout)
    clear ag y
    ag      = get_ag(tout(i));
    y(1)    = theta_out(i);
    y(2)    = theta_out_d(i);
    data.theta_dd(i) = get_theta_ddot(geometry,y,par,ag);
    if y(1) == 0
      data.theta_dd(i) = 0;
    end
  end
  try
    par.theta_c = inp.theta_c;
  end
  data.par = par;
end
```

Code B.1: Main file SDOF rigid rocking.

B.2.2 Get Functions

```
function [f, fe] = get_ode(geometry,state)
  if state.uplift
    if isequal(geometry,'flat_ext')
      f   = @ode_flat_ext_rigid_column;
      fe  = @events_flat_ext_rigid_column;
```

```
    elseif isequal(geometry,'flat')
      f   = @ode_flat_rigid_column_frame;
      fe  = @events_flat_rigid_column_frame;
    elseif isequal(geometry,'curved')
      f   = @ode_curved_rigid_column_frame;
      fe  = @events_curved_rigid_column_frame;
    else
      error('No correct geometry defined.');
    end
  else
    f   = @ode_uplift;
    fe  = @events_uplift;
  end
end

function options = get_ode_options(fe,ode)
  options = odeset('Events',fe);
  try
    options.Refine = ode.Refine;
  catch
    % default values
  end
  try
    options.RelTol = ode.RelTol;
  catch
    options.RelTol = 1e-12;
    % warning('Default values used.');
  end
  try
    options.AbsTol = ode.AbsTol;
  catch
    options.AbsTol = 1e-12;
    % warning('Default values used.');
  end
  try
    options.MaxStep = ode.MaxStep;
  catch
    options.MaxStep = 1e-2;
%     warning('Default values used.');
  end
end

function ag = get_ag(t)
  global excitation
  ind = find(excitation.t < t,1,'last');
  if isempty(ind)
    ag = 0;
  else
    try
      ag = excitation.ag(ind) + (excitation.ag(ind+1)-excitation.ag(ind)) * ...
        (t-excitation.t(ind)) / (excitation.t(ind+1)-excitation.t(ind));
    catch
      ag = 0;
    end
  end
end

function sig = get_sig(ag,theta)
  % sometimes Matlab returns crazy values for sat because of the sign
  % function.
  if sign(theta) == 0
    if sign(ag) > 0
      sig = -1;
    elseif sign(ag) < 0
      sig = 1;
    else
      sig = 0;
    end
  else
    sig = sign(theta);
  end
end

function th_dd = get_theta_ddot(geometry,y,par,ag)
  theta   = y(1);
  theta_d = y(2);
  sig = get_sig(ag,theta);
  sat = sig * par.alpha - theta;
```

```
  if isequal(geometry,'flat_ext')
    sapt = sig * par.alpha_p - theta;
    if strcmp(par.comp,'linear')
      th_dd = -par.p^2 * (sapt+ag/par.g);
    else
      th_dd = -par.p^2 * (sin(sapt)+ag/par.g*cos(sapt));
    end
  elseif isequal(geometry,'flat')
    if strcmp(par.comp,'linear')
      th_dd = -par.p^2 * (sat+ag/par.g);
    else
      th_dd = -par.p^2 * (sin(sat)+ag/par.g*cos(sat));
    end
  elseif isequal(geometry,'curved')
    sbt = sig * par.beta - theta;
    if abs(theta) > par.beta % rocking
      if strcmp(par.comp,'linear')
        % th_dd = -par.p^2 * (sig * par.alpha_p - theta + ag/par.g);
        th_dd = -par.p^2 * (sig * par.alpha - theta + ...
          sig * 2 * par.rho * par.beta + ag/par.g);
      else
        th_dd = (- (1+2*par.gamma) * ( par.g/par.R * (sin (sat) + ...
          2*par.rho*cos (par.alpha) * (sin (sbt) +sin (theta) ) ) + ...
          ag/par.R* (cos (sat) +2*par.rho*cos (par.alpha) * ...
          (cos (sbt)-cos (theta) ) ) ) ) / ...
          (par.lambda + (1+4*par.gamma)*(1 + 4*par.rho*cos(par.alpha)*...
          (cos(par.alpha-par.beta)-cos(par.alpha)) + ...
          8*par.rho^2*cos(par.alpha)^2*(1-cos(par.beta))));
      end
    else % rolling
      if strcmp(par.comp,'linear')
        th_dd = -par.p^2 * (sig * par.alpha - theta * (1-2*par.rho) + ag/par.g);
      else
        th_dd = (- (1+2*par.gamma) * ( par.g/par.R * (sin (sat) + ...
          2*par.rho*cos (par.alpha) *sin (theta) ) + ...
          ag/par.R* (cos (sat) +2*par.rho*cos (par.alpha) * ...
          (1-cos (theta) ) ) ) - ...
          (1+4*par.gamma)*theta_d^2* (2*par.rho*cos (par.alpha) * sin (sat) + ...
          4*par.rho^2*cos (par.alpha)^2 *sin (theta) ) ) / ...
          (par.lambda + (1+4*par.gamma)*(1 + 4*par.rho*cos(par.alpha)*...
          (cos(sat)-cos(par.alpha)) + ...
          8*par.rho^2*cos(par.alpha)^2*(1-cos(theta))));
      end
    end
  else
    Warning('No correct geometry defined.');
  end
end
```

Code B.2: Get functions SDOF rigid rocking.

B.2.3 ODE Functions

```
function dydt = ode_uplift(¬,¬,¬,¬,¬)
  dydt(1,1) = 0;
  dydt(2,1) = 0;
end

function dydt = ode_flat_ext_rigid_column(t,y,par,geometry)
  ag = get_ag(t);
  dydt(1,1) = y(2);
  dydt(2,1) = get_theta_ddot(geometry,y,par,ag);
end

function dydt = ode_flat_rigid_column_frame(t,y,par,geometry)
  ag = get_ag(t);
  dydt(1,1) = y(2);
  dydt(2,1) = get_theta_ddot(geometry,y,par,ag);
end

function dydt = ode_curved_rigid_column_frame(t,y,par,geometry)
  ag = get_ag(t);
  dydt(1,1) = y(2);
  dydt(2,1) = get_theta_ddot(geometry,y,par,ag);
end
```

Code B.3: ODE functions SDOF rigid rocking.

B.2.4 ODE Events

```
function [value,isterminal,direction] = events_uplift(t,¬,par,¬)
  ag = get_ag(t);
  up = 1.000 * par.ug_up;
  value       = [-up-ag up-ag 1 1 1 1];
  isterminal  = [1 1 0 0 0 0];   % 0: do nothing, 1: stop the integration
  direction   = zeros(1,6);   % Negative and positive direction
end

function [value,isterminal,direction] = events_flat_ext_rigid_column(¬,y,¬,¬)
  theta = y(1);
  value       = [0 0 abs(theta)-pi/4 theta 0 0];
  isterminal  = [0 0 1 1 0 0];   % 0: do nothing, 1: stop the integration
  direction   = zeros(1,6);   % Negative and positive direction
end

function [value,isterminal,direction] = events_flat_rigid_column_frame(¬,y,¬,¬)
  theta = y(1);
  value       = [0 0 abs(theta)-pi/4 theta 0 0];
  isterminal  = [0 0 1 1 0 0];   % 0: do nothing, 1: stop the integration
  direction   = zeros(1,6);   % Negative and positive direction
end

function [value,isterminal,direction] = events_curved_rigid_column_frame(¬,y,par,¬)
  theta = y(1);
  value       = [0 0 abs(theta)-pi/4 theta abs(theta)-par.beta abs(theta)-par.beta];
  isterminal  = [0 0 1 1 1 1];   % 0: do nothing, 1: stop the integration
  direction   = [zeros(1,4) 1 -1];   % Negative and positive direction
end
```

Code B.4: ODE events SDOF rigid rocking.

APPENDIX C

TIME HISTORIES

C.1 Bidirectional Ground Motions

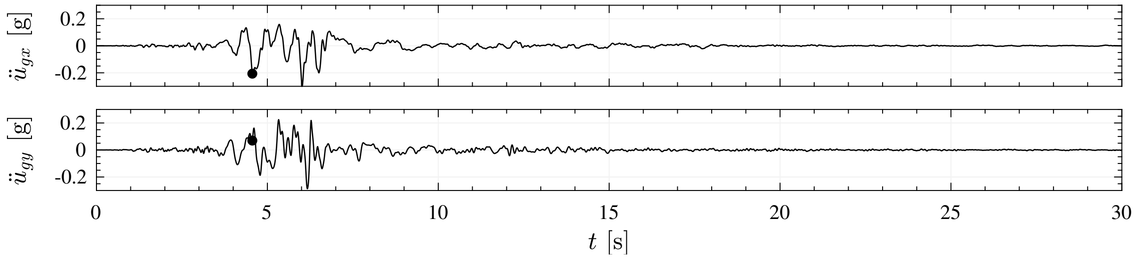

Figure C.1: Kobe.

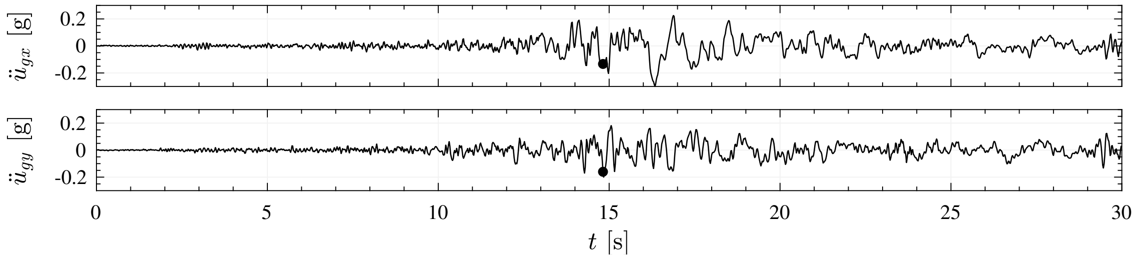

Figure C.2: Landers.

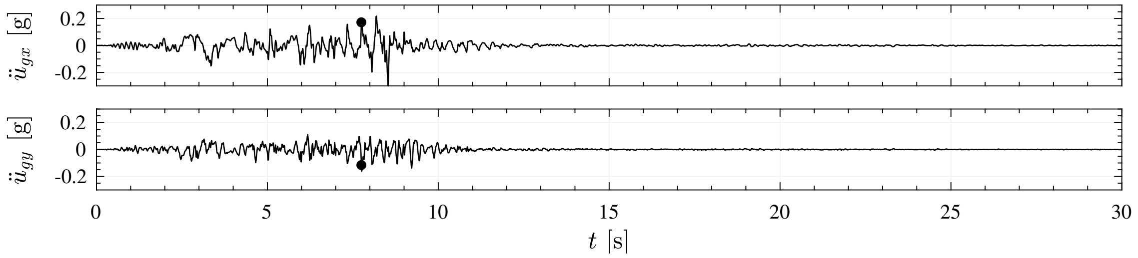

Figure C.3: San Fernando.

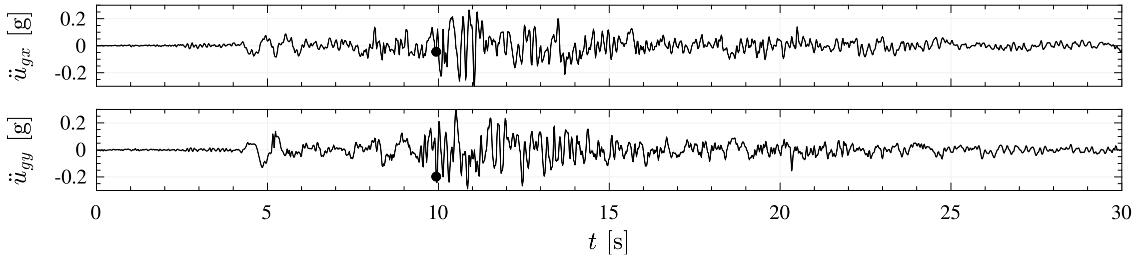

Figure C.4: Tabas.

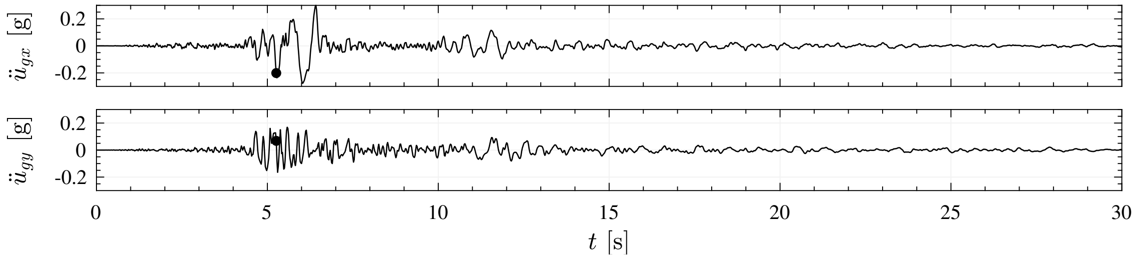

Figure C.5: Whittier Narrows.

C.2 Rocking Podium Structure Experiments

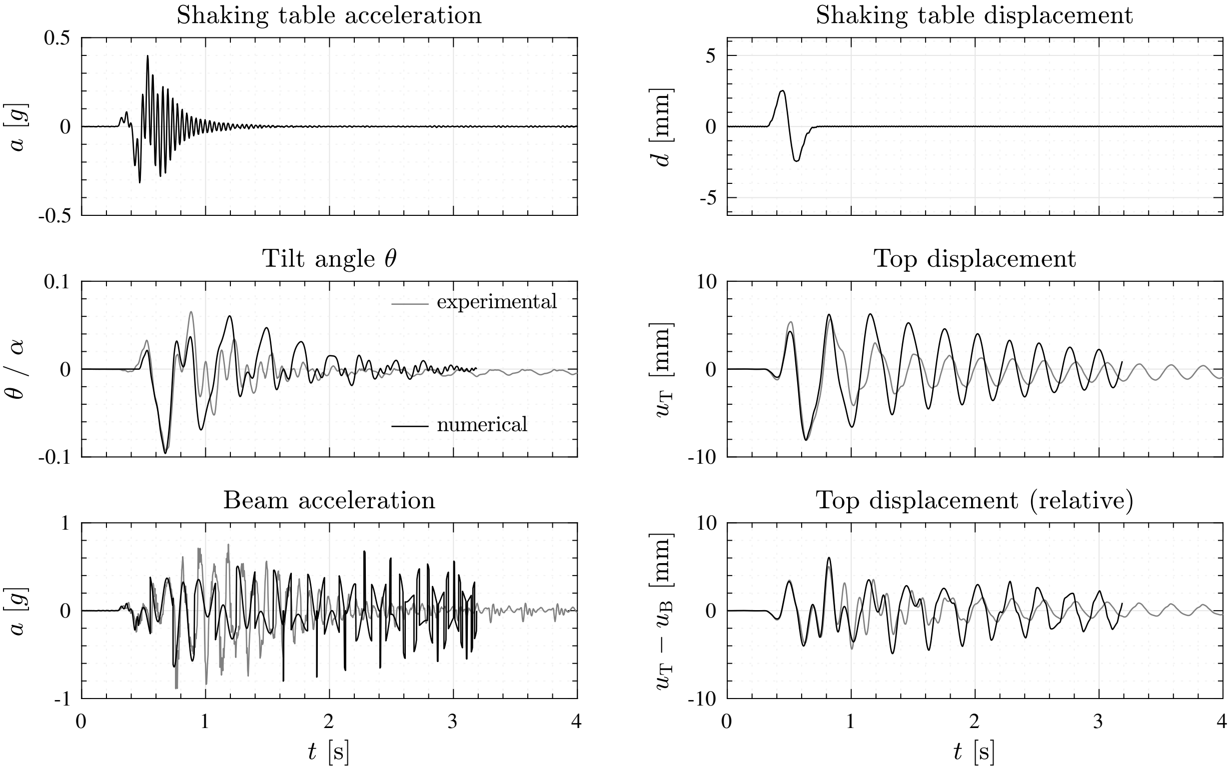

Figure C.6: Response comparison (Test No. 1).

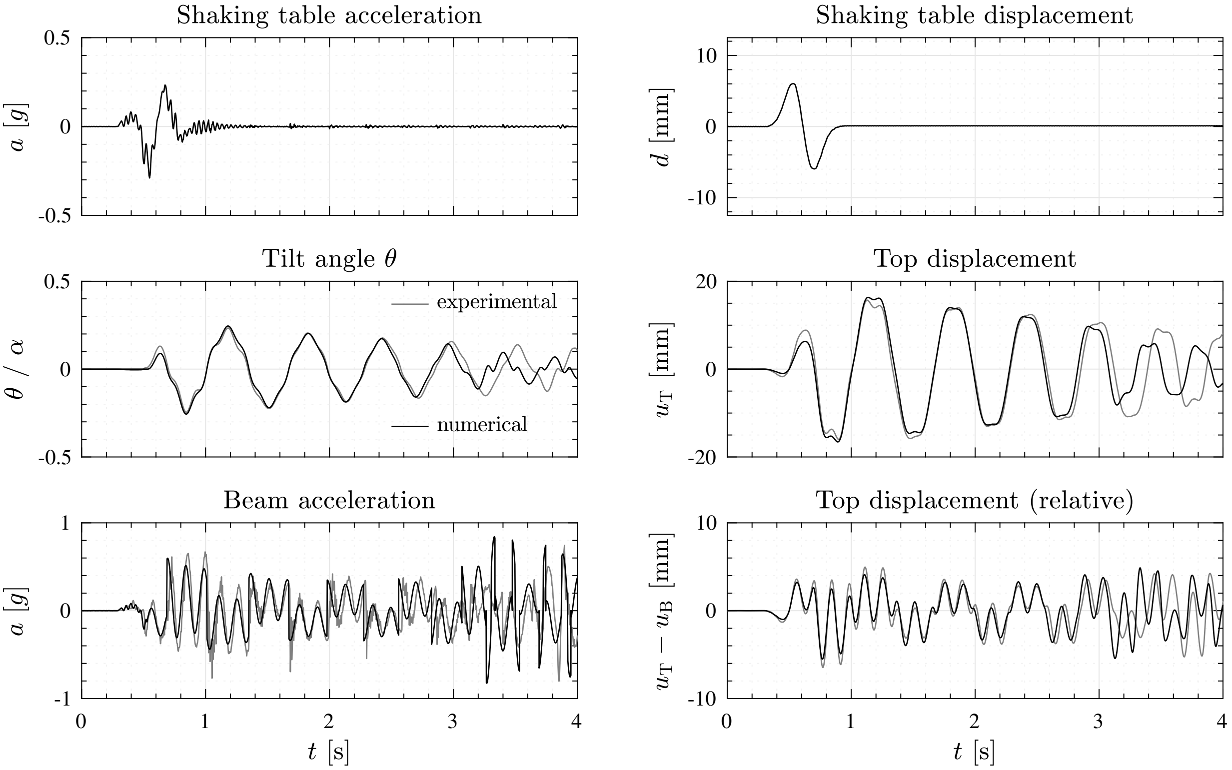

Figure C.7: Response comparison (Test No. 2).

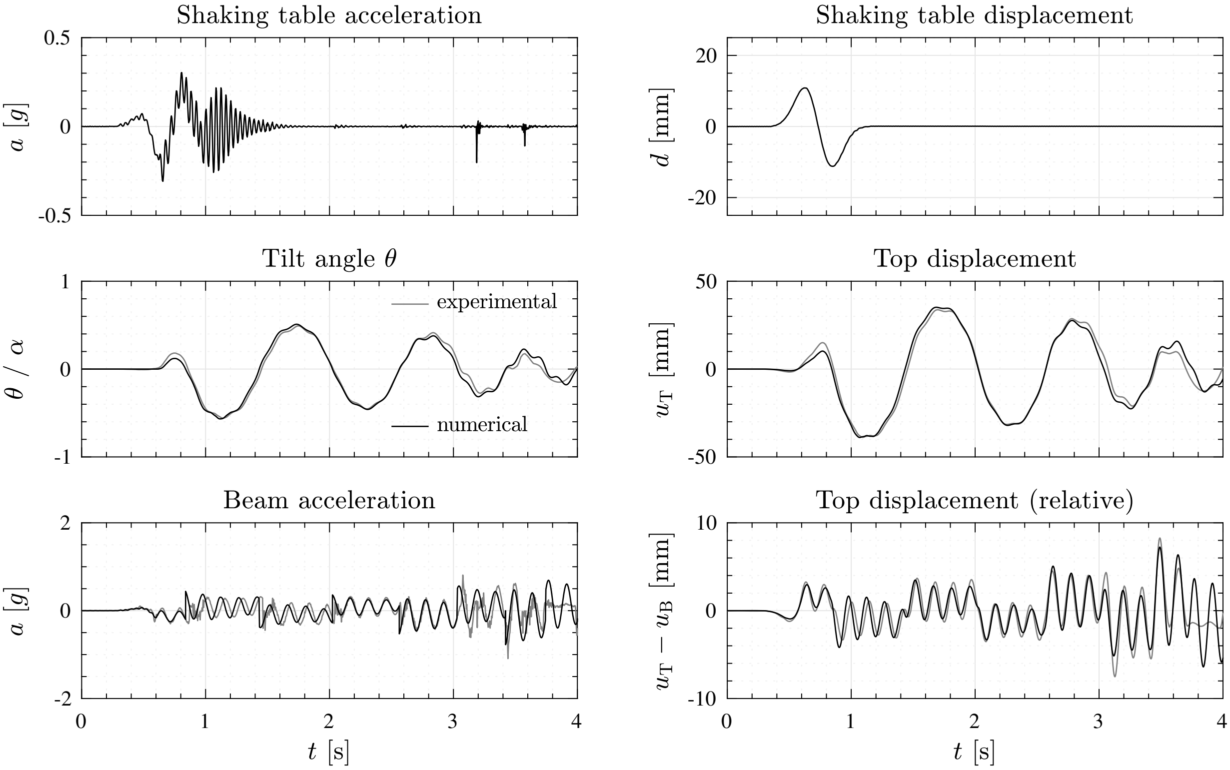

Figure C.8: Response comparison (Test No. 3).

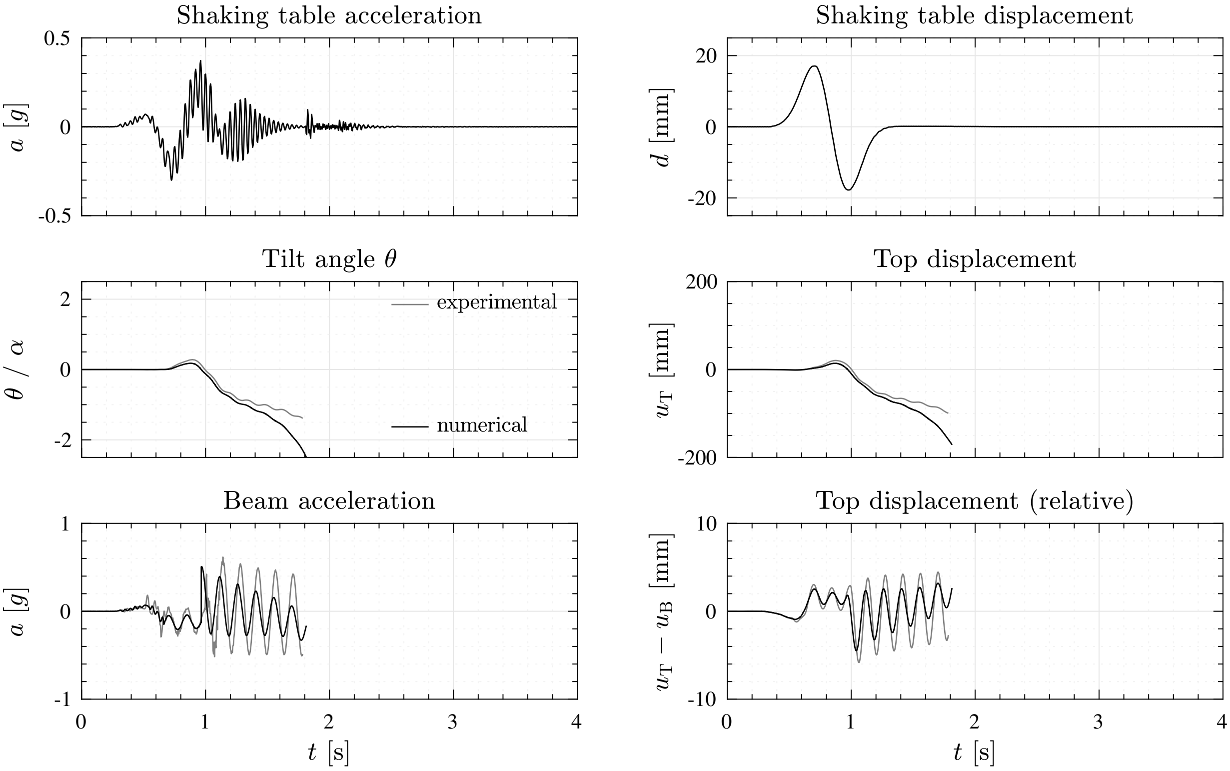

Figure C.9: Response comparison (Test No. 4).

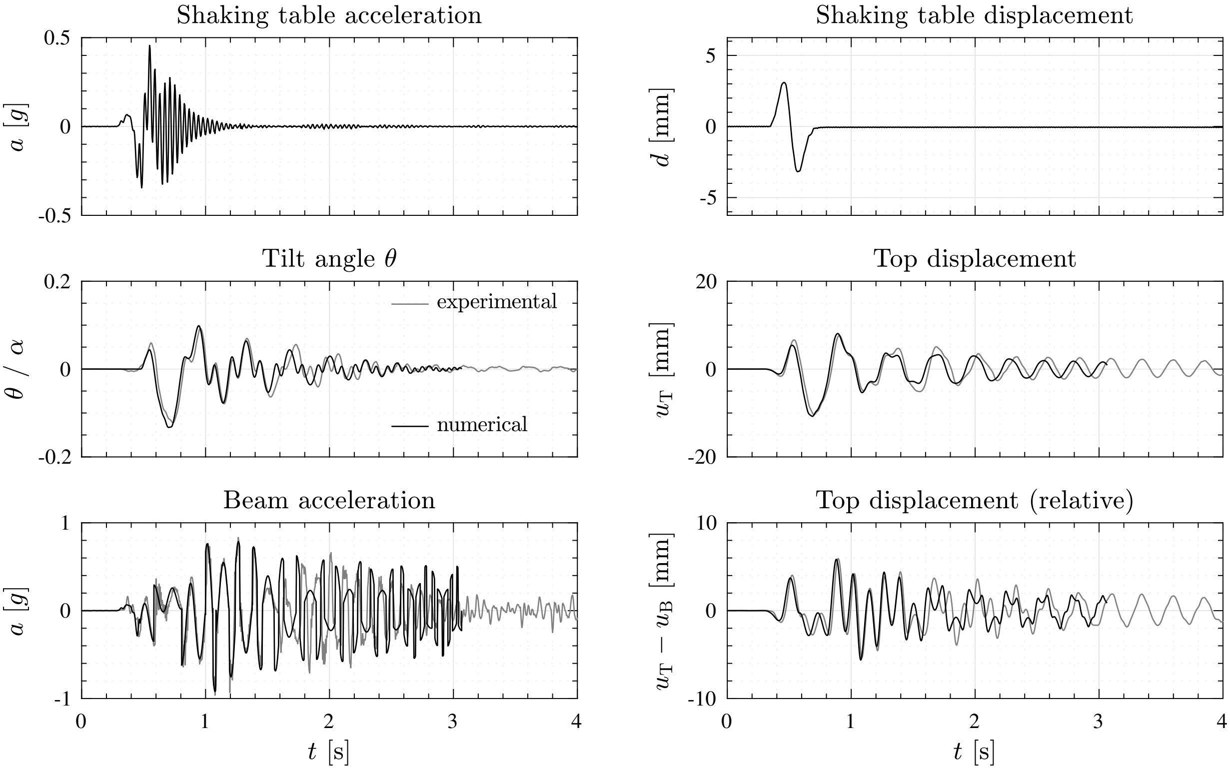

Figure C.10: Response comparison (Test No. 5).

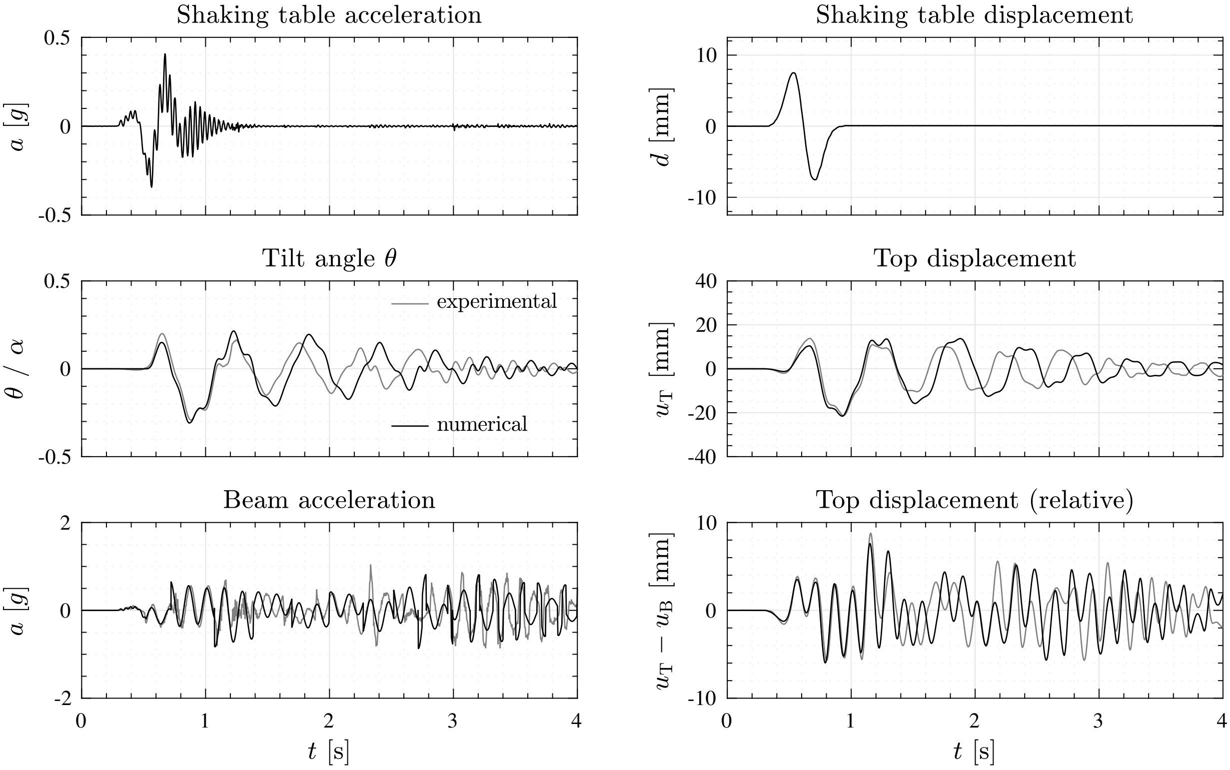

Figure C.11: Response comparison (Test No. 6).

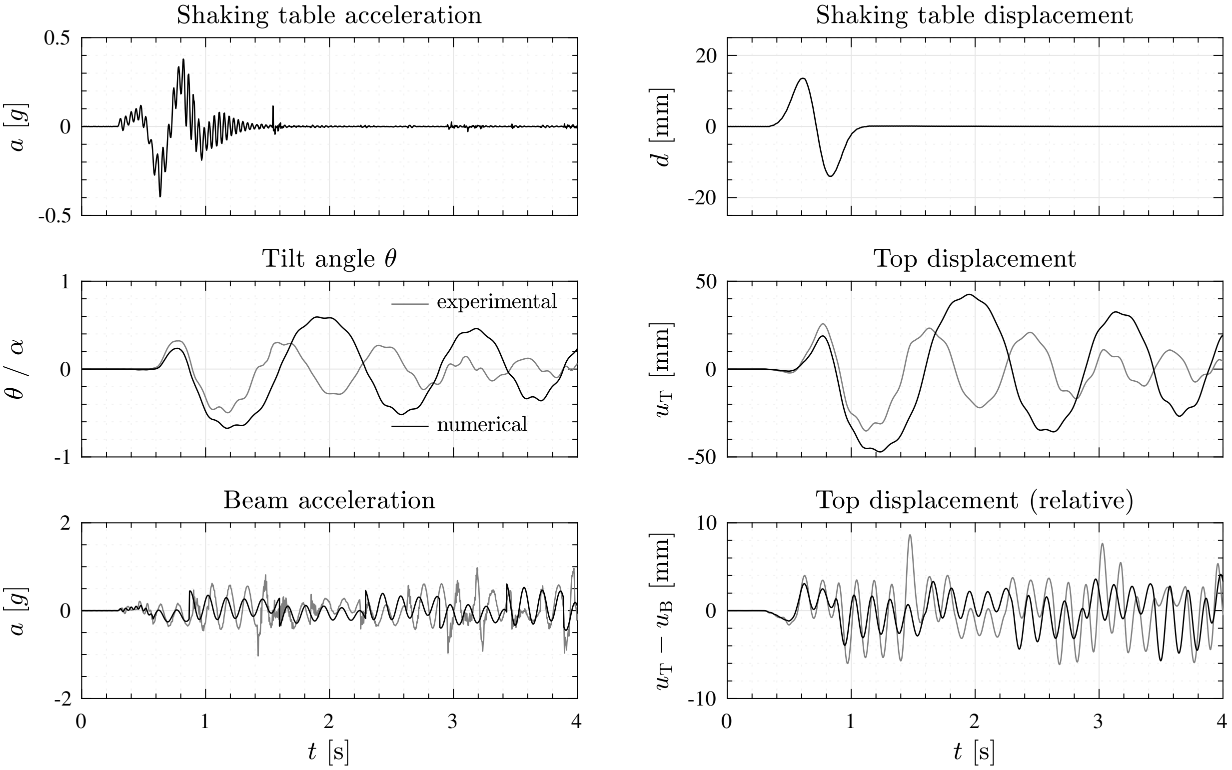

Figure C.12: Response comparison (Test No. 7).

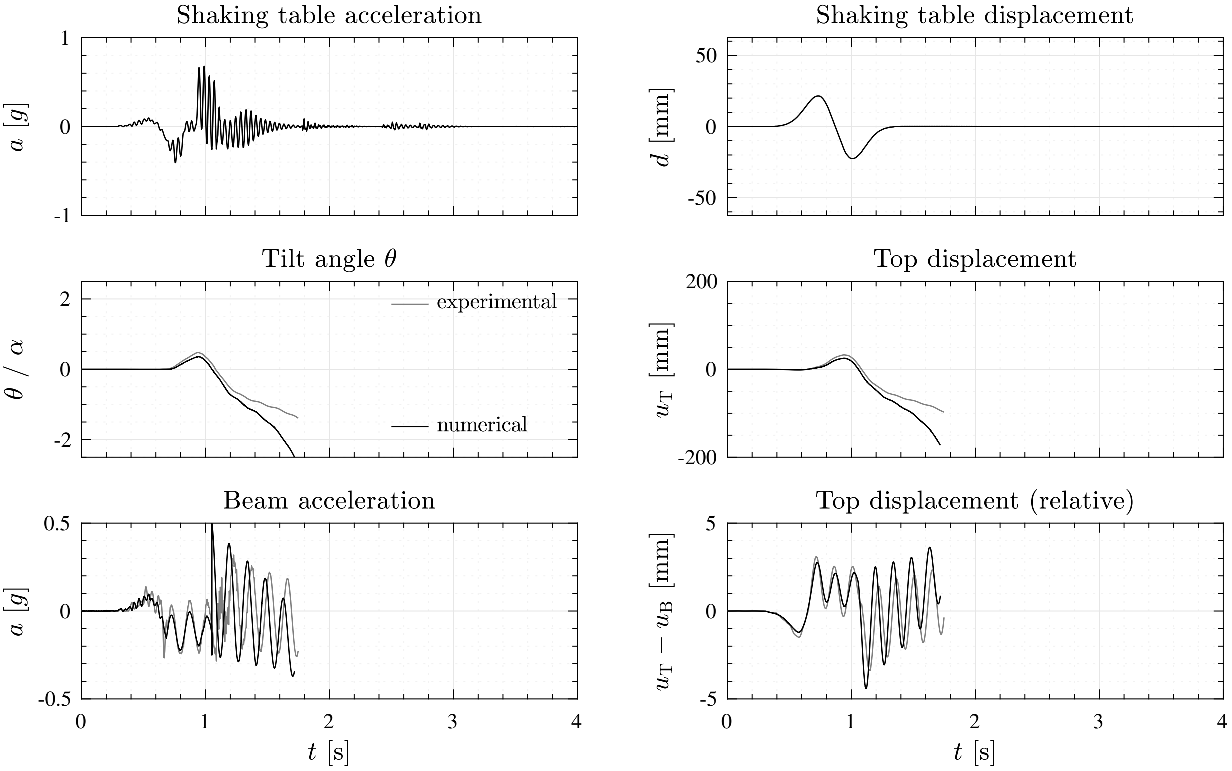

Figure C.13: Response comparison (Test No. 8).

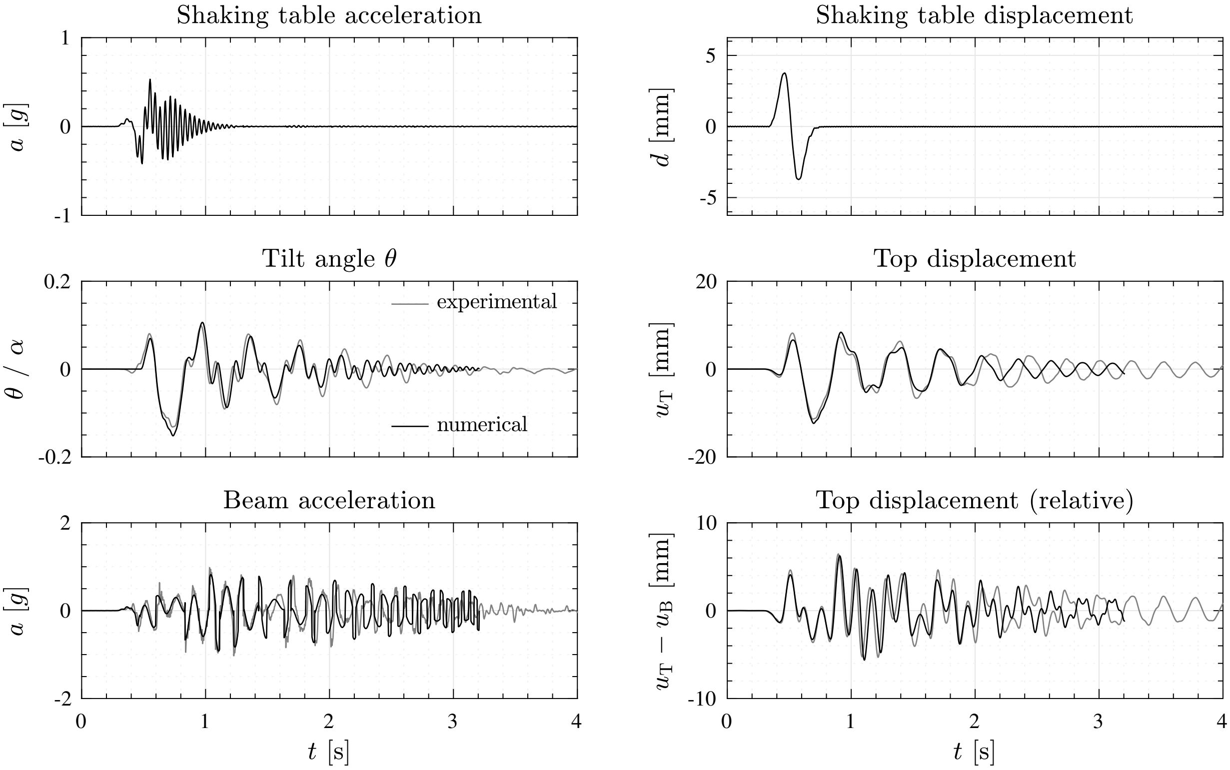

Figure C.14: Response comparison (Test No. 9).

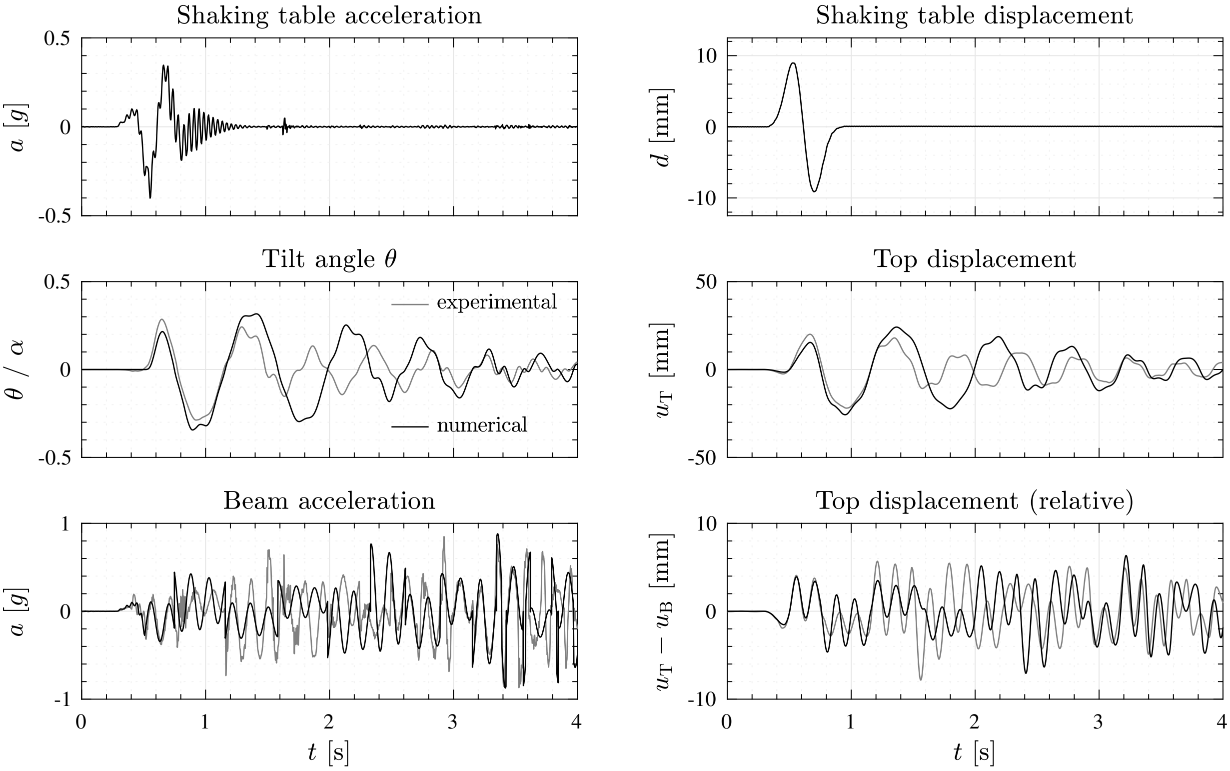

Figure C.15: Response comparison (Test No. 10).

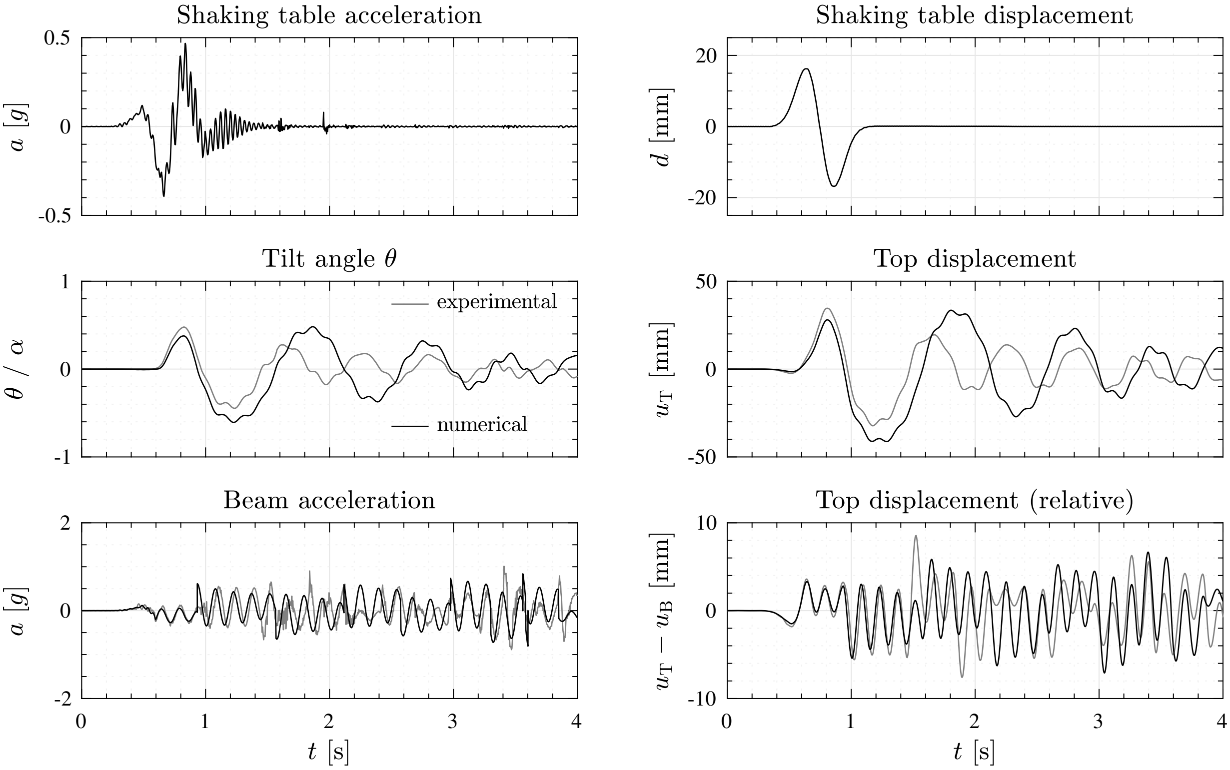

Figure C.16: Response comparison (Test No. 11).

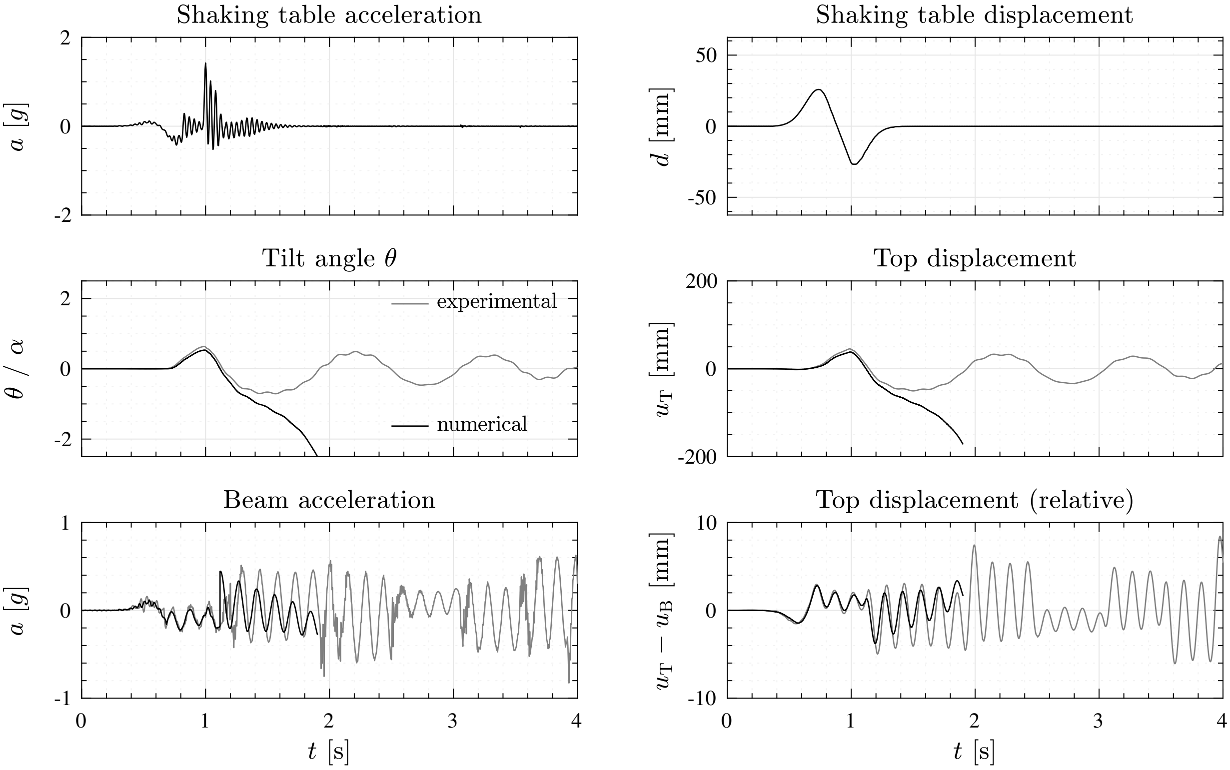

Figure C.17: Response comparison (Test No. 12).

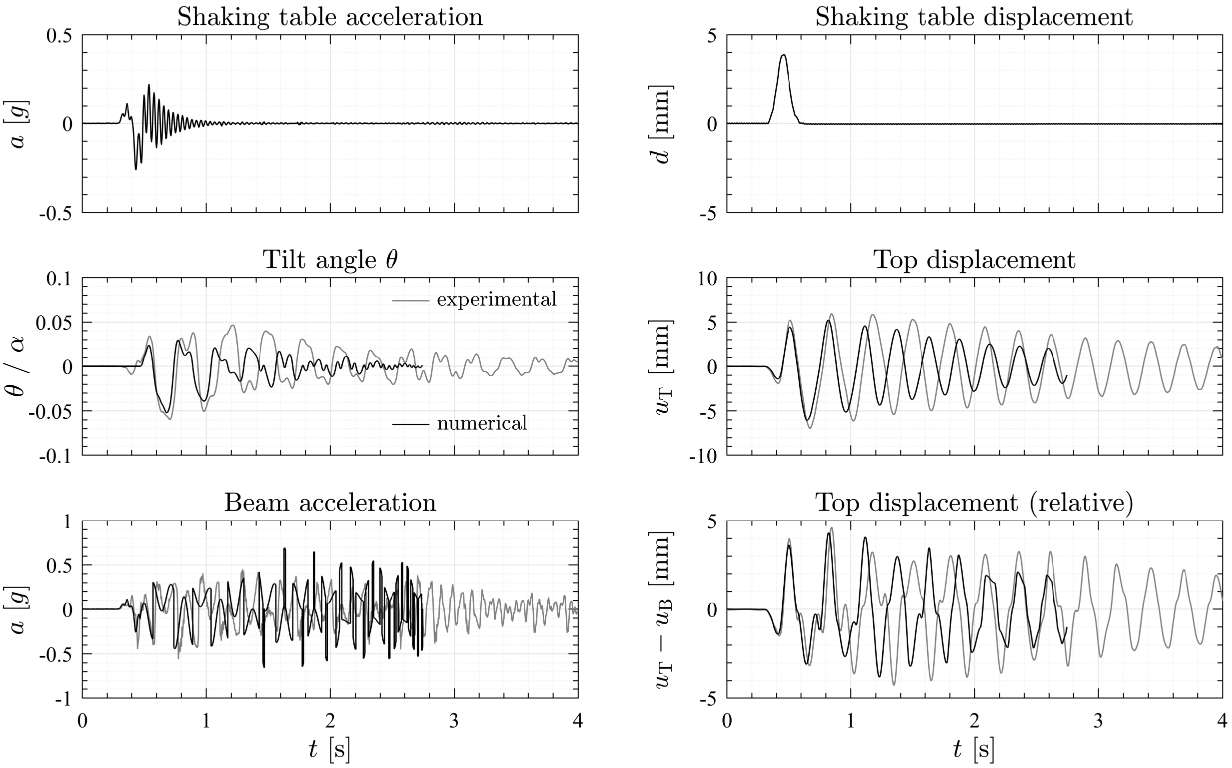

Figure C.18: Response comparison (Test No. 13).

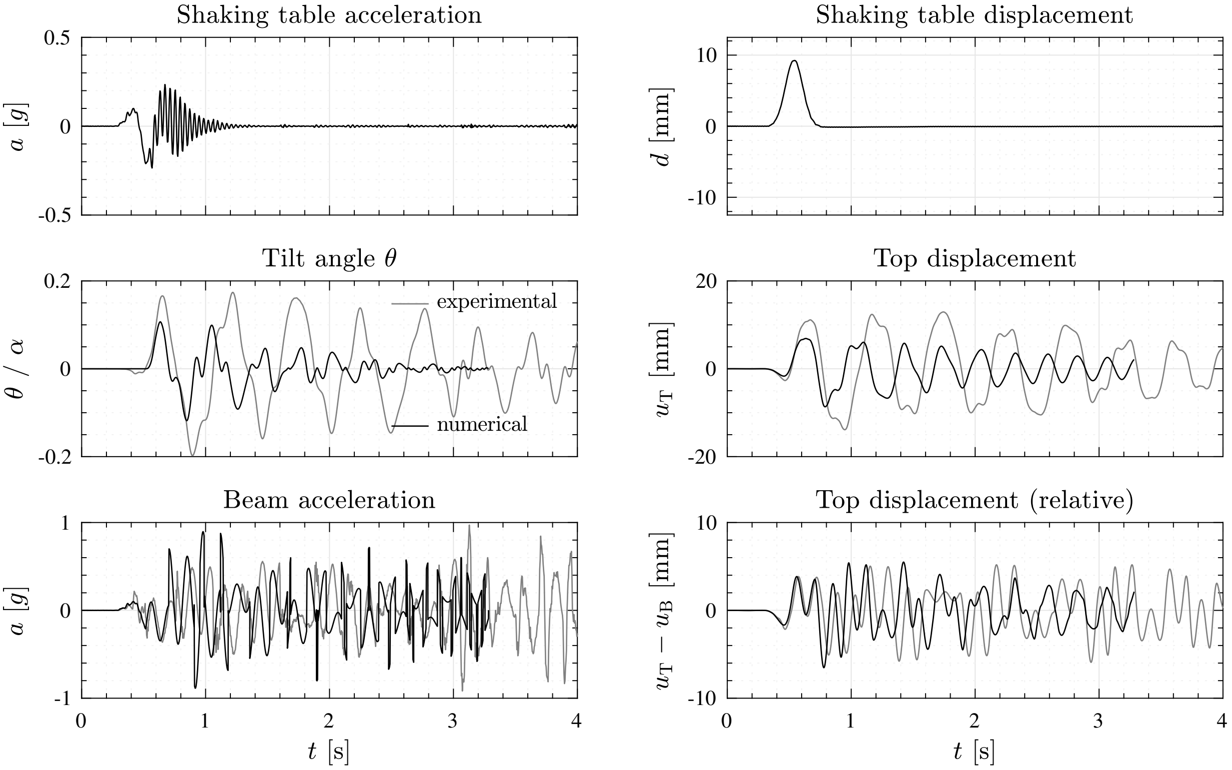

Figure C.19: Response comparison (Test No. 14).

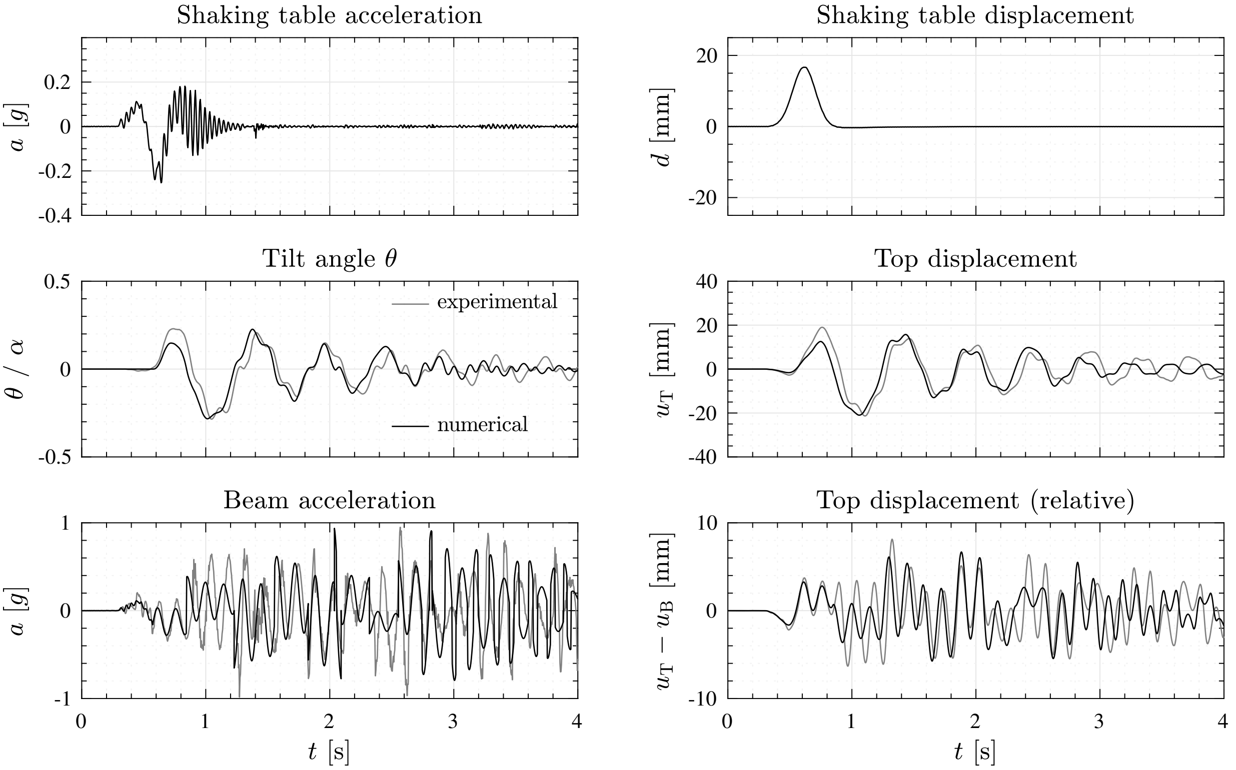

Figure C.20: Response comparison (Test No. 15).

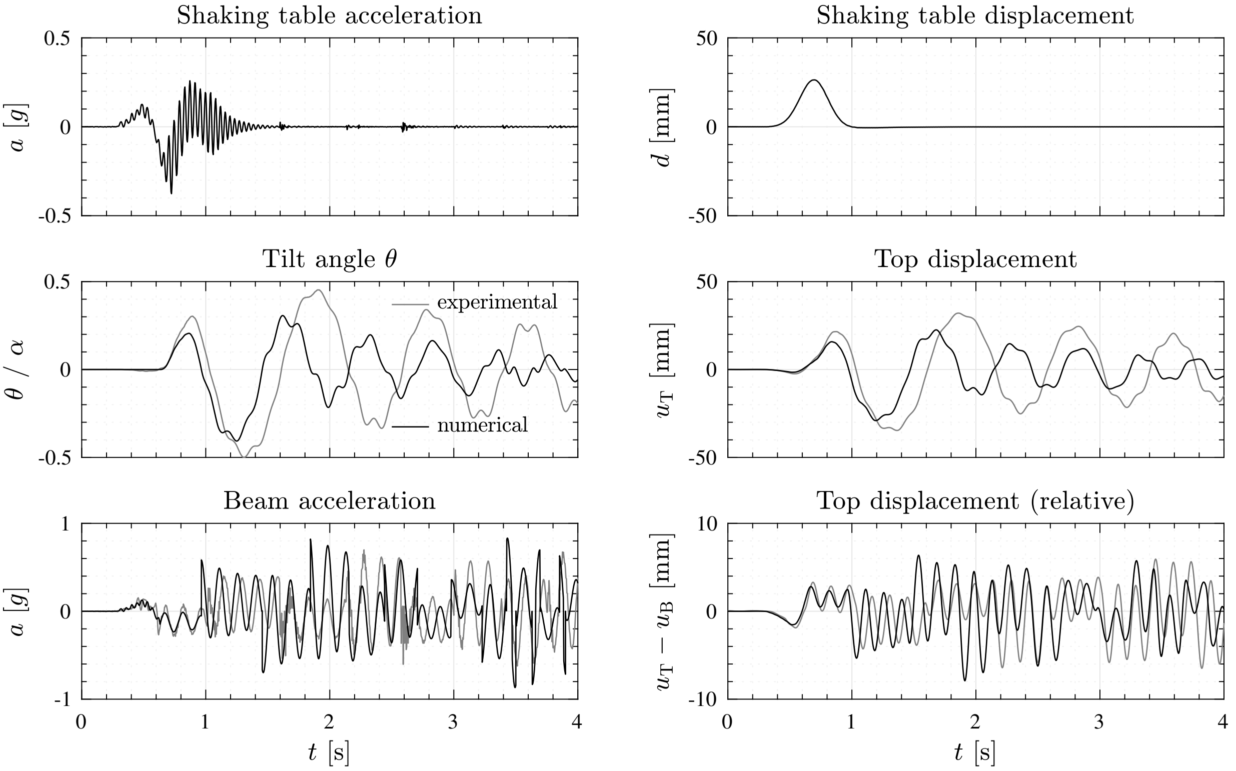

Figure C.21: Response comparison (Test No. 16).

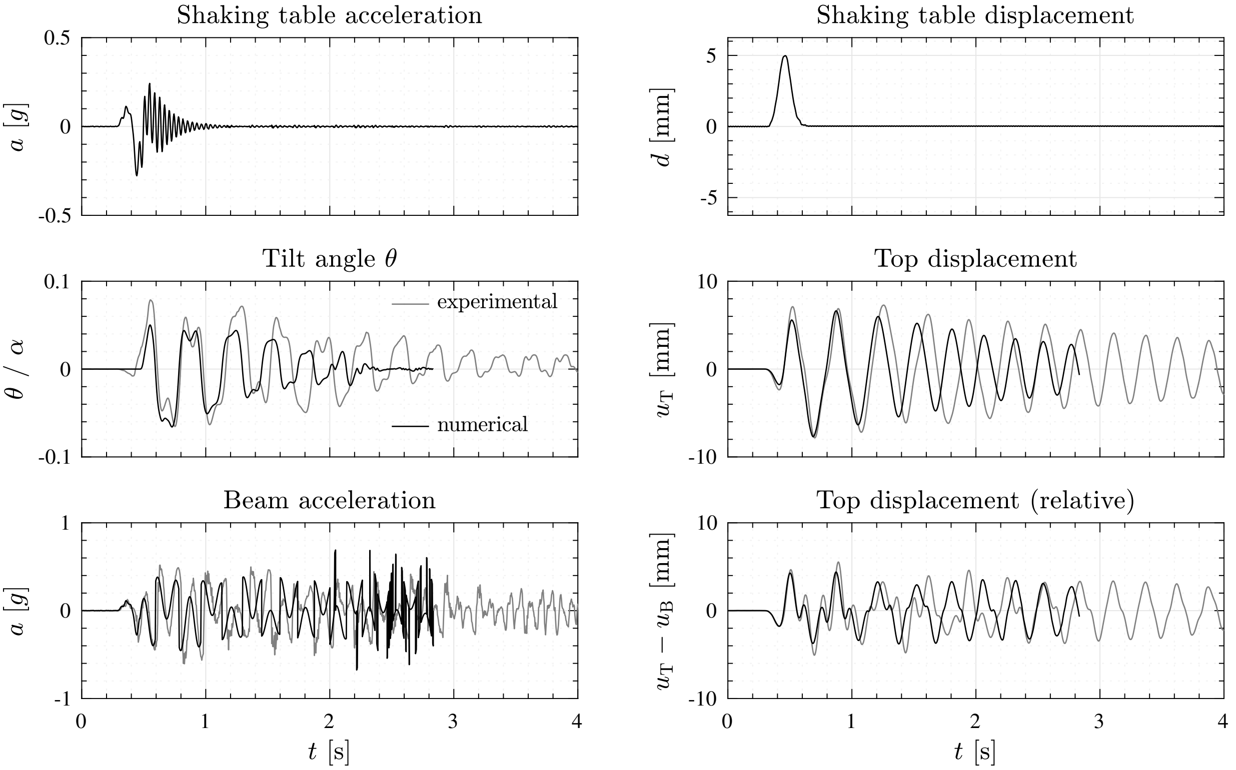

Figure C.22: Response comparison (Test No. 17).

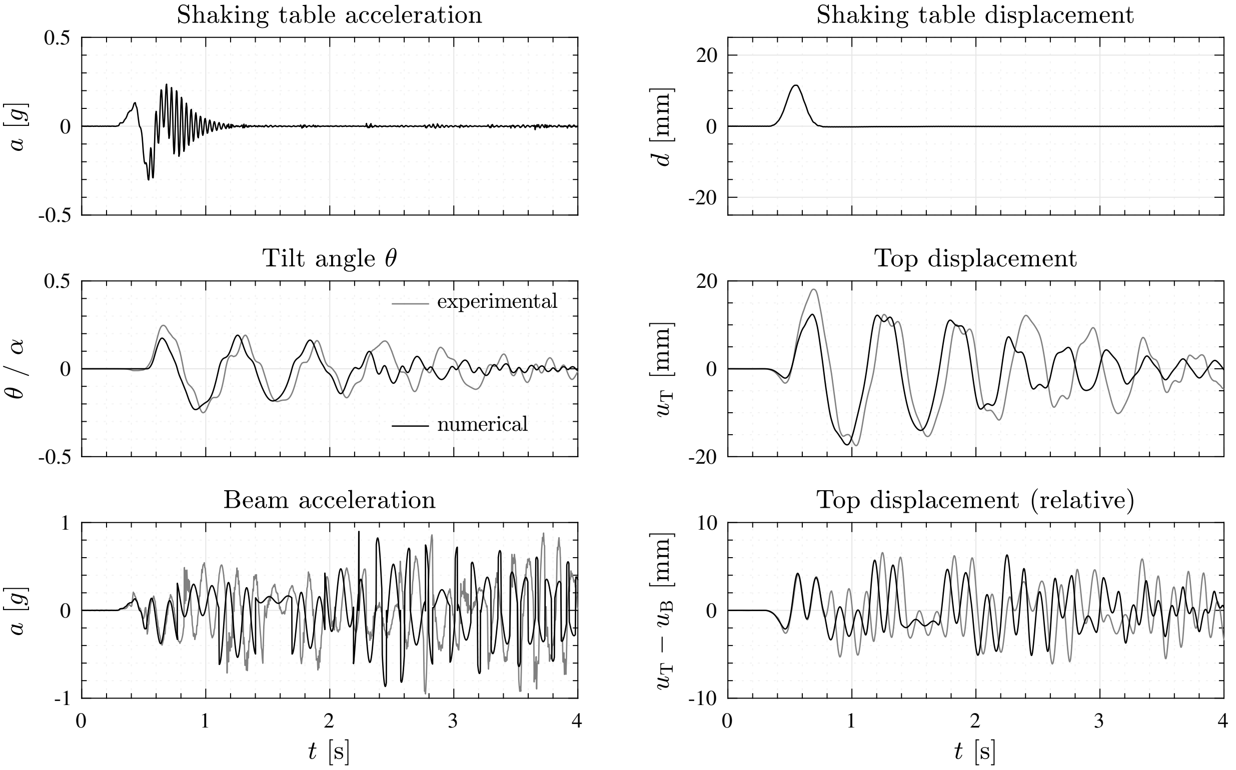

Figure C.23: Response comparison (Test No. 18).

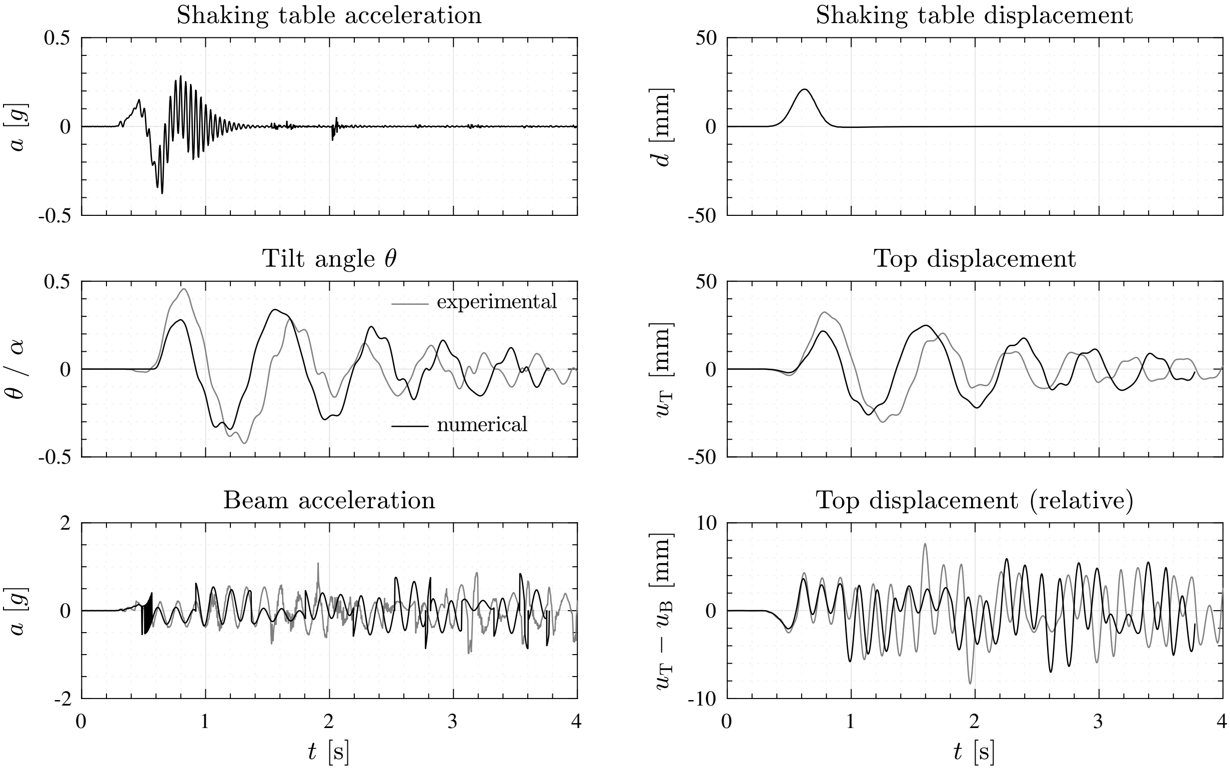

Figure C.24: Response comparison (Test No. 19).

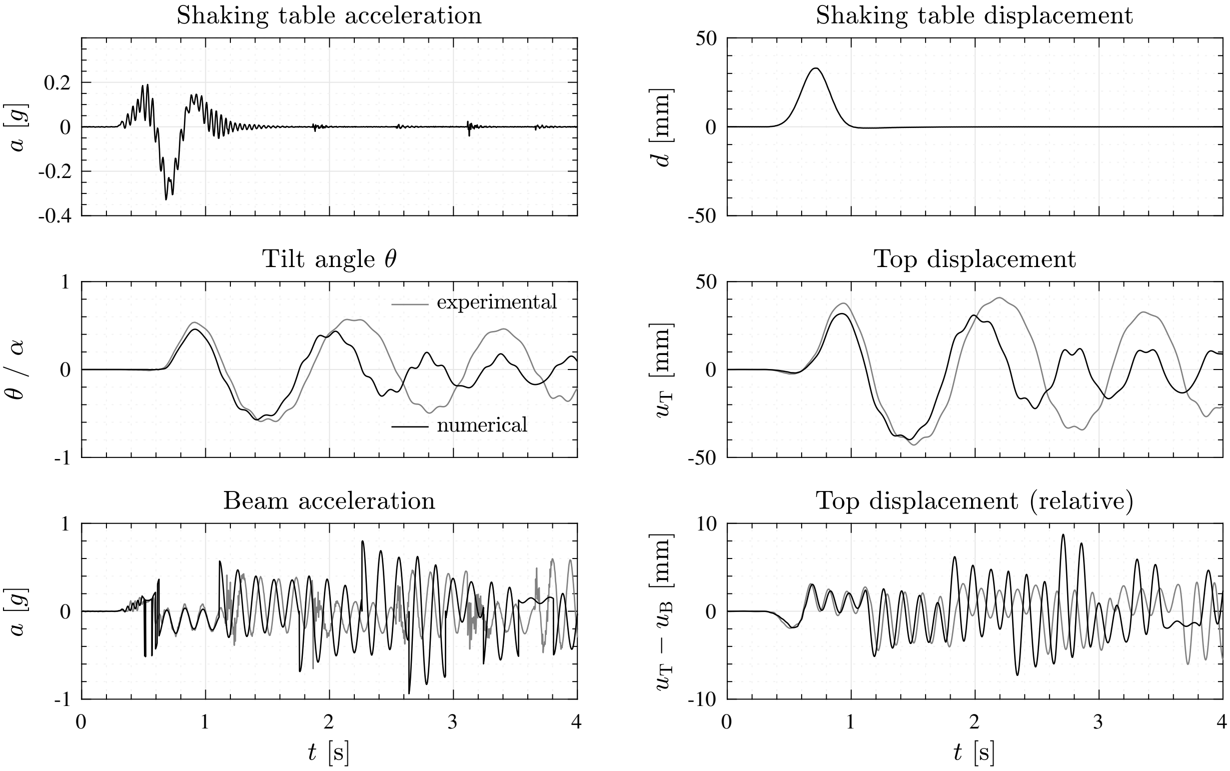

Figure C.25: Response comparison (Test No. 20).

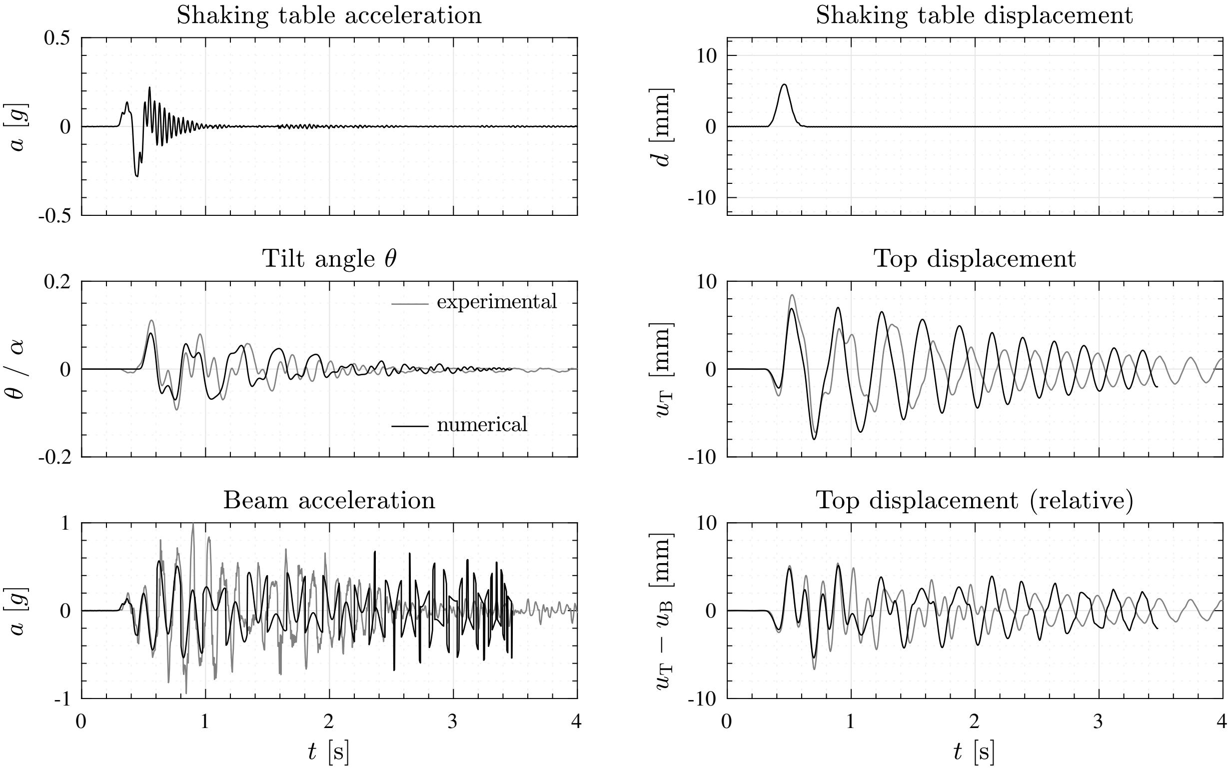

Figure C.26: Response comparison (Test No. 21).

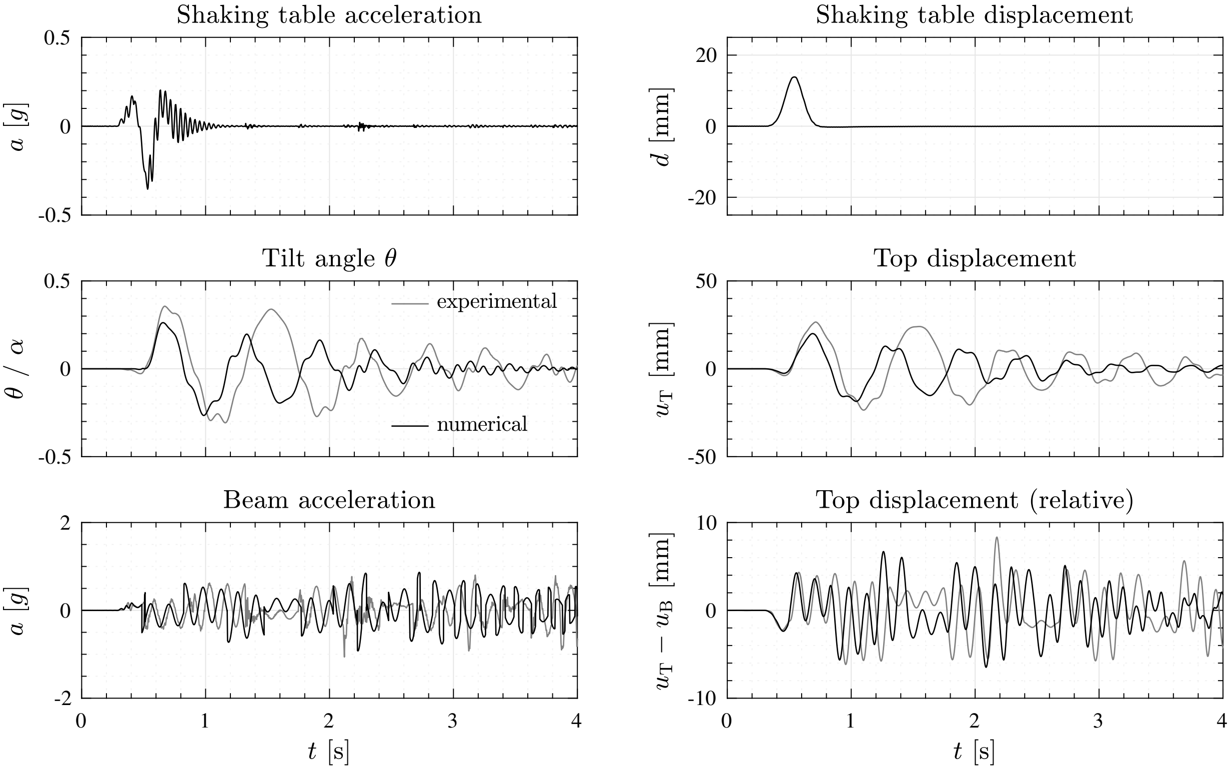

Figure C.27: Response comparison (Test No. 22).

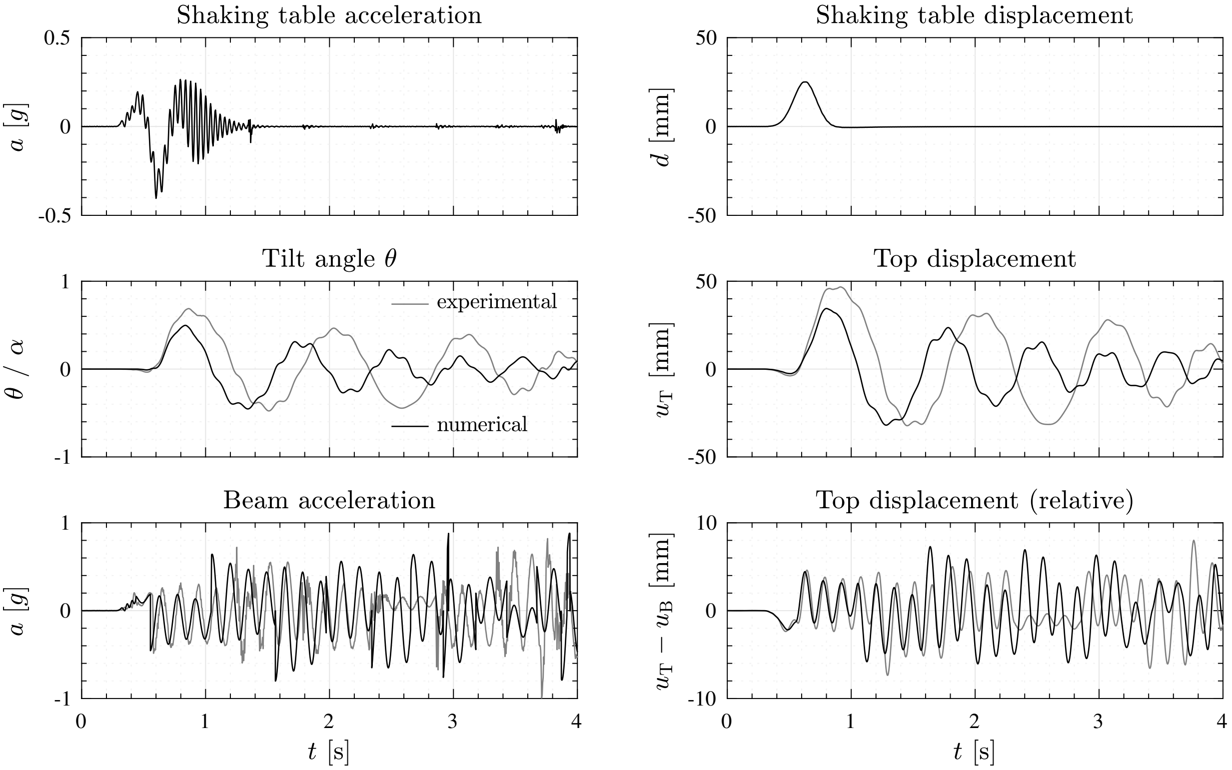

Figure C.28: Response comparison (Test No. 23).

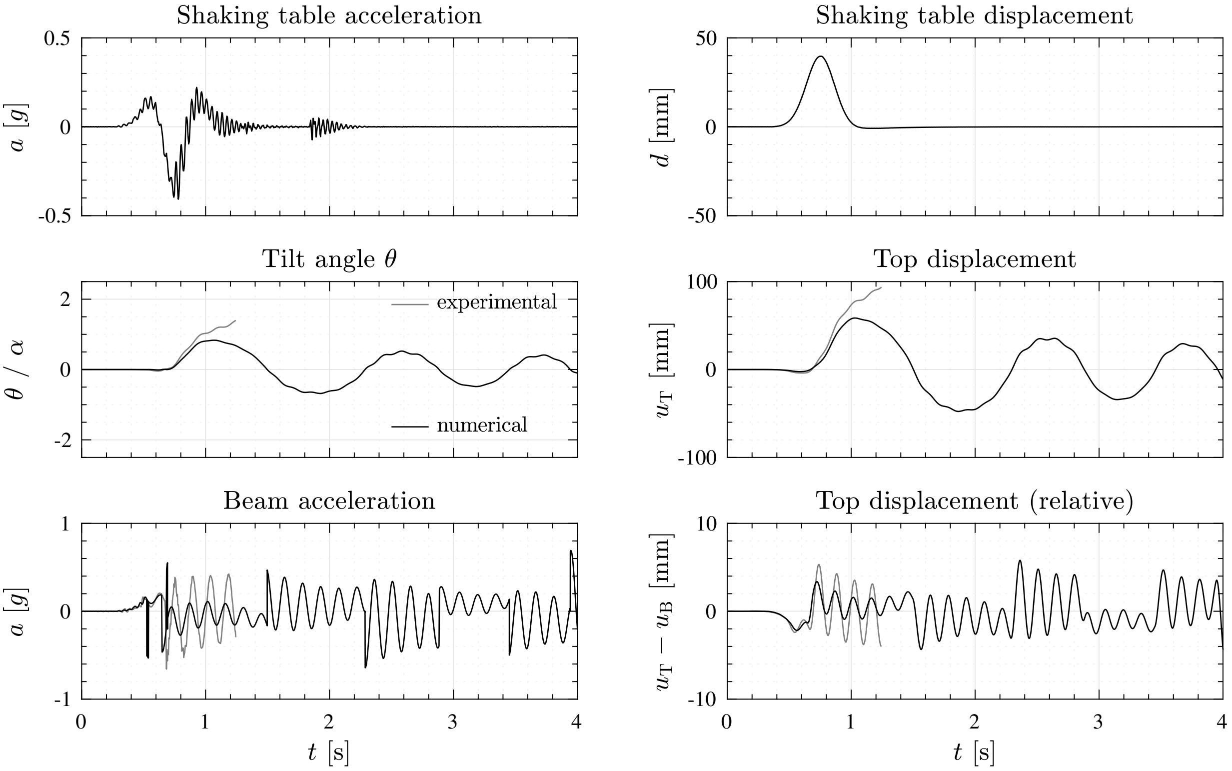

Figure C.29: Response comparison (Test No. 24).

C.3 Modified Rigid Columns: Free Vibration Tests

C.3.1 Specimen F01

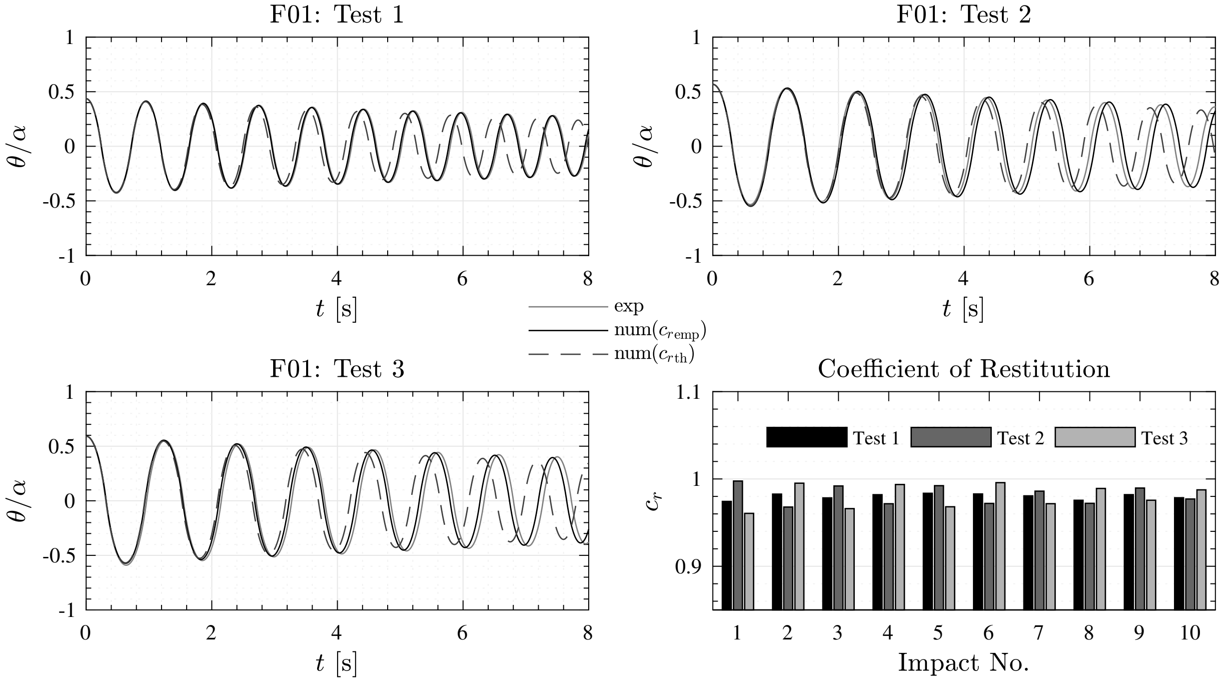

Figure C.30: Specimen F01.

C.3.2 Specimen F02

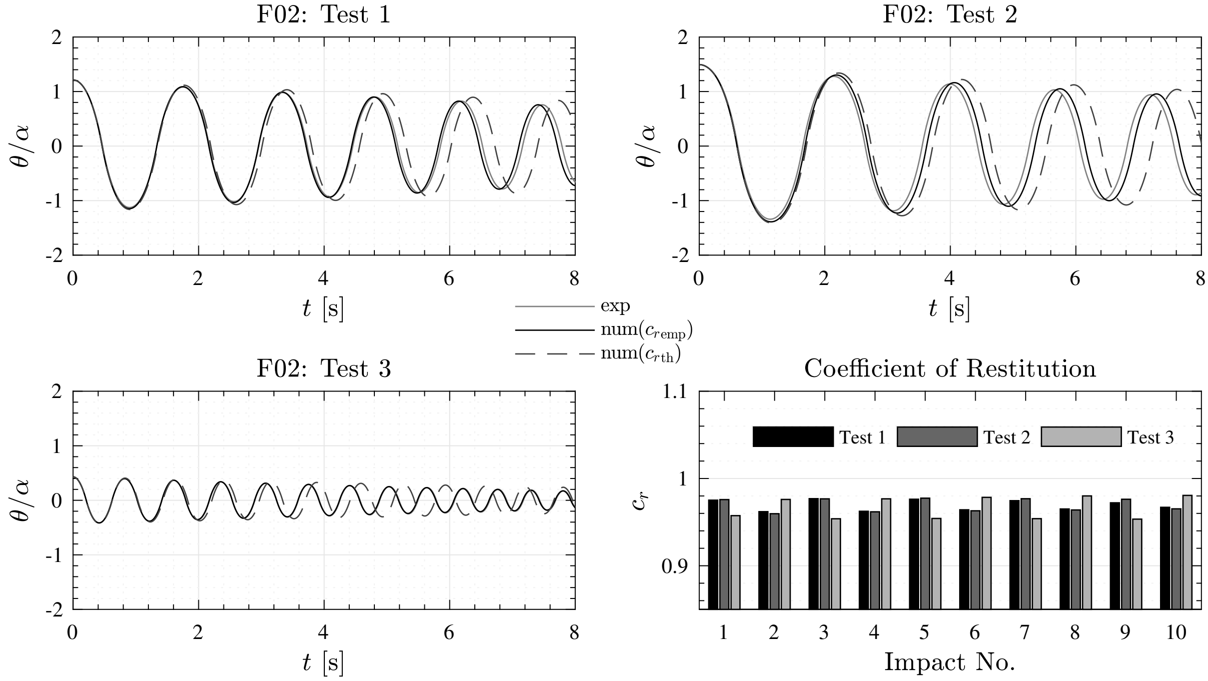

Figure C.31: Specimen F02.

C.3.3 Specimen F03

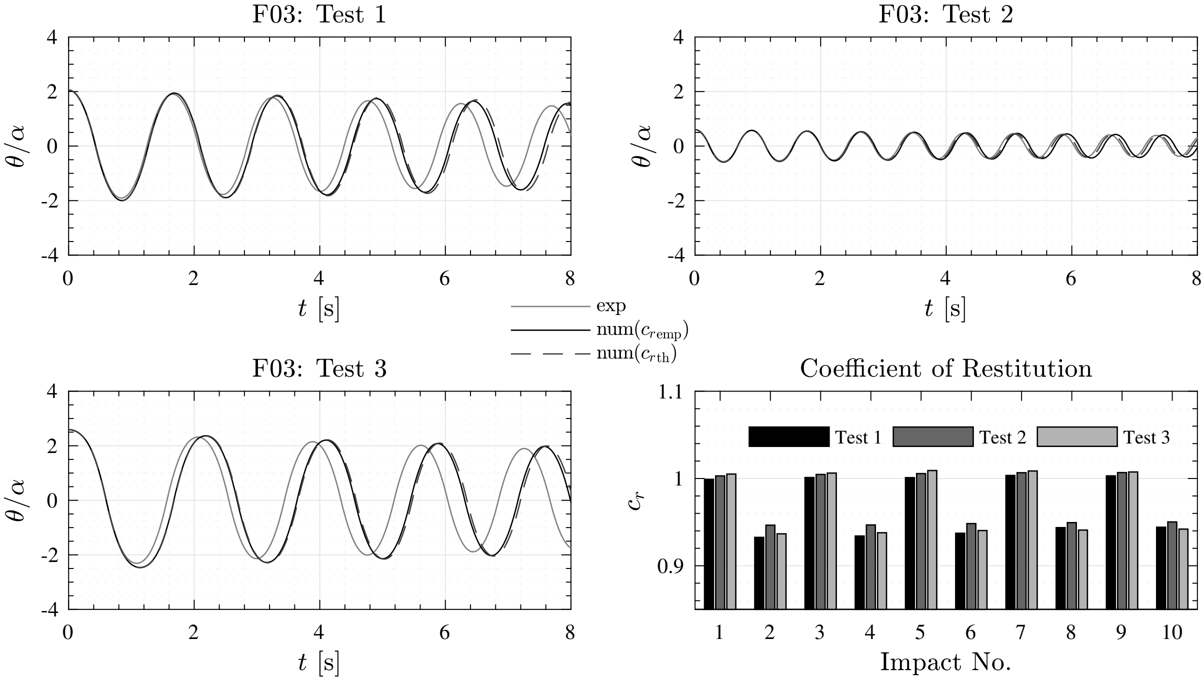

Figure C.32: Specimen F03.

C.3.4 Specimen F04

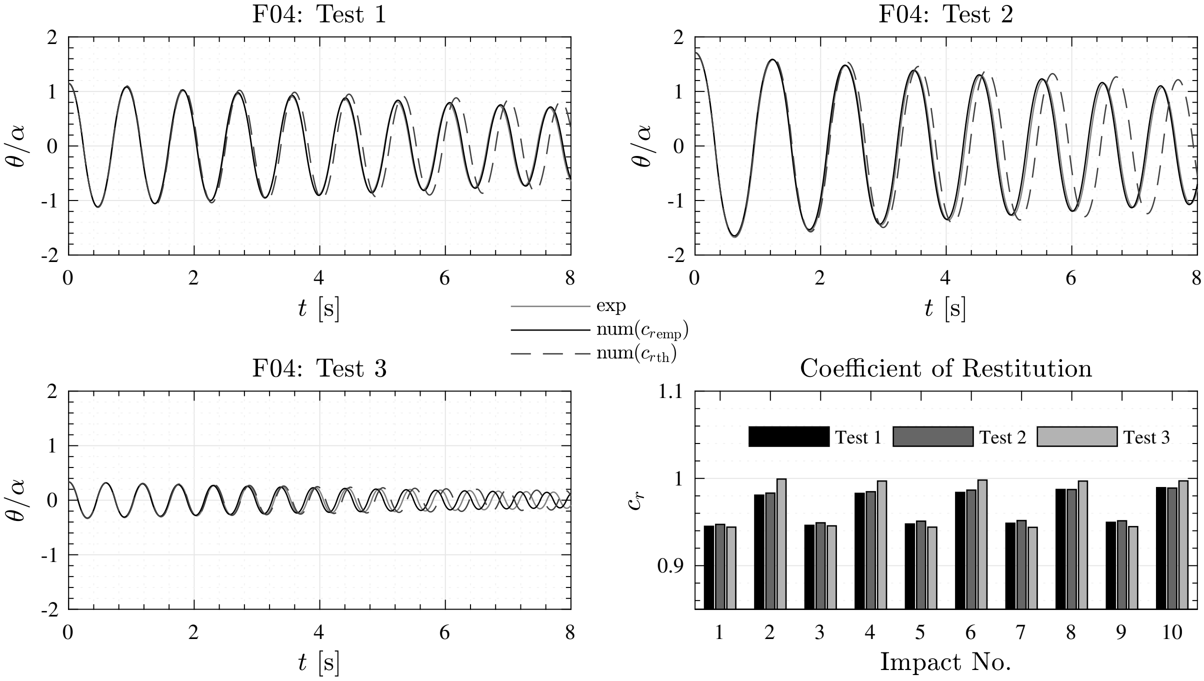

Figure C.33: Specimen F04.

C.3.5 Specimen F05

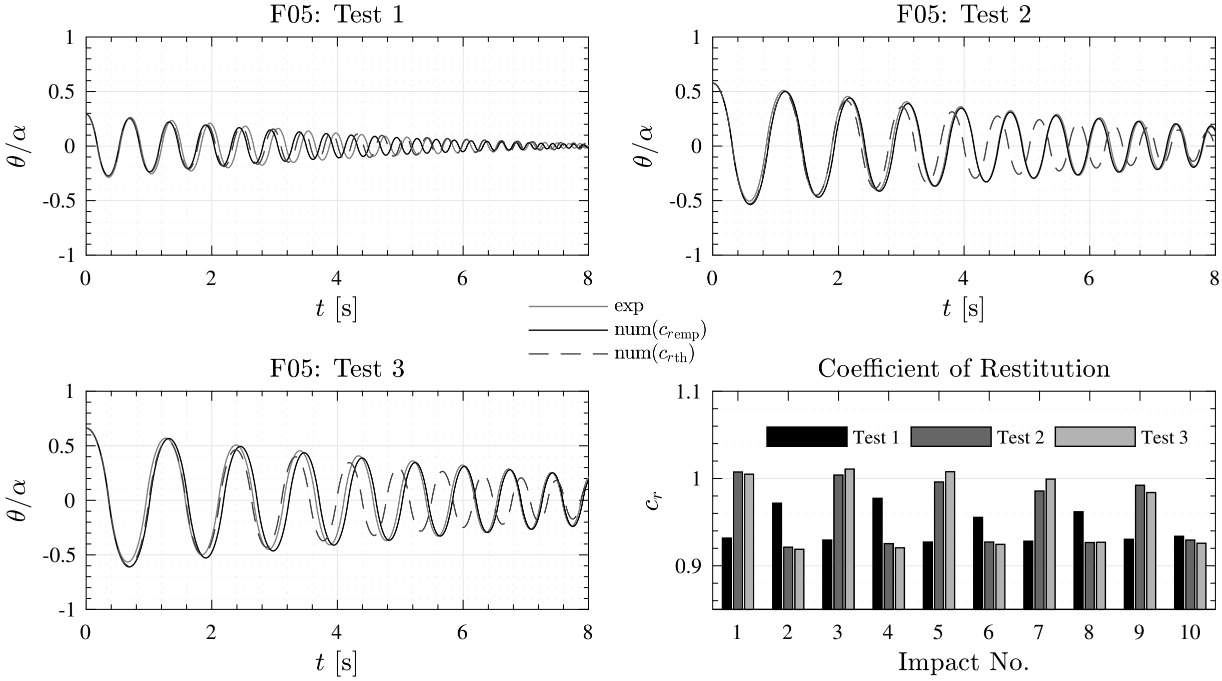

Figure C.34: Specimen F05.

C.3.6 Specimen F06

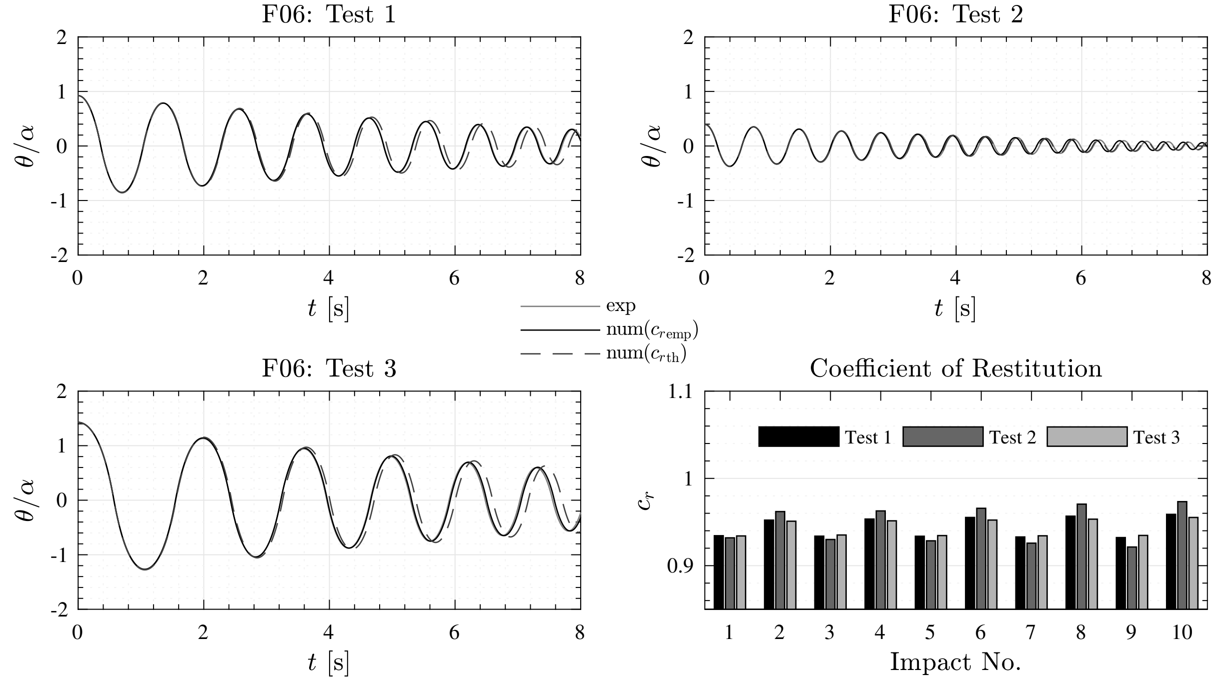

Figure C.35: Specimen F06.

C.3.7 Specimen F07

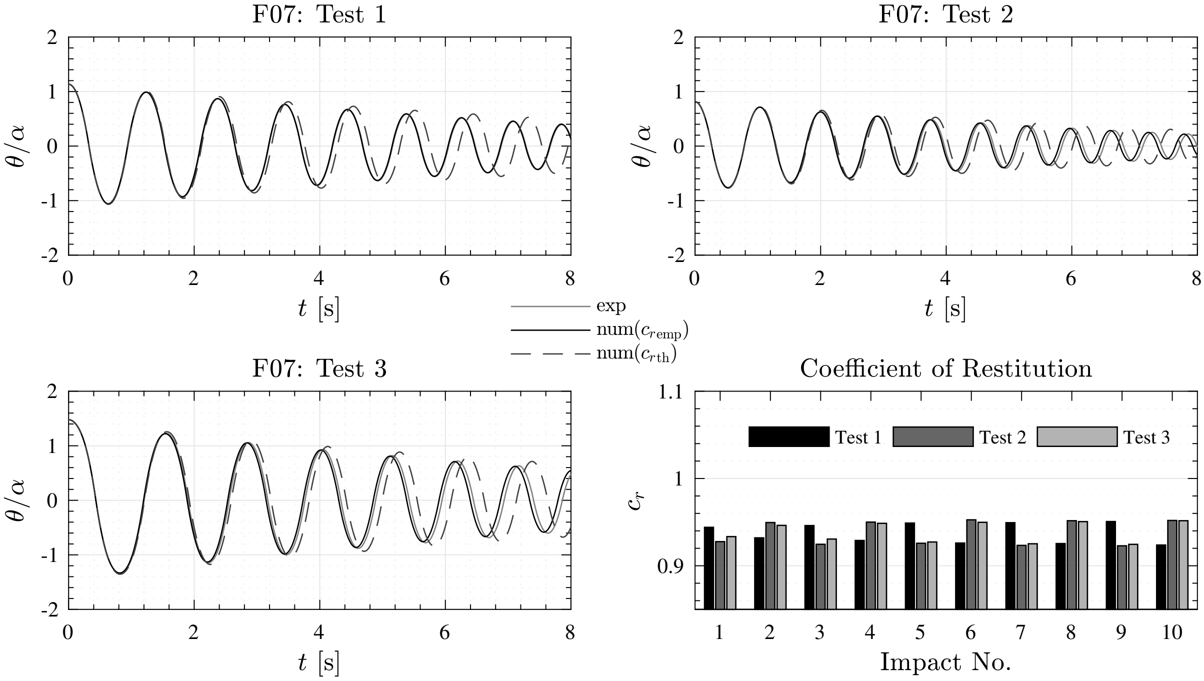

Figure C.36: Specimen F07.

C.3.8 Specimen F08

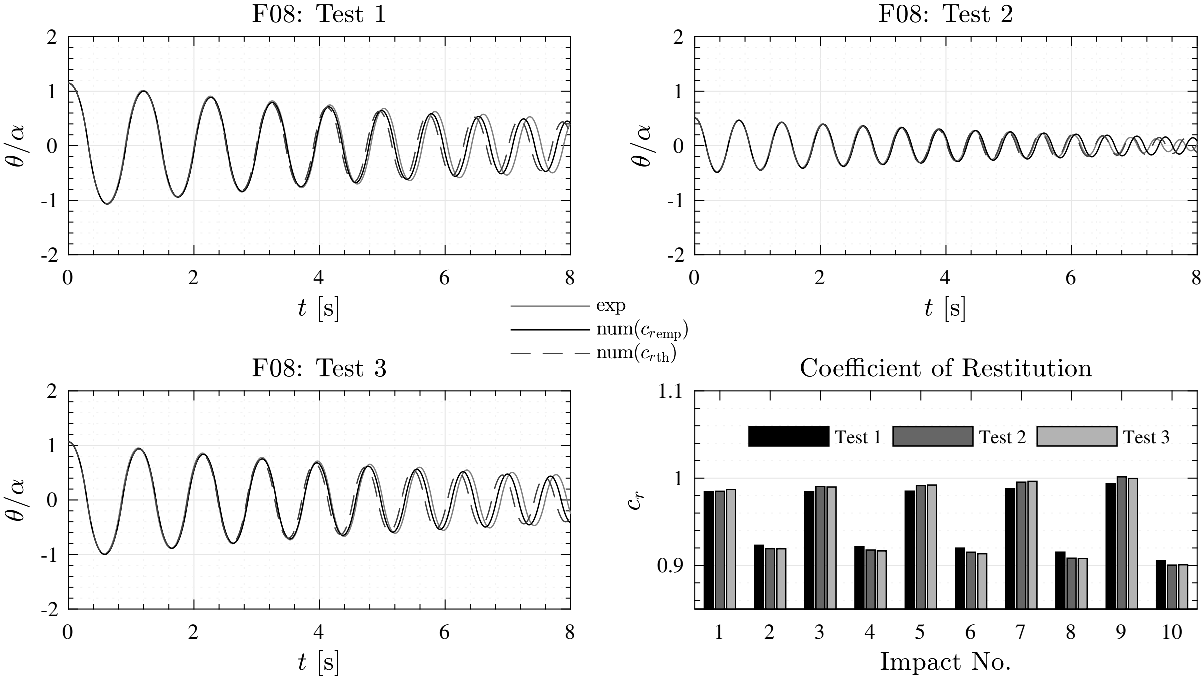

Figure C.37: Specimen F08.

APPENDIX D

TECHNICAL DRAWINGS

D.1 Modified Columns

D.1.1 Linking Plate

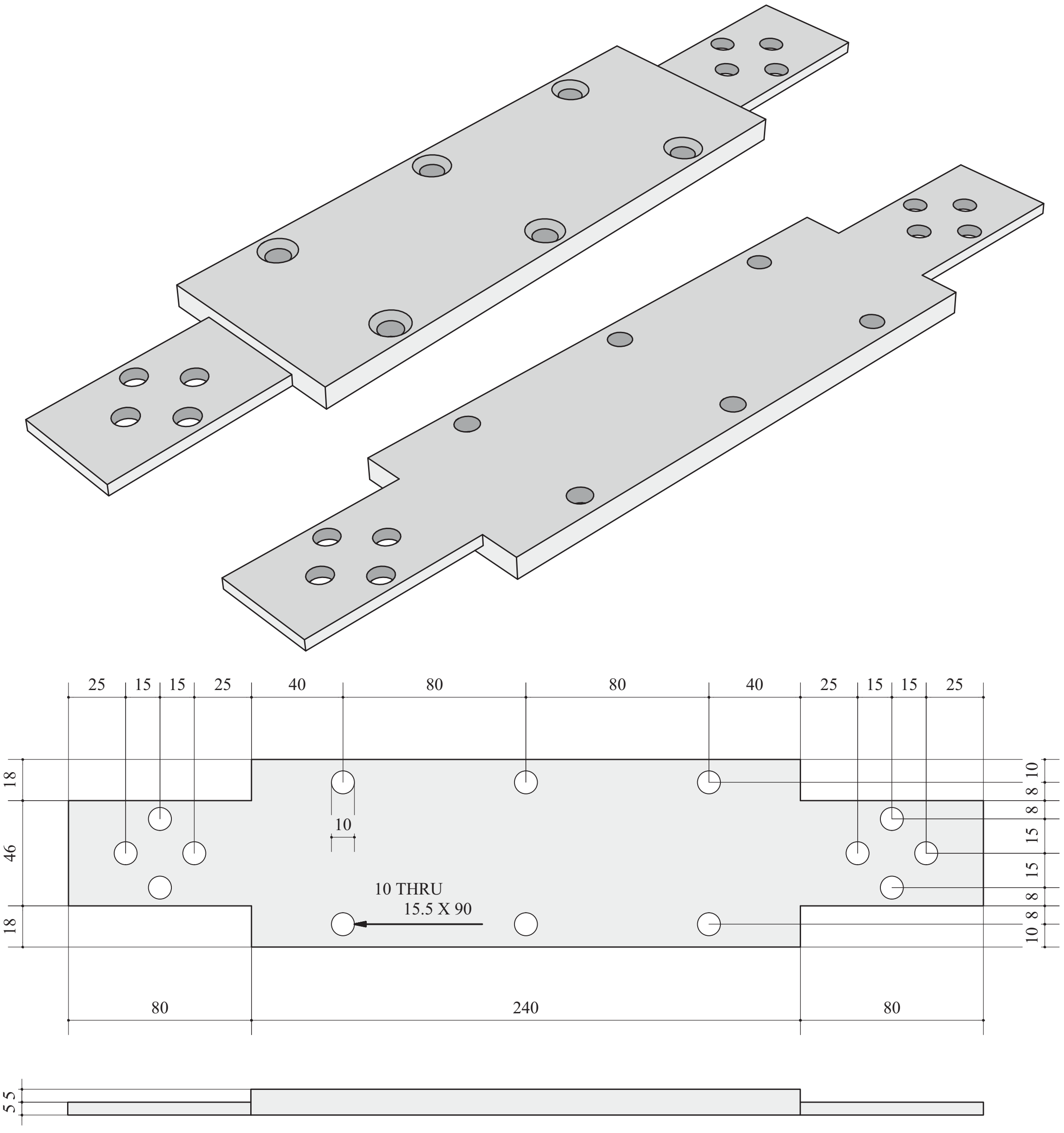

Figure D.1: Linking plate (Units [mm]).

D.1.2 Block

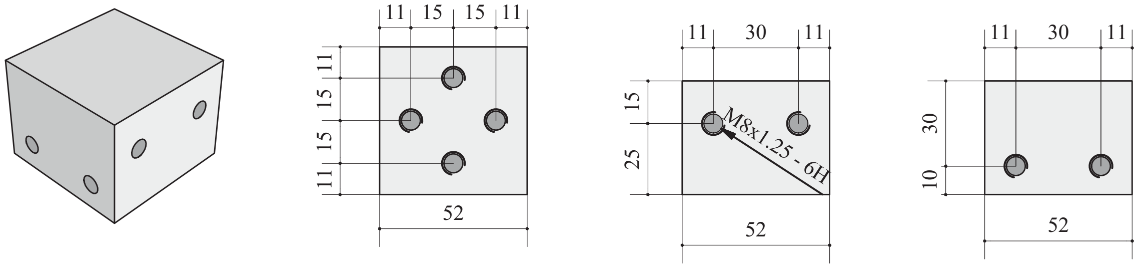

Figure D.2: Block (Units [mm]).

D.1.3 Bases

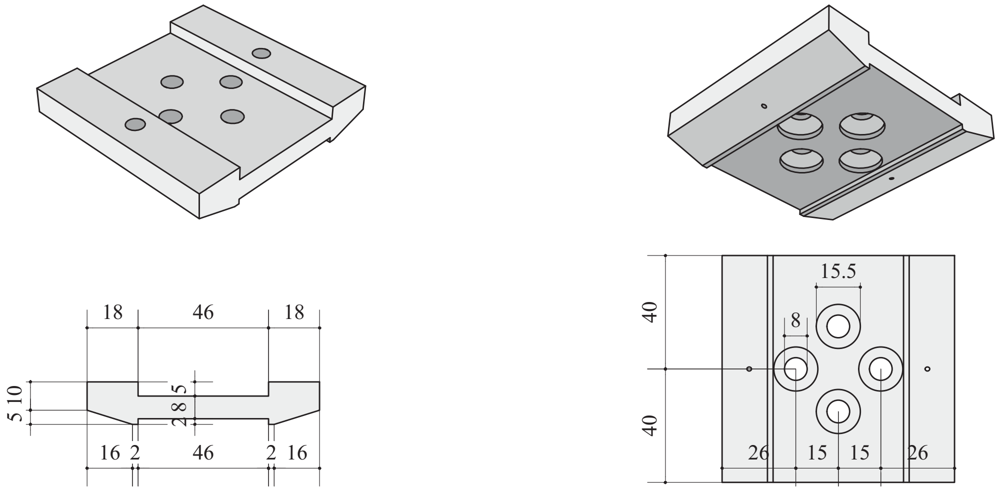

Figure D.3: Base F01 (Units [mm]).

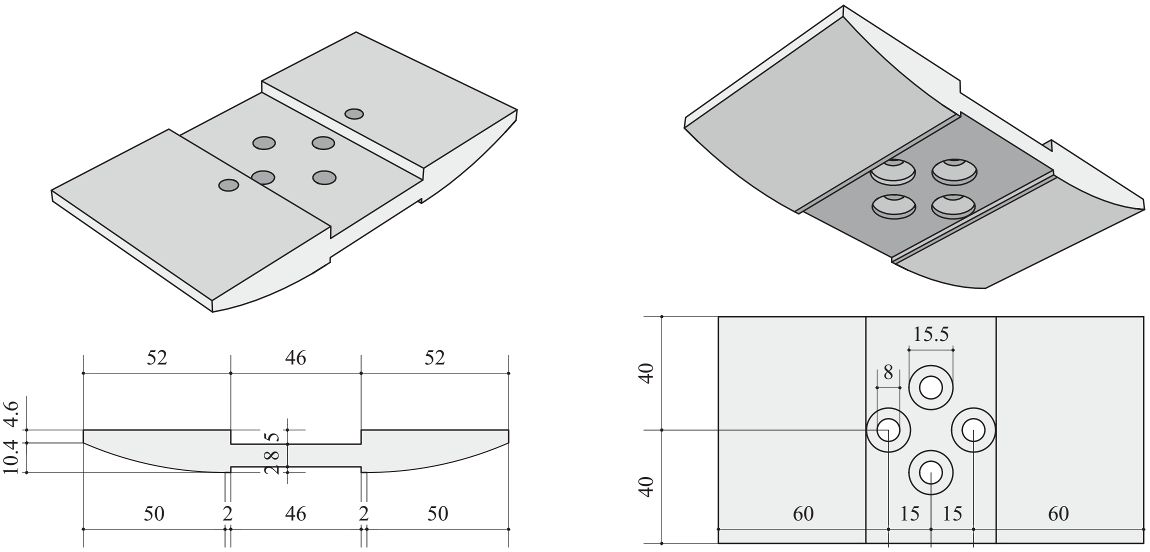

Figure D.4: Base F02 (Units [mm]).

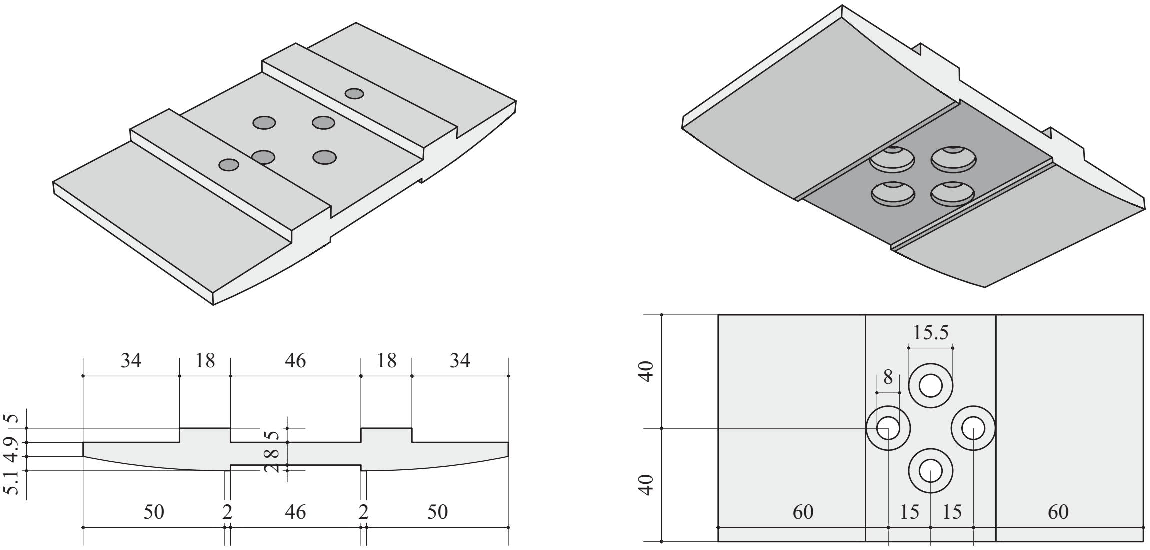

Figure D.5: Base F03 (Units [mm]).

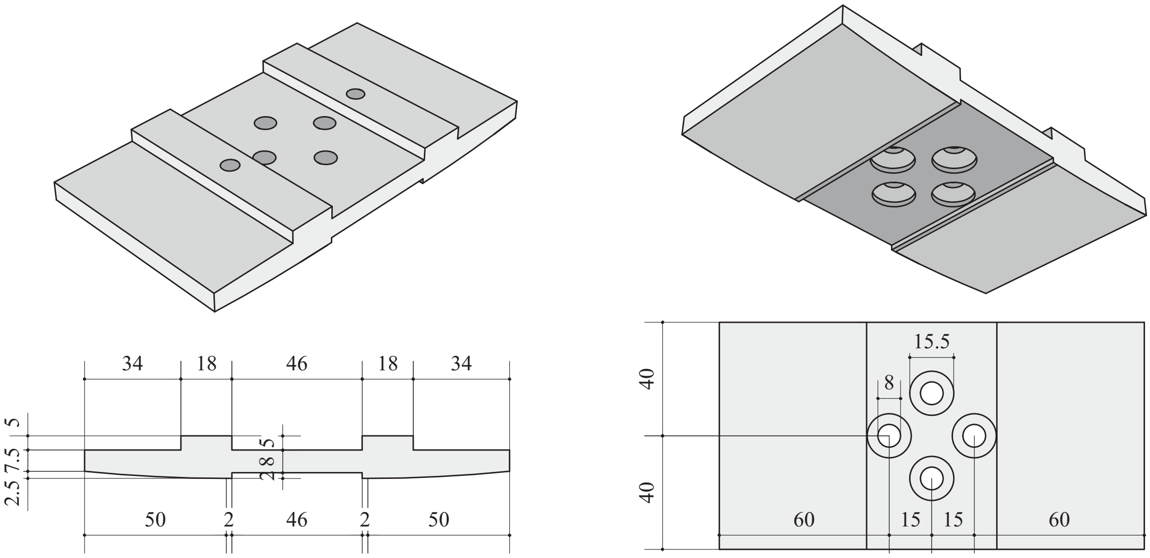

Figure D.6: Base F04 (Units [mm]).

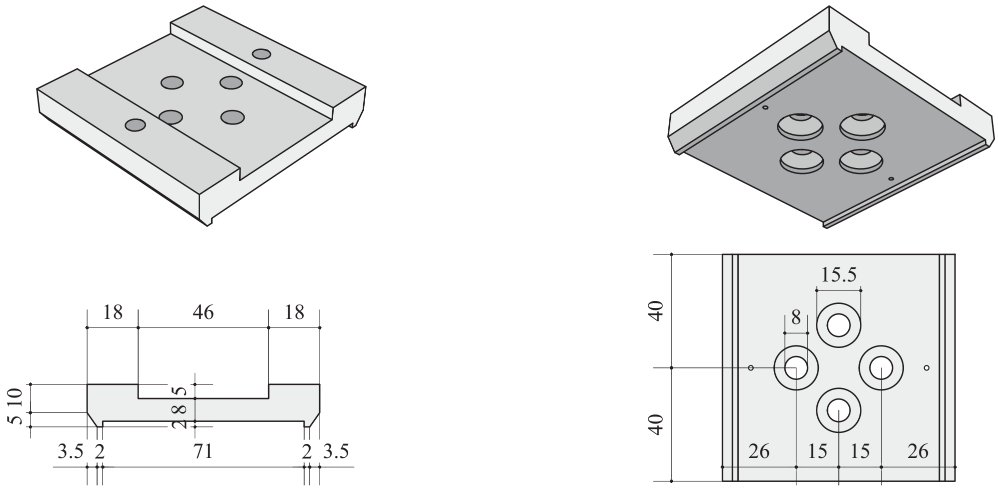

Figure D.7: Base F05 (Units [mm]).

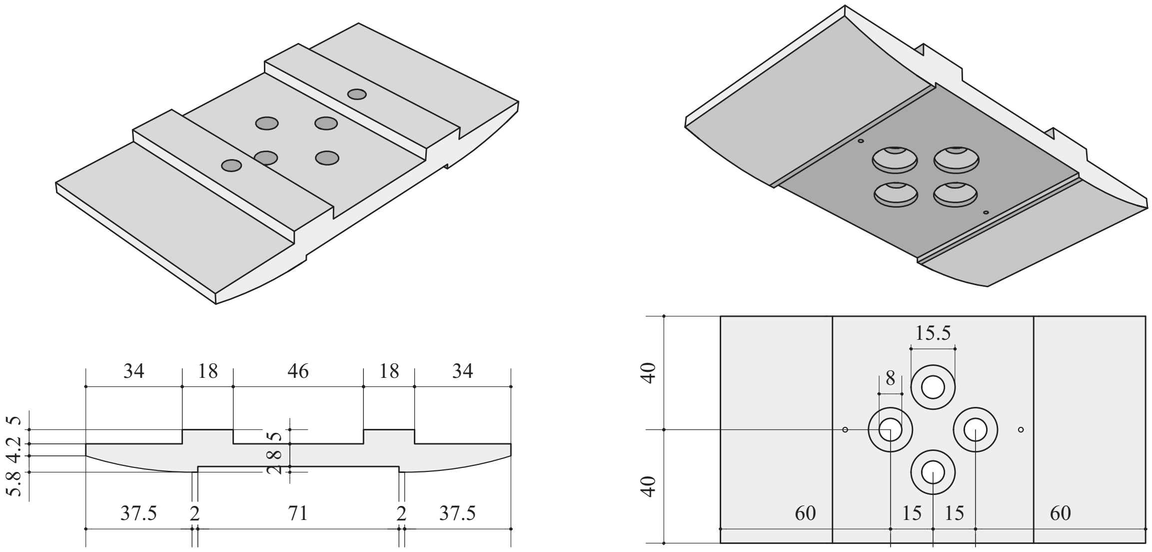

Figure D.8: Base F06 (Units [mm]).

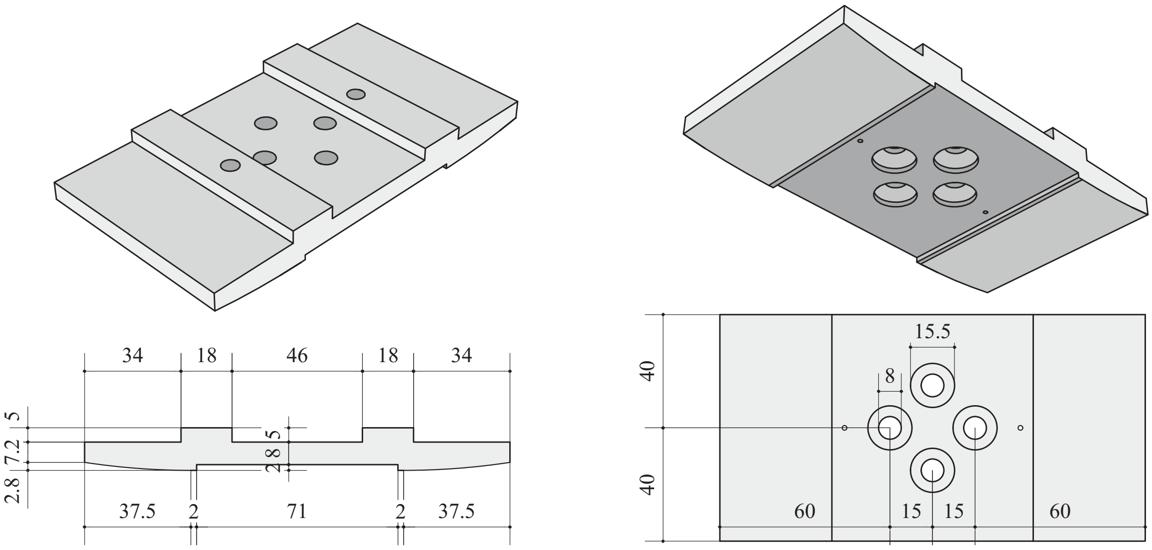

Figure D.9: Base F07 (Units [mm]).

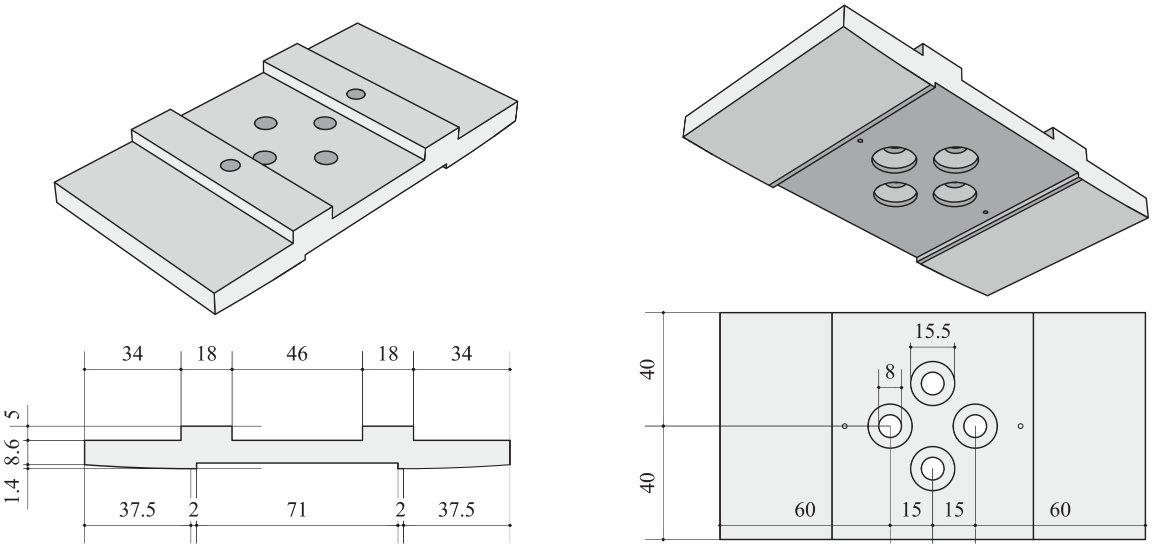

Figure D.10: Base F08 (Units [mm]).

D.1.4 Hollow Column

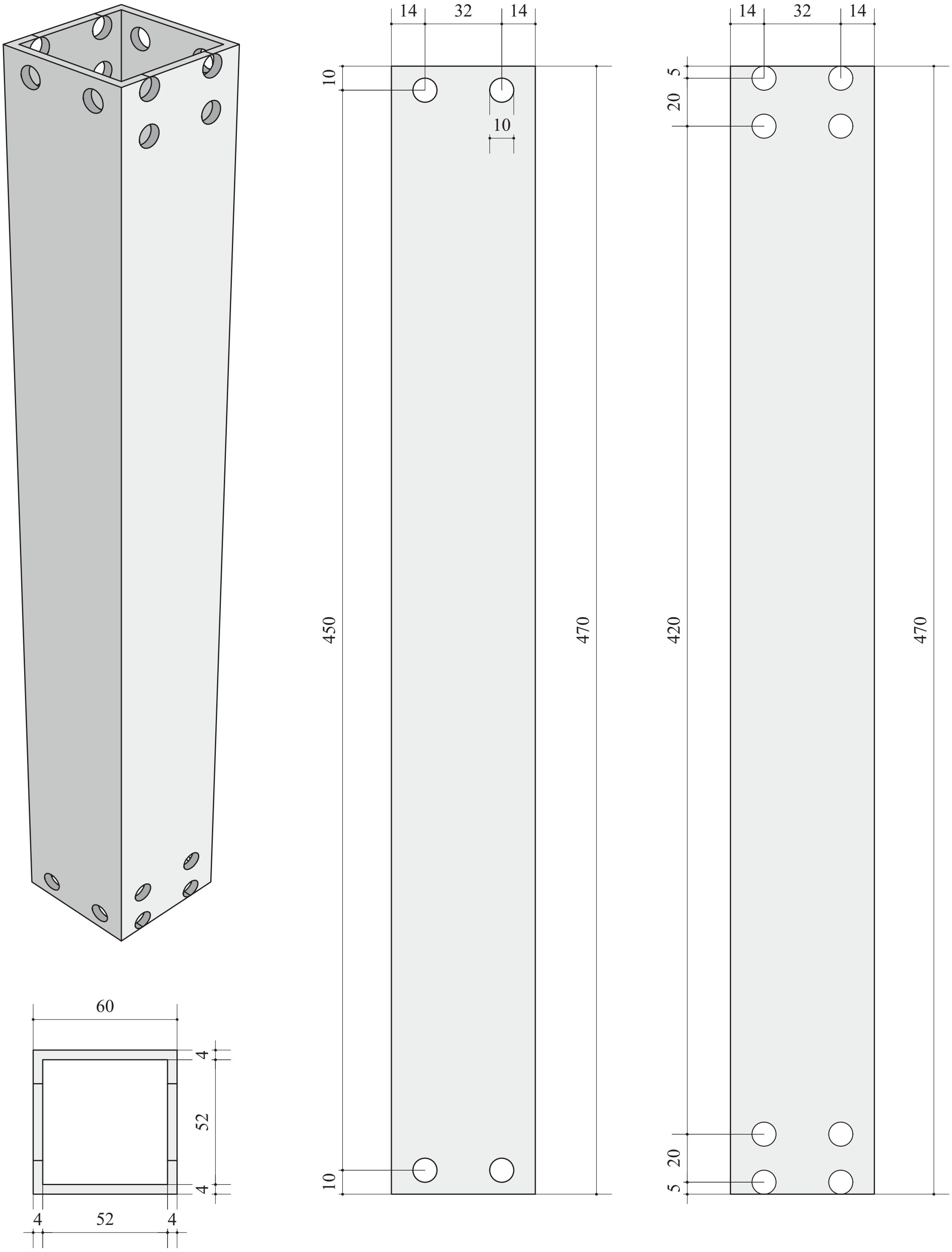

Figure D.11: Hollow column (Units [mm]).

BIBLIOGRAPHY

[1] Bachmann J. A., Vassiliou M. F., and Stojadinović B. Rocking of a rigid block on a curved foundation. In *Book of Abstracts: Engineering Mechanics Institute Conference*, San Francisco, 2015. Stanford University.

[2] Bachmann J. A., Blöchlinger P., Wellauer M., Vassiliou M. F., and Stojadinović B. Experimental investigation of the seismic response of a column rocking and rolling on a concave base. In *ECCOMAS Congress 2016: 7th European Congress on Computational Methods in Applied Sciences and Engineering*, Heraklion, 2016.

[3] Bachmann J. A., Jost C., Studemann Q., Vassiliou M. F., and Stojadinović B. An analytical model for the dynamic response of an elastic SDOF system fixed on top of a rocking single-story frame structure: experimental validation. In *ECCOMAS Congress 2016: 7th European Congress on Computational Methods in Applied Sciences and Engineering*, pages 1–40, Heraklion, 2016.

[4] Bachmann J. A., Vassiliou M. F., and Stojadinović B. Dynamic response of an elastic SDOF system fixed on top of a rocking podium frame structure: modelling. In *World Conference on Earthquake Engineering*, Santiago de Chile, 2017.

[5] Bachmann J. A., Vassiliou M. F., and Stojadinovic B. Dynamics of rocking podium structures. *Earthquake Engng Struct Dyn*, may 2017, **46**(14):2499–2517.

[6] Burger S., Egger M., Bachmann J. A., Vassiliou M. F., and Stojadinović B. Behavior of inverted pendulum cylindrical structures that rock and wobble during earthquakes. In *World Conference on Earthquake Engineering*, Santiago de Chile, 2017.

[7] Vassiliou M. F., Burger S., Egger M., Bachmann J. A., Broccardo M., and Stojadinovic B. The three-dimensional behavior of inverted pendulum cylindrical structures during earthquakes. *Earthquake Engng Struct Dyn*, 2017, **46**(14):2261–2280.

[8] Bachmann J. A., Strand M., Vassiliou M. F., Broccardo M., and Stojadinovic B. Probabilistic Validation of the Housner Rocking Model. In *COMPDYN 2017: 6th International Conference on Computational Methods in Structural Dynamics and Earthquake Engineering*, pages 1–16, Rhodes, 2017.

[9] Bachmann J. A., Strand M., Vassiliou M. F., Broccardo M., and Stojadinović B. Is rocking motion predictable? *Earthquake Engng Struct Dyn*, feb 2018, **47**(2):535–552.

[10] Blöchlinger P. and Wellauer M. *Experimental and analytical investigation of the seismic response of a column rocking and rolling on a concave base.* Master project, ETH Zurich, 2015.

[11] Fankhauser C. *Dynamic response of structures that roll and rock on the support surface.* Master thesis, ETH Zurich, 2017.

[12] Egger M. and Burger S. *Three-dimensional analysis of rocking and rolling of a rigid cylinder.* Master project, ETH Zurich, 2015.

[13] Burger S. *Three-dimensional motion of a rigid cylinder constrained to rock and roll on its circumference.* Master thesis, ETH Zurich, 2016.

[14] Studemann Q. and Jost C. *Experimental and analytical investigation of a seismic response of a rocking frame.* Master thesis, ETH Zurich, 2015.

[15] Strand M. *Statistical Validation of Rigid Body Rocking Response Models Against Experimental and Numerical Data.* Master thesis, ETH Zurich, 2017.

[16] Housner G. W. The Behavior of inverted Pendulum Structures during Earthquakes. *Bulletin of the Seismological Society of America*, 1963, **53**(2):403–417.

[17] Rangitikei South Viaduct. *www.YouTube.com*, 2016, (accessed Aug 2018).

[18] Chouw N. Low-Damage Design Philosophy for Future Earthquake-Resistant Structures. In *ASME 2017 Pressure Vessels and Piping Conference*, page V008T08A034. American Society of Mechanical Engineers, 2017.

[19] Makris N. A half-century of rocking isolation. *Earthquakes and Structures*, dec 2014, **7**(6):1187–1221.

[20] Milne J. Seismic experiments. *Transactions of the Seismological Society of Japan*, 1885, 8:1–82.

[21] Kirkpatrick P. Seismic Measurements by the Overthrow of Columns. *Bulletin of the Seismological Society of America*, 1927, **17**(2):95–109.

[22] Yim C.-S., Chopra A. K., and Penzien J. Rocking response of rigid blocks to earthquakes. *Earthquake Engng Struct Dyn*, 1980, **8**(6):565–587.

[23] Psycharis I. N. and Jennings P. C. Rocking of slender rigid bodies allowed to uplift. *Earthquake Engng Struct Dyn*, jan 1983, **11**(1):57–76.

[24] Spanos P. D. and Koh A.-S. Rocking of Rigid Blocks Due to Harmonic Shaking. *Journal of Engineering Mechanics*, nov 1984, **110**(11):1627–1642.

[25] Zhang J. and Makris N. Rocking Response of Free-Standing Blocks under Cycloidal Pulses. *Journal of Engineering Mechanics*, may 2001, **127**(5):473–483.

[26] Dimitrakopoulos E. G. and DeJong M. J. Revisiting the rocking block: closed-form solutions and similarity laws. *Proceedings of the Royal Society A: Mathematical, Physical and Engineering Sciences*, aug 2012, **468**(2144):2294–2318.

[27] Dimitrakopoulos E. G. and DeJong M. J. Overturning of Retrofitted Rocking Structures under Pulse-Type Excitations. *Journal of Engineering Mechanics*, aug 2012, **138**(8):963–972.

[28] Vassiliou M. F. and Makris N. Analysis of the rocking response of rigid blocks standing free on a seismically isolated base. *Earthquake Engng Struct Dyn*, feb 2012, **41**(2):177–196.

[29] DeJong M. J. and Dimitrakopoulos E. G. Dynamically equivalent rocking structures. *Earthquake Engng Struct Dyn*, aug 2014, **43**(10):1543–1563.

[30] Makris N. The Role of the Rotational Inertia on the Seismic Resistance of Free-Standing Rocking Columns and Articulated Frames. *Bulletin of the Seismological Society of America*, oct 2014, **104**(5):2226–2239.

[31] Makris N. and Kampas G. Size Versus Slenderness: Two Competing Parameters in the Seismic Stability of Free-Standing Rocking Columns. *Bulletin of the Seismological Society of America*, feb 2016, **106**(1):104–122.

[32] Makris N. and Vassiliou M. F. Sizing the slenderness of free-standing rocking columns to withstand earthquake shaking. *Archive of Applied Mechanics*, oct 2012, **82**(10-11):1497–1511.

[33] Mander J. B. and Cheng C.-T. Seismic resistance of bridge piers based on damage avoidance design. Technical report, State University of New York, Buffalo (NY), 1997.

[34] Cheng C.-T. Shaking table tests of a self-centering designed bridge substructure. *Engineering Structures*, 2008, **30**(12):3426–3433.

[35] Deng L., Kutter B. L., and Kunnath S. K. Probabilistic seismic performance of rocking-foundation and hinging-column bridges. *Earthquake Spectra*, 2012, **28**(4):1423–1446.

[36] Sakai J. and Mahin S. A. Analytical investigations of new methods for reducing residual displacements of reinforced concrete bridge columns PEER-2004/02. Technical report, University of California, Berkeley, CA, 2004.

[37] Wacker J. M., Hieber D. G., Stanton J. F., and Eberhard M. O. Design of precast concrete piers for rapid bridge construction in seismic regions. *Research Rep*, 2005.

[38] Vassiliou M. F. *Analytical investigation of the dynamic response of a pair of columns capped with a rigid beam and of the effect of seismic isolation on rocking structures*. PhD thesis, Doctoral dissertation, Dept. of Civil Engineering, Univ. of Patras, Greece (in Greek), 2010.

[39] Makris N. and Vassiliou M. F. Planar rocking response and stability analysis of an array of free-standing columns capped with a freely supported rigid beam. *Earthquake Engng Struct Dyn*, mar 2013, **42**(3):431–449.

[40] Makris N. and Vassiliou M. F. Are Some Top-Heavy Structures More Stable? *Journal of Structural Engineering*, may 2014, **140**(5):06014001: 1–5.

[41] Dimitrakopoulos E. G. and Giouvanidis A. I. Seismic Response Analysis of the Planar Rocking Frame. *Journal of Engineering Mechanics*, jul 2015, **141**(7):04015003: 1–13.

[42] Makris N., Alexakis H., Kampas G., Strepelias I., Kolonas C., and Bousias S. Seismic protection of bridges with rocking piers which recenter with gravity. *Report EEAM*, 2015, 1.

[43] Vassiliou M. F. and Makris N. Dynamics of the Vertically Restrained Rocking Column. *Journal of Engineering Mechanics*, dec 2015, **141**(12):04015049: 1–10.

[44] Makris N. and Vassiliou M. F. Dynamics of the Rocking Frame with Vertical Restrainers. *Journal of Structural Engineering*, oct 2015, **141**(10):04014245: 1–13.

[45] Dimitrakopoulos E. G. and DeJong M. J. Seismic overturning of rocking structures with external viscous dampers. In *Computational methods in earthquake engineering*, pages 243–258. Springer, 2013.

[46] Giouvanidis A. I. and Dimitrakopoulos E. G. Seismic Performance of Rocking Frames with Flag-Shaped Hysteretic Behavior. *Journal of Engineering Mechanics*, may 2017, **143**(5):04017008: 1–13.

[47] Contento A. and Di Egidio A. Investigations into the benefits of base isolation for non-symmetric rigid blocks. *Earthquake Engng Struct Dyn*, jun 2009, **38**(7):849–866.

[48] Dar A., Konstantinidis D., and El-Dakhakhni W. W. Evaluation of ASCE 43-05 Seismic Design Criteria for Rocking Objects in Nuclear Facilities. *Journal of Structural Engineering*, nov 2016, **142**(11):04016110: 1–13.

[49] Wikipedia. Fukushima Daiichi nuclear disaster (2011). (accessed Aug 2018).

[50] Makris N. and Konstantinidis D. The Rocking Spectrum and the Shortcomings of Design Guidelines. Technical Report Aug. 2001, University of California, Berkeley, 2001.

[51] Federal Emergency Management Agency (FEMA). Prestandard and commentary for the seismic rehabilitation of buildings. Technical report, Washington, DC, 2000.

[52] Papastamatiou D. and Psycharis L. Seismic response of classical monuments-a numerical perspective developed at the Temple of Apollo in Bassae, Greece. *Terra Nova*, 1993, **5**(6):591–601.

[53] Winkler T., Meguro K., and Yamazaki F. Response of rigid body assemblies to dynamic excitation. *Earthquake Engng Struct Dyn*, 1995, **24**(10):1389–1408.

[54] Psycharis I. N., Papastamatiou D. Y., and Alexandris A. P. Parametric investigation of the stability of classical columns under harmonic and earthquake excitations. *Earthquake Engng Struct Dyn*, aug 2000, **29**(8):1093–1109.

[55] Papantonopoulos C., Psycharis I. N., Papastamatiou D. Y., Lemos J. V., and Mouzakis H. P. Numerical prediction of the earthquake response of classical columns using the distinct element method. *Earthquake Engng Struct Dyn*, sep 2002, **31**(9):1699–1717.

[56] Mouzakis H. P., Psycharis I. N., Papastamatiou D. Y., Carydis P. G., Papantonopoulos C., and Zambas C. Experimental investigation of the earthquake response of a model of a marble classical column. *Earthquake Engng Struct Dyn*, sep 2002, **31**(9):1681–1698.

[57] Psycharis I. N., Lemos J. V., Papastamatiou D. Y., Zambas C., and Papantonopoulos C. Numerical study of the seismic behaviour of a part of the Parthenon Pronaos. *Earthquake Engng Struct Dyn*, nov 2003, **32**(13):2063–2084.

[58] Konstantinidis D. and Makris N. Seismic response analysis of multidrum classical columns. *Earthquake Engng Struct Dyn*, aug 2005, **34**(10):1243–1270.

[59] Komodromos P., Papaloizou L., and Polycarpou P. Simulation of the response of ancient columns under harmonic and earthquake excitations. *Engineering Structures*, aug 2008, **30**(8):2154–2164.

[60] Papaloizou L. and Komodromos P. Planar investigation of the seismic response of ancient columns and colonnades with epistyles using a custom-made software. *Soil Dynamics and Earthquake Engineering*, nov 2009, **29**(11-12):1437–1454.

[61] Ambraseys N. and Psycharis I. N. Earthquake stability of columns and statues. *Journal of Earthquake Engineering*, 2011, **15**(5):685–710.

[62] Stefanou I., Psycharis I., and Georgopoulos I.-O. Dynamic response of reinforced masonry columns in classical monuments. *Construction and Building Materials*, 2011, **25**(12):4325–4337.

[63] Sextos A., Nalmpantis S., Faraonis P., Skiada D., and Stylianidis K. Probabilistic Seismic Hazard Assessment Through Geometrically Non-Linear Back-Analysis of Byzantine and Roman Monuments. In *10th HSTAM*, Chania, Greece, 2013.

[64] Kounadis A. N. Rocking instability under ground motion of large statues freely standing atop elastically supported cantilevers. *Archive of Applied Mechanics*, jul 2014, **84**(7):933–951.

[65] Drosos V. and Anastasopoulos I. Shaking table testing of multidrum columns and portals. *Earthquake Engng Struct Dyn*, sep 2014, **43**(11):1703–1723.

[66] Oliveto G., Caliò I., and Greco A. Large displacement behaviour of a structural model with foundation uplift under impulsive and earthquake excitations. *Earthquake Engng Struct Dyn*, mar 2003, **32**(3):369–393.

[67] Ma Q. T. M. *The mechanics of rocking structures subjected to ground motion*. PhD thesis, University of Auckland, New Zealand, 2010.

[68] Vassiliou M. F., Mackie K. R., and Stojadinović B. Dynamic response analysis of solitary flexible rocking bodies: modeling and behavior under pulse-like ground excitation. *Earthquake Engng Struct Dyn*, aug 2014, **43**(10):1463–1481.

[69] Acikgoz S. and DeJong M. J. The rocking response of large flexible structures to earthquakes. *Bulletin of Earthquake Engineering*, apr 2014, **12**(2):875–908.

[70] Vassiliou M. F., Truniger R., and Stojadinović B. An analytical model of a deformable cantilever structure rocking on a rigid surface: development and verification. *Earthquake Engng Struct Dyn*, dec 2015, **44**(15):2775–2794.

[71] Wiebe L. and Christopoulos C. A cantilever beam analogy for quantifying higher mode effects in multistorey buildings. *Earthquake Engng Struct Dyn*, 2015, **44**(11):1697–1716.

[72] Acikgoz S. and DeJong M. J. The interaction of elasticity and rocking in flexible structures allowed to uplift. *Earthquake Engng Struct Dyn*, mar 2012, **41**(11):1–18.

[73] Acikgoz S. and DeJong M. J. An investigation of the dynamics of rocking isolation for earthquake-resilient design. In *ECCOMAS 2016*, 2016.

[74] Acikgoz S. and DeJong M. J. Analytical modelling of multi-mass flexible rocking structures. *Earthquake Engng Struct Dyn*, oct 2016, **45**(13):2103–2122.

[75] Peña F., Prieto F., Lourenço P. B., Campos Costa A., and Lemos J. V. On the dynamics of rocking motion of single rigid-block structures. *Earthquake Engng Struct Dyn*, dec 2007, **36**(15):2383–2399.

[76] Truniger R., Vassiliou M. F., and Stojadinović B. An analytical model of a deformable cantilever structure rocking on a rigid surface: experimental validation. *Earthquake Engng Struct Dyn*, dec 2015, **44**(15):2795–2815.

[77] Giouvanidis A. I. and Dimitrakopoulos E. G. Nonsmooth dynamic analysis of sticking impacts in rocking structures. *Bulletin of Earthquake Engineering*, may 2017, **15**(5):2273–2304.

[78] Psycharis I. N., Fragiadakis M., and Stefanou I. Seismic reliability assessment of classical columns subjected to near-fault ground motions. *Earthquake Engng Struct Dyn*, jun 2013, **42**(14):n/a–n/a.

[79] Dimitrakopoulos E. G. and Paraskeva T. S. Dimensionless fragility curves for rocking response to near-fault excitations. *Earthquake Engng Struct Dyn*, sep 2015, **44**(12):2015–2033.

[80] Bakhtiary E. and Gardoni P. Probabilistic seismic demand model and fragility estimates for rocking symmetric blocks. *Engineering Structures*, 2016, 114:25–34.

[81] Koh A.-S. and Mustafa G. Free Rocking of Cylindrical Structures. *Journal of Engineering Mechanics*, jan 1990, **116**(1):35–54.

[82] Koh A.-S. and Hsiung C.-M. Base Isolation Benefits of 3-D Rocking and Uplift. I: Theory. *Journal of Engineering Mechanics*, jan 1991, **117**(1):1–18.

[83] Koh A.-S. and Hsiung C.-M. Base Isolation Benefits of 3-D Rocking and Uplift. II: Numerical Example. *Journal of Engineering Mechanics*, jan 1991, **117**(1):19–31.

[84] Stefanou I., Vardoulakis I., and Mavraganis A. Dynamic motion of a conical frustum over a rough horizontal plane. *International Journal of Non-Linear Mechanics*, 2011, **46**(1):114–124.

[85] Srinivasan M. and Ruina A. Rocking and rolling: A can that appears to rock might actually roll. *Physical Review E*, dec 2008, **78**(6):066609.

[86] Pappas A., Sextos A., Porto F. d., and Modena C. Efficiency of alternative intensity measures for the seismic assessment of monolithic free-standing columns. *Bulletin of Earthquake Engineering*, oct 2016.

[87] Konstantinidis D. and Makris N. The dynamics of a rocking block in three dimensions. In *8th HSTAM International Congress on Mechanics*, number Sept, pages 12 – 14, Patras, Greece, 2007.

[88] Zulli D., Contento A., and Di Egidio A. 3D model of rigid block with a rectangular base subject to pulse-type excitation. *International Journal of Non-Linear Mechanics*, jul 2012, **47**(6):679–687.

[89] Chatzis M. N. and Smyth A. W. Modeling of the 3D rocking problem. *International Journal of Non-Linear Mechanics*, may 2012, **47**(4):85–98.

[90] Chatzis M. N. and Smyth A. W. Three-dimensional dynamics of a rigid body with wheels on a moving base. *Journal of Engineering Mechanics*, 2012, **139**(4):496–511.

[91] Greenbaum R. J. Y., Smyth A. W., and Chatzis M. N. Monocular computer vision method for the experimental study of three-dimensional rocking motion. *Journal of Engineering Mechanics*, 2015, **142**(1):4015062.

[92] Mathey C., Feau C., Politopoulos I., Clair D., Baillet L., and Fogli M. Behavior of rigid blocks with geometrical defects under seismic motion: an experimental and numerical study. *Earthquake Engng Struct Dyn*, 2016, **45**(15):2455–2474.

[93] Beck J. L. and Skinner R. I. The seismic response of a reinforced concrete bridge pier designed to step. *Earthquake Engng Struct Dyn*, 1973, **2**(4):343–358.

[94] Sharpe R. D. and Skinner R. I. The seismic design of an industrial chimney with rocking base. *Bulletin of the New Zealand National Society for Earthquake Engineering*, 1983, **16**(2):98–106.

[95] Polyakov S. V. *Design of Earthquake Resistant Structures*. MIR Publishers, Moscow, english tr edition, 1974.

[96] Huckelbridge A. A. and Clough R. W. Earthquake simulation tests of a nine story steel frame with columns allowed to uplift. Technical report, University of California, Berkeley, CA, 1977.

[97] Ricles J. M., Sause R., Garlock M. M., and Zhao C. Posttensioned Seismic-Resistant Connections for Steel Frames. *Journal of Structural Engineering*, feb 2001, **127**(2):113–121.

[98] Priestley M. J. N., Sritharan S., Conley J. R., and Pampanin S. Preliminary Results and Conclusions from the PRESSS Five-story Precast Concrete Test Building. Technical report, University of California, San Diego, CA, 1999.

[99] Liu R. and Palermo A. Low Damage Design and Seismic Isolation: What's the difference? In *2015 NZSEE Conference*, 2015.

[100] Zeris C. Seismic Response of Rocking Oscillators on a Soft Story: Elastic Response. *Journal of Structural Engineering*, aug 2015, **141**(8):04014196.

[101] Cherepinskiy Y. Seismic isolation of buildings with application of the kinematics bases. In *13th WCEE*, Vancouver, 2004.

[102] Uzdin A. M., Doronin F. A., Davydova G. V., Avidon G. E., and Karlina E. A. Performance analysis of seismic-insulating elements with negative stiffness. *Soil Mechanics and Foundation Engineering*, 2009, **46**(3):15–21.

[103] Semenov S. and Kurzanov A. Kinematic base isolation systems. *www.YouTube.com*, 2011, (accessed Mar 2016).

[104] Semenov S. Protection against earthquake. *www.YouTube.com*, 2015, (accessed Mar 2016).

[105] Priestley M. J. N., Evison R. J., and Carr A. J. Seismic response of structures free to rock on their foundations. *Bulletin of the New Zealand National Society for Earthquake Engineering*, 1978, **11**(3):141–150.

[106] Makris N. and Konstantinidis D. The rocking spectrum and the limitations of practical design methodologies. *Earthquake Engng Struct Dyn*, feb 2003, **32**(2):265–289.

[107] Aslam M., Scalise D. T., and Godden W. G. Earthquake rocking response of rigid bodies. *Journal of the Structural Division*, 1980, **106**(2):377–392.

[108] Lipscombe P. R. and Pellegrino S. Free Rocking of Prismatic Blocks. *Journal of Engineering Mechanics*, jul 1993, **119**(7):1387–1410.

[109] Truniger R. E., Vassiliou M. F., and Stojadinović B. Experimental Study on the Interaction between Elasticity and Rocking. In *10th U.S. NCEE*, pages 1–11, Anchorage, Alaska, 2014.

[110] Sargent R. G. Verification and validation of simulation models. *Journal of Simulation*, feb 2013, **7**(1):12–24.

[111] Jennings P. C., Housner G. W., and Tsai N. C. Simulated earthquake motions. Technical report, Earthquake Engineering Research Laboratory, California Institute of Technology, Pasadena, California, Pasadena, California, 1968.

[112] Di Egidio A. and Contento A. Base isolation of slide-rocking non-symmetric rigid blocks under impulsive and seismic excitations. *Engineering Structures*, 2009, **31**(11):2723–2734.

[113] Barenblatt G. I. *Scaling, self-similarity, and intermediate asymptotics: dimensional analysis and intermediate asymptotics*, volume 14. Cambridge University Press, Cambridge, UK, 1996.

[114] Wikipedia. Dimensional analysis. (accessed Sep 2018).

[115] Wikipedia. Similitude (model). (accessed Sep 2018).

[116] Zohuri B. *Dimensional Analysis and Self-Similarity Methods for Engineers and Scientists.* Springer International Publishing, 2015.

[117] Buckingham E. On physically similar systems; illustrations of the use of dimensional equations. *Physical review*, 1914, **4**(4):345.

[118] Wikipedia. Sounion. (accessed Aug 2018).

[119] Hall J. F., Heaton T. H., Halling M. W., and Wald D. J. Near-Source Ground Motion and its Effects on Flexible Buildings. *Earthquake Spectra*, nov 1995, **11**(4):569–605.

[120] Makris N. and Chang S.-P. Effect of viscous, viscoplastic and friction damping on the response of seismic isolated structures. *Earthquake Engng Struct Dyn*, jan 2000, **29**(1):85–107.

[121] Makris N. and Vassiliou M. F. The existence of 'complete similarities' in the response of seismic isolated structures subjected to pulse-like ground motions and their implications in analysis. *Earthquake Engng Struct Dyn*, aug 2011, **40**(10):1103–1121.

[122] Vassiliou M. F. and Makris N. Estimating time scales and length scales in pulselike earthquake acceleration records with wavelet analysis. *Bulletin of the Seismological Society of America*, 2011, **101**(2):596–618.

[123] Vaschy A. Sur les lois de similitude en physique. In *Annales télégraphiques*, volume 19, pages 25–28, 1892.

[124] Siano D. B. Orientational analysis—a supplement to dimensional analysis—I. *Journal of the Franklin Institute*, 1985, **320**(6):267–283.

[125] Ricker N. Further developments in the wavelet theory of seismogram structure. *Bulletin of the Seismological Society of America*, 1943, **33**(3):197–228.

[126] Ricker N. Wavelet functions and their polynomials. *Geophysics*, 1944, **9**(3):314–323.

[127] Makris N. and Vassiliou M. F. The dynamics of the rocking frame. In *Seismic Assessment, Behavior and Retrofit of Heritage Buildings and Monuments*, pages 37–59. Springer, 2015.

[128] Psycharis I. N. Effect of Base Uplift on Dynamic Response of SDOF Structures. *Journal of Structural Engineering*, mar 1991, **117**(3):733–754.

[129] Simoneschi G., Leo A. M. d., and Di Egidio A. Effectiveness of oscillating mass damper system in the protection of rigid blocks under impulsive excitation. *Engineering Structures*, 2017, 137:285–295.

[130] Makris N. and Vassiliou M. F. Rocking Response and Stability Analysis of an array of free-standing Columns capped with a free-standing rigid Beam. In *COMPDYN 2013*, number June, 2013.

[131] Chopra A. K. and Yim S. C. S. Simplified Earthquake Analysis of Structures with Foundation Uplift. *Journal of Structural Engineering*, apr 1985, **111**(4):906–930.

[132] Kafle B., Lam N. T. K., Gad E. F., and Wilson J. Displacement controlled rocking behaviour of rigid objects. *Earthquake Engng Struct Dyn*, dec 2011, **40**(15):1653–1669.

[133] Gelagoti F., Kourkoulis R., Anastasopoulos I., and Gazetas G. Rocking-isolated frame structures: margins of safety against toppling collapse and simplified design approach. *Soil Dynamics and Earthquake Engineering*, jan 2012, **32**(1):87–102.

[134] Ancheta T. D., Darragh R. B., Stewart J. P., Seyhan E., Silva W. J., Chiou B. S.-J., Wooddell K. E., Graves R. W., Kottke A. R., Boore D. M., Kishida T., and Donahue J. L. NGA-West2 Database. *Earthquake Spectra*, aug 2014, **30**(3):989–1005.

[135] Mashal M. and Palermo A. Experimental testing of emulative and post-tensioned earthquake damage resistant technologies for accelerated bridge construction. In *Proc. 16th World Conference on Earthquake Engineering, 16WCEE 2017*, 2017.

[136] Wikipedia. Euler Angles. (accessed Sep 2018).

[137] Adamidis O., Gazetas G., Anastasopoulos I., and Argyrou C. Equivalent-linear stiffness and damping in rocking of circular and strip foundations. *Bulletin of Earthquake Engineering*, jun 2014, **12**(3):1177–1200.

[138] Winkler E. Vorträge über Eisenbahnbau, Heft 1, 2, Verlag H. *Dominicus, Prag*, 1867.

[139] Rayleigh L. Theory of Sound f 109. *Ed*, 1877, 1:93.

[140] Brune J. N. Tectonic stress and the spectra of seismic shear waves from earthquakes. *Journal of geophysical research*, 1970, **75**(26):4997–5009.

[141] Moffatt H. K. Euler's disk and its finite-time singularity. *Nature*, 2000, **404**(6780):833.

[142] Engh G. v. d., Nelson P., and Roach J. Analytical dynamics: numismatic gyrations. *Nature*, 2000, **408**(6812):540.

[143] Bachmann H., Wenk T., Baumann M., and Lestuzzi P. Der neue ETH-Erdbebensimulator. *Schweizer Ingenieur und Architekt*, 1999, 4:63–67.

[144] NDI O. C. H. D. Northern Digital Inc., Waterloo, Ontario, Canada, 2009.

[145] Kalliontzis D., Sritharan S., and Schultz A. Improved Coefficient of Restitution Estimation for Free Rocking Members. *Journal of Structural Engineering*, dec 2016, **142**(12):06016002: 1–7.

[146] Chatzis M. N., Espinosa M. G., and Smyth A. W. Examining the Energy Loss in the Inverted Pendulum Model for Rocking Bodies. *Journal of Engineering Mechanics*, may 2017, **143**(5):04017013: 1–12.

[147] ElGawady M. A., Ma Q., Butterworth J. W., and Ingham J. Effects of interface material on the performance of free rocking blocks. *Earthquake Engng Struct Dyn*, apr 2011, **40**(4):375–392.

[148] Wittich C. and Hutchinson T. Rocking bodies with arbitrary interface defects: Analytical development and experimental verification. *Earthquake Engng Struct Dyn*, jul 2017, pages 1–17.

[149] Rezaeian S. and Der Kiureghian A. A stochastic ground motion model with separable temporal and spectral nonstationarities. *Earthquake Engng Struct Dyn*, 2008, **37**(13):1565–1584.

[150] Rezaeian S. and Der Kiureghian A. Simulation of synthetic ground motions for specified earthquake and site characteristics. *Earthquake Engng Struct Dyn*, 2010, **39**(10):1155–1180.

[151] Broccardo M. and Der Kiureghian A. Simulation of near-fault ground motions using frequency-domain discretization. In *10th U.S. NCEE*, pages 1–11, Anchorage, Alaska, 2014.

[152] Broccardo M. and Dabaghi M. A spectral-based stochastic ground motion model with a non-parametric time-modulating function. In *12th international conference on structural safety and reliability, Vienna*, pages 1–10, 2017.

[153] Wasserman L. *All of Statistics: A Concise Course in Statistical Inference*. Springer Science & Business Media, New York, 2013.

[154] Kolmogorov A. N. *Sulla determinazione empirica di una legge di distribuzione*. 1933.

[155] Smirnoff N. Sur les écarts de la courbe de distribution empirique. *Matematicheskii Sbornik*, 1939, **48**(1):3–26.

[156] Massey F. J. The Kolmogorov-Smirnov Test for Goodness of Fit. *Journal of the American Statistical Association*, mar 1951, **46**(253):68–78.

[157] Giouvanidis A. I. and Dimitrakopoulos E. G. Rocking amplification and strong-motion duration. *Earthquake Engng Struct Dyn*, 2018, **0**(0).

[158] Vassiliou M. F., Mackie K. R., and Stojadinović B. A finite element model for seismic response analysis of deformable rocking frames. *Earthquake Engng Struct Dyn*, mar 2017, **46**(3):447–466.

[159] Tsiavos A., Vassiliou M. F., Mackie K. R., and Stojadinović B. R_y-μ-T_n Relations for Seismically Isolated Structures. In *COMPDYN 2013*, 2013.

[160] MATLAB. *version 9.3.0.713579 (R2017b)*. The MathWorks Inc., Natick, Massachusetts, 2017.

[161] MathWorks. MathWorks Documentation. (accessed Oct 2018).